

1. Report No. FHWA/TX-91+1180-1F		2. Government Accession No.		3. Recipient's Catalog No.	
4. Title and Subtitle DESIGN AND BEHAVIOR OF THIN WALLS IN HOLLOW CONCRETE BRIDGE PIERS AND PYLONS				5. Report Date November 1990	
				6. Performing Organization Code	
7. Author(s) A. W. Taylor, R. B. Rowell, and J. E. Breen				8. Performing Organization Report No. Research Report 1180-1F	
9. Performing Organization Name and Address Center for Transportation Research The University of Texas at Austin Austin, Texas 78712-1075				10. Work Unit No.	
				11. Contract or Grant No. Research Study 3-5-88/0-1180	
12. Sponsoring Agency Name and Address Texas State Department of Highways and Public Transportation; Transportation Planning Division P. O. Box 5051 Austin, Texas 78763-5051				13. Type of Report and Period Covered Final	
				14. Sponsoring Agency Code	
15. Supplementary Notes Study conducted in cooperation with the U. S. Department of Transportation, Federal Highway Administration Research Study Title: "Wall Thickness Criteria for Hollow Piers and Pylons"					
16. Abstract <p>This report is the final report of a three-year research program and summarizes an investigation which examined the behavior of thin-walled hollow concrete box sections such as those typically used in the cross-sections of hollow concrete bridge piers and pylons. A series of accurate and realistic scale model tests were used to document the behavior and the typical effects of walls with different unsupported length-to-thickness ratios. Analytical studies were used to verify observed behavior and to examine the effect of variables.</p> <p>This work is part of Research Project 3-5-88/0-1180 entitled, "Wall Thickness Criteria for Hollow Piers and Pylons." The research was conducted by the Phil M. Ferguson Structural Engineering Laboratory as part of the overall research programs of the Center for Transportation Research of The University of Texas at Austin. The work was supported by the Texas State Department of Highways and Public Transportation and the Federal Highway Administration under an agreement between The University of Texas at Austin and the State Department of Highways and Public Transportation.</p> <p>Liaison with the State Department of Highways and Public Transportation was maintained through their technical coordinator, Mr. David McDonald. The authors would like to particularly acknowledge the valuable contributions of Mr. McDonald who provided important information on current design and construction practices for hollow concrete bridge piers and pylons.</p> <p>The overall design, construction, testing, and analysis of data was the direct responsibility of Andrew W. Taylor, Assistant Research Engineer. He was assisted in the experimental phases by Randall B. Rowell, Assistant Research Engineer, and in the analytical phases by Tan D. Tran, Assistant Research Engineer. The overall study was directed by John E. Breen, who holds the Nasser I. Al-Rashid Chair in Civil Engineering.</p> <p>This final report is based primarily on the dissertation of the senior author, Dr. Andrew W. Taylor.</p>					
17. Key Words hollow concrete box sections, cross-sections, thin-walled, bridge piers, pylons, walls, scale model tests, length- to- thickness ratios, design			18. Distribution Statement No restrictions. This document is available to the public through the National Technical Information Service, Springfield, Virginia 22161.		
19. Security Classif. (of this report) Unclassified		20. Security Classif. (of this page) Unclassified		21. No. of Pages 318	22. Price

**DESIGN AND BEHAVIOR OF THIN WALLS
IN HOLLOW CONCRETE BRIDGE
PIERS AND PYLONS**

by

A. W. Taylor
R. B. Rowell
J. E. Breen

Research Report Number 1180-1F

Research Project 3-5-88/0-1180

Wall Thickness Criteria for Hollow Piers and Pylons

conducted for

**Texas State Department of Highways
and Public Transportation**

in cooperation with the

**U. S. Department of Transportation
Federal Highway Administration**

by the

CENTER FOR TRANSPORTATION RESEARCH

Bureau of Engineering Research

THE UNIVERSITY OF TEXAS AT AUSTIN

November 1990

NOT INTENDED FOR CONSTRUCTION,
PERMIT, OR BIDDING PURPOSES

J. E. Breen, P.E. (Texas No. 18479)

Research Supervisor

The contents of this report reflect the views of the authors, who are responsible for the facts and the accuracy of the data presented herein. The contents do not necessarily reflect the official views or policies of the Federal Highway Administration or the State Department of Highways and Public Transportation. This report does not constitute a standard, specification, or regulation.

There was no invention or discovery conceived or first actually reduced to practice in the course of or under this contract, including any art, method, process, machine, manufacture, design or composition of matter, or any new and useful improvement thereof, or any variety of plant which is or may be patentable under the patent laws of the United States of America or any foreign country.

PREFACE

This report is the final report of a three-year research program and summarizes an investigation which examined the behavior of thin-walled hollow concrete box sections such as those typically used in the cross-sections of hollow concrete bridge piers and pylons. A series of accurate and realistic scale model tests were used to document the behavior and the typical effects of walls with different unsupported length-to-thickness ratios. Analytical studies were used to verify observed behavior and to examine the effect of variables.

This work is part of Research Project 3-5-88/0-1180 entitled, "Wall Thickness Criteria for Hollow Piers and Pylons." The research was conducted by the Phil M. Ferguson Structural Engineering Laboratory as part of the overall research programs of the Center for Transportation Research of The University of Texas at Austin. The work was supported by the Texas State Department of Highways and Public Transportation and the Federal Highway Administration under an agreement between The University of Texas at Austin and the State Department of Highways and Public Transportation.

Liaison with the State Department of Highways and Public Transportation was maintained through their technical coordinator, Mr. David McDonald. The authors would like to particularly acknowledge the valuable contributions of Mr. McDonald who provided important information on current design and construction practices for hollow concrete bridge piers and pylons.

The overall design, construction, testing, and analysis of data was the direct responsibility of Andrew W. Taylor, Assistant Research Engineer. He was assisted in the experimental phases by Randall B. Rowell, Assistant Research Engineer, and in the analytical phases by Tan D. Tran, Assistant Research Engineer. The overall study was directed by John E. Breen, who holds the Nasser I. Al-Rashid Chair in Civil Engineering.

This final report is based primarily on the dissertation of the senior author, Dr. Andrew W. Taylor.

SUMMARY

Hollow concrete piers and pylons are commonly used in the construction of long-span cable-stayed and box girder bridges. Hollow sections are used because they offer the advantages of high bending and torsional stiffnesses, reduced substructure weight, and consequential savings in foundation costs. Recent designs have called for hollow piers and pylons with high wall width-to-thickness ratios. Such slender walls present the possibility of failure due to local buckling. While the local buckling behavior of thin-walled metallic compression members has been studied extensively, little is known about the corresponding behavior for thin-walled concrete members.

The objectives of this study were to investigate experimentally and analytically the behavior of hollow thin-walled concrete compression members and to obtain methods for reliably predicting their behavior. A series of tests was performed in which twelve one-fifth scale short hollow rectangular concrete pier specimens were loaded to failure under combined axial load and uniaxial bending about the weak axis. Both monolithically cast and segmentally-constructed post-tensioned specimens were tested. An analytical model was developed which predicts the strength of thin-walled hollow rectangular concrete compression members subject to simultaneous axial load and uniaxial bending. This model includes the effects of local buckling of a thin compression flange.

Based on the experimental and analytical results obtained in this study it was determined that closed box rectangular concrete compression members with wall width-to-thickness ratios less than 15 are unaffected by local compression flange buckling. Members with wall width-to-thickness ratios of 15 or greater may exhibit reduced strengths due to local compression flange buckling. No fundamental difference was observed between the behavior of monolithically cast and segmentally-constructed post-tensioned specimens, other than the slightly reduced capacities of the segmental specimens due to internal post-tensioning forces. Design guidelines for thin-walled concrete compression members are presented. These include both general criteria for methods of analysis and specific recommendations for detailing of reinforcement.

IMPLEMENTATION

The successful conclusion of this project is reflected in specific guidance to designers regarding both analysis procedures for detailing the effect of wall slenderness on cross-section capacity as well as reinforcement detailing provisions for thin-walled hollow concrete compression members. The recommendations are applicable both to cast-in-situ piers as well as segmentally constructed piers using precast sections. No comprehensive test information on such segmental construction has previously been reported.

Specific recommendations are made for changes in the AASHTO Bridge Design Specifications to reflect the reduced capacity of hollow bridge piers with wall slenderness ratios greater than fifteen. Neglect of these effects could substantially reduce the safety and reserve capacity of such important members. In addition, the current AASHTO specifications give inadequate guidance regarding the proper reinforcement detailing for hollow piers and pylons. Several specific detailing requirements are presented and recommended for inclusion in the AASHTO Bridge Design Specifications. Their adoption would ensure more consistent detailing to properly develop the strength potential of this type construction.

Table of Contents

	Page
Chapter 1..... Introduction.....	1
1.1..... Background	1
1.1.1..... Use of Hollow Sections in Bridge Piers and Pylons.....	1
1.1.2..... Wall Slenderness	1
1.2..... History.....	3
1.3..... Overview of Study	4
1.3.1..... Objectives and Scope.....	4
1.3.2..... Research Method	4
1.4..... Design Methods.....	10
1.4.1..... Design Code Provisions	10
1.4.2..... Practical Considerations Governing Wall Thickness.....	12
1.4.3..... Loading Conditions	12
1.5..... Construction Methods.....	14
1.6..... Previous Experimental and Analytical Work	15
1.6.1..... Local Stability of Rectangular Sections	15
1.6.2..... Previous Tests and Analyses of Hollow Concrete Sections..	17
1.6.3..... Previous Tests and Analyses of Isolated Concrete Plates.....	21
1.7..... Related Problems	25
1.7.1..... Folded Plates.....	25
1.7.2..... Hollow Circular Sections.....	25
1.7.3..... Marine Structures	26
1.7.4..... Effective Width of Flanged Sections	26
 Chapter 2..... Experimental Program.....	 28
2.1..... Overview	28
2.2..... Scale Modeling.....	33
2.3..... Design of Specimens.....	34

	Page
2.3.1..... Reinforcement Detailing	34
2.3.2..... Choice of Post-Tensioning Stress	49
2.4..... Materials	50
2.4.1..... Concrete	50
2.4.2..... Reinforcement.....	60
2.4.3..... Post-Tensioning Ducts.....	62
2.4.4..... Epoxy	63
2.4.5..... Grout.....	64
2.5..... Fabrication of Specimen	64
2.5.1..... Formwork and Construction Methods.....	64
2.5.2..... Mixing and Placing Concrete.....	71
2.5.3..... Epoxying	72
2.5.4..... Post-Tensioning and Grouting.....	72
2.6..... Loading Arrangement.....	73
2.6.1..... Test Machines.....	73
2.6.2..... Pin Bearings.....	77
2.6.3..... Geometric Tolerances.....	78
2.7..... Instrumentation	78
2.7.1..... Load.....	78
2.7.2..... Displacements.....	79
2.7.3..... Strains.....	81
2.7.4..... Wall Thickness and Straightness Measurements.....	88
2.8..... Test Procedure	89
2.8.1..... Data Acquisition System.....	89
2.8.2..... Steps in Testing.....	89
Chapter 3..... Experimental Results.....	92
3.1..... Overview	92
3.2..... Accuracy and Limitations of Test Data.....	92
3.3..... Test Results	97

	Page
3.3.1..... 1M10 (Monolithic, 15" x 30", 2.5" walls, $X_u/t = 10.0$)	97
3.3.2..... 2M10 (Monolithic, 12" x 24", 2.0" walls, $X_u/t = 10.0$)	102
3.3.3..... 3M14 (Monolithic, 20" x 40", 2.5" walls, $X_u/t = 14.0$)	107
3.3.4..... 4M18 (Monolithic, 20" x 40", 2.0" walls, $X_u/t = 18.0$)	112
3.3.5..... 5S9 (Segmental, 15" x 30", 2.5" walls, $X_u/t = 8.8$).....	117
3.3.6..... 6S16 (Segmental, 20" x 40", 2.0" walls, $X_u/t = 15.5$).....	122
3.3.7..... 7S22 (Segmental, 20" x 40", 1.5" walls, $X_u/t = 21.7$).....	129
3.3.8..... 8ML25 (Multiple-Lift, 20" x 40", 1.5" walls, $X_u/t = 24.7$) .	135
3.3.9..... 9MLP22 (Multiple-Lift, Post-tensioned, 20" x 40", 1.5" walls, $X_u/t = 21.7$).....	140
3.3.10..... 10ML18 (Multiple-Lift, 20" x 40", 2.0" walls, $X_u/t = 18.0$)	147
3.3.11..... 11ML34 (Multiple-Lift, 20" x 40", 1.1" walls, $X_u/t = 33.6$)	153
3.3.12..... 12S29 (Segmental, 20" x 40", 1.1" walls, $X_u/t = 29.3$)	160
3.4. Discussion of Experimental Results	167
3.4.1..... Compression Flange Behavior.....	167
3.4.2..... Axial Shortening Behavior	168
3.4.3..... Center Line Deformations	169
3.4.4..... Cracking	169
3.4.5..... Location of Failure	172
3.4.6..... Wall Slenderness Ratio	172
3.4.7..... Plane Sections Remain Plane.....	175
3.4.8..... Post-Tensioning Bars.....	176
3.4.9..... Reinforcement Details.....	176
3.4.10..... Reinforcement Ratio.....	178
3.4.11..... Concrete Strength.....	178
3.4.12..... Method of Construction.....	180
3.4.13..... Post-Tensioning Effects	183

	Page
Chapter 4..... Analytical Model.....	185
4.1..... Overview	185
4.2..... Notation.....	185
4.3..... Constitutive Models	186
4.3.1..... Concrete Constitutive Model	186
4.3.2..... Non-Post-Tensioned Reinforcing Steel Constitutive Model..	188
4.3.3..... Post-Tensioned Steel Constitutive Model.....	189
4.4..... Plate Buckling Model	189
4.4.1..... Calculation of Buckling Stress.....	189
4.4.2..... Plate Buckling in an Eccentrically Loaded Cross Section.....	196
4.4.3..... Verification of Plate Buckling Model.....	197
4.4.4..... Computer Program PLCRST	200
4.5..... Section Capacity Model.....	200
4.5.1..... Computing P and M for a Given Strain Distribution	200
4.5.2..... Computing the Axial Load - Moment Interaction Diagram..	201
4.5.3..... Computer Program HOLMP	203
Chapter 5..... Model Verification and Design Recommendations .	204
5.1..... Overview	204
5.2..... Input Data for Analytical Model.....	204
5.3..... Plate Buckling Model	208
5.3.1..... Computed Buckling Stresses of Compression Flanges.....	208
5.3.2..... Concrete Plate Buckling Parameter Study	209
5.4..... Section Capacity Model.....	213
5.4.1..... Computed Capacities of Test Specimens of Present Study...	218
5.4.2..... Computed Capacities of Test Specimens of Jobse and Moustafa	229
5.4.3..... Computed Capacities of Test Specimens of Poston et al.....	232
5.4.4..... Computed Capacities of Test Specimens of Procter	232
5.5..... Discussion of Experimental and Analytical Results	233

	Page
5.5.1..... Effect of Wall Slenderness Ratio on Section Capacity	233
5.5.2..... Interaction of Local and Overall Buckling	240
5.5.3..... Hollow Concrete Compression Member Failure Criteria	241
5.6..... Design Recommendations	248
5.6.1..... Analytical Methods	248
5.6.2..... Detailing of Hollow Concrete Cross Sections.....	250
5.6.3..... Proposed AASHTO Specifications.....	253
Chapter 6..... Summary, Conclusions and Recommendations.....	256
6.1..... Summary of Study Limitations	256
6.2..... Test Program Summary.....	256
6.3..... Analytical Model Summary.....	257
6.4..... Principal Conclusions.....	258
6.5..... Recommendations for Future Research.....	259

List of Tables

	Page
Table 1.1 Typical Cross Sections.....	5
Table 1.2 Classes of Loads Acting on Piers and Pylons.....	13
Table 2.1 Geometric Properties of Test Specimens	30
Table 2.2 Material Properties of Test Specimens	31
Table 2.3 Concrete Mix Proportions	51
Table 3.1 Summary of Test Results.....	95
Table 3.2 Taut String Line Readings of Column Center Line Deflections	96
Table 5.1 Computed Flange Buckling Stresses.....	210
Table 5.2 Experimental and Computed Capacities of Test Specimens ..	215
Table 5.3 Ratio of Experimental to Computed Capacities of Tests Specimens	216
Table 5.4 Statistical Data for Ratios of Experimental to Computed Capacities of Test Specimens.....	217
Table 5.5 Basis of Calculations for Figures 5.17 to 5.20	234
Table 5.6 Ratios of Experimental to Computed Compression Flange Failure Strains.....	243
Table 5.7 Statistical Data for Ratios of Experimental to Computed Failure Strains of Test Specimens	244

List of Figures

	Page
Figure 1.1..... Houston Ship Channel Bridge.....	2
Figure 1.2..... Brotonne Bridge.....	2
Figure 1.3..... Denny Creek Bridge.....	3
Figure 1.4..... Definition of Wall Slenderness Ratio.....	3
Figure 1.5..... Hollow Stub Column Tests by Procter	18
Figure 1.6..... Hollow Column Biaxial Bending Tests by Poston et al.....	19
Figure 1.7..... Hollow Segmental Column Tests by Jobse and Moustafa....	20
Figure 1.8..... Rectangular Plate Simply Supported on Four Edges.....	21
Figure 2.1..... Typical Tests Specimen.....	29
Figure 2.2..... Typical Lateral Reinforcement Details Used in Practice.....	35
Figure 2.3..... Typical Test Specimen Cross Section Detail	38
Figure 2.4..... Spacing of Lateral Reinforcement and Cross Ties in Test Specimens.....	39
Figure 2.5..... Cross Sections for Specimens 1M10 and 5S9.....	40
Figure 2.6..... Cross Section for Specimen 2M10.....	41
Figure 2.7..... Cross Section for Specimen 3M14.....	42
Figure 2.8..... Cross Sections for Specimens 4M18, 6S16 and 10ML18....	43
Figure 2.9..... Cross Sections for Specimens 7S22, 8ML25 and 9MLP22..	44
Figure 2.10	45
Figure 2.11	45
Figure 2.11	45
Scaled ASTM C33 Aggregates.....	55
Figure 2.12	55
Figure 2.12	55
Figure 2.12	55
Figure 2.13	57
Figure 2.13	57
Figure 2.13	57
Figure 2.14	61
Figure 2.14	61
Figure 2.14	61
Figure 2.15	61
Figure 2.15	61
Figure 2.15	61
Figure 2.16	63
Figure 2.16	63
Figure 2.16	63

	Page
Figure 2.17 Load Head Reinforcement.....	66
Figure 2.18 Completed Bottom Load Head.....	66
Figure 2.19 Reinforcement Cage for Hollow Test Section.....	67
Figure 2.20 Wall Thickness Spacer.....	67
Figure 2.21 Outer Transparent Plastic Forms.....	68
Figure 2.22 Multiple-Lift and Segmental Specimen Formwork.....	69
Figure 2.23 Pieces of a Segmental Specimen.....	69
Figure 2.24 Shear Keys.....	70
Figure 2.25 600 kip Capacity Universal Test Machine.....	74
Figure 2.26 1200 kip Capacity Test Machine, Side View.....	75
Figure 2.27 1200 kip Capacity Test Machine, Top View.....	76
Figure 2.28 1200 kip Capacity Test Machine.....	77
Figure 2.29 Pin Bearing.....	78
Figure 2.30 Instrument Frames Installed on Specimen.....	79
Figure 2.31 Instrument Frames.....	80
Figure 2.32 Load Head and Test Machine Displacements.....	82
Figure 2.33 Taut String Line Schematic.....	83
Figure 2.34 Taut String Line Installed on Specimen.....	83
Figure 2.35 Gage Positions on Compression Face, Specimen 1M10.....	84
Figure 2.36 Gage Positions on Compression Face, Specimen 2M10.....	85
Figure 2.37 Gage Positions on Compression Face, Specimen 3M14.....	85
Figure 2.38 Gage Positions on Compression Face, Specimens 4M18 and 10ML18.....	86
Figure 2.39 Gage Positions on Compression Face, Specimen 5S9.....	86
Figure 2.40 Gage Positions on Compression Face, Specimen 6S16.....	87
Figure 2.41 Gage Positions on Compression Face, Specimens 7S22, 8ML25, 9MLP22.....	87
Figure 2.42 Gage Positions on Compression Face, Specimens 11ML34 and 12S29.....	88

	Page
Figure 2.43 Measured Deviation of Wall Thickness	
From Design Wall Thickness.....	90
Figure 3.1 Specimen 3M14 Strain Distribution	
Over Compression Flange	94
Figure 3.2 Specimen 10ML18 Strain Distribution	
Over Compression Flange	94
Figure 3.3 Specimen 1M10 Compression Flange	99
Figure 3.4 Specimen 1M10 Tension Flange.....	99
Figure 3.5 Specimen 1M10 Compression Flange Close-Up.....	100
Figure 3.6 Specimen 1M10 Bottom Load Head	100
Figure 3.7 Specimen 1M10 Compression Flange Profile.....	101
Figure 3.8 Specimen 1M10 Cross Section Strain Distribution.....	101
Figure 3.9 Specimen 1M10 Moment-Curvature Curve	102
Figure 3.10 Specimen 2M10 Compression Flange	103
Figure 3.11 Specimen 2M10 Compression Flange Close-Up.....	104
Figure 3.12 Specimen 2M10 "Tension" Flange.....	104
Figure 3.13 Specimen 2M10 Failure Region Close-Up.....	105
Figure 3.14 Specimen 2M10 Bottom Load Head	105
Figure 3.15 Specimen 2M10 Compression Flange Profile.....	106
Figure 3.16 Specimen 2M10 Cross Section Strain Distribution.....	106
Figure 3.17 Specimen 2M10 Moment-Curvature Curve	107
Figure 3.18 Specimen 3M14 Compression Flange	108
Figure 3.19 Specimen 3M14 Tension Flange.....	109
Figure 3.20 Specimen 3M14 Compression Flange Close-Up.....	109
Figure 3.21 Specimen 3M14 Reinforcement in Failure Zone.....	110
Figure 3.22 Specimen 3M14 Aerial View.....	110
Figure 3.23 Specimen 3M14 Compression Flange Profile.....	111
Figure 3.24 Specimen 3M14 Cross Section Strain Distribution.....	111
Figure 3.25 Specimen 3M14 Moment-Curvature Curve	112
Figure 3.26 Specimen 4M18 Compression Flange	113

	Page
Figure 3.27 Specimen 4M18 "Tension" Flange	114
Figure 3.28 Specimen 4M18 Compression Flange Close-Up	114
Figure 3.29 Specimen 4M18 Side Face	115
Figure 3.30 Specimen 4M18 Compression Flange Profile.....	115
Figure 3.31 Specimen 4M18 Cross Section Strain Distribution.....	116
Figure 3.32 Specimen 4M18 Moment-Curvature Curve	116
Figure 3.33 Specimen 5S9 Aerial View	119
Figure 3.34 Specimen 5S9 Compression Flange.....	119
Figure 3.35 Specimen 5S9 Compression Flange Close-Up	120
Figure 3.36 Specimen 5S9 Side Face Close-Up	120
Figure 3.37 Specimen 5S9 Compression Flange Profile.....	121
Figure 3.38 Specimen 5S9 Cross Section Strain Distribution	121
Figure 3.39 Specimen 5S9 Moment-Curvature Curve.....	122
Figure 3.40 Specimen 6S16 Compression Flange.....	124
Figure 3.41 Specimen 6S16 "Tension" Flange.....	125
Figure 3.42 Specimen 6S16 Compression Flange Close-Up.....	125
Figure 3.43 Specimen 6S16 "Tension" Flange Close-Up.....	126
Figure 3.44 Specimen 6S16 Side Face Close-Up.....	126
Figure 3.45 Specimen 6S16 Post-Tensioning Anchorages	127
Figure 3.46 Specimen 6S16 Compression Flange Profile	127
Figure 3.47 Specimen 6S16 Cross Section Strain Distribution.....	128
Figure 3.48 Specimen 6S16 Moment-Curvature Curve	128
Figure 3.49 Specimen 7S22 Compression Flange	130
Figure 3.50 Specimen 7S22 "Tension" Flange.....	131
Figure 3.51 Specimen 7S22 Compression Flange Close-Up.....	131
Figure 3.52 Specimen 7S22 Interior View of Post-Tensioning Bar	132
Figure 3.53 Specimen 7S22 Interior View of Load Head.....	132
Figure 3.54 Specimen 7S22 Side Face Close-Up.....	133
Figure 3.55 Specimen 7S22 Compression flange Profile	133
Figure 3.56 Specimen 7S22 Cross Section Strain Distribution.....	134

	Page
Figure 3.57 Specimen 7S22 Moment-Curvature Curve	134
Figure 3.58 Specimen 8ML25 Compression Flange.....	136
Figure 3.59 Specimen 8ML25 "Tension" Flange	136
Figure 3.60 Specimen 8ML25 Compression Flange Close-Up	137
Figure 3.61 Specimen 8ML25 Aerial View	137
Figure 3.62 Specimen 8ML25 Side Face Close-Up	138
Figure 3.63 Specimen 8ML25 Compression Flange Profile.....	138
Figure 3.64 Specimen 8ML25 Cross Section Strain Distribution	139
Figure 3.65 Specimen 8ML25 Moment-Curvature Curve.....	139
Figure 3.66 Specimen 8ML25 Axial Shortening Curve	140
Figure 3.67 Specimen 9MLP22 Compression Flange.....	142
Figure 3.68 Specimen 9MLP22 "Tension" Flange.....	142
Figure 3.69 Specimen 9MLP22 Compression Flange Close-Up.....	143
Figure 3.70 Specimen 9MLP22 Interior View of Post-Tensioning Bar ...	143
Figure 3.71 Specimen 9MLP22 Side Face Close-Up.....	144
Figure 3.72 Specimen 9MLP22 Compression Flange Profile.....	144
Figure 3.73 Specimen 9MLP22 Cross Section Strain Distribution	145
Figure 3.74 Specimen 9MLP22 Compression Flange Strains at Mid Height.....	145
Figure 3.75 Specimen 9MLP22 Moment-Curvature Curve.....	146
Figure 3.76 Specimen 9MLP22 Axial Shortening Curve	146
Figure 3.77 Specimen 10ML18 Compression Flange	148
Figure 3.78 Specimen 10ML18 "Tension" Flange.....	149
Figure 3.79 Specimen 10ML18 Compression Flange Close-Up.....	149
Figure 3.80 Specimen 10ML18 Side Face Close-Up.....	150
Figure 3.81 Specimen 10ML18 Compression Flange Displacement at Failure.....	150
Figure 3.82 Specimen 10ML18 Compression Flange Profile	151
Figure 3.83 Specimen 10ML18 Cross Section Strain Distribution.....	151

	Page
Figure 3.84 Specimen 10ML18 Compression Flange	
Strains at Mid-Height.....	152
Figure 3.85 Specimen 10ML18 Moment-Curvature Curve	152
Figure 3.86 Specimen 10ML18 Axial Shortening Curve.....	153
Figure 3.87 Specimen 11ML34 Compression Flange	155
Figure 3.88 Specimen 11ML34 "Tension" Flange.....	155
Figure 3.89 Specimen 11ML34 Compression Flange Close-Up.....	156
Figure 3.90 Specimen 11ML34 Compression Flange	
Displacement at Failure.....	156
Figure 3.91 Specimen 11ML34 Side Face Close-Up.....	157
Figure 3.92 Specimen 11ML34 Compression Flange Profile	157
Figure 3.93 Specimen 11ML34 Cross Section Strain Distribution.....	158
Figure 3.94 Specimen 11ML34 Compression Flange	
Strains at Mid-Height.....	158
Figure 3.95 Specimen 11ML34 Moment-Curvature Curve	159
Figure 3.96 Specimen 11ML34 Axial Shortening Curve.....	159
Figure 3.97 Specimen 12S29 Compression Flange.....	161
Figure 3.98 Specimen 12S29 "Tension" Flange	162
Figure 3.99 Specimen 12S29 Compression Flange Close-Up	162
Figure 3.100..... Specimen 12S29 Interior View of Failure Region.....	163
Figure 3.101..... Specimen 12S29 Interior View of Post-Tensioning Bar.....	163
Figure 3.102..... Specimen 12S29 Post-Tensioning Anchorage.....	164
Figure 3.103..... Specimen 12S29 Side Face Close-Up	164
Figure 3.104..... Specimen 12S29 Compression Flange Profile.....	165
Figure 3.105..... Specimen 12S29 Cross Section Strain Distribution.....	165
Figure 3.106..... Specimen 12S29 Compression Flange	
Strains at Mid-Height.....	166
Figure 3.107..... Specimen 12S29 Moment-Curvature Curve.....	166
Figure 3.108..... Specimen 12S29 Axial Shortening Curve	167
Figure 3.109..... Transverse Stress Isobars in an Edge-Loaded Plate.....	170

	Page
Figure 3.110..... Maximum Transverse Tensile Stress vs. Extent of Loaded Area	171
Figure 3.111..... Moment-Curvature Data for Monolithic and Multiple-Lift Specimens.....	174
Figure 3.112..... Moment Curvature Data for Segmental Specimens.....	174
Figure 3.113..... Moment-Curvature Data for Specimens 3M14 and 4M18	179
Figure 3.114..... Moment-Curvature Data for Specimens 1M10 and 5S9	182
Figure 3.115..... Moment-Curvature Data for Monolithic and Segmental Specimens	183
Figure 3.116..... Moment-Curvature Data for Specimens 8ML25 and 9MLP22	184
Figure 4.1..... Hognestad Constitutive Model.....	187
Figure 4.2..... Compression Flange of Hollow Rectangular Cross Section .	190
Figure 4.3..... Local Wall Buckling in a Square and Rectangular Cross Section.....	190
Figure 4.4..... Buckling Coefficient k for Various Boundary Conditions....	191
Figure 4.5..... Typical Family of Curves Defining k and m for Plate With Long Edges Elastically Restrained Against Rotation ...	194
Figure 4.6..... Definitions of Initial and Tangent Concrete Moduli	195
Figure 4.7..... Comparison of Plate Buckling Model With Experiments of Swartz.....	199
Figure 4.8..... Comparison of Plate Buckling Model With Experiments of Ernst.....	199
Figure 4.9..... Cross Section Strain Distribution.....	201
Figure 4.10 Typical Interaction Diagram	202
Figure 4.11 Typical Moment-Curvature Diagram for Constant P	202
Figure 5.1..... Effect of Concrete Strength on Plate Buckling Stress.....	211
Figure 5.2..... Method of Comparing Observed and Calculated Capacities..	214
Figure 5.3..... Interaction Diagrams for Specimen 1M10	218
Figure 5.4..... Interaction Diagrams for Specimen 2M10	220

	Page
Figure 5.5..... Interaction Diagrams for Specimen 3M14	220
Figure 5.6..... Interaction Diagrams for Specimen 4M18	222
Figure 5.7..... Interaction Diagrams for Specimen 5S9	224
Figure 5.8..... Interaction Diagrams for Specimen 6S16.....	224
Figure 5.9..... Interaction Diagrams for Specimen 7S22.....	225
Figure 5.10 Interaction Diagrams for Specimen 8ML25	226
Figure 5.11 Interaction Diagrams for Specimen 9MLP22.....	226
Figure 5.12 Interaction Diagrams for Specimen 10ML18.....	227
Figure 5.13 Interaction Diagrams for Specimen 11ML34.....	228
Figure 5.14 Interaction Diagrams for Specimen 12S29	229
Figure 5.15 Interaction Diagrams for Specimen 1 of Jobse and Moustafa	230
Figure 5.16 Interaction Diagrams for Specimen 2A of Jobse and Moustafa	231
Figure 5.17 Experimental/Analytical Results Excluding Local Wall Buckling, and Excluding Non-Post-Tensioned Reinforcement in Segmental Specimens	235
Figure 5.18 Experimental/Analytical Results Including Local Wall Buckling, and Excluding Non-Post-Tensioned Reinforcement in Segmental Specimens	235
Figure 5.19 Experimental/Analytical Results Excluding Local Wall Buckling, and Including Non-Post-Tensioned Reinforcement in Segmental Specimens	236
Figure 5.20 Experimental/Analytical Results Including Local Wall Buckling, and Including Non-Post-Tensioned Reinforcement in Segmental Specimens	236
Figure 5.21 Data From Figure 5.17 With Proposed Designb Curve.....	239
Figure 5.22 Failure Strain Ratio vs. Wall Slenderness Ratio.....	245
Figure 5.23 Definition of Wall Slenderness Ratio.....	254

Chapter 1

Introduction

1.1. Background

1.1.1. *Use of Hollow Sections in Bridge Piers and Pylons*

Hollow concrete piers and pylons are often used in the construction of long-span box girder and cable-stayed bridges. Hollow sections are used because they offer the advantages of high bending and torsional stiffnesses, reduced substructure weight, and consequential savings in foundations costs. Hollow sections are particularly attractive for tall piers and pylons where bending moments may dominate the design, and for segmental box girder bridges built using the balanced cantilever method, where the bending and torsional stiffnesses of the pier shaft are important. A survey of domestic and foreign bridge designers conducted in 1980 indicated that 81% of the bridge piers constructed between 1960 and 1980 over 100 feet tall had hollow cross sections¹.

Figures 1.1 to 1.3 show examples of bridges which incorporate hollow piers and pylons. The Houston Ship Channel Bridge was constructed using the balanced cantilever method, as shown in Figure 1.1. The piers are rectangular in cross section, measuring 38 by 20 feet with walls 24 inches thick. The Brotonne Bridge near Rouen, France, Figure 1.2, is a cable-stayed bridge incorporating hollow pylons which are roughly octagonal in cross section. At the base each pylon measures 30 feet on a side overall, with a wall thickness of about 20 inches. The pier shafts of the Denny Creek Bridge near Seattle, Figure 1.3, are rectangular in cross section. They measure 16 by 10 feet and the wall thickness is 24 inches.

1.1.2. *Wall Slenderness*

With the increasing use of higher strength concretes, and with improved construction methods, it is now possible to construct hollow concrete sections with relatively slender walls. Figure 1.4 defines the "wall slenderness ratio:" the unsupported wall width divided by the wall thickness. Hollow rectangular sections with wall slenderness ratios in the range of 15 to 20 are now common, and sections

with slenderness ratios up to 26.8 have been constructed¹⁰. Such slender walls present the possibility of failure due to local buckling. While the local buckling behavior of thin-walled metallic compression members has been studied extensively, little is known about the corresponding behavior for thin-walled concrete members.



Figure 1.1: Houston Ship Channel Bridge

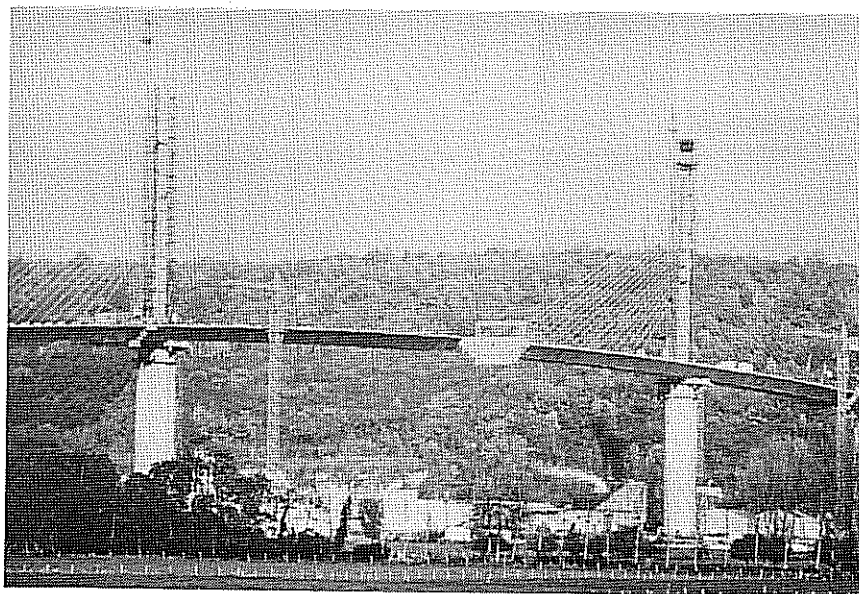


Figure 1.2: Brotonne Bridge

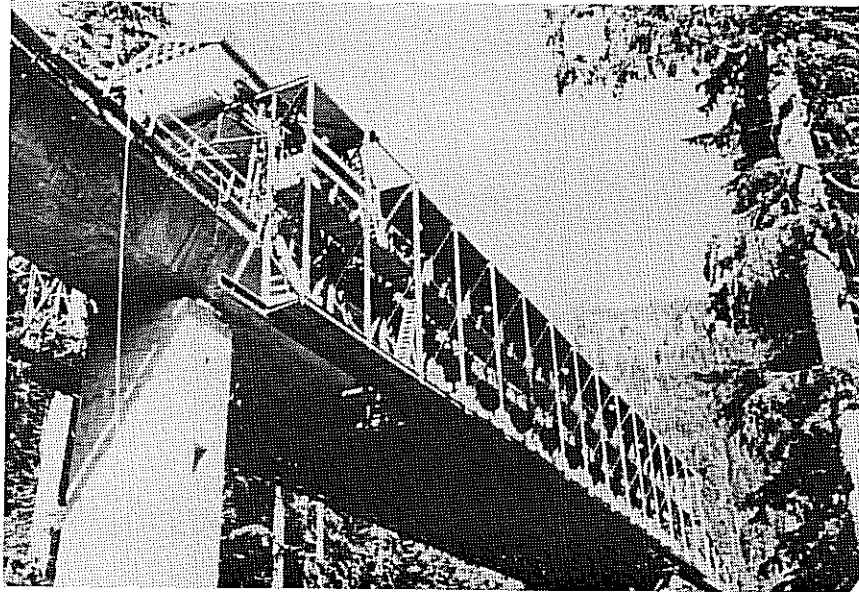
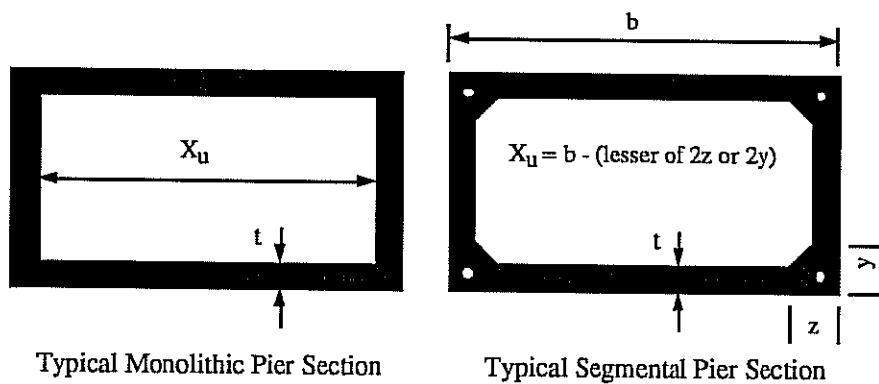


Figure 1.3: Denny Creek Bridge



$$\text{Wall Slenderness Ratio} = \frac{X_u}{t}$$

Figure 1.4: Definition of Wall Slenderness Ratio

1.2. History

Table 1.1 shows cross sections of hollow concrete bridge piers and pylons built between 1963 and 1990. The listing is not exhaustive, but it is representative of the hollow sections constructed during that period. It can be seen that hollow piers and pylons take on a wide variety of cross-sectional shapes, but the rectangular section is

the most common. It can also be seen that at least two bridges have been built with piers having wall slenderness ratios well over 20: the Mosel River Bridge in 1972 with wall slenderness ratio 26.8, and the Glade Creek Bridge in 1988 with wall slenderness ratio 23.1. Not all of the piers and pylons shown in Table 1.1 are hollow over their entire height. Short solid sections are sometimes incorporated at locations where a pier or pylon might be impacted by a vehicle or ship, at the top of a pier where loads are transferred from the superstructure, and near the cable anchorages of pylons.

1.3. Overview of Study

1.3.1. Objectives and Scope

The objectives of this research program are to investigate experimentally and analytically the behavior of thin-walled concrete compression members and to obtain methods for reliably predicting their behavior. There are four main elements of the study: a review of the state-of-the-art of analysis and design of hollow concrete piers and pylons; a program of experiments on one-fifth scale hollow concrete pier specimens; an analytical treatment of the local buckling behavior of thin-walled concrete compression members; and a set of proposed design guidelines for hollow bridge piers and pylons.

The scope of the research is limited to hollow concrete sections with planar walls subject to simultaneous compression and uniaxial bending about the weak axis. No consideration is given to overall, or "Euler", column buckling, seismic loading or ductility. Both monolithic and segmental post-tensioned construction are addressed. The maximum wall slenderness ratio explored in the experimental program was 33.6 and the concrete strength range covered by the experiments was approximately 3500 to 8000 psi cylinder strength.

1.3.2. Research Method

The first phase of the research was a comprehensive review of the domestic and foreign literature dealing with hollow concrete bridge piers and pylons. Related topics were also investigated, including the behavior of thin-walled metallic

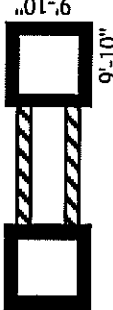
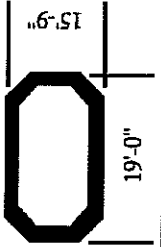



NAME	LOCATION	YEAR	BRIDGE TYPE	MAX. X_u/t	t in.	HEIGHT ft.	CROSS SECTION	REF's.
Bougen Bridge	Brest, France	1963	Cast in place segmental box girder, 3 spans. Cast-in-place dual piers with architectural infill walls.	10.5	9.5	148		56
Eifelbrücke Bridge	Eifel, W. Germany	1965	Cast-in-place "mushroom" pier heads with flat plate spans, 9 spans. Cast-in-place piers.	7.0	14	328		57 58 59
Oleron Viaduct	Oleron Island, France	1966	Precast segmental box girder, 46 spans. Cast-in-place piers	16.7	12	82		60
Mosel River Bridge	Dieblich, W. Germany	1972	Steel box girder, 6 spans. Cast-in-place piers	26.8	10	408		10
Ravensboch Valley Bridge	Valkenburg, Holland	1975	Incrementally launched segmental box girder, 8 spans. Cast-in-place piers.	12.5	16	77		61

Table 1.1: Typical Cross Sections

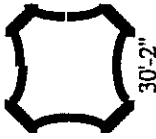

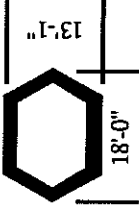

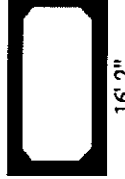
NAME	LOCATION	YEAR	BRIDGE TYPE	MAX. Xu/t	t in.	HEIGHT ft.	CROSS SECTION	REF's.
Brotonne Bridge (Pylons Below Deck)	Rouen, France	1977	Precast / cast-in-place segmental cable-stayed box girder, 3 main spans. Cast-in-place pylons.	Approx. 7	20 (min.)	160 (below deck)		62
Denny Creek Bridge	Seattle, Washington	1978	Cast-in-place box girder, 20 spans. Cast-in-place piers.	6.0	24	160		63
Salingsund Bridge	Thisted, Denmark	1978	Precast segmental box girder, 19 spans. Cast-in-place piers.	7.8	16	72		64
Kochertal Bridge	Heilbronn W. Germany	1979	Cast-in-place segmental box girder, 9 spans. Cast-in-place piers.	15.0	36	600		65
Seven Mile Bridge	Monroe County, Florida	1980	Precast segmental box girder, 266 spans. Precast segmental piers.	14.8	10	58		66

Table 1.1 (Continued): Typical Cross Sections

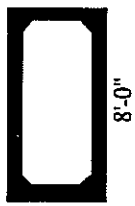

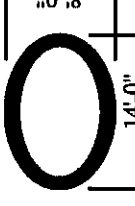

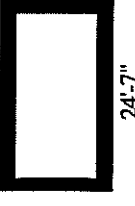
NAME	LOCATION	YEAR	BRIDGE TYPE	MAX. Xu/t	t in.	HEIGHT ft.	CROSS SECTION	REF's.
Escatawpa River Bridge	Jackson County Mississippi	1983	Multiple spans, precast segmental piers.	7.0	8	78		67
Houston Ship Channel Bridge	Pasadena, Texas	1982	Cast-in-place segmental box girder, 3 main spans. Cast-in-place piers.	17.0	24	161		68 69
Sunshine Skyway Bridge Approach Piers	Tampa, Florida	1983	Cable-stayed precast segmental box girder. Precast segmental approach piers.	N.A.	10	130		70
Nantua Viaduct	Nantua, France	1985	Precast segmental box girder, 10 spans. Cast-in-place piers.	10.2	16	253		71
Alex Fraser Bridge	Vancouver, Canada	1986	Cable-stayed steel plate girder, 3 main spans. H-shaped cast-in-place pylons.	10.5	24	506		72

Table 1.1 (Continued) Typical Cross Sections


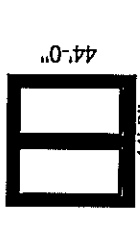
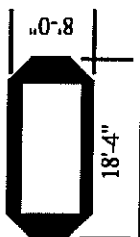


NAME	LOCATION	YEAR	BRIDGE TYPE	MAX. X_u/t	t in.	HEIGHT ft.	CROSS SECTION	REF's.
Schottwien Bridge	Schottwien, Austria	1988	Cast-in-place segmental box girder, 4 spans. Cast-in-place piers.	18.6	20	258		73
Glade Creek Bridge	Beckley, West Virginia	1988	Steel truss, 3 spans. Cast-in-place hourglass- shaped piers.	23.1	21	351		12
Dessouk Bridge	Dessouk, Egypt	1988	Cast-in-place segmental box girder, 3 spans. Cast-in-place piers.	8.9	18.5	65		74
Houston Ship Channel Bridge Approach Piers	Baytown, Texas	1990	Cable-stayed steel plate girder, 3 main spans. Cast-in-place piers.	12.7	12	135		75
Houston Ship Channel Bridge Pylon Legs	Baytown, Texas	1990	Cable-stayed steel plate girder, 3 main spans. Double diamond-shaped cast-in-place pylons.	16	12	440		75

Table 1.1 (Continued): Typical Cross Sections

compression members, buckling of concrete plates, scale model testing of concrete structures, and bridge construction practices. Bridge engineers were consulted personally regarding certain specific bridge designs. This literature review provided a basis for formulating the subsequent experimental program and analytical model.

The experimental program consisted of compression tests to failure of twelve one-fifth scale hollow pier specimens. The cross section shape of the specimens was rectangular, with a 2:1 aspect ratio. Eight of the specimens were monolithic and four were post-tensioned segmental. The specimen length was chosen so that overall Euler buckling was prevented, but local plate buckling could occur. The wall slenderness ratio ranged from 8.8 to 33.6. The specimens were loaded by an eccentric axial load to induce simultaneous compression and uniaxial bending about the weak axis. Instrumentation included measurements of load, reinforcement strains, and displacements, including the displaced shape of the compression face of the section. The principal variables investigated in the experimental program were wall slenderness, monolithic vs. segmental construction, degree of post-tensioning (some or none), concrete strength, and reinforcement details.

The analytical model was developed in two stages. First, a model was derived for the critical buckling stress of a slender concrete plate subject to in-plane uniformly distributed loads along two opposite edges. Material nonlinearities, the presence of reinforcement, and elastic rotational restraints along the two unloaded edges were taken into account. This model was implemented in a computer program called PLCRST and a parameter study was conducted. Second, the results of the concrete plate buckling model were incorporated in a computer program, called HOLMP, which predicts overall section capacity for hollow thin-walled concrete compression members. In this program the capacity of the section may be limited by either material failure or local wall buckling. The section capacity model was verified by comparison with experimental results.

On the basis of the experimental observations and analytical modeling design guidelines were developed for hollow thin-walled concrete compression members. These guidelines are presented in the form of suggested provisions for the American Association of State Highway and Transportation Officials *Standard Specifications for Highway Bridges*³.

1.4. Design Methods

1.4.1. Design Code Provisions

A brief review is given here of the major design codes in the United States and Europe which could be applied in the design of thin-walled hollow concrete compression members.

The United States concrete building design code, ACI 318-89 *Building Code Requirements for Reinforced Concrete*², contains no specific provisions dealing with thin-walled compression members. However it does contain some related provisions which could be interpreted as applying to thin-walled sections. Chapter 14 of the specification addresses the design of axially loaded concrete walls. Section 14.3 describes requirements for reinforcement details in walls. Section 14.4 requires that walls be treated as compression members, and that stability and secondary moments must be considered. Chapter 19 applies to thin shells and folded plate structures. Section 19.2.8 requires a stability analysis of thin shells, and the associated commentary specifies several factors to consider in the analysis: initial imperfections, large deflections, creep and shrinkage, inelasticity, cracking, the influence of reinforcement, and deformations of supports. Section 19.4 concerns reinforcement of thin shells, and lays out requirements for minimum reinforcement, maximum spacing and some details peculiar to thin shells.

The United States AASHTO *Standard Specifications for Highway Bridges*³ makes no reference to hollow concrete compression members and contains no specific provisions regarding the stability of walls. A general requirement for the stability analysis of slender compression members is set out in Section 8.15.4. Minimal guidance is provided for detailing reinforcement in walls.

Guidance for minimum wall thicknesses of concrete chimneys is provided by the American Concrete Institute Draft Standard ACI 307-XX⁴. The Standard does not specifically address local stability of circular sections, but most of the minimum wall thickness requirements are apparently imposed to guard against wall buckling. The minimum allowed wall thickness is 6 inches when the inside chimney diameter is less than 20 feet, an 8 inch minimum thickness is imposed for chimneys taller than 300

feet, and the minimum thickness must be increased one-eighth inch for every foot increase in internal diameter above 28 feet.

The European *CEB-FIP Model Code for Concrete Structures*⁵ does not specifically mention hollow concrete sections, but it does contain some provisions regarding plates subject to in-plane loads. Section 9.2.3 requires a second order analysis for slender plates, but does not specify the slenderness ratio which defines a plate as being slender. Section 18.1 contains provisions for minimum reinforcement in walls.

The Swiss concrete design code SIA-162⁶ makes no specific reference to thin-walled concrete compression members. Section 3.26 addresses the safety of concrete panels and requires a second order analysis for slender panels. The same requirement is imposed on thin shells in Section 3.27.

The German specification DIN 1045⁷, Section 25.2 contains specific provisions governing thin-walled concrete compression members. The absolute minimum wall thickness permitted for cast-in-place thin-walled members is 4 inches, and the limit for plant-manufactured precast members is 2 inches. (Presumably such thin walls would contain only a single layer of reinforcement). If the wall slenderness ratio is greater than or equal to 10, local wall stability must be investigated according to Section 25.5. Section 25.5 deals with walls, and Section 25.5.4.2 gives formulas for "effective wall heights" for slender walls simply supported on two, three or four edges. These formulas are derived from classical elastic plate buckling theory. Section 25.5.4.3 specifies that once effective wall heights have been determined the general provisions for safety of slender columns must be applied, as outlined in Sections 17.4 and 17.9.

The New Zealand *Code of Practice for the Design of Concrete Structures*⁸ does not specifically address thin-walled hollow concrete compression members. However, it does contain extensive provisions governing the design of walls. Special attention is given to detailing requirements for shear walls designed to resist lateral earthquake loads. Section 10.3.2 stipulates that the unsupported length or width of bearing walls shall not be greater than 25 times the wall thickness.

In summary, most of the major United States and European Codes can be interpreted as requiring a stability analysis of slender plates subject to in-plane loads;

however, little guidance is given on what constitutes a "slender plate." Other than the German specification none of the codes specifically address local buckling of thin-walled hollow concrete compression members. The German provisions are based on a simplified linear elastic buckling analysis which does not reflect the true boundary conditions of the component plates of a hollow section, nor the actual material properties. In the German specification further calculations of safety against wall instability are referenced to code provisions which were originally derived for columns.

1.4.2. *Practical Considerations Governing Wall Thickness*

Besides the design code restrictions on wall slenderness discussed above, there are some practical considerations which limit the thickness of walls. First, in very thin walls the reinforcement cages interfere with concrete placement. Normally walls are reinforced with two curtains of steel, one near each face. Code requirements for minimum concrete cover over reinforcement, combined with a minimum practical space between reinforcement cages of about 4 inches limit the minimum wall thickness to about 8 inches. Second, as walls become thinner the deleterious effects of construction errors in thickness and flatness become more significant. The minimum wall thickness for any hollow pier or pylon actually constructed appears to be 8 inches, and the minimum thickness used by many designers is evidently 10 inches. The 1983 edition of *Beton-Kalender*⁹, the annual publication outlining current German practice, states that "box piers are built with walls 8 to 12 inches thick." One might conceive of an extreme value of a practically feasible thin-walled concrete section as a rectangular pier measuring about 36 by 18 feet (see typical pier sizes in Table 1.1) with 10 inch thick walls. Such a hypothetical limit would have a slenderness ratio of 41.2. Although such a pier will probably never be constructed, this demonstrates that the practical upper limit of wall slenderness for thin-walled concrete compression members is about 40. The highest wall slenderness achieved in an actual bridge pier appears to be 26.8.

1.4.3. *Loading Conditions*

Hollow piers and pylons are subject to a wide range of loading types and

intensities over the life of a bridge. Throughout the construction phase, under service conditions, under occasional overloads, and during repair and maintenance procedures the magnitudes and points of application of loads change. Table 1.2 shows ten classes of loads and the periods when these loads are likely to affect piers and pylons.

While the designer must consider all probable combinations of these loads, two conditions most often control the pier or pylon design: the combination of dead, construction and wind loads during the construction phase; and the combination of dead, live and wind (or earthquake) loads during the service life phase of the structure.

	Construction Phase	Service Phase	Maintenance and Repair Phase
Dead Loads	•	•	•
Construction Loads	•		•
Normal Traffic Loads		•	•
Traffic Overloads		•	
Wind Loads	•	•	•
Earthquake Loads		•	
Second Order Effects	•	•	•
Thermal Loading	•	•	•
Support Movements	•	•	•
Creep and Shrinkage	•	•	•
Snow and Ice	•	•	
Ship Collision		•	

Table 1.2: Classes of Loads Acting on Piers and Pylons

During construction tall piers and pylons stand isolated and wind loads induce high bending moments. The design bending moments predicted during construction of the Mosel River Bridge¹⁰ were large enough that the tensile strength of the concrete was exceeded and a cracked moment of inertia for the pier cross section had

to be considered. The balanced free cantilever method of construction can also impose large bending moments on piers and pylons during the construction phase. With this type of construction the most severe design moments usually occur when the free cantilever has reached its maximum length, the cantilever is unbalanced by one segment, and wind loads induce an uplift force on one side of the cantilever¹¹.

During the service life phase of the structure piers and pylons are joined together by the superstructure and become part of a framework. For this configuration a detailed frame analysis of the entire bridge is required, including the effects of the usual dead, live and lateral loads, as well as the effects of shrinkage, creep and temperature changes. In the design of the Glade Creek Bridge a three-dimensional model of the entire bridge was analysed and it was found that the pier design was controlled by a biaxial bending moment case¹².

While bending moments during the construction phase or service life phase of a bridge often control design of the piers or pylons, significant axial loads must also be considered. These arise from the dead weight of the pier or pylon itself, the dead weight of the superstructure and live traffic loads. Axial loads are an especially important consideration with hollow cross sections. One of the principal advantages of hollow sections is their high bending stiffness: the moment of inertia of a solid cross section is greatly increased by spreading the material out into a thin-walled hollow section. However, in doing this the designer should avoid making the walls of the section too thin, thereby creating a danger of local wall buckling under combined axial and bending loads.

1.5. Construction Methods

Several methods are used for constructing hollow piers and pylons. The preferred method depends on factors such as whether the section is cast-in-place or precast, the complexity of the cross section and the desired architectural finish.

If a pier or pylon is cast-in-place and the cross section shape is simple, ideally rectangular with small corner fillets, then the section may be slip formed. Slip forming is a process in which the interior and exterior forms are raised slowly and continuously by hydraulic jacks. Fresh concrete is placed at the top of the forms and by the time the concrete emerges from the bottom of the forms it is strong enough to

support its own weight and the work above. Although slip forming presents some technical difficulties, once a slip forming operation is set up casting can go very quickly, often at a rate of 15 to 20 vertical feet per day. Some designers dislike the surface finish of slip-formed members.

The most common method of constructing cast-in-place piers and pylons is to use jump forms, also called climbing forms or gang forms. The member is cast in successive lifts: when the concrete of one lift has gained sufficient strength the formwork is removed and raised in preparation for the next lift. Once a casting system is worked out a lift can be constructed every two to four days.

If a pier or pylon is made of segments which are post-tensioned together, the segments are usually cast at a remote precasting yard and transported to the bridge site. The segments are "match cast" in a vertical position to insure a perfect fit at the joints: the bottom edge of each new segment is cast directly against the top edge of the previous segment. Shear keys are formed at the segment interface to provide shear resistance and to aid in alignment during assembly. When the segments are assembled on site, epoxy is placed in the joints between segments. A light temporary post-tensioning stress is then applied by high strength steel strands or threaded rods running through ducts cast in the segment walls. After the epoxy has cured, the full specified post-tensioning force is applied. Segmental construction offers the advantages of ease of erection, plant-controlled casting conditions and flexibility in fabrication scheduling. Segment sizes are often limited by transport capacities, and great care must be taken to maintain geometric control during the match casting process.

1.6. Previous Experimental and Analytical Work

1.6.1. Local Stability of Rectangular Sections

The fundamental work on the elastic stability of thin-walled, axially loaded rectangular sections was done by the National Advisory Committee for Aeronautics in the early 1940's^{13,14,15,16}. Only short, concentrically loaded compression members were considered. The wider faces of the cross section were treated as plates whose longitudinal edges were elastically restrained against rotation by the

shorter faces of the cross section. The degree of rotational restraint depends on the relative plate bending stiffnesses of the narrow and wide faces of the section. Applying appropriate boundary and compatibility conditions a solution was obtained for the buckling coefficient of a wide face. This solution was obtained in the form of transcendental equations, which allowed a range of cases to be solved by hand and the results presented in tabular form.

Most of the subsequent work on buckling of rectangular sections focused on metals, especially steel and aluminum. A great number of experimental and theoretical studies have been performed on hollow rectangular metallic sections, which have been reviewed by various authors^{17,18,19,20,21,22,23,24}. Almost all of these studies focused on the problems associated with residual stresses, post buckling strength, and "interaction buckling," the interdependence of local plate buckling and overall Euler buckling.

Thin-walled concrete sections differ from metallic sections in several important respects. First, the material behavior for steel sections is usually modeled as elastoplastic, while the material behavior of concrete is characterized by nonlinear ascending and descending branches of the stress-strain curve. Second, residual stresses are not present in concrete sections, as they are in metallic sections (though a uniform initial strain is sometimes imposed on a concrete cross section by post-tensioning). Third, reinforced concrete is nonhomogeneous: the presence of steel reinforcing bars affects the bending stiffness of concrete plates, and therefore the plate buckling stress. Finally, a thin concrete plate cannot be expected to demonstrate any reliable post-buckling capacity. After initial local buckling concrete plates tend to crack. This cracking results in greatly reduced plate membrane tensile stiffness and plate bending stiffness. Because post-buckling strength depends primarily on plate membrane tensile stiffness, and to a lesser extent on plate bending stiffness, a thin concrete plate cannot develop any appreciable post buckling capacity. This has been confirmed by tests on isolated concrete plates³⁵ where the observed post-buckling strength averaged 13% of the buckling strength. In some instances there was no post-buckling strength.

Because of the differences outlined above most of the analytical results obtained for thin-walled metallic sections are not applicable to thin-walled concrete sections.

In the present study an analysis method had to be developed specifically for concrete cross sections. This analysis takes into account the concrete material nonlinearities, the presence of reinforcing steel, the presence of post-tensioning tendons, and initial concrete and steel strains caused by the post-tensioning force.

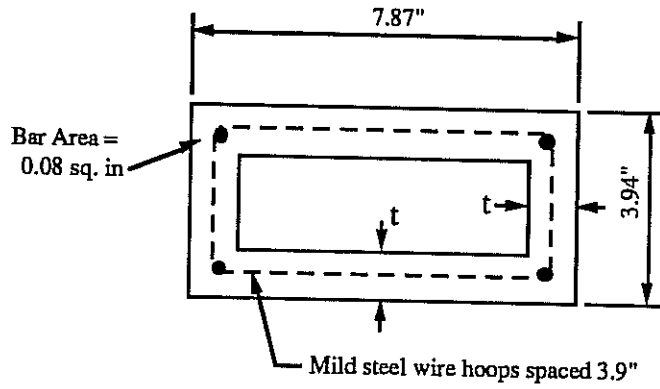
1.6.2. Previous Tests and Analyses of Hollow Concrete Sections

Seven previous studies of hollow concrete sections have been performed. These are reviewed briefly below.

Procter²⁵ reported on six small model hollow rectangular stub columns tested under concentric loading. These tests are summarized in Figure 1.5. The range of wall slenderness ratios in these tests was low, between 2.4 and 7.5, so the failure loads were apparently unaffected by local wall buckling. No special analysis procedure was developed in conjunction with these tests.

Poston et al.²⁶ tested three hollow rectangular concrete columns in biaxial bending: one with a single interior cell, one with two cells, and one with three cells. Figure 1.6 summarizes these tests. As with Procter's tests, the range of wall slenderness ratios was low, between 1.9 and 7.6. The test results were compared to the results of a finite strip program called BIMPFI (in which local wall buckling was not considered), and good agreement was found.

Jobse and Moustafa^{27, 28} tested two thin-walled hollow column specimens, both with wall slenderness ratio of 32.0. These specimens were made up of three precast box segments epoxied together and post-tensioned. Jobse's tests are summarized in Figure 1.7. These are the only known tests on thin-walled concrete sections previous to this study. Jobse and Moustafa also developed an analytical model for the capacity of the section which accounts for local instability of slender walls. However the boundary conditions assumed for the component plates were not realistic and the effects of post-tensioning may not have been properly considered.



All specimens 9.8" long
 All specimens loaded concentrically

Cube strength = 7300 psi

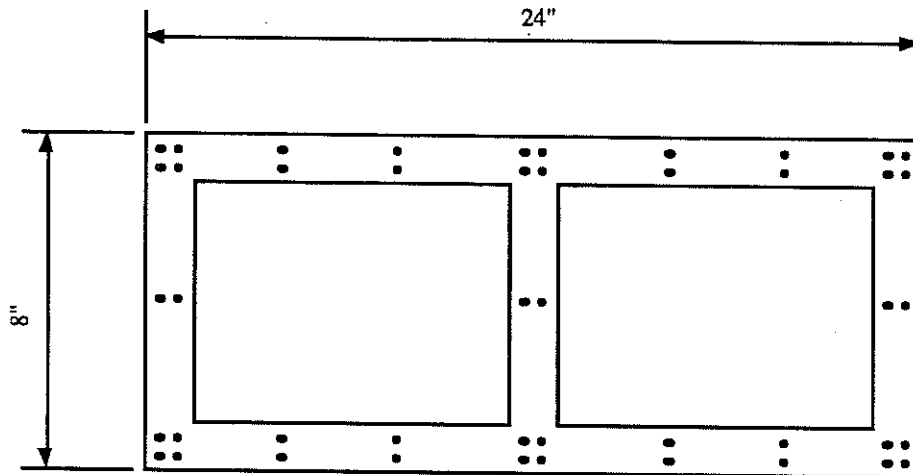
Cylinder strength = (5/6) x cube strength

$\sigma_y = 75.3$ ksi

Calculated Capacity = (Concrete Area x 0.85 x cylinder strength) + (Steel Area x σ_y)

Specimen Number	t inches	X_u/t	Concrete Area sq. in.	Steel Area sq. in.	Calculated Capacity kips	Test Capacity kips	Test Capacity / Calc. Capacity
1	0.83	7.5	16.53	.32	110	91	0.83
2	1.02	5.7	19.61	.32	126	125	0.99
3	1.24	4.3	22.82	.32	142	139	0.98
4	1.42	3.5	25.15	.32	154	162	1.05
5	1.63	2.8	27.55	.32	166	163	0.98
6	1.79	2.4	29.14	.32	175	166	0.95
7	Solid	0	30.69	.32	183	187	1.02

Figure 1.5: Hollow Stub Column Tests by Procter



Two-Cell Cross Section
(All cross sections 8" x 24" with 1, 2, or 3 cells, or solid)

All walls 2.5" thick

Concrete cover 0.5"

Lateral reinforcement in layers spaced every 2"

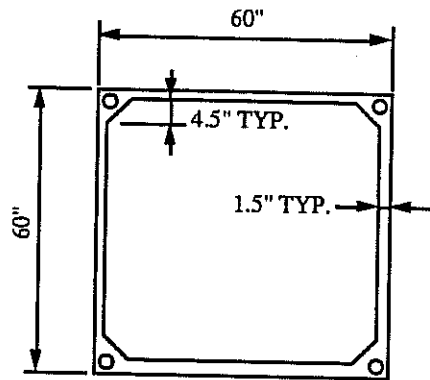
Longitudinal reinforcement content 1.5% to 1.8%

Longitudinal reinforcement yield stress = 61.1 ksi

Specimens are loaded by three hydraulic rams, one acting concentrically, and two acting at two orthogonal eccentricities to create simultaneous axial load and biaxial bending.

Spec. No.	No. Cells	X_u/t	f_c psi	Observed Failure Loads			Predictions by BIMPHI		
				Ptotal kips	Mweak kip-in	Mstrong kip-in	Ptotal kips	Mweak kip-in	Mstrong kip-in
1	1	7.6	4160	272	480	1440	272	560	1685
2	2	3.3	4300	290	590	1770	290	565	1695
3	3	1.9	5000	340	695	2085	340	640	1920
4	Solid	0	3950	329	680	2110	329	665	1955

Figure 1.6: Hollow Column Biaxial Bending Tests by Poston et al.



Three segments post-tensioned and epoxied together. Total length 180".

Each face reinforced with one layer of 4 x 4 - W4 x W4 welded wire fabric.

All walls 1.5 inches thick. $X_u/t = 32.0$

Area of post-tensioning steel = 5.0 sq. in.

Specimen Number	f_c psi	Post-Tensioning Concrete Stress psi	Eccentricity inches	Failure Load kips
1	8680	1218	4.9	1613
2A	9880	1218	20.2	1346

Figure 1.7: Hollow Segmental Column Tests by Jobse and Moustafa

Two test programs have been conducted to study the effects of lateral seismic loads on the behavior of hollow concrete compression members. Zahn, Park and Priestly²⁹ tested six hollow circular columns subject to simultaneous axial load and cyclic lateral load. One end of each column was pinned. The other end was fully fixed against rotation, but permitted to translate laterally. Application of a cyclic lateral load at the fixed end caused a plastic hinge to form at that end. The ratio of cross section diameter to wall thickness in these tests range from 4.2 to 7.3. Mander, Priestly and Park^{30,31} performed similar tests on four hollow square columns. Cyclic lateral loads were applied and the ductile behavior of the plastic hinge region was observed. The wall slenderness ratio in of these tests was 4.25. Since these two test program were concerned primarily with cross section ductility, they are not directly relevant to the present study. However, they do provide some information about the reinforcement requirements for hollow piers and pylons subject to seismic loads.

As a part of the present research program Rowell³² investigated the differences

between monolithically cast-in-place and precast segmental hollow concrete bridge piers. Based on experimental observations and an analytical study his general conclusion was that there was no difference in behavior between the two types of construction, other than the normally expected reduction in axial capacity for segmental piers, due to the post-tensioning force.

1.6.3. Previous Tests and Analyses of Isolated Concrete Plates

An analytical model for the behavior of thin-walled concrete sections must consider the buckling behavior of the component plates. In order to calibrate such a model comparisons must be made with tests on isolated slender concrete plates. The type of test most useful in the present study is one in which a thin rectangular plate, supported on all four edges, is loaded concentrically by a uniformly distributed load along two opposite edges. In most of the tests which have been performed on slender concrete plates the plate has been supported only along the two loaded edges, so that the plate performs essentially as a broad, pin-ended column. Only a few test programs have been performed with the plates supported on all four edges. These are reviewed below.

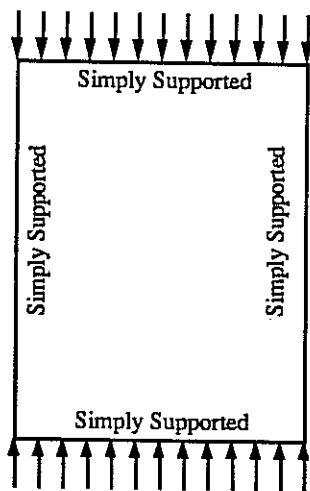


Figure 1.8: Rectangular Plate Simply Supported on Four Edges

Ernst^{33,34} studied ten concrete plates supported and loaded as in Figure 1.8. The slenderness ratios of the plates varied from 27 to 80. Five of the plates were 40 inches square, and five were 40 inches wide by 20 inches tall. Reinforcement was

placed in a single layer at the center of the plate.

In analyzing his results Ernst applied the tangent modulus approach: linear elastic buckling theory is modified by replacing the constant elastic modulus of elasticity by an instantaneously varying tangent modulus. The tangent modulus was found empirically from concrete cylinder tests. The presence of reinforcing steel was neglected in the analysis because the steel was located in the middle plane of the plate and the percentage of steel was low. Accidental eccentricities in loading were accounted for in the analysis by measuring the through-thickness concrete strain distribution at low axial loads. Even though behavior such as cracking and orthogonality were neglected, it was found that the tangent modulus method provided a good prediction of the buckling load. This is a significant result, because it indicates that the tangent modulus method might be a viable approach for predicting the buckling load of panels with other edge conditions and load configurations. Ernst demonstrated that in order to obtain optimal results with the tangent modulus method, a stress-strain curve must be obtained from a specimen reinforced in the same way as the member being analyzed. However, conservative results could be obtained by neglecting the presence of reinforcement.

Probably the most significant concrete plate buckling study to date was conducted by Swartz et al.^{35,36,37}. Twenty-four rectangular plates were loaded as shown in Figure 1.8. Initial imperfections, cracking, creep and shrinkage were neglected. Unlike the tests by Ernst, the reinforcing steel was not located in a layer at mid-thickness, but in two equal layers near the faces of the plate. Thus, because the reinforcement affected the bending stiffness of the plate, the steel was taken into account in the analysis.

To accomplish this Swartz made use of an analysis by Sherbourne et al.³⁸ of orthotropic, rectangular plates in uniaxial compression. This theory permits the inclusion of terms reflecting the presence of different amounts of reinforcing steel in the transverse and longitudinal directions, as well as the different concrete stiffnesses in the two directions resulting from material nonlinearities. Swartz analyzed the behavior of the twenty-four test specimens by Sherbourne's orthotropic theory, and by the special case of Sherbourne's theory when isotropy is assumed. Furthermore, for both orthotropic and isotropic behavior, an analysis was performed by the tangent

modulus and the double modulus buckling theories. The stress-strain relationship of the concrete was represented by the ascending branch of a parabola.

It was found that all four of the analyses predicted the experimental buckling loads fairly well. However, the isotropic analysis incorporating the tangent modulus method gave consistently conservative, yet reasonably accurate, predictions. Other advantages of this analysis are its simplicity relative to the other three methods, and it is the only one of the methods which results in a closed form solution for the buckling load. Swartz concluded that an isotropic plate theory which includes the effects of reinforcement, and incorporates the tangent modulus is adequate for predicting the buckling load of rectangular plates simply supported on all four edges.

A series of 15 tests on plates simply supported on three or four sides was performed by Kordina et al.^{39,40,41}. The plates were supported as in Figure 1.8, but the loading was applied eccentrically in a rather unusual pattern: over the width of the plate the magnitude of the eccentricity varied according to a quadratic parabola, with maximum eccentricity near the center of the plate and minimum eccentricity near the corners. The purpose of the variable eccentricity was to prevent premature crushing failure near the corners of the plates, but it is not made clear how the variable eccentricity influenced the overall failure load of the plates. An attempt was made by Kordina et al. to analyse the test results using a method proposed by Storkebaum⁴² and also using a linear elastic finite element program. The researchers report the analyses were inadequate to predict the observed experimental behavior, so no analytical results are reported. In view of the unusual loading conditions and inconclusive analytical results it does not appear that this series of tests is useful in the present study.

Storkebaum⁴² tested six walls with slenderness ratios 20 to 30, simply supported on all four edges, in order to confirm his analytical procedure. The walls were all square and they were uniaxially loaded along two edges at an eccentricity between 20% and 80% of the wall thickness. The analysis procedure was based on replacing the concrete plate with an equivalent grid of concrete beams. The results of the analysis depend strongly on a constant which is a function of plate torsional stiffnesses. The analytical results can be made to agree fairly well with the experimental results provided the correct torsional stiffness constant is chosen. No

general method is given for obtaining the torsional constant.

Wiegand⁴³ performed a nonlinear buckling analysis of thin concrete plates simply supported on all four edges using an energy method. The results of the analysis are not compared with any experimental data. As with Storckenbaum's solution, the analysis is very sensitive to a plate torsion constant and no method for obtaining the constant is given. Wiegand recognizes the sensitivity of the solution to the torsional constant and recommends further research in that area.

Aghayere and MacGregor⁴⁴ performed a series of tests on nine slender reinforced concrete plates simply supported on all four edges and subject to simultaneous in-plane and transverse loads. The purpose of this study was to investigate the coupling effect between the two types of loading. None of the plates was tested under in-plane loading only. Seven of the plates were square and two had a height-to-width ratio of 1.5. The slenderness ratios varied from 29 to 43.

A finite element solution, incorporating both material and geometric nonlinearities was performed, and satisfactory comparisons with the experimental results were obtained⁴⁵. In addition a parametric study of 26 hypothetical plates was carried out. Because of the combined in-plane and transverse loading most of the results of this parameter study do not apply to the present study. However, a significant general finding of the parameter study was that the behavior of slender concrete plates is sensitive to the boundary conditions. For this reason in the present study the actual edge restraints on the component concrete panels of hollow concrete sections have been considered carefully.

The ideal experimental data for calibrating a model of thin-walled concrete section behavior would be a set of tests performed on plates elastically restrained against rotation at their edges. However no such tests exist. For reasons cited above in the reviews of each thin-plate test program the best available sets of plate tests are those performed by Ernst and Swartz et al. on plates concentrically loaded and simply supported along their edges. As part of the present research program Tran⁴⁶ developed an analytical model for the buckling behavior of thin, rectangular reinforced concrete plates. The model was verified using the data from the tests of Ernst and Swartz et al. The model was then extended to the case where the unloaded edges of the plate are elastically restrained against rotation, and the results were

compared with data from tests on thin-walled hollow concrete sections.

1.7. Related Problems

1.7.1. *Folded Plates*

Concrete folded plate assemblies are usually used for roof structures and, as such, are not subject to high axial loads. Nonetheless, in-plane forces induced by overall bending of the plate assembly may be sufficient to cause local plate buckling. Guralnick et al.⁴⁷ have presented a review of buckling in concrete folded plate structures. The authors conclude that a reasonable prediction of the local buckling stress can be obtained using the tangent modulus method. It is further recommended that this approach be applied to the analysis of all thin-shelled concrete structures.

Swartz and Rosebraugh⁴⁸ used an energy method and the tangent modulus approach to predict local buckling in folded plate assemblies. They demonstrated that local plate buckling would occur in three theoretical examples: for $f'_c = 4000$ psi and width-to-thickness ratios of 27, 40 and 60, the critical buckling stresses were 0.83, 0.75 and 0.57 of f'_c . They also suggested that small surface imperfections (deviations in flatness and thickness) could be ignored if the width-to-thickness ratio was less than about 64.

1.7.2. *Hollow Circular Sections*

Pipe piles, chimneys and certain bridge piers are examples of cylindrical hollow concrete sections subject to high axial loads. While the local buckling behavior of circular sections is much different from that of rectangular sections, some findings on the behavior of circular sections are generally applicable to hollow sections.

The local stability of axially loaded cylindrical shells has been studied extensively. However, most of this work has been done for metal and plastic shells. Seide⁴⁹ presents a review of the available work on local buckling of cylindrical concrete shells under a variety of loading conditions. Seide notes that most linear elastic solutions for shell buckling give poor results when compared to experiments on concrete shells, but that certain rational corrections can be applied to obtain better agreement. In particular, Griggs⁵⁰ found that reasonable predictions of buckling

stresses for cylindrical concrete panels can be obtained using the tangent modulus approach.

1.7.3. Marine Structures

Flat and curved concrete plates are elements of both cellular barges and cellular submerged offshore drilling platforms. Most of the plate elements in such structures are subject to a combination of in-plane loads and high transverse loads from hydrostatic pressure, but the internal diaphragms of these structures are often subject exclusively to in-plane loads. An example of the latter case is the internal cell walls of deep offshore platforms. Furnes⁵¹ has reviewed buckling of plate and shell elements in offshore structures. He recommends a tangent modulus approach, based on the experimental work of Swartz et al.^{35,36,37}

1.7.4. Effective Width of Flanged Sections

The concept of a fictitious "effective" compression flange width, smaller than the true flange width, is often incorporated in design methods to account for nonuniform stress distributions in thin-walled sections.

In the case of "T" and box girders subject to bending the effective width approach is necessary because of the so-called "shear lag" effect in the compression flange: compression stresses are not uniform over the width of the compression flange, but are highest where internal horizontal shear forces are transferred from the web(s) to the flange^{52,53,54,55}. When the effective width approach is used in this sense, to compensate for shear lag effects, the effective width is not appropriate for use in calculating the buckling stress of a compression flange of a hollow pier: local buckling is most likely when axial forces are high and bending moments low (near the top of the column moment-axial load interaction diagram), resulting in minimal shear lag effects.

The effective width concept is also invoked in the analysis of thin-walled metallic compression members. In this case the nonuniformity of stresses across a compression flange has two causes. First, residual stresses are locked in near the plate edges from flame cutting, welding and cold-forming processes. Second, in many configurations of plate assemblies a plate can develop membrane tensile

stresses after initial buckling, resulting in reserve post-buckling strength for that plate. In the post-buckled state the stress distribution across the width of the plate is not uniform so an effective plate width is used. Since there are no residual stresses in hollow concrete sections, and since concrete plates cannot safely be assumed to have any post buckling strength (due to cracking after buckling and the resulting loss of stiffness) the effective width concept developed for metallic compression members is not applicable in the present study.

Chapter 2

Experimental Program

2.1. Overview

The experimental program consisted of compression tests to failure of twelve one-fifth scale thin-walled rectangular hollow column specimens. The specimens were loaded eccentrically to induce simultaneous axial compression and uniaxial bending about the weak axis of the column. The main variables investigated in the test program were wall slenderness, concrete strength, detailing of reinforcement, segmental vs. monolithic construction, and post-tensioning effects.

The length of the specimens, 72 inches, was chosen to permit local plate buckling of the thin walls, but to suppress overall, or "Euler" buckling of the column. Solid, heavily reinforced load heads, cast integrally with each specimen, distributed the load from the test machine to the hollow concrete cross section. A typical test specimen is shown in Figure 2.1, and the geometric and material properties of all twelve specimens are given in Tables 2.1 and 2.2.

Since the principal aim of this study is to investigate local buckling of thin-walled cross sections all but one of the specimens was loaded at a low value of eccentricity, typically 5% of the cross section depth. This induced failure near the top of the column axial load-moment interaction diagram, where the influence of local wall buckling is most pronounced. One specimen was loaded at an eccentricity which caused failure near the balance point of the interaction diagram.

The numbering scheme for the test specimens conveys information about the essential feature of each specimen. The first field of each specimen name is a number, 1 through 12, designating the order of fabrication of the specimens. The second field is one to three letters long: M means the hollow portion of the specimen was cast monolithically in a single lift 72 inches high; ML means the hollow portion was cast in multiple lifts (three lifts each 24 inches high), and the longitudinal reinforcement runs continuously through all lifts; S means the specimen is segmental and post-tensioned, and the hollow portion consists of three match-cast segments, each 24 inches high; and MLP means the specimen is of the ML type with added

post-tensioning. The third field designates the approximate wall slenderness ratio of the specimen. For example, specimen 7S22 was the seventh specimen cast, it is segmental, and it has an approximate wall slenderness ratio of 22.

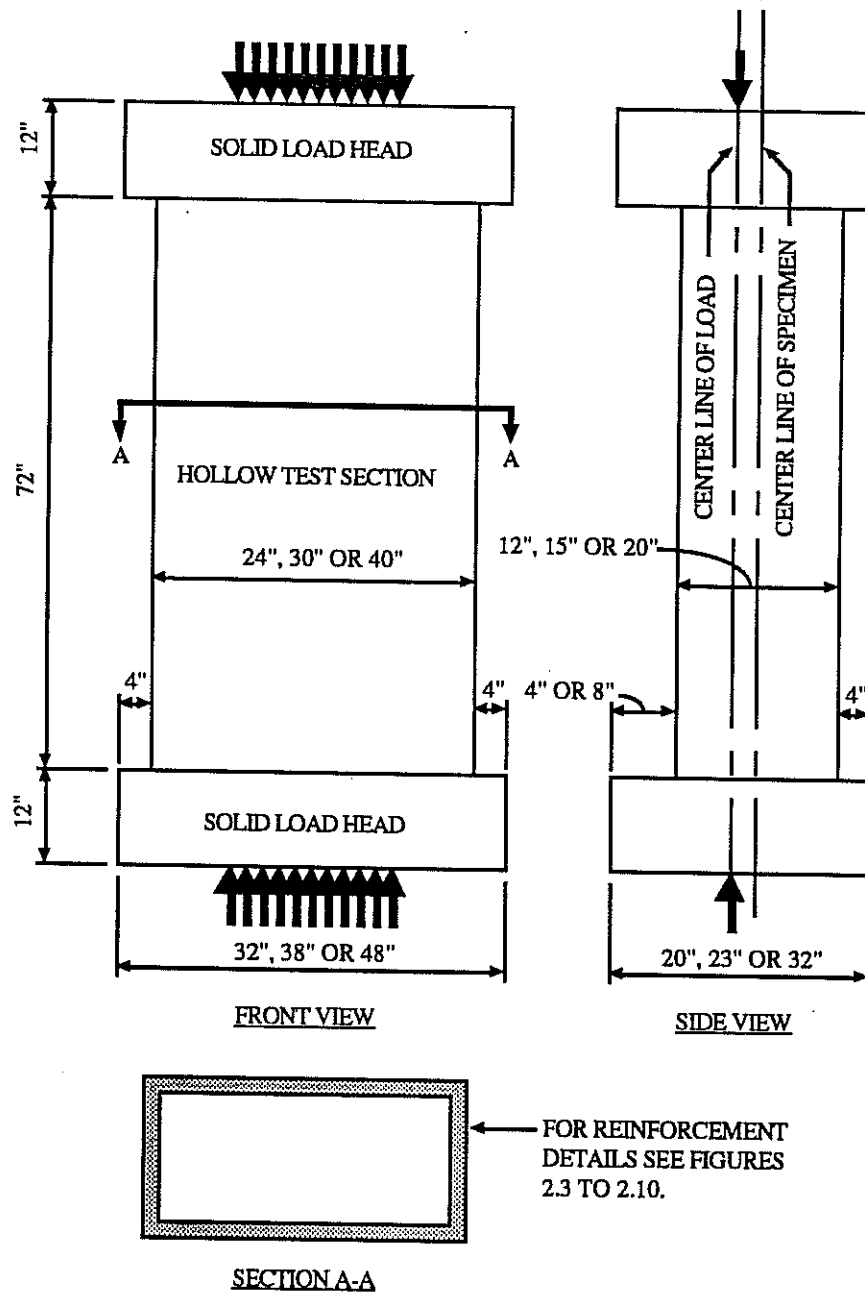


Figure 2.1: Typical Test Specimen

Specimen Number	Wall Slenderness Ratio	Section Depth inches	Section Breadth inches	Nominal Wall Thickness inches	Average Wall Thickness inches	Concrete Area sq. in.	Mild Steel Area sq. in.	Number of Bars	Reinf. Ratio	P.T. Steel Area sq. in.
1M10	10.0	15	30	2.5	2.55	200	4.37	92	0.022	-
2M10	10.0	12	24	2.0	2.03	128	2.09	44	0.016	-
3M14	14.0	20	40	2.5	2.56	275	4.37	92	0.016	-
4M18	18.0	20	40	2.0	2.13	224	3.42	72	0.015	-
5S9	8.8	15	30	2.5	2.46	201	4.37	92	0.022	1.12
6S16	15.5	20	40	2.0	2.07	232	3.42	72	0.015	3.40
7S22	21.7	20	40	1.5	1.57	176	3.42	72	0.019	1.12
8ML25	24.7	20	40	1.5	1.55	171	3.42	72	0.020	-
9MLP22	21.7	20	40	1.5	1.49	176	3.42	72	0.019	1.12
10ML18	18.0	20	40	2.0	2.04	224	3.42	72	0.015	-
11ML34	33.6	20	40	1.125	1.16	130	3.42	72	0.026	-
12S29	29.3	20	40	1.125	1.16	136	3.42	72	0.025	1.12

Table 2.1: Geometric Properties of Test Specimens

Spec. No.	Bottom Load Head		Bottom Section		Middle Section		Top Section		Top Load Head		Slow Cylinder Tests for Failed Section		
	f _c psi	Age at Test days	f _c psi	Age at Test days	f _c psi	Age at Test days	f _c psi	Age at Test days	f _c psi	Age at Test days	f _c psi	Strain at f _c	Time to f _c , min.
1M10	6650	91	-	-	7860	39	-	-	7990	35	7780	0.00302	35
2M10	9980	96	-	-	3170	63	-	-	9550	59	-	-	-
3M14	9980	177	-	-	3540	144	-	-	9550	140	3380	.00278	56
4M18	11670	91	-	-	7700	64	-	-	12270	41	7660	.00300	37
5S9	12210	118	<u>6830</u>	85	5700	82	5990	75	12930	69	-	-	-
6S16	8030	50	5460	39	5210	36	<u>4840</u>	31	8990	28	4230	.00252	25
7S22	7920	115	<u>6920</u>	105	7100	99	6890	92	7910	86	6360	.00230	23
8ML25	8020	72	7040	65	6800	63	<u>6310</u>	58	11080	42	5940	.00264	26
9MLP22	9570	48	6360	37	6470	35	<u>6460</u>	30	9550	27	5860	.00245	25
10ML18	8780	119	6740	108	6960	106	<u>6680</u>	104	9460	99	6390	.00264	30
11ML34	9140	64	5660	48	5450	43	<u>5260</u>	38	8850	35	5020	.00270	20
12S29	8130	41	<u>4680</u>	34	4600	29	4750	24	8070	16	4400	.00260	18

Note: Strength is underlined for failed section of multi-lift and segmental specimens.

Table 2.2: Material Properties of Test Specimens

Spec. No.	Longit. Reinf.		Lateral Reinf.		Mortar		Post-Tensioning Stresses in Post-Tensioning Steel			Post-Tensioning Stresses in Concrete		
	Yield ksi	Ult. ksi	Yield ksi	Ult. ksi	f _c psi	Age at Test days	Nominal ksi	Losses ksi	Net ksi	Nominal ksi	Losses ksi	Net ksi
1M10	75.1	90.4	77.7	91.5	-	-	-	-	-	-	-	-
2M10	75.1	90.4	77.7	91.5	-	-	-	-	-	-	-	-
3M14	75.1	90.4	77.7	91.5	-	-	-	-	-	-	-	-
4M18	75.1	90.4	77.7	91.5	-	-	-	-	-	-	-	-
5S9	75.1	90.4	77.7	91.5	2350	7	124.9	18.3	106.6	696	102	594
6S16	75.1	90.4	77.7	91.5	2200	4	50.1	13.1	37.0	735	192	543
7S22	75.1	90.4	89.1	100.2	2810	73	114.8	18.0	96.8	730	115	615
8ML25	75.1	90.4	89.1	100.2	-	-	-	-	-	-	-	-
9MLP22	75.1	90.4	89.1	100.2	2840	9	114.7	18.3	96.4	729	116	613
10ML18	75.1	90.4	89.1	100.2	-	-	-	-	-	-	-	-
11ML34	75.1	90.4	89.1	100.2	-	-	-	-	-	-	-	-
12S29	75.1	90.4	89.1	100.2	4200	12	87.2	16.3	70.9	717	134	583

Table 2.2 (Continued): Material Properties of Test Specimens

2.2. Scale Modeling

Because of limitations on experimental loading capabilities it was necessary to test scale model specimens in this study. Below is a brief discussion of the principles of scale model testing of concrete structures and the rationale behind the choice of the test specimens for the experimental program.

One of the earliest applications of scale model testing of concrete structures was a series of experiments performed by Robert Maillart in 1908 and 1913-14 on scale model flat plate floor systems⁷⁶. In the 1930's the behavior of concrete gravity and arch dams was studied extensively using small scale models⁷⁷. Since that time numerous model studies of a wide variety of types of concrete structures have been carried out, and a large body of knowledge has been assembled regarding the similitude between scaled concrete models and full size structures^{78,79,80}. As a result of this past work two general classes of concrete models have been distinguished: "direct" and "indirect" models.

A "direct" model mirrors the prototype structure in every respect except geometric scale: all material properties and structural details of the model and prototype are identical except for size. In this case the only fundamental difference between the model and prototype is the mass density, which can be neglected if self weight and dynamic considerations are unimportant.

With "indirect" modeling one or more properties of the prototype are distorted in the model: modulus of elasticity, ultimate stress, ultimate strain, member cross section geometry, and connection details are examples of areas where distortions are often present. In this case the principles of dimensional analysis^{80,81} must be applied to obtain valid comparisons between the indirect model and the prototype. Even when a proper dimensional analysis has been performed questions often arise about how accurately the model behavior represents the prototype behavior.

Another distinction between direct and indirect models, important in the present study, is that indirect models cannot reliably be used to study inelastic behavior and ultimate strength^{77,81}. Therefore, a direct modeling approach had to be taken in the experimental program of this study. Direct modeling of concrete structures requires relatively large scale specimens in order to accurately simulate reinforcement details

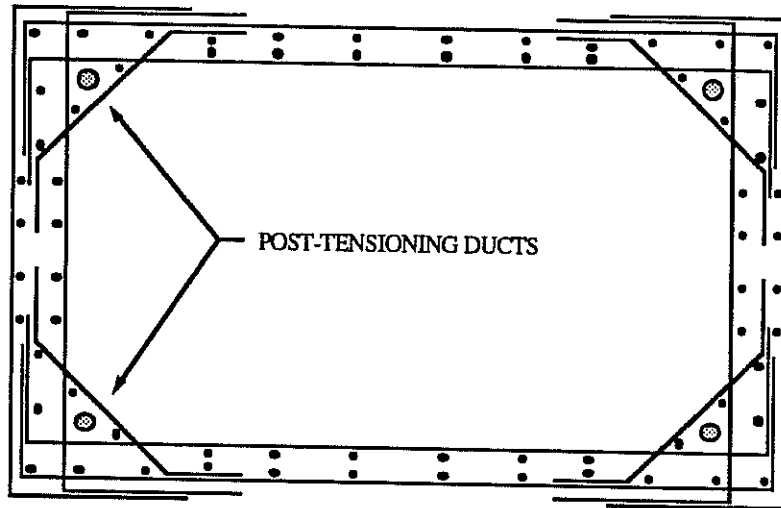
and concrete material properties: Fialho⁸² notes that direct models of concrete structures are usually constructed at one-fifth to one-tenth scale, and that direct models smaller than one-tenth scale may not be reliable. When all factors had been considered, including the available test loading capacity, the desired range of wall slenderness ratios, and most importantly the constructibility of accurate details in direct scale models, one-fifth scale specimens were selected for the experimental program of this study. Since the tests are not dynamic, and since the self weight of the specimens has a negligible effect on their behavior, mass density similitude does not need to be considered in these experiments.

In any model test geometric tolerances must be strictly controlled since even minor imperfections can significantly influence the behavior of small-scale specimens. This is especially true in the study of the stability of thin plates and shells, where initial geometric imperfections can play an important roll in the failure mode. For this reason special care was taken to insure accurate geometric control of the test specimens in this study. Particular attention was payed to the flatness and thickness of the walls of the hollow cross section.

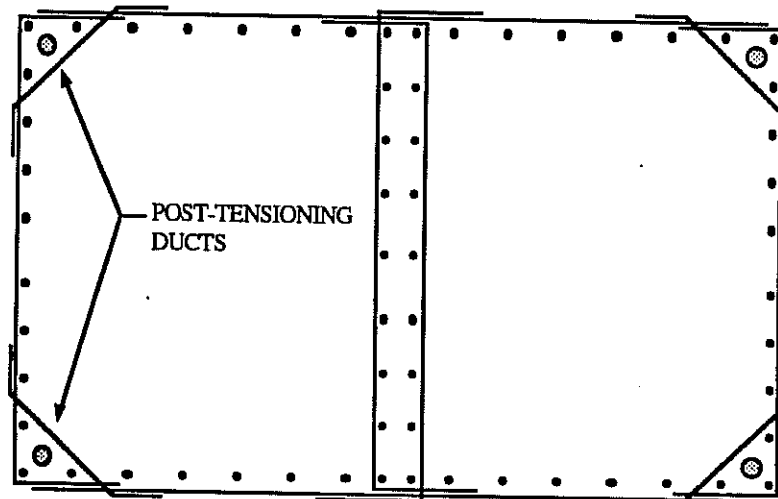
2.3. Design of Specimens

2.3.1. Reinforcement Detailing

The primary objective in designing the reinforcement details of the test specimens was to reproduce, at a smaller scale, the reinforcement details of full size piers and pylons. Since reinforcement details for piers and pylons are by no means standardized the test specimen details were designed to reflect a general consensus of current practice. Towards this end plans and details from about twenty bridge projects, both domestic and foreign, were collected and reviewed. A summary of typical detailing practices for hollow piers and pylons is given herein along with the reasons why certain details were selected for the test specimens. Cross sections from typical hollow concrete piers and pylons are illustrated in Figure 2.2. The cross sections and reinforcement details for all twelve test specimens are shown in Figure 2.3 to 2.10.

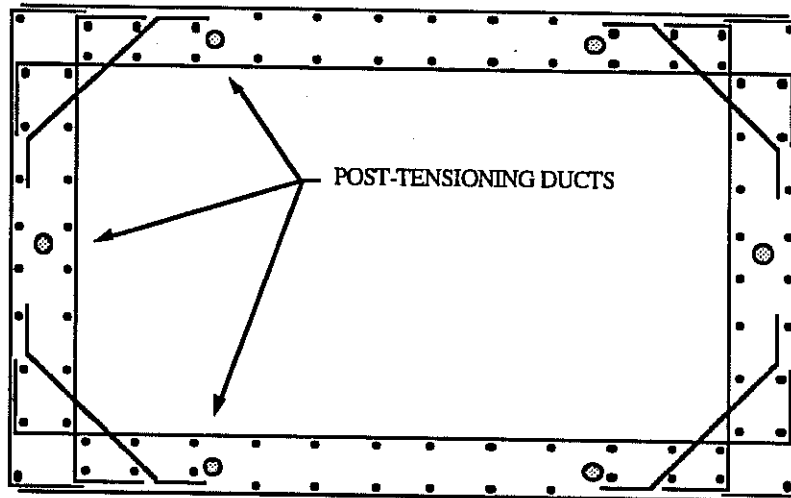


SCHEMATIC - NOT TO SCALE

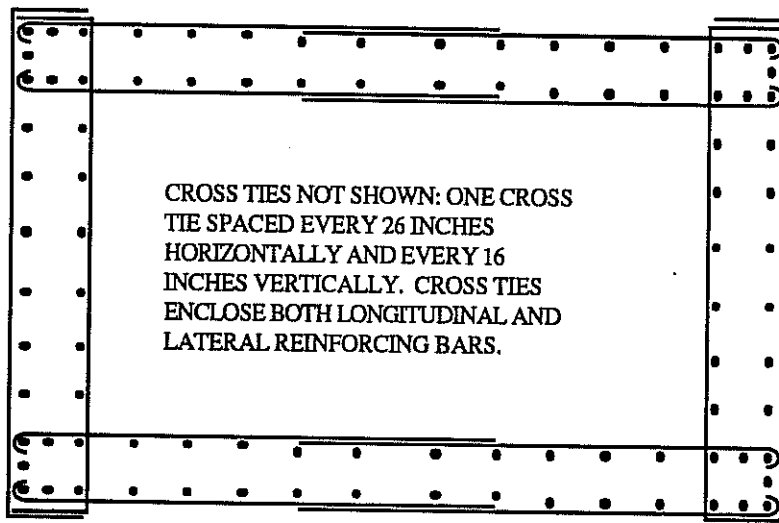


SCHEMATIC - NOT TO SCALE

Figure 2.2: Typical Lateral Reinforcement Details Used in Practice

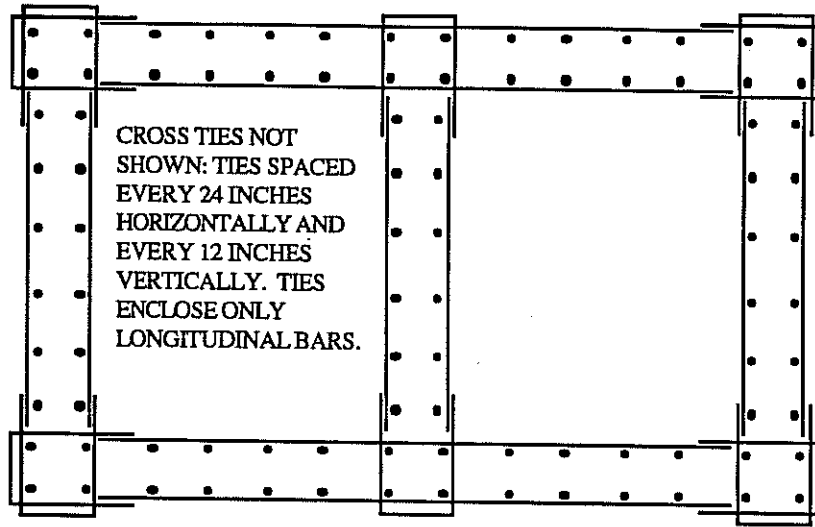


SCHEMATIC - NOT TO SCALE

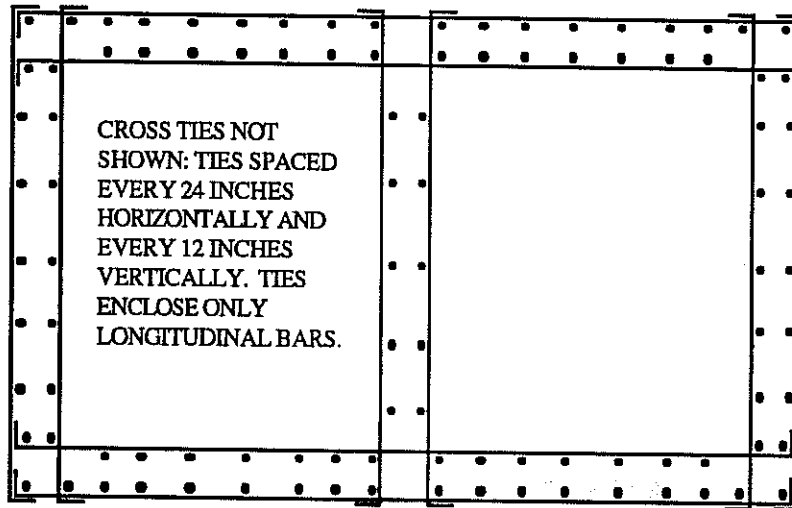


SCHEMATIC - NOT TO SCALE

Figure 2.2 (Continued): Typical Lateral Reinforcement Details Used in Practice



SCHEMATIC - NOT TO SCALE



SCHEMATIC - NOT TO SCALE

Figure 2.2 (Continued): Typical Lateral Reinforcement Details Used in Practice

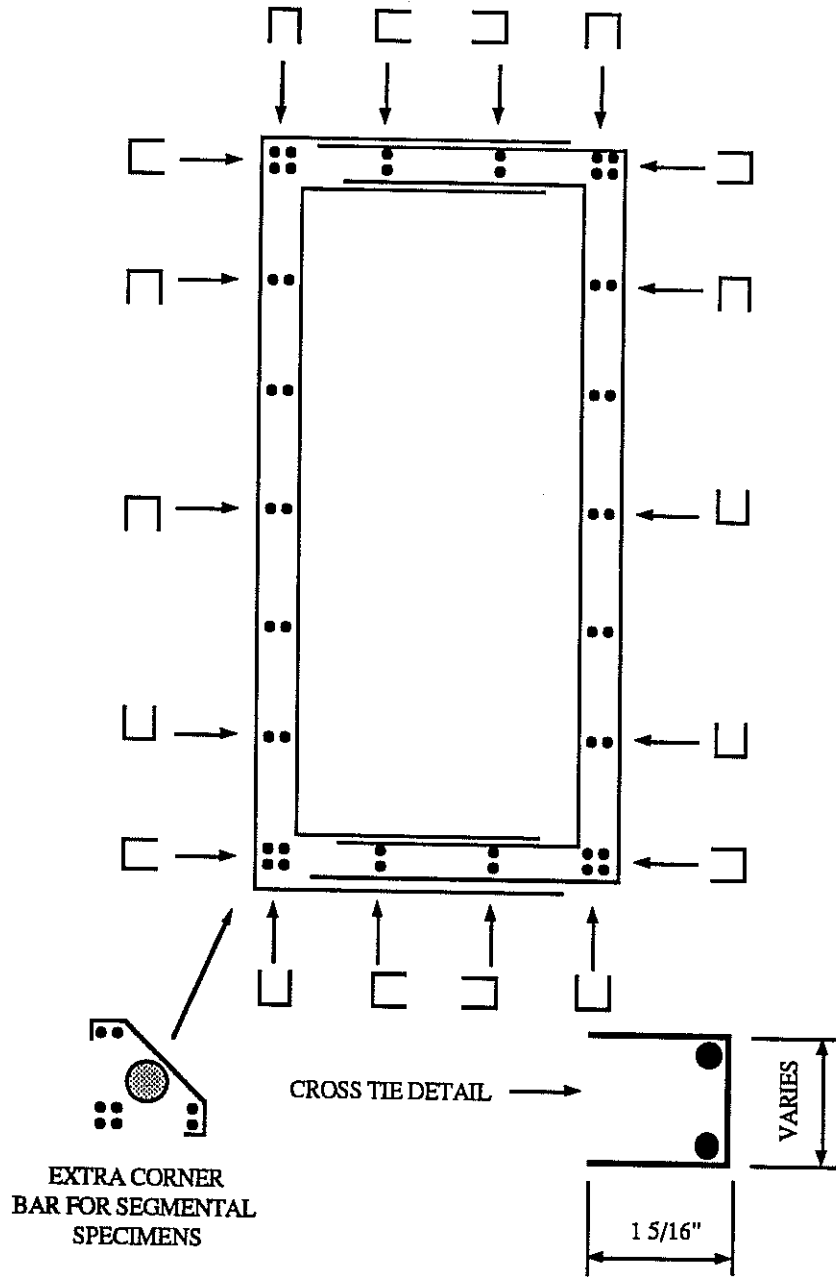


Figure 2.3: Typical Test Specimen Cross Section Detail

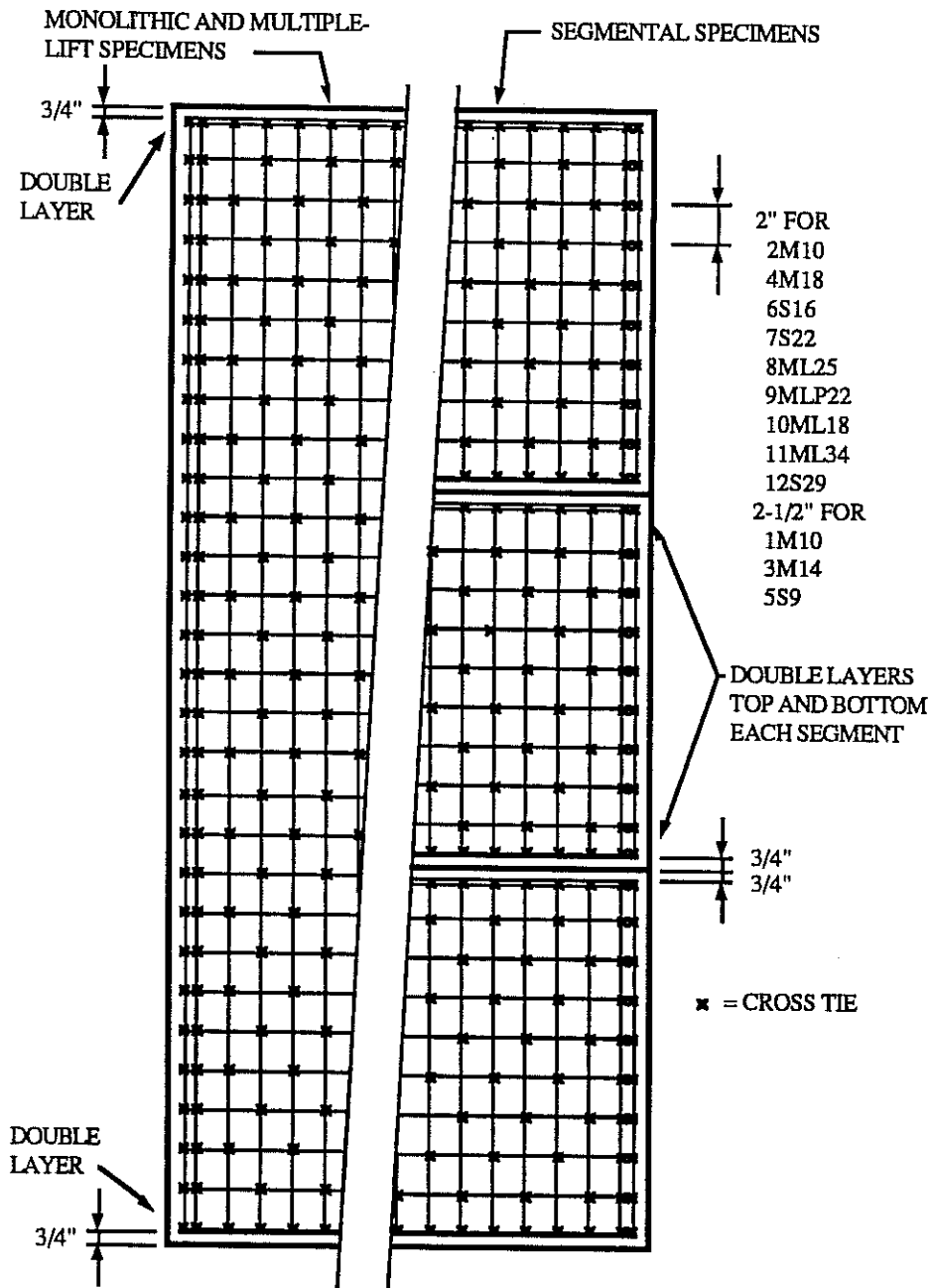


Figure 2.4: Spacing of Lateral Reinforcement and Cross Ties in Test Specimens

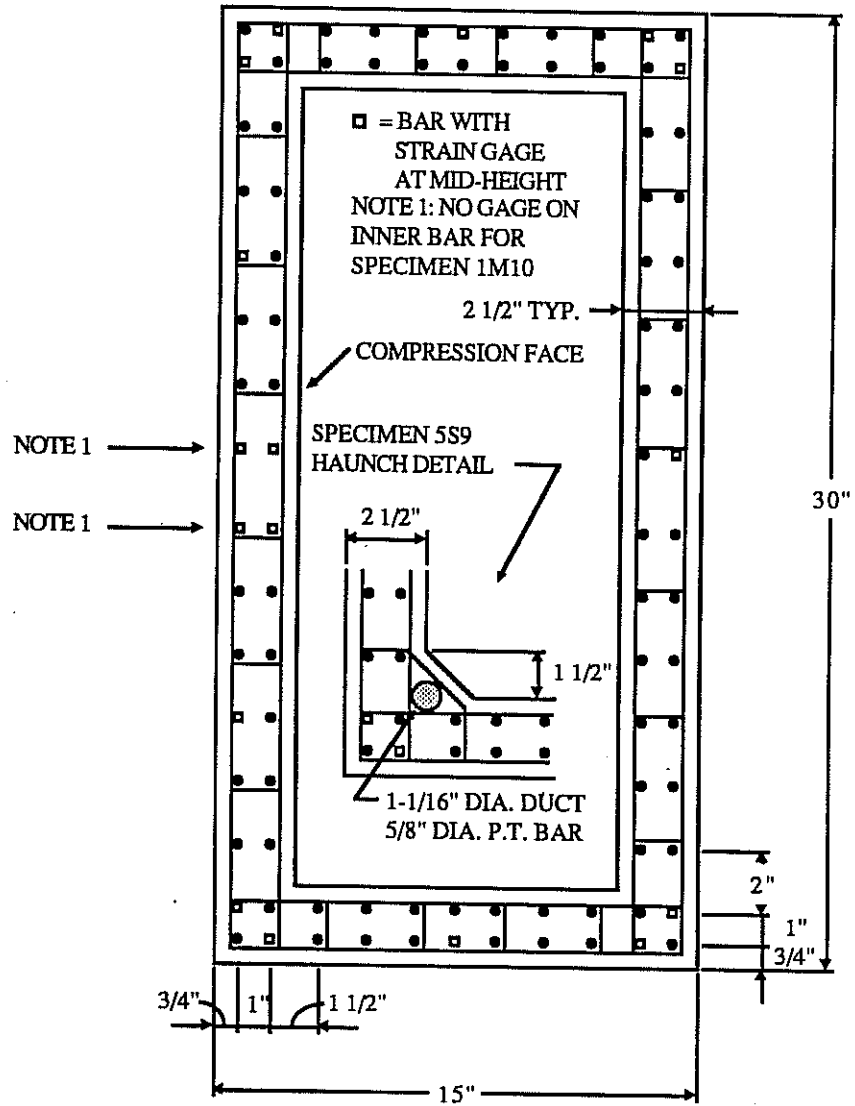


Figure 2.5: Cross Section for Specimens 1M10 and 5S9

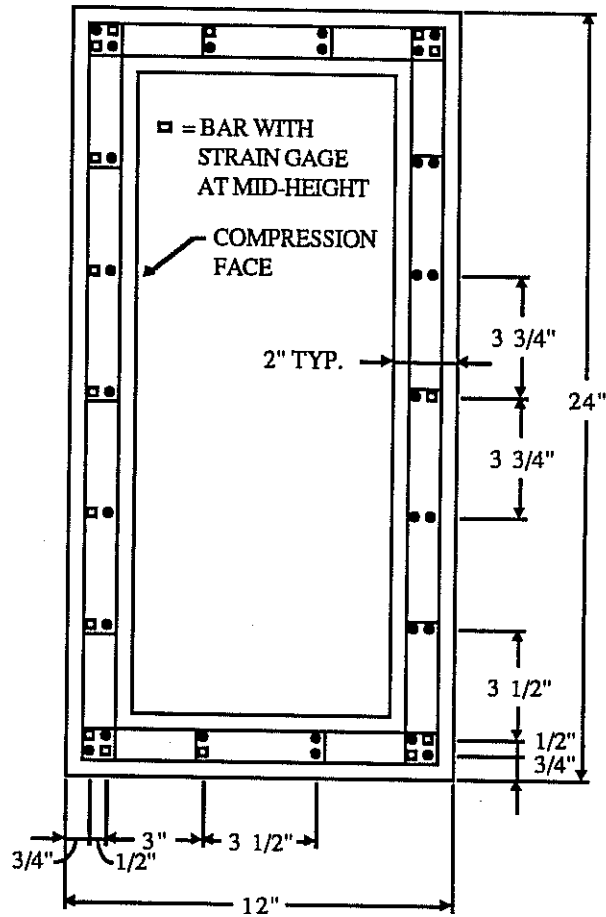


Figure 2.6: Cross Section for Specimen 2M10

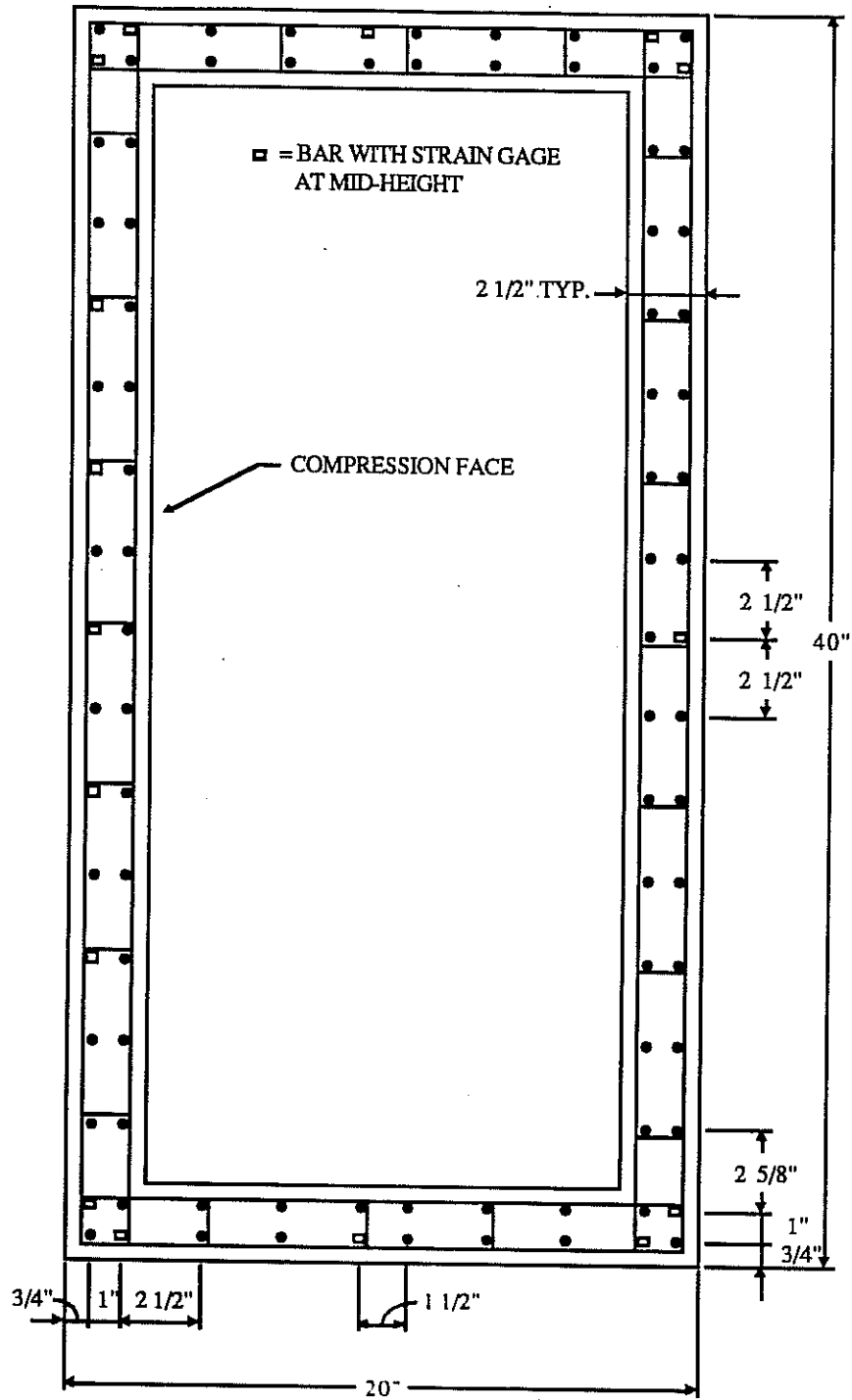


Figure 2.7: Cross Section for Specimen 3M14

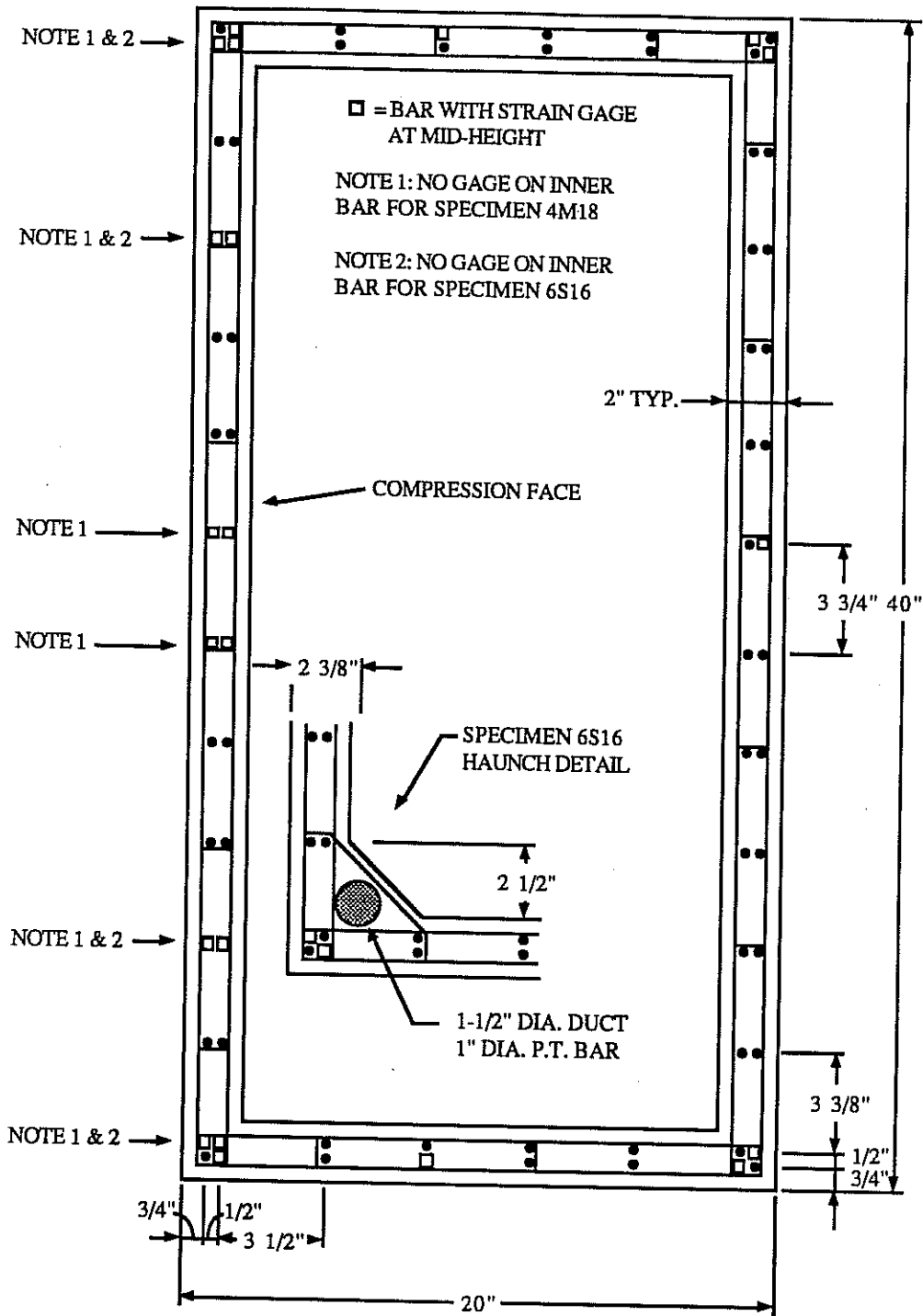


Figure 2.8: Cross Sections for Specimens 4M18, 6S16 and 10ML18

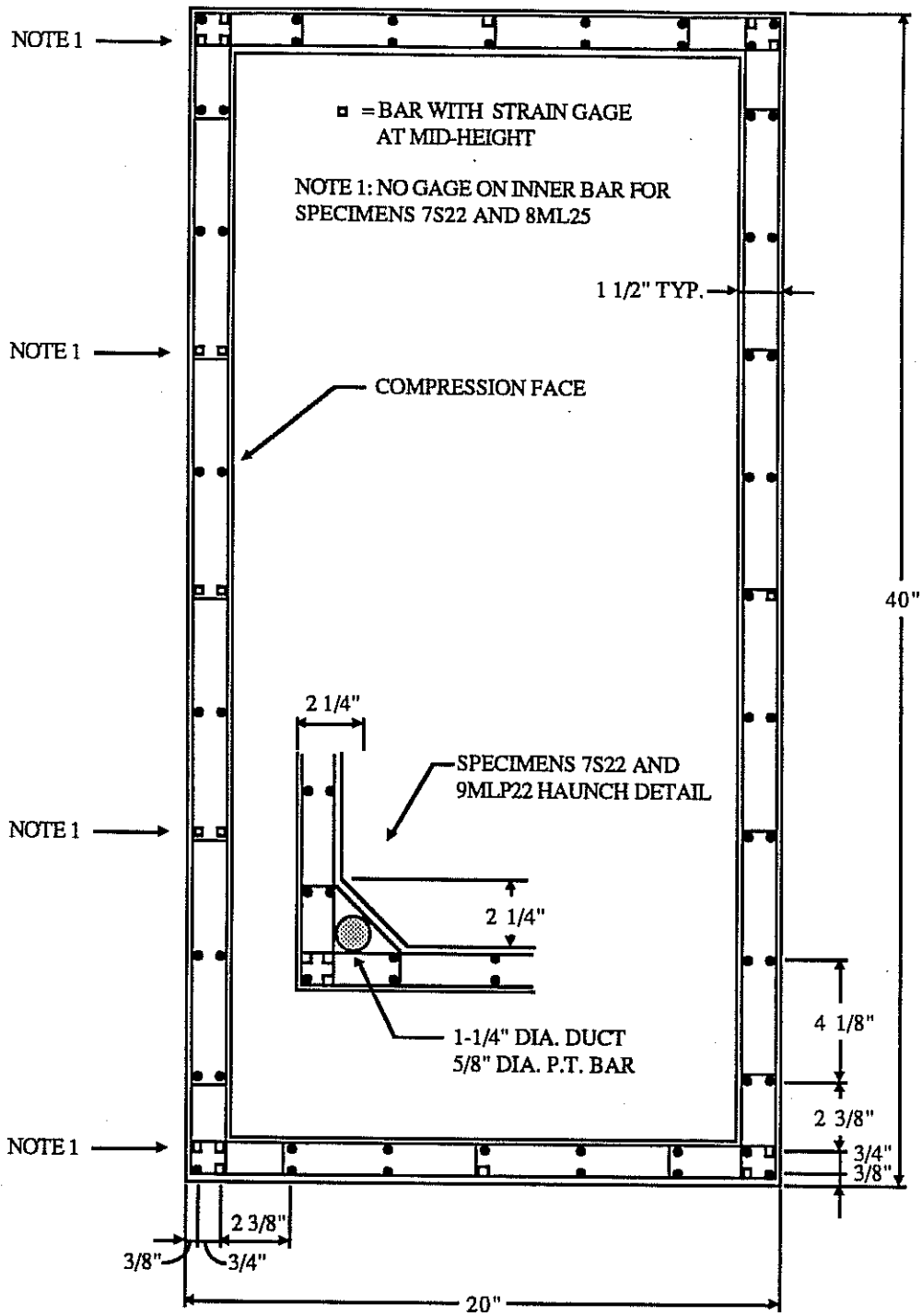


Figure 2.9: Cross Sections for Figures 7S22, 8ML25 and 9MLP22

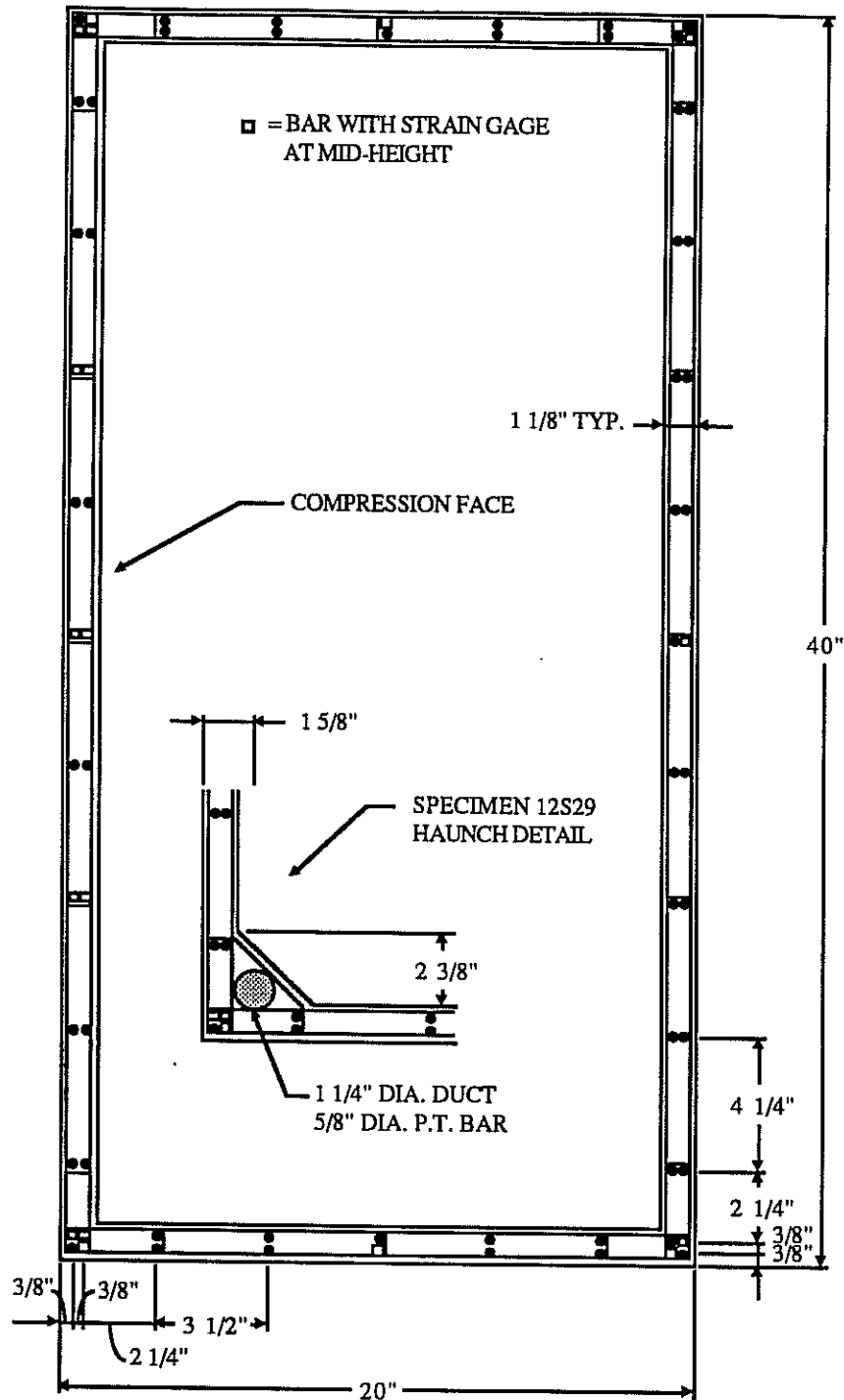


Figure 2.10: Cross Sections for Specimens 11ML34 and 12S29

The reinforcement ratio (concrete area of the cross section divided by the area of mild steel reinforcement) of most hollow sections is low: a range of 0.19% to 1.6% with an average of 0.7% was found for the bridges surveyed. Designs at the low end of this range are probably based on one of two special interpretations of code provisions. First, the low reinforcement ratios might be based not on code provisions for columns, but on code provisions for walls: the *ACI Building Code Requirements for Reinforced Concrete*² specifies a minimum of 0.12% vertical reinforcement in walls, but 1.0% in columns; the *New Zealand Code of Practice for Concrete Structures*⁸ requires a minimum of 0.12% in walls, but 0.8% in columns. Second, the low reinforcement ratios could be based on the *AASHTO Standard Specifications for Highway Bridges*³ provision that the minimum area of steel in a column may be reduced below 1.0% provided the full axial capacity of the column is underutilized.

In the experimental program a slightly higher range of reinforcement content than is used in normal practice was chosen: 1.5% to 2.6% with an average of 1.9%. This was done for two reasons. First, it was desirable to minimize the possibility of local crushing failure in the specimens, since the main purpose of the study was to investigate wall instability. For this reason limits were placed on the maximum lateral spacing of longitudinal bars, increasing slightly the percentage of steel in the cross section. Second, theoretical investigations indicated that the reinforcement content, up to several percent, has little influence on the overall strength or local buckling behavior of hollow sections which fail on the compression branch of the column interaction diagram. Since all the specimens were tested on the compression branch the slightly higher reinforcement content was not expected to affect the behavior of the specimens.

In the majority of the plans reviewed two curtains of reinforcing steel were provided in each wall of the pier or pylon. A few plans called for a single curtain of steel in each wall, but there is no apparent reason why one curtain was used instead of two, other than for cost savings. The *ACI Building Code Requirements for Reinforced Concrete*² requires that walls greater than 10 inches thick contain two layers of reinforcement. The *New Zealand Code of Practice for Concrete Structures*⁸ requires two layers of steel in walls thicker than 8 inches. The *CEB-FIP Model Code*

for *Concrete Structures*⁵ encourages two layers of reinforcement in all walls. Because of these provisions all twelve test specimens were designed with two curtains of steel in each wall.

A wide variety of lateral reinforcement details was observed in practice. Some representative details are illustrated in Figure 2.2. The detailing of corner bars is particularly problematic from a construction standpoint. The corner region must be adequately confined by a closed hoop of reinforcement, yet the cage must be easy to assemble and not too congested. A common solution to this problem is the use of two "hairpin" bars, which can be slid in from the two outer faces at the corner of the specimen. This type of detail was adopted for the test specimens and was observed to perform well in confining the concrete at the corner regions. In some typical observed design details lateral bars are lap spliced in the middle of a face. For the test specimens large U-shaped lateral bars were used, which required a lap splice at the middle of each short face. In retrospect this was a poor detail, as discussed in Section 3.4.9; however this particular detail did not appear to significantly influence the behavior of the test specimens.

The vertical spacing of horizontal layers of reinforcement varied widely in the bridge plans reviewed. In some cases layers were spaced very closely together, as little as 0.17 times the wall thickness ($0.17t$), apparently to improve the ductility of piers and pylons in seismically active regions. These spacings are possibly based on the work of Paulay, Priestley and Park^{83,84} on the ductility of bridge substructures, and in the related area of the ductility of concrete shear walls for buildings. The maximum layer spacing observed in the bridge plans was $1.25t$. The *ACI Building Code Requirements for Reinforced Concrete*² and the *New Zealand Code of Practice for Concrete Structures*⁸ limit the maximum vertical spacing of horizontal bars in non-seismically reinforced walls to $3.0t$ or 18 inches, whichever is less. The *AASHTO Standard Specifications for Highway Bridges*³ does not contain provisions for vertical spacing of lateral reinforcement in walls. The *CEB-FIP Model Code for Concrete Structures*⁵ permits a maximum spacing of 12 inches. The vertical spacings of lateral bars for the test specimens were selected to be in general agreement with the observed design practice and code provisions for non-seismically reinforced walls: $1.0t$ in specimens 1M10 to 6S18 and 10ML18, $1.3t$ in specimens 7S22 to 9MLP22;

and 1.8t in specimens 11ML34 and 12S29. The slightly higher relative spacing in the thinner walled specimens was necessary to reduce congestion of the reinforcement.

Lateral spacing of vertical bars in the observed bridge details varied from 0.2 to 1.25 times the wall thickness. The *ACI Building Code Requirements for Reinforced Concrete*² and the *New Zealand Code of Practice for Concrete Structures*⁸ permit a maximum spacing of vertical bars in non-seismically reinforced walls of 3.0t or 18 inches, whichever is less. The *AASHTO Standard Specifications for Highway Bridges*³ permit a lateral spacing of the lesser of 1.5t or 18 inches. The *CEB-FIP Model Code for Concrete Structures*⁵ allows the lesser of 2.0t or 12 inches. In choosing the lateral spacing of the vertical bars for the test specimens a tradeoff had to be made between maximum spacing and overall reinforcement ratio of the cross section. If the maximum spacing provisions of the design codes were observed then, given the size of the available scale model deformed bars, the reinforcement ratios of the cross sections would be unrealistically high, on the order of 4% to 6%. Since keeping the overall reinforcement ratio of the specimens to a reasonable value was deemed to be more important than the lateral spacing of vertical bars, the spacing limits of the design codes were not met for some specimens. Most of the specimens had bar spacings of 0.8t to 2.8t and specimens 11ML34 and 12S29 had spacings of 3.8t. The variation over this range of bar spacings did not appear to have any effect on the failure modes of the specimens.

Typical reinforcement details at the haunches of segmental specimens are shown in Figure 2.2. The most common haunch detail consists of a straight bar, with a shallow bend at each end, running diagonally across the haunch. This nominally ties the post-tensioning duct into the corner region. In a few cases a special closed hoop, which fully encloses the duct, is provided in the haunch region. While the second detail is clearly superior it is also more difficult to construct because the closed reinforcement hoops must be threaded over the ducts and longitudinal reinforcing bars. A compromise between these two haunch details was used for the test specimens: a straight bar with a 90-degree bend at each end which ties the post tensioning duct into the corner region, as shown in Figure 2.3.

In some of the pier and pylon plans reviewed cross ties are provided between the

two curtains of steel in each wall. There does not seem to be a consistent rationale determining whether or not cross ties are provided in a particular design, although cross ties are usually provided for piers and pylons in seismically active regions. When cross ties are provided there is no apparent agreement on how many cross ties are required: in some designs cross ties are distributed sparsely over the faces of the member, while in other designs cross ties are provided at every intersection of vertical and horizontal bars. For the test specimens cross ties were provided at every other intersection of vertical and horizontal bars in a "checker board" pattern. Additional cross ties were installed at the top and bottom edge of every monolithic and multi-lift specimen, and at the top and bottom edge of each segment of segmental specimens, Figure 2.4. The cross ties consisted of a short straight bar with 90-degree bends at the ends and long bend legs. Normally a 135-degree bend or full hook should be specified for at least one end of the cross tie, but two 90-degree bends were used in this case to minimize reinforcement congestion in the walls.

The concrete cover for reinforcement in the reviewed bridge plans varied from 1.5 to 3 inches. The minimum concrete cover required by the major design codes for bridge piers varies from about 1.25 to 2 inches. In the test specimens minimum concrete cover requirements were sometimes not met in the interest of obtaining thin walls and high wall slenderness ratios: to scale, minimum concrete covers varied from 0.6 to 2.5 inches. The main purpose of concrete cover is to provide protection against corrosion of the reinforcement. It was believed that violating the code provisions for minimum concrete cover would not significantly affect the structural behavior of the specimens.

2.3.2. *Choice of Post-Tensioning Stress*

The post-tensioning stress applied to the test specimens was chosen to reflect typical levels applied to full-scale piers and pylons. A review of plans and contract documents for bridges with hollow segmental piers and pylons indicated that a typical level of post-tensioning was 300 to 1000 psi concrete stress (before calculated losses). Therefore, in this test program an intermediate value of 700 psi was chosen. Table 2.2 shows the level of post-tensioning applied to each specimen and the calculated losses. The method used to calculate losses is discussed in Section 2.5.4.

2.4. Materials

2.4.1. Concrete

The proper method for geometrically scaling the concrete mix was carefully considered. Often so-called "micro-concrete" mixes, incorporating scaled and graded sands for coarse aggregate and plaster-of-Paris as a binder, are used in small-scale studies of concrete structures. However these materials usually present similitude problems because their stress-strain curves are not the same as the prototype concrete. Since a "direct" modeling approach is taken in the present study and since the scale of the specimens is relatively large, it was felt that the best approach would be to design the model concrete as a normal Portland cement concrete mix, but to use scaled coarse aggregate. Johnson⁸⁵, Carpenter et al.⁸⁶ and Aldridge and Breen⁸⁷ all recommend this method for concrete models in about the one-quarter to one-eighth scale range: scaled coarse aggregates are used in the model concrete mix, but fines in the sand smaller than a No. 200 sieve are eliminated, as they require excess water and make the fresh concrete unworkable.

In reviewing the plans of existing hollow concrete piers and pylons it was found that the specified concrete strengths usually fall in the range of 4000 to 6000 psi, with an average of about 5300 psi. In the test program the concrete strengths investigated varied from 3200 to 7900 psi with an average of about 5800 psi. The mix proportions for all 52 batches of concrete used in the test program are shown in Table 2.3. The constituents of the model concretes used in the test specimens are described below.

Specimen Number	Batch	Lab or Ready Mix	Batch Size CY	Course Agg. Type	Course Agg. lb/CY	Sand lb/CY	Water lb/CY	Cemt. lb/CY	Fly Ash lb/CY	Super-plast. Type	Super-plast. oz./CY	Water Red. oz./CY	Water in CA %	Water in Sand %	Slump inches
1M10	Bot. L.H.	R	4	2	1625	1552	139	752	-	2	112	17	N.A.	5.70	7
	Middle	R	5.5	2	1625	1556	147	563	-	2	84	17	N.A.	5.86	8
	Top L.H.	L	.18	1	1568	1365	254	611	-	2	24	-	.11	1.38	6
2M10	Bot. L.H.	R	3	2	1760	1187	229	524	232	1	61	23	N.A.	5.53	8
	Middle	R	3	2	1640	1760	77	384	-	1	40	-	N.A.	5.74	8
	Top L.H.	R	3	2	1760	1200	194	540	222	1	60	22	N.A.	5.56	7
3M14	Bot. L.H.	R	3	2	1760	1187	229	524	232	1	61	23	N.A.	5.53	8
	Middle	R	3	2	1640	1760	77	384	-	1	40	-	N.A.	5.74	8
	Top L.H.	R	3	2	1760	1200	194	540	222	1	60	22	N.A.	5.56	7
4M18	Bot. L.H.	R	3	2	1760	1187	229	524	232	1	61	23	N.A.	5.53	8
	Middle	R	3	2	1640	1760	77	384	-	1	40	-	N.A.	5.74	8
	Top L.H.	R	3	2	1760	1200	194	540	222	1	60	22	N.A.	5.56	7
5S9	Bot. L.H.	R	3	2	1733	1213	151	528	218	1	100	22	N.A.	4.90	10
	Middle	R	3	2	1560	1387	126	528	226	1	133	22	N.A.	5.34	10
	Top L.H.	R	3	2	1733	1213	151	528	218	1	100	22	N.A.	4.90	10
5S9	Bot. L.H.	R	3	2	1560	1387	126	528	226	1	133	22	N.A.	5.34	10
	Bot. Seg.	L	.18	1	1568	1517	306	588	-	-	-	-	2.19	5.32	5
	Mid. Seg.	L	.22	1	1568	1503	290	588	-	-	-	-	0.55	1.59	5
5S9	Top Seg.	L	.22	1	1568	1503	325	588	-	-	-	-	2.02	6.21	5
	Top L.H.	R	3	2	1733	1213	151	528	218	1	100	22	N.A.	4.90	10

Course Aggregate 1: 3/8" crushed dolomitic limestone
Course Aggregate 2: 3/8" washed river gravel

Superplasticizer 1: Naphthalene based
Superplasticizer 2: Melamine based

Table 2.3 : Concrete Mix Proportions

Specimen Number	Batch	Lab or Ready Mix	Batch Size CY	Coarse Agg. Type	Coarse Agg. lb/CY	Sand lb/CY	Water lb/CY	Cemt. lb/CY	Fly Ash lb/CY	Super-plast. Type	Super-plast. oz./CY	Water Red. oz./CY	Water in CA %	Water in Sand %	Slump inches
6S18	Bot. L.H.	R	3	2	1820	1155	147	524	233	1	79	22	N.A.	4.25	10
	Bot. Seg.	L	.22	1	1577	1505	276	623	-	-	-	-	.19	2.38	8.5
	Mid. Seg.	L	.22	1	1577	1505	276	623	-	-	-	-	.19	2.38	9
	Top Seg.	L	.22	1	1577	1505	276	623	-	-	-	-	.19	2.38	8.5
	Top L.H.	R	3	2	1790	1160	147	534	278	1	63	22	N.A.	5.13	10
7S22	Bot. L.H.	R	3	2	1880	1187	244	540	231	1	79	22	N.A.	5.06	6.5
	Bot. Seg.	L	.22	1	1485	1514	281	658	-	1	40	-	.16	2.43	7.5
	Mid. Seg.	L	.22	1	1485	1514	299	658	-	1	40	-	.16	2.43	5.5
	Top Seg.	L	.22	1	1485	1514	281	658	-	1	40	-	.16	2.43	7
	Top L.H.	R	3	2	1790	1160	170	524	236	1	55	22	N.A.	5.10	7
8ML25	Bot. L.H.	R	3	2	1790	1187	141	540	208	1	63	22	N.A.	4.99	8.5
	Bot. Lift	L	.22	1	1485	1514	281	658	-	1	40	-	.13	2.79	8.5
	Mid. Lift	L	.22	1	1485	1514	281	658	-	1	20	-	.13	2.79	8
	Top Lift	L	.22	1	1485	1514	281	658	-	1	20	-	.13	2.79	8
	Top L.H.	R	3	2	1790	1160	106	528	224	1	78	22	N.A.	5.21	6
9MLP22	Bot. L.H.	R	3	2	1790	1173	137	534	216	1	76	22	N.A.	5.49	7.5
	Bot. Lift	L	.22	1	1493	1523	264	658	-	1	18	-	.72	3.00	8
	Mid. Lift	L	.22	1	1493	1523	264	658	-	1	18	-	.72	3.00	7.5
	Top Lift	L	.22	1	1493	1523	264	658	-	1	18	-	.72	3.00	8
	Top L.H.	R	3	2	1790	1173	128	536	210	1	78	22	N.A.	5.33	7

Coarse Aggregate 1: 3/8" crushed dolomitic limestone
 Coarse Aggregate 2: 3/8" washed river gravel
 Superplasticizer 1: Naphthalene based
 Superplasticizer 2: Melamine based

Table 2.3 (Continued): Concrete Mix Proportions

Specimen Number	Batch	Lab or Ready Mix	Batch Size CY	Coarse Agg. Type	Coarse Agg. lb/CY	Sand lb/CY	Water lb/CY	Cemt. lb/CY	Fly Ash lb/CY	Super-plast. Type	Super-plast. oz./CY	Water Red. oz./CY	Water in CA %	Water in Sand %	Slump inches
10ML18	Bot. L.H.	R	3	2	1790	1173	87	524	250	1	63	22	N.A.	5.20	9
	Bot. Lift	L	.22	1	1500	1512	242	705	-	1	18	-	1.21	3.40	6.5
	Mid. Lift	L	.22	1	1244	1250	242	705	-	1	27	-	1.21	3.40	9
	Top Lift	L	.22	1	1500	1512	242	705	-	1	27	-	1.21	3.40	8
	Top L.H.	R	3	2	1790	1187	142	522	248	1	63	22	N.A.	5.10	10
11ML34	Bot. L.H.	R	3	2	1790	1173	172	530	236	1	63	23	N.A.	5.21	9
	Bot. Lift	L	.22	1	1378	1641	290	658	-	1	18	-	1.36	2.83	8
	Mid. Lift	L	.22	1	1378	1641	290	658	-	1	18	-	1.36	2.83	8
	Top Lift	L	.22	1	1378	1641	290	658	-	1	18	-	1.36	2.83	8
	Top L.H.	R	3	2	1790	1173	65	534	216	1	63	22	N.A.	5.27	8
12S29	Bot. L.H.	R	3	2	1790	1160	141	524	230	1	64	22	N.A.	4.91	5
	Bot. Seg.	L	.22	1	1382	1643	284	658	-	1	18	-	1.66	2.97	9
	Mid. Seg.	L	.22	1	1382	1643	284	658	-	1	22	-	1.66	2.97	9
	Top Seg.	L	.22	1	1382	1643	284	658	-	1	18	-	1.66	2.97	8
	Top L.H.	R	3	2	1790	1187	156	526	222	1	63	22	N.A.	5.34	8

Coarse Aggregate 1: 3/8" crushed dolomitic limestone
 Coarse Aggregate 2: 3/8" washed river gravel
 Superplasticizer 1: Naphthalene based
 Superplasticizer 2: Melamine based

Table 2.3 (Continued): Concrete Mix Proportions

2.4.1.1. Coarse Aggregate

Two types of model coarse aggregate were used, depending on whether the concrete was supplied by a batch plant or mixed at the laboratory. The batch plant aggregate was a 3/8 inch washed river gravel and the laboratory aggregate was a 3/8 inch crushed dolomitic limestone. No difference in the performance of concretes made from the two types of aggregate was expected⁸⁸ or observed. Gradation curves for both aggregate types are shown in Figure 2.11. In the case of the laboratory aggregate two gradation curves are shown for two shipments of aggregate. Lab Aggregate No. 2 was used only for specimens 11ML34 and 12S29, which had very thin walls. This shipment was originally received as 3/8 inch aggregate, but it was sieved to eliminate all particles larger than 0.25 inches.

In Figure 2.11 the model aggregate gradation curves are compared with one-fifth scale gradation curves for standard aggregate types defined by ASTM C33 "Specification for Concrete Aggregates"⁸⁹. It can be seen that the batch plant aggregate and Lab Aggregate No. 1 correspond well to a scaled version of ASTM C33 size No. 3 aggregate, which has a maximum aggregate size of 2 inches. Lab Aggregate No. 2 corresponds roughly to a scaled version of ASTM C33 size No. 467 aggregate, which has a maximum aggregate size of 1.5 inches. The maximum size aggregate used in prototype piers and pylons is about 1.5 inches, so some of the model aggregate is slightly oversized. However, this was not expected to significantly affect the material properties of the model concrete.

2.4.1.2. Sand

The gradation curves for sand used in both the laboratory and batch plant mixes are shown in Figure 2.12. Both sands meet the gradation requirements of ASTM C33. As was mentioned above, no attempt was made to scale the sand of the concrete mixes, as excessive fines would lead to an unworkable mix.

2.4.1.3. Cement

Type I or Type II Portland cement was used in all concrete mixes. The two types are identical in performance except Type II is resistant to sulfate attack.

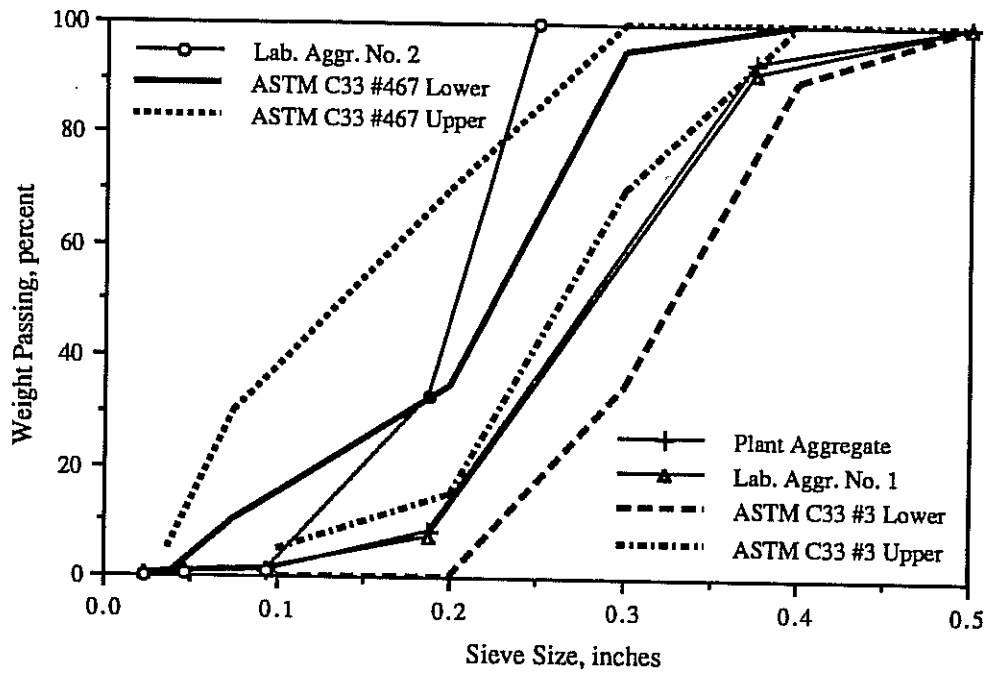


Figure 2.11: Aggregate Gradation Compared to Scaled ASTM C33 Aggregates

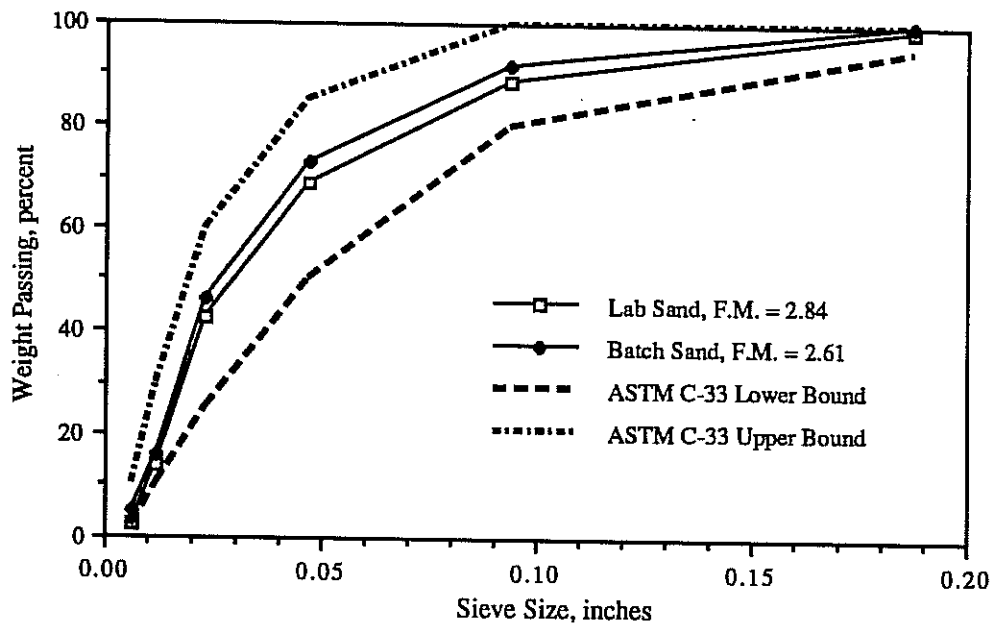


Figure 2.12: Sand Gradation Compared to ASTM C33 Sand

2.4.1.4. Admixtures

Superplasticizing and water reducing agents were added to the concrete mixes to improve workability. The types and quantities of admixtures used are shown in Table 2.3.

2.4.1.5. Concrete Material Properties

The compressive strength and stress-strain properties of concrete were measured by two types of tests on 6 inch by 12 inch cylinders: a standard cylinder compression test to measure compression strength, and a slow, displacement-controlled compression test to obtain the stress-strain curve of the concrete.

Cylinder compression strength tests were conducted just before or just after each hollow pier specimen test. The cylinder testing machine was a "Forney" 600 kip capacity model. The rate of loading was 60,000 to 70,000 pounds per minute and the cylinders were capped by neoprene bearing pads confined within steel end caps. A minimum of three cylinders were tested for each section of the hollow pier specimen.

Stress-strain curve cylinder tests were generally made within 24 hours after the completion of a hollow pier test. Because these tests were lengthy, only two cylinders were tested from the section of the specimen which failed. The stress-strain curve tests were conducted in the same test machine as the standard cylinder tests, but with sulfur cylinder caps and at a much slower rate of loading. Because the particular machine used is very stiff the descending branch of the stress-strain curve could be obtained. This was accomplished by closing the loading valve when the peak value of stress was reached, then slowly bleeding in only enough hydraulic fluid to provide the small displacements necessary for the unloading branch of the curve. Strains were computed from measured load head displacements.

Table 2.2 contains material data from both the slow and fast cylinder tests. It can be seen that on the average the slow cylinder tests gave about 6% lower values of f_c than the faster standard cylinder tests. Figures 2.13 shows plots of the stress-strain curves from each specimen. (Stress-strain cylinder tests were not performed for specimens 2M10 and 5S9). Also shown on the same plots is an analytical stress-strain curve, which will be discussed in Section 4.3.1.

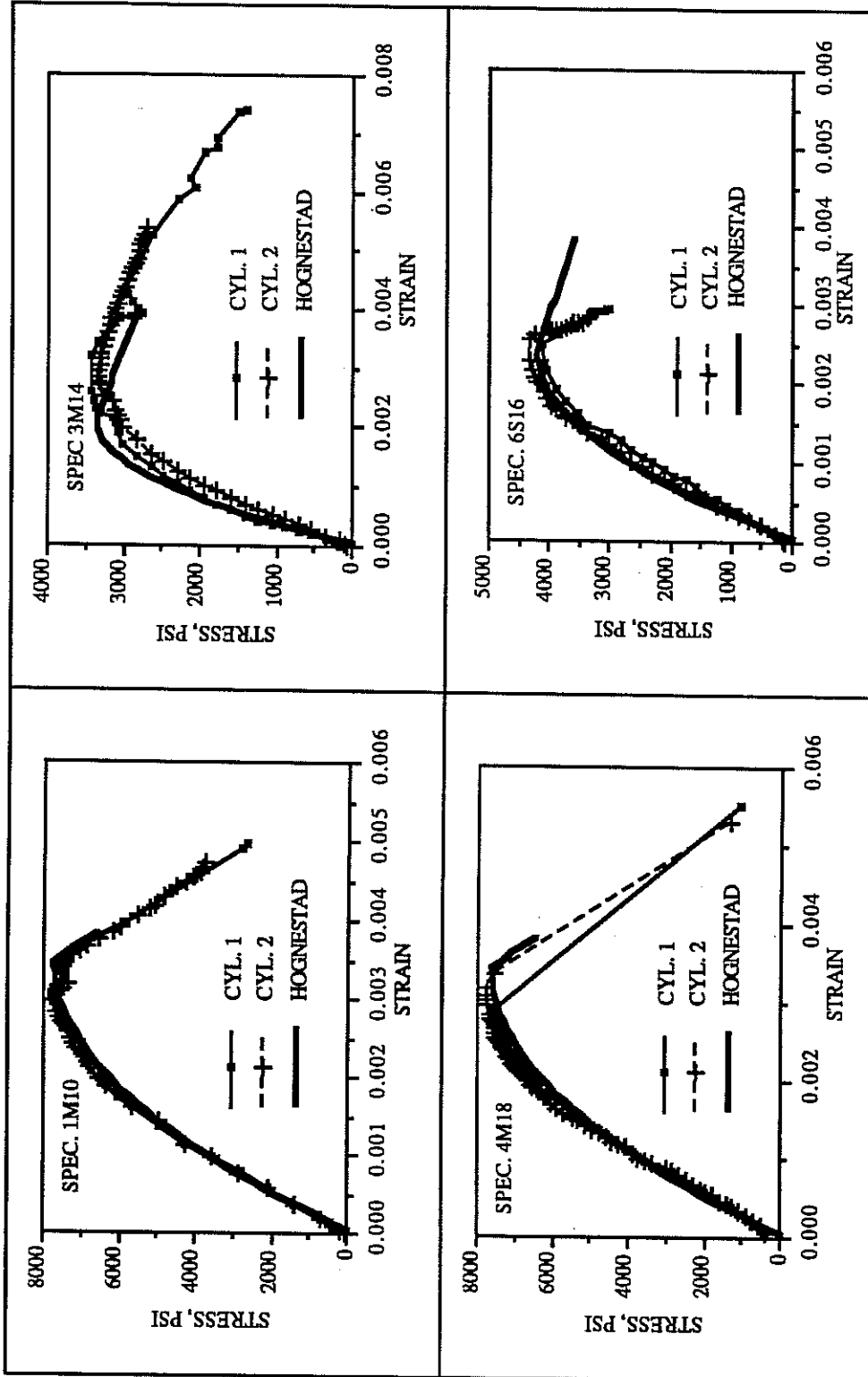


Figure 2.13: Concrete Stress-Strain Curves

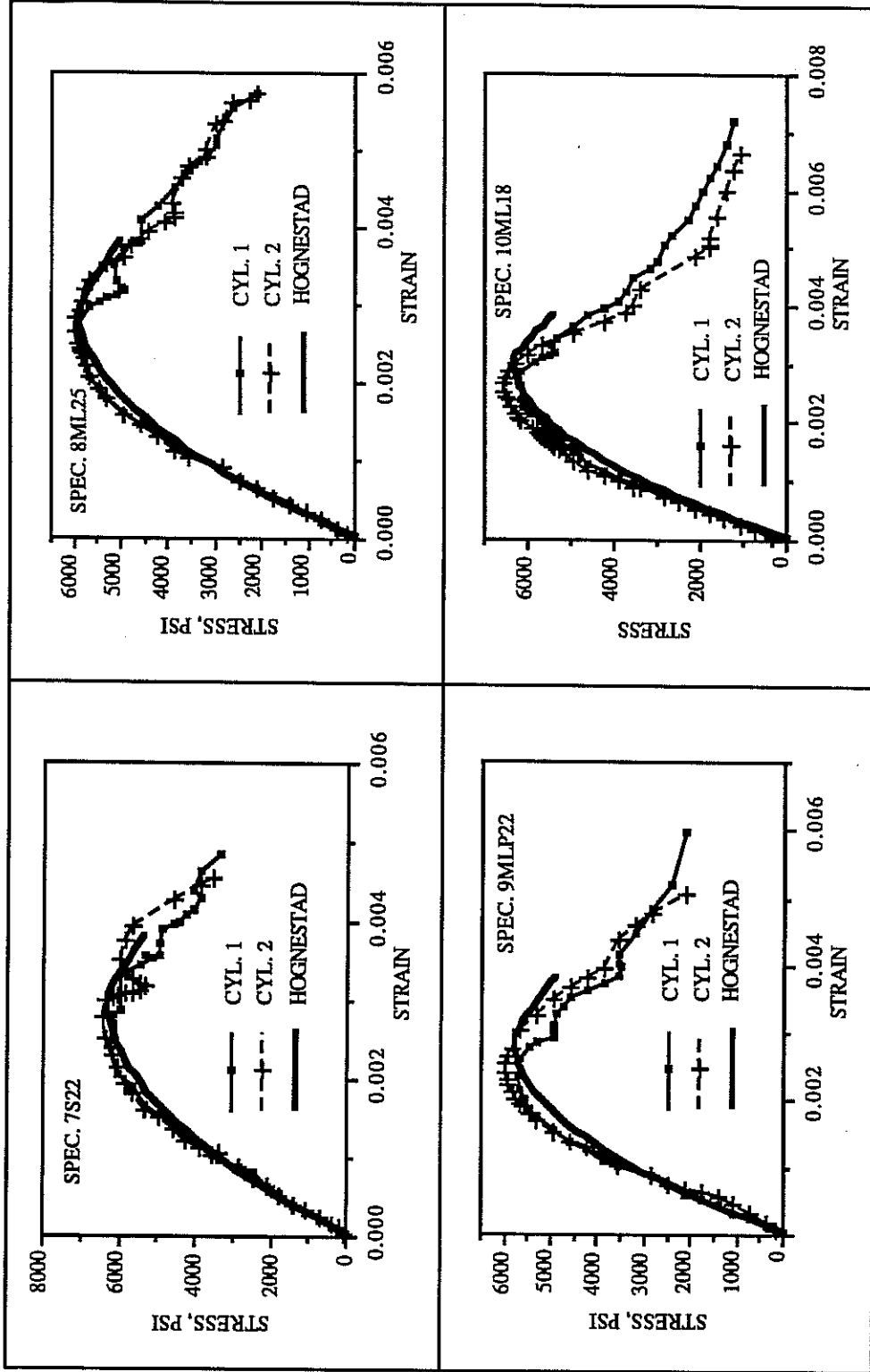


Figure 2.13 (Continued): Concrete Stress-Strain Curves

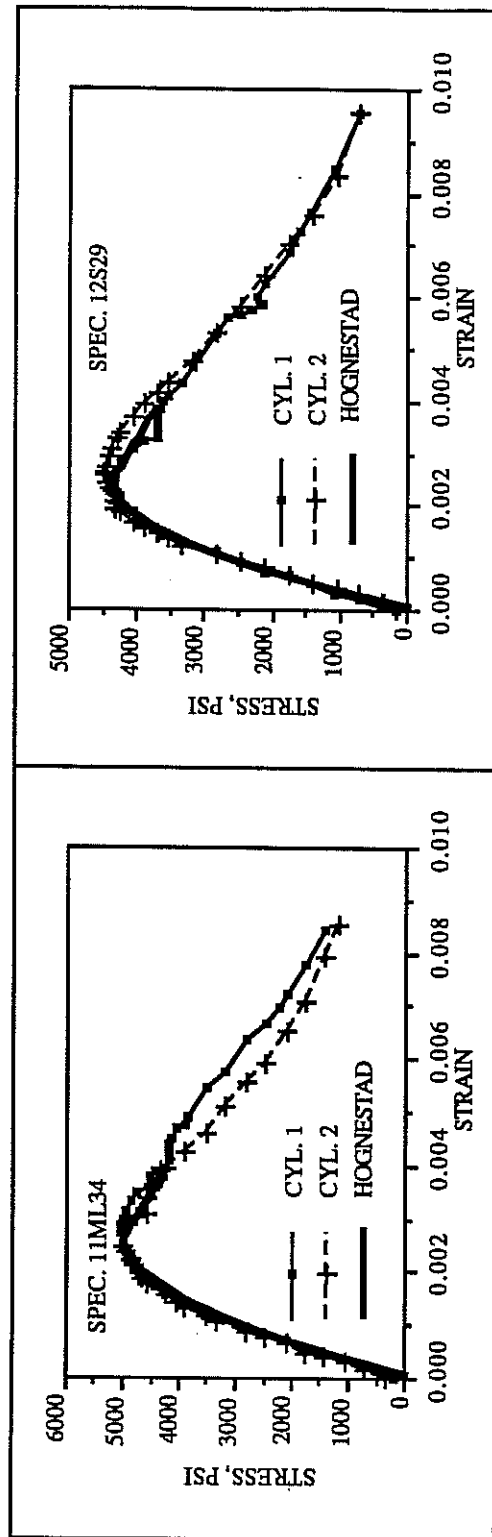


Figure 2.13 (Continued): Concrete Stress-Strain Curves

2.4.2. Reinforcement

2.4.2.1. Longitudinal Reinforcement

The main longitudinal reinforcement of all specimens was 6mm diameter hot-rolled deformed bars (equivalent to a No. 2 bar in the United States sizing system), imported from Sweden. At full scale this is equivalent to a No. 9 bar. While the longitudinal bar size in shorter hollow bridge piers is usually about No. 4, tall hollow bridge piers and pylons often contain larger longitudinal bars, in the No. 6 to No. 9 range.

Five tensile tests were run on random samples taken from the shipment of bars. Strains were measured by electrical resistance strain gages. Figure 2.14 shows a typical stress-strain curve for a bar. The average yield stress of the bars, using the 0.2% offset method, is 75.1 ksi, the average ultimate stress 90.4 ksi, the average elongation at break 9.9% and the average modulus of elasticity 28,900 ksi. The bars meet the ASTM A615 "Standard Specification for Deformed and Plain Billet-Steel Bars for Concrete Reinforcement"⁹⁰ requirements for material properties and deformation geometry of No. 3 bars (no specification is available for No. 2 bars). The cross section area of a bar, determined by weighing and measuring the lengths of several short pieces of bar, is 0.048 square inches.

2.4.2.2. Lateral Reinforcement

Lateral reinforcement was made of 10 gage (0.135 inches diameter) smooth wire, which is equivalent to about a No. 5 bar in full scale. Commonly No. 4 bars are used for lateral reinforcement in the prototype structure, but the slightly oversize (to scale) 10 gage wire was used because it was readily available with the desired material properties. Deformed wire was not used because it is not produced commercially in small sizes. However, it was felt that deformations on the lateral reinforcement were not essential because lateral reinforcement has a secondary effect on the pier behavior. Bond between the wire and the concrete was aided by the wire being lightly rusted.

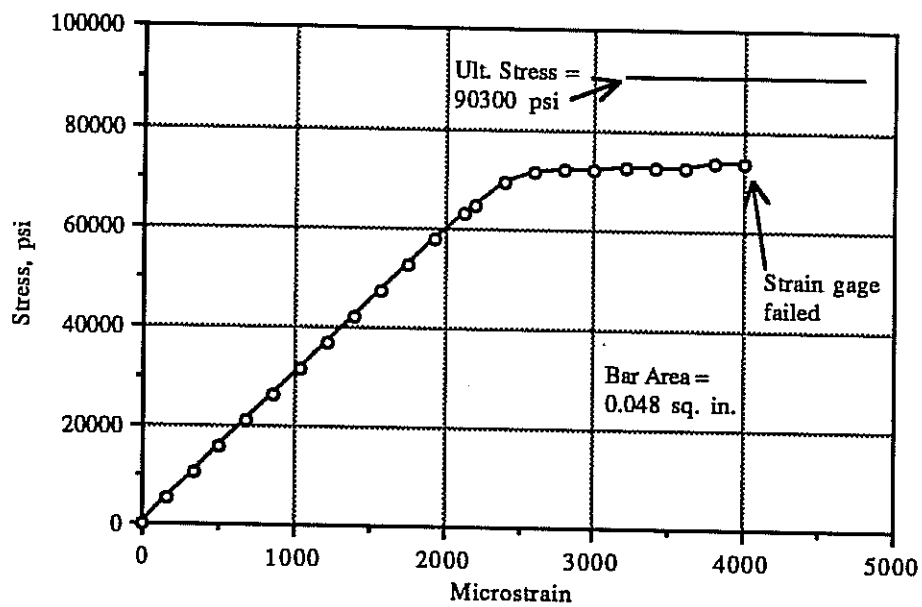


Figure 2.14: Stress-Strain Curve for Longitudinal Reinforcement

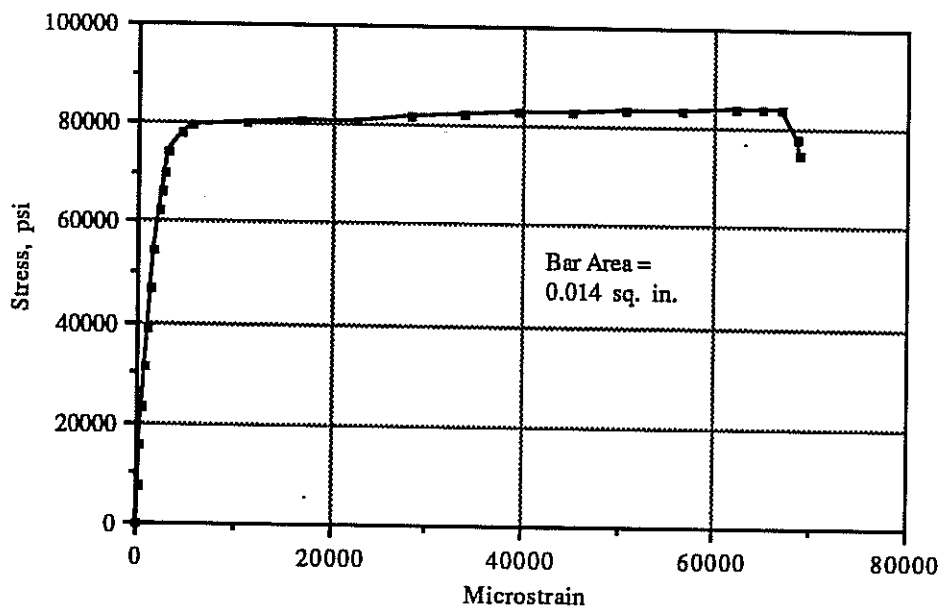


Figure 2.15: Stress-Strain Curve for Lateral Reinforcement

Cold-drawn wire was purchased, then heat treated to improve its ductility. Figure 2.15 shows a typical stress-strain curve from one of the 16 tensile tests conducted on random samples of the heat treated wire. Strains were measured in these tests by an extensometer with an 8 inch gage length. Two shipments of wire were purchased for lateral reinforcement: Shipment 1 was used in specimens 1M10 to 6S18, and Shipment 2 was used in specimens 7S22 to 12S29. The two shipments had slightly different material properties after heat treating: Shipment 1 had an average yield stress (by the 0.2% offset method) of 77.7 ksi, ultimate stress of 98.8 ksi and elongation at break of 7.5%; Shipment 2 had a yield stress of 89.1 ksi, ultimate stress of 100.2 ksi and elongation at break of 7.5%. Although the yield and ultimate stresses are higher than would normally be expected for reinforcement, they meet the ASTM A615 yield and ultimate strength requirements for Grade 60 reinforcement. The ductility of the wire is fairly good, but the elongation at break is about one-fifth less than the minimum allowed by ASTM A615.

2.4.2.3. Post-Tensioned Tendons

High strength "Dywidag" threaded rods were used for the tendons in all post-tensioned specimens. After the rods were stressed an expansive Portland cement grout was pumped into the ducts. For most post-tensioned specimens 5/8 inch diameter bars were used, but 1 inch diameter bars were used in specimen 6S16. Mill reports of material properties of the 5/8 inch bars were provided by the manufacturer: the yield stress was 138.2 ksi, ultimate stress 167.2 ksi and elongation at break 9.5%. Nominal material properties of the 1 inch bars were obtained from the manufacturer's literature: the yield stress was 123 ksi and ultimate stress 150 ksi.

2.4.3. *Post-Tensioning Ducts*

The post-tensioning ducts used in specimen 5S9 were made of smooth plastic electrical conduit. The sections of the conduit were left in place after casting the various pieces of the specimen. This plastic conduit was found to perform unsatisfactorily because it was smooth: there was no mechanical interlock between the grout in the duct and the concrete walls of the specimen. When specimen 5S9 failed the post-tensioning bars slipped within their ducts and protruded from the ends

of the specimen, as shown in Figure 2.16.

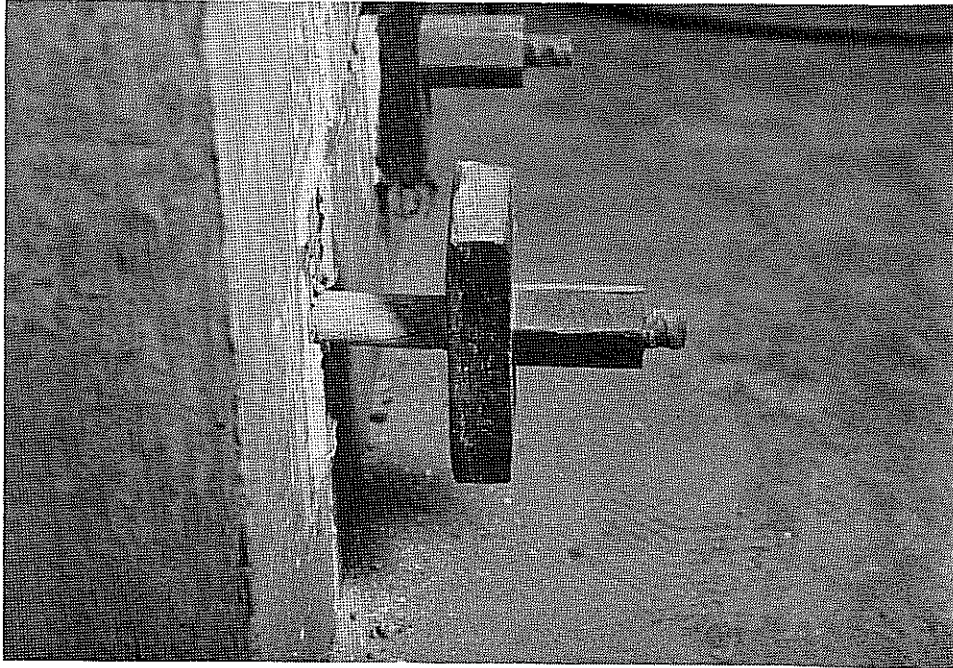


Figure 2.16: Post-Tensioning Bar Slip in Smooth Plastic Duct

In all subsequent specimens a corrugated metal duct was used. It was found that the most convenient method of construction was to use pieces of duct which were as long as the entire specimen (8 feet, including load heads). After casting of the specimen was completed each metal duct was extracted by "uncoiling" it from inside its hole at one end of the specimen. This left a hole with annular corrugations running the full length of the specimen, and the pieces of the specimen could be separated without interference from the ducts. In general ducts formed in this manner performed well.

2.4.4. *Epoxy*

A single brand of epoxy was used for all segmental specimens, "Industrial Coating Specialties Corporation B-75 Span Epoxy," which complies with Section

4.33.13 of the AASHTO *Standard Specifications for Highway Bridges*³.

Preliminary material tests for compressive strength of the epoxy were performed according to ASTM D695-88 "Standard Test Method for Compressive Properties of Rigid Plastics"⁹¹. It was found that at the time of test of any specimen the epoxy compressive strength was at least 12,000 psi, about twice the strength of the concrete of any hollow pier segment.

2.4.5. *Grout*

A fluid cement grout was pumped into the ducts of of the post-tensioned specimens after post-tensioning. The grout mixture was one used commonly by the Texas Department of Highways and Public Transportation. Batch proportions for the grout were 94 pounds Type II Portland cement, 45.8 pounds water and 0.94 pounds "Interplast," an expansive admixture. At the time of grouting 2-inch mortar cubes were cast for testing the compressive strength of the grout. The cubes were loaded at a rate of 4000 to 12000 pounds per minute and failure was obtained in 20 to 80 seconds. Grout cube strengths are shown in Table 2.2.

2.5. **Fabrication of Specimen**

2.5.1. *Formwork and Construction Methods*

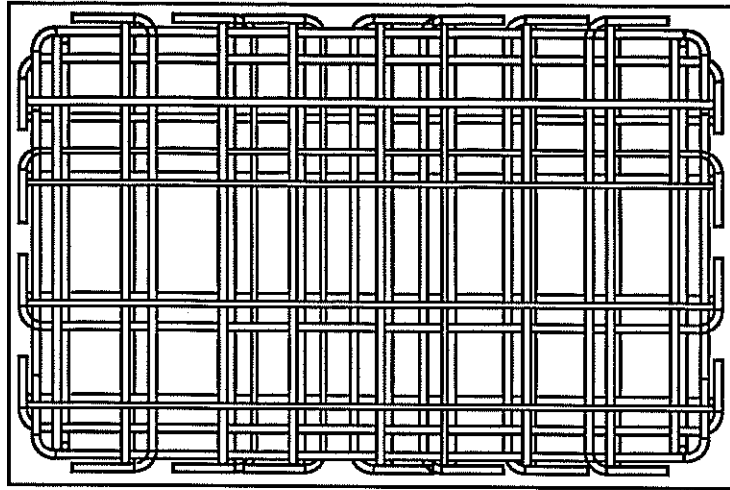
All twelve test specimens were fabricated using the same type of formwork, with only minor modifications made to accommodate the different specimen geometries. A frame supported all the formwork for casting each specimen. The base of the frame consisted of a box in which the solid bottom load head was cast. Above the bottom load head the hollow tests section of the specimen was cast using an inner plywood core form and an outer shell form made of transparent plastic. The top solid load head was cast in an upper box form. In all phases of construction every effort was made to insure accurate alignment and straightness of the completed specimen. Details of fabrication of each of the three types of specimens - monolithic, multiple-lift, and segmental - are given below.

2.5.1.1. Monolithic Specimens

The first stage in constructing a monolithic specimen was to cast the solid bottom load head. Each load head was heavily reinforced, as shown in Figure 2.17. Stub reinforcing bars, projecting from the top surface of the load head, were lap spliced with the main longitudinal bars of the hollow test section, Figure 2.18. A construction joint between the bottom load head and the hollow test section was formed by roughening the top surface of the fresh concrete to a depth of about 0.25 inches in the vicinity of the stub bars. An inner core form, a closed box made of plywood and coated with a layer of black PVC plastic, was attached to the top of the bottom load head by bolts cast in the load head. After aligning the inner form the reinforcement cage for the hollow test section was tied, Figure 2.19. The longitudinal bars of this cage projected up into the box form for the top solid load head, so no lap splices were required at the top end of the specimen.

Small wooden spacers were tied to the reinforcement cage. These maintained accurate spacing between the inner box form and outer shell form, (i.e., accurate wall thickness in the completed specimen). Two notches in each spacer positioned the layers of reinforcement within the thickness of the wall, Figure 2.20. The spacers measured 0.25 inches by 0.38 inches by the thickness of the wall, and they were spaced randomly over the faces of the specimens. A maximum of two spacers was placed for every three square feet of wall area, and it appeared that the presence of these spacers had no affect on the location or mode of failure of the specimens.

When the reinforcement cage was completed the outer transparent plastic form was installed, Figure 2.21, and concrete was placed from the top of the form. The placing procedures are described in Section 2.5.2 below. The top surface of the concrete was roughened to form a construction joint between the hollow test section and the top load head. After 24 to 48 hours the center core form was removed by breaking out horizontal particle board diaphragms inside the form, collapsing the side walls inward, and drawing the pieces out the top. A plywood plug was fitted into the top of the void in the hollow test section. This plug and the bottom end piece of the inner box form were the only form pieces remaining inside the completed specimen. The last stage in construction was installing the reinforcement cage and placing the concrete for the upper concrete load head.



PLAN VIEW OF REINFORCEMENT CAGE. ALL BARS #4 GRADE 60
ARRANGED IN FOUR LAYERS. 3.2% STEEL BY VOLUME

Figure 2.17: Load Head Reinforcement

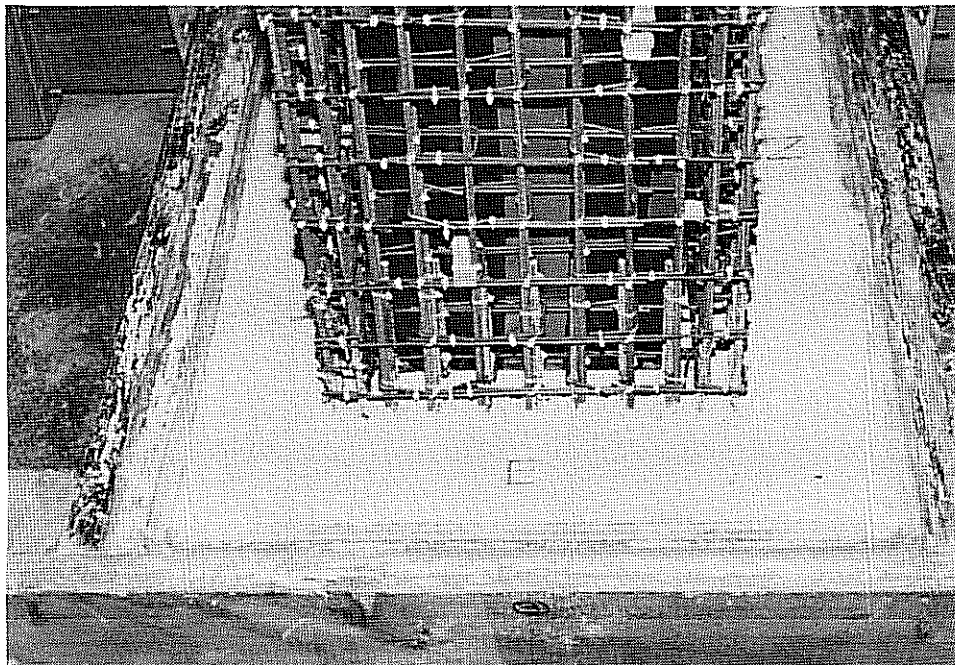


Figure 2.18: Completed Bottom Load Head

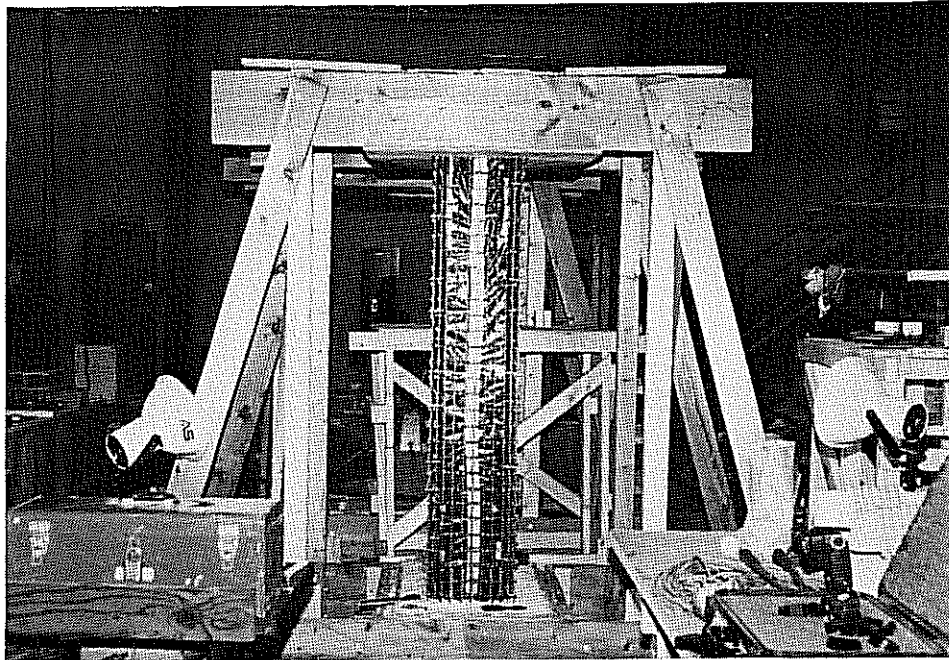


Figure 2.19: Reinforcement Cage for Hollow Test Section

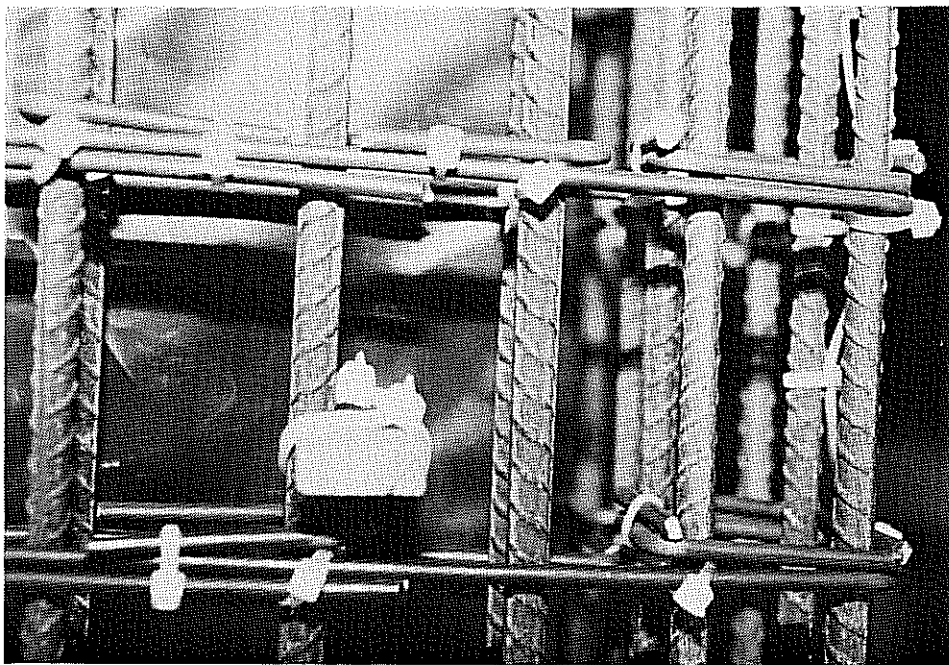


Figure 2.20: Wall Thickness Spacer

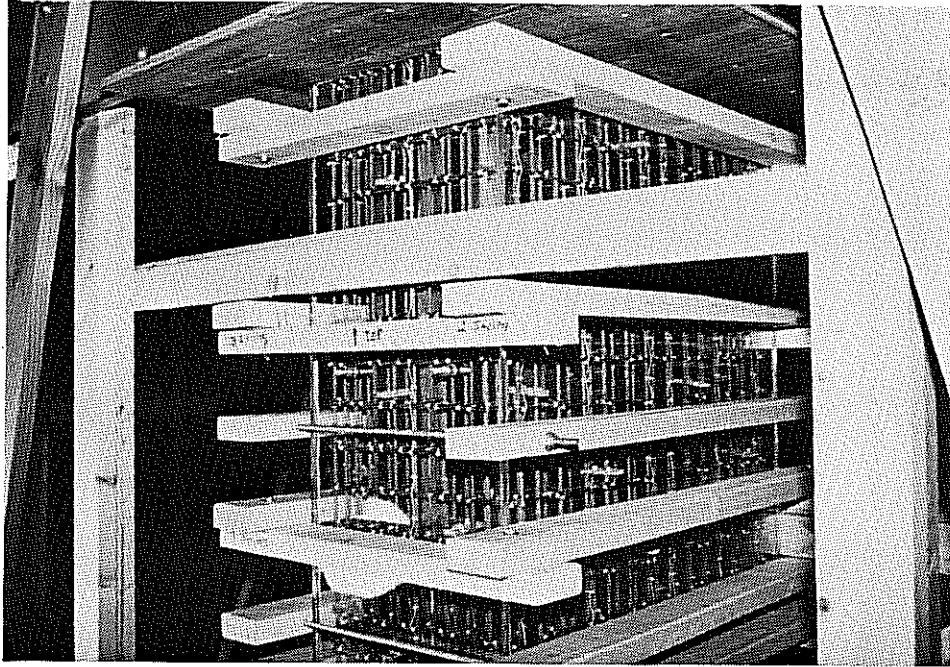


Figure 2.21: Outer Transparent Plastic Forms

2.5.1.2. Multiple-Lift Specimens

Multiple-lift specimens were fabricated in exactly the same manner as monolithic specimens except that the hollow pier section was cast in three 24 inch high lifts. The outer formwork for a single lift is shown in Figure 2.22. Construction joints were made between lifts by roughening the top surface of the fresh concrete. All three lifts were cast in as short a span of time as possible in order to obtain similar concrete strengths in the lifts at the time of testing. The time lag between casting of lifts can be found by examining the "age at test" columns in Table 2.2.

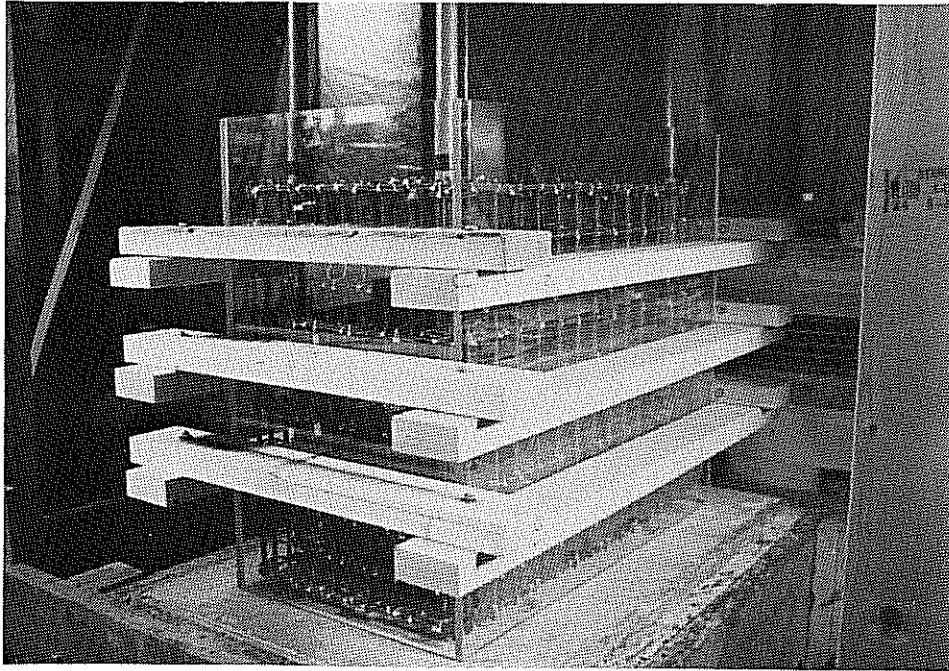


Figure 2.22: Multiple-Lift and Segmental Specimen Formwork

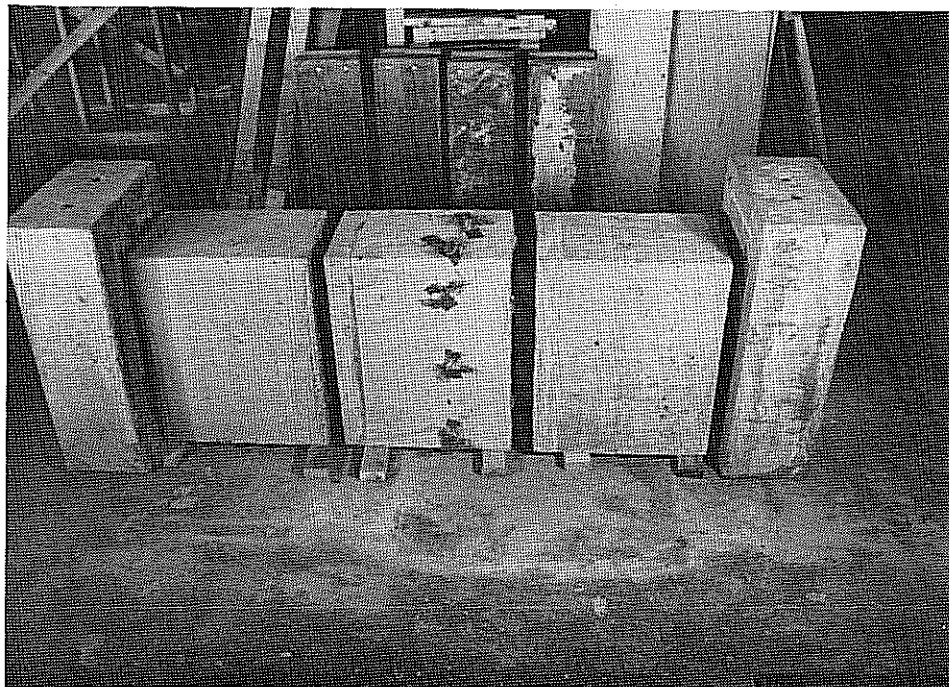


Figure 2.23: Pieces of a Segmental Specimen

2.5.1.3. Segmental Specimens

Segmental specimens were very similar to multiple lift specimens except for the presence of post-tensioning ducts in the haunched corners of the void, and the type of joint formed between lifts. At each of the four joints in a segmental specimen (two between the load heads and the hollow test section, and two between segments in the hollow test section) the fresh concrete was troweled smooth and wooden shear key formers were pressed into the surface to form indentations, Figure 2.24. After the concrete had set and the shear key formers had been removed a bond breaking agent was spread over the surface of the joint. The next segment was "match cast" directly against this joint surface. When the specimen was completed all five pieces (two solid load heads and three hollow segments) could be broken apart easily at the joints, Figure 2.23.

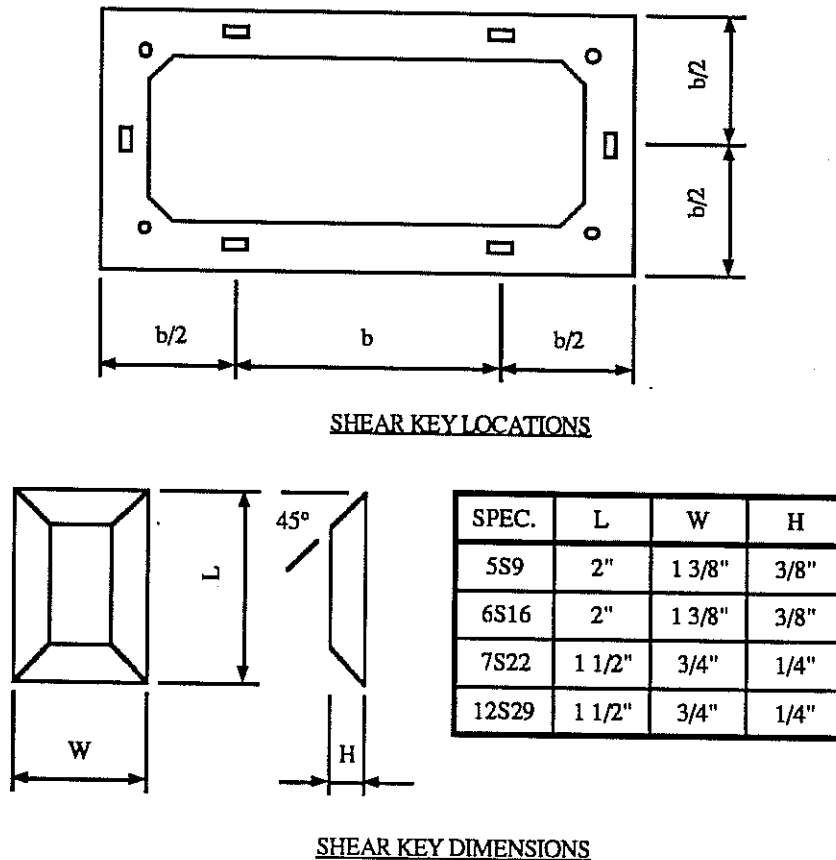


Figure 2.24: Shear Keys

2.5.2. *Mixing and Placing Concrete*

2.5.2.1. *Mixing*

Concrete was obtained either by truck from a remote ready-mix batch plant or, when only a small quantity was required, was mixed at the laboratory using a six-cubic-foot capacity drum mixer. The mixing method used for each casting operation is indicated in Table 2.3. When concrete was mixed in the laboratory the procedures outlined in ASTM C192-81 "Standard Method of Making and Curing concrete Tests Specimens in the Laboratory,"⁹² were followed.

2.5.2.2. *Consolidation*

The consolidation of concrete in tall, thin walls was considered carefully before beginning the test program. Sample walls were constructed and various consolidation methods tested. Satisfactory results were obtained by combining a number of techniques. First, the walls were constructed with a minimum of obstructions between the two curtains of steel. This allowed concrete to fall freely to the bottom of the forms. Second, concrete mixes with high slumps, between 6 and 10 inches, were used. High slump was obtained, without segregation of the concrete, by the addition of superplasticizing agents. Third, internal vibrators were used for consolidation. Two types of vibrators were used: a flexible shaft vibrator 72 inches long and 0.875 inches in diameter; and various shapes and lengths of steel rods which were vibrated by clamping them to the end of a conventional concrete vibrator. The transparent plastic outer forms permitted visual monitoring of consolidation. Finally, the technique of placing concrete was found to be important. Best results were obtained when concrete was poured very slowly, a small amount at a time, to prevent the concrete from jamming between the curtains of reinforcement.

2.5.2.3. *Curing and Form Removal*

Curing methods and durations varied depending upon the casting. Load heads were generally cured for at least three days under wet burlap. Monolithic specimens were cured by leaving the outer forms in place for at least three days. The hollow segments of segmental specimens and of multiple-lift specimens could not be cured

as long because segments had to be cast in rapid succession: the outer transparent plastic forms were generally removed 24 to 48 hours after casting. Wet burlap was not applied to the outer surface because it interfered with placing the outer forms for the next segment. In all cases the concrete test cylinders were stripped at exactly the same time as curing was stopped so that the cylinder strength would be representative of the concrete strength in the load head or specimen wall.

2.5.3. Epoxying

The mixing and application of epoxy were carried out according to the epoxy manufacturer's instructions. Epoxy was applied by hand to both surfaces of a joint in a layer about 0.05 inches thick. Immediately after applying the epoxy, a contact stress of 100 psi was applied and held for 24 hours. Good distribution of the epoxy was confirmed by observations of an epoxy bead squeezing out around all joints.

2.5.4. Post-Tensioning and Grouting

Segmental specimens were post-tensioned by means of four hydraulic cylinders operated by four independent hand pumps. The post tensioning force applied to the first segmental specimen, number 5S9, was monitored by four load cells, and the load was correlated with readings on four hydraulic pressure dial gages. The post-tensioning force for subsequent specimens was monitored using the dial gages alone.

Losses in post-tensioning force due to creep, shrinkage and relaxation were estimated using methods recommended by the Prestressed Concrete Institute⁹³. There were no elastic shortening losses because elastic shortening occurs instantaneously and the actual post-tensioning load was monitored as it was applied. Mechanical seating losses were assumed to be zero because of the method used for locking off the forces in the post-tensioning rods: When the desired post-tensioning load was reached the lock-off nut was turned with a wrench until the post-tensioning force (monitored by devices located behind the lock-off nut in the load train) decreased about 10%. This indicated that the lock-off nut carried 10% of the total load applied to the bar and was seated firmly against the bearing plate. When the full load was released to the lock-off nut further seating losses were minimal. Estimated post-tensioning losses at the time of test are shown in Table 2.2.

Pressure grouting of the post-tensioning ducts was carried out shortly after post-tensioning. The grout tubes were flushed with water prior to grouting. During grouting the grout was allowed to flow freely through the tubes after they were filled in order to eliminate air and water pockets.

2.6. Loading Arrangement

2.6.1. Test Machines

The specimens were loaded to failure in two test machines: a 600 kip capacity Universal testing machine, and a 1200 kip capacity compression testing machine built specifically for this study. Specimens 1M10 and 2M10 were tested in the 600 kip machine and the remaining specimens were tested in the 1200 kip machine.

The 600 kip capacity "Riehle" universal testing machine is shown in Figure 2.25. Load is applied through four mechanical screws driven by an electric motor. Specimens were tested in a vertical position in this machine.

The 1200 kip capacity machine is shown in Figures 2.26 to 2.28. The machine consists of two concrete reaction blocks joined by eight 1-3/8 inch diameter "Dywidag" high-strength threaded bars. One of the reaction blocks is fixed to the reaction floor against rotation and translation. The other block is allowed to translate freely along the longitudinal axis of the machine on rollers, but is restrained against lateral translation and rotation by steel outriggers (the outriggers are not shown in Figures 2.26 and 2.27 for clarity). These outriggers are bolted to the reaction floor and bear against the block through teflon-coated plates which are heavily greased. Load is applied to the test specimen by a 1200 kip capacity hydraulic ram with 12-inch stroke, attached to the face of the fixed reaction block. Since specimens were tested in a horizontal position in this machine they had to be supported vertically at each end, but permitted to move freely in a horizontal plane. This was accomplished by providing at each end a concrete pedestal topped by a flat steel plate, on which were placed about one-hundred 0.5 inch diameter steel ball bearings. Another flat plate was placed on top of the ball bearings and the specimen was placed on top of the plate. With this system the resistance of a specimen to lateral movement was less than 50 pounds.

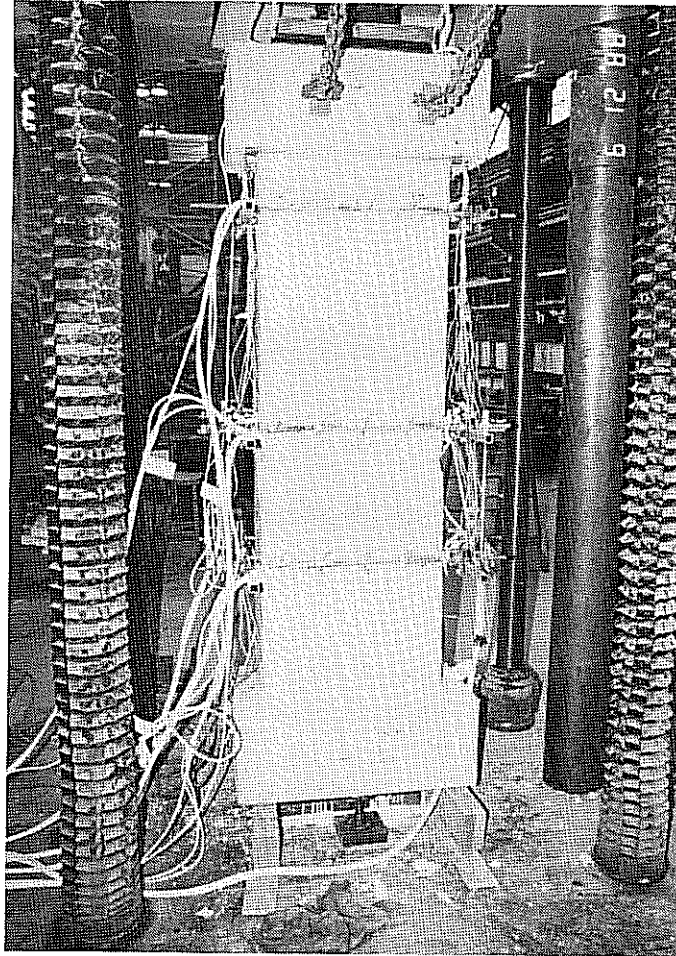


Figure 2.25: 600 kip Capacity Universal Testing Machine

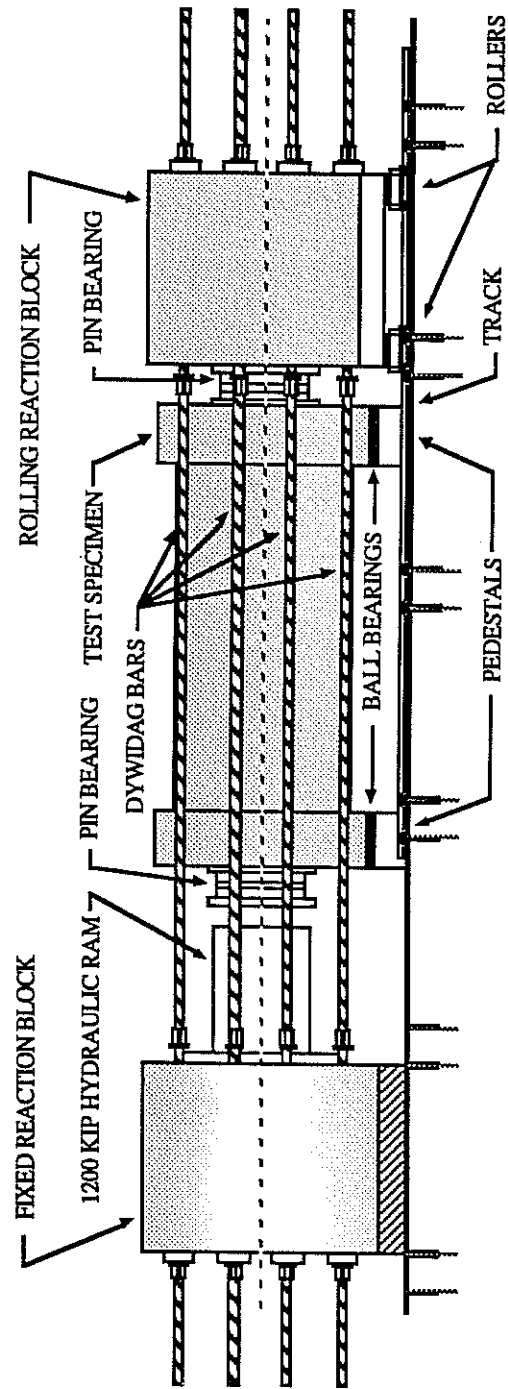


Figure 2.26: 1200 kip Capacity Test Machine, Side View

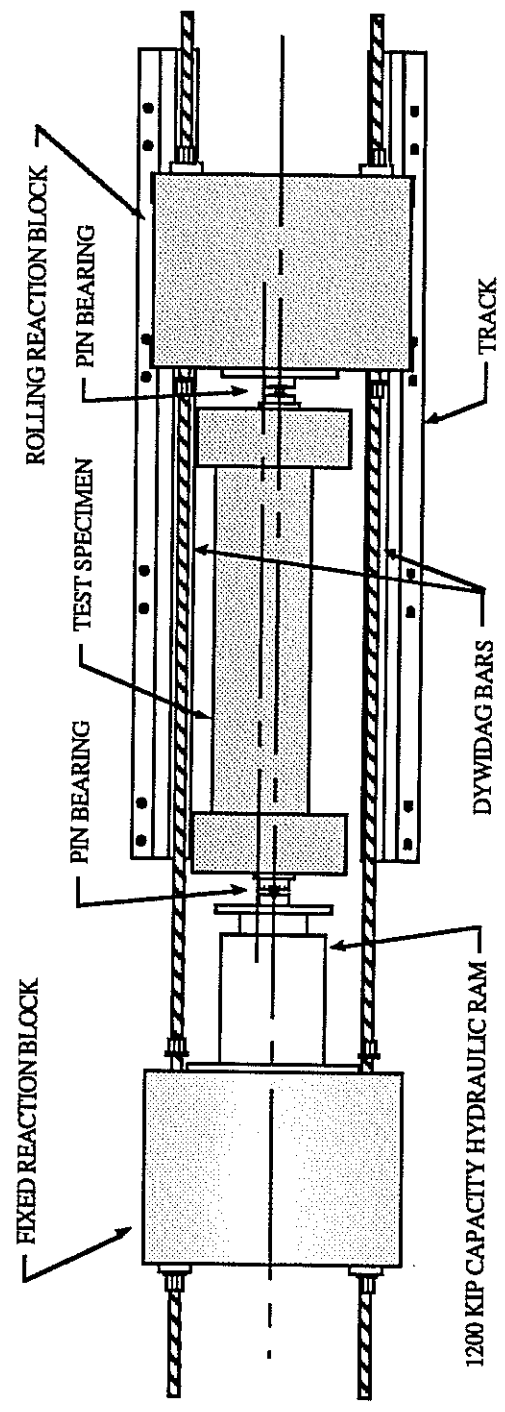


Figure 2.27: 1200 kip Capacity Test Machine, Top View

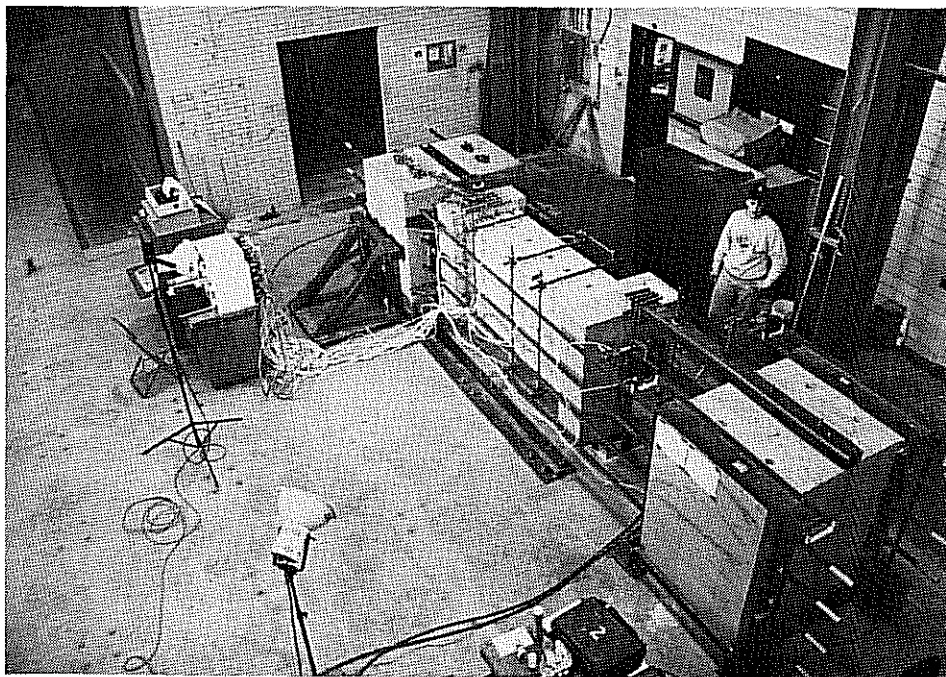


Figure 2.28: 1200 Kip Capacity Test Machine

2.6.2. Pin Bearings

Hardened steel pin bearings were used to provide pinned-end loading conditions for the hollow pier specimens. The design of these bearings permitted application of longitudinal loads to the specimen but prevented transfer of significant bending moments through the bearing assembly. The pin bearings are illustrated in Figure 2.29. The pin is made from hardened, precision-ground stock, and the bearing plates are made from grade A588 steel. It can be seen that the trough in each bearing plate was made by two parallel passes, offset by 0.1 inches, of a 2-inch diameter ball-ended milling machine cutter. Because of this offset the shape of the trough cross section is not perfectly semi-circular and the cylindrical pin is prevented from binding. Free movement of the pin bearing assembly was also promoted by applying a thick coating of colloidal copper grease or "anti-seizing compound" to all parts. This lubricant prevents the binding of steel parts subject to very high contact stresses, such as bolt threads.

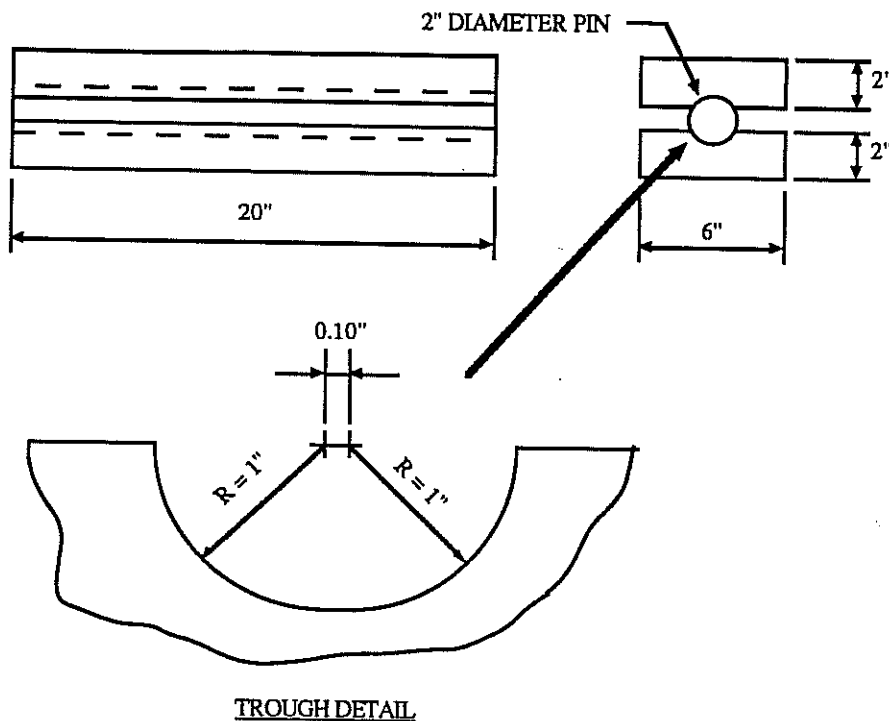


Figure 2.29: Pin Bearing

2.6.3. Geometric Tolerances

Every effort was made to insure correct alignment of the test machine and test specimen. However, an error in the assumed point of application of the load is unavoidable. Based on the tolerances followed in the design and construction of the test machine and in setting up each test specimen the estimated error in the point of application of the load is ± 0.15 inches.

2.7. Instrumentation

2.7.1. Load

Load was measured in the 600 kip capacity universal testing machine by built-in load cells and a digital readout. Load was measured in the 1200 kip capacity test machine by a hydraulic pressure transducer connected to the data acquisition system. In addition hydraulic pressure was monitored visually by a dial gage during testing. Both the 600 kip and 1200 kip test machines were calibrated using a 1000 kip

capacity load cell certified by the National Institute of Standards and Technology. The maximum estimated error in load readings is $\pm 1\%$.

2.7.2. Displacements

Displacements were measured using linear displacement potentiometers with a range of 2.0 inches and an accuracy of ± 0.001 inches. The potentiometers were positioned to measure four general classes of displacements: the profile of the compression face of the specimen; curvature of the specimen; rotation of the specimen load heads; and displacements of the test machine. The positions of these four classes of potentiometers are described below.

Fifteen potentiometers were used to measure the compression face profile. These were positioned on three rigid frames mounted on the specimen as shown in Figures 2.30 and 2.31 . With this arrangement the local out-of-plane distortion of the compression face was measured along three lines running across the width of the face. Because of the three separate local reference frames global distortion of the plate, due to overall bending of the column was eliminated from the measurements. Local out-of-plane distortions at the boundaries of the plate were assumed to be zero.

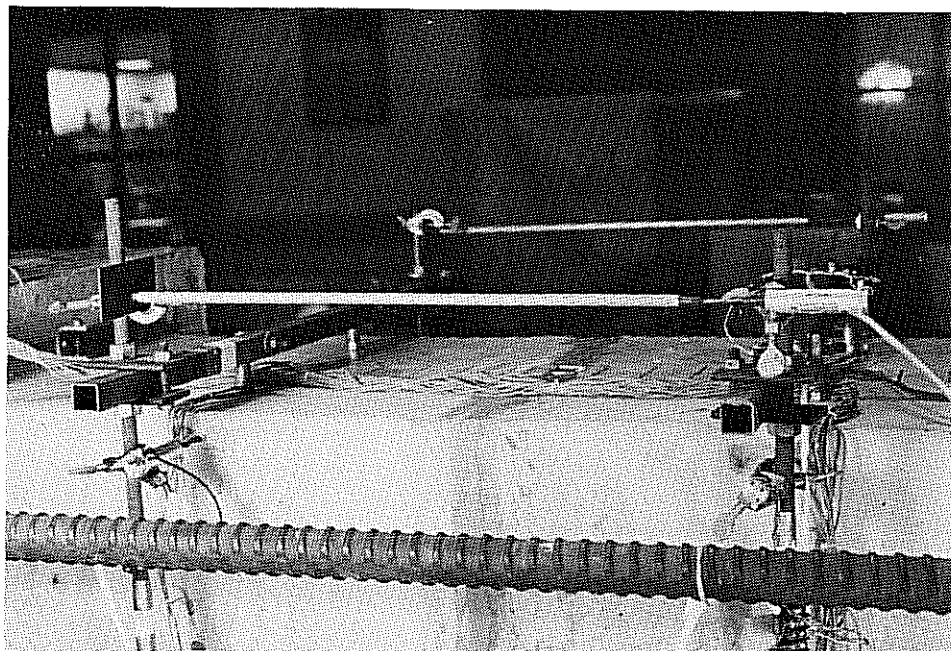


Figure 2.30: Instrument Frames Installed on Specimen

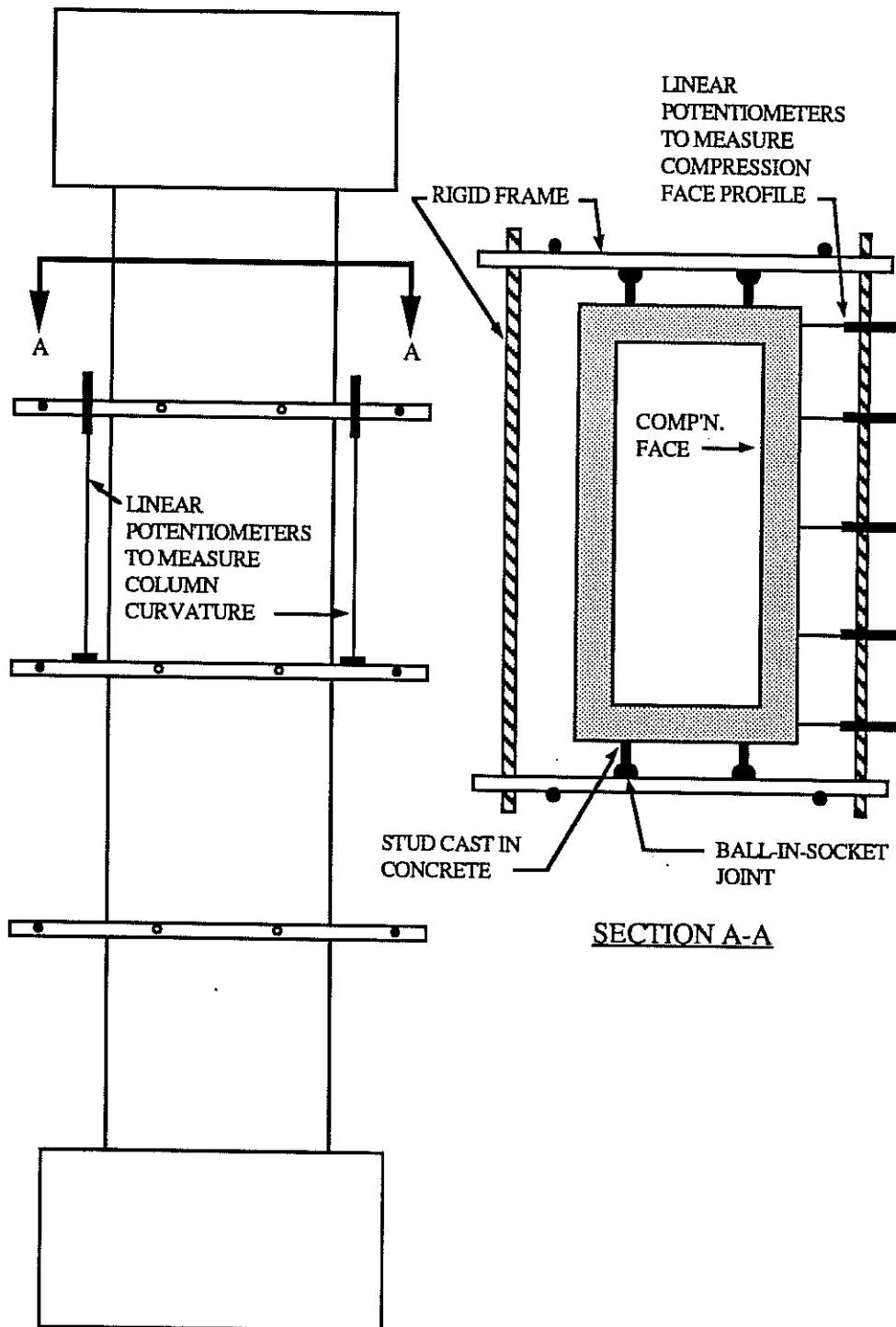


Figure 2.31: Instrument Frames

Curvature of the column was measured by potentiometers mounted on two rigid frames attached to the cross section, Figures 2.30 and 2.31. Curvature was calculated from the known geometry of the potentiometer positions and the recorded potentiometer displacements.

Displacements of the specimen load head and of the 1200 kip test machine were measured by the arrangement of potentiometers shown in Figure 2.32. An insufficient number of potentiometer was used in the initial part of the test program, so complete data for load head and test machine displacements was obtained only for specimens 8ML25 to 12S29.

A fifth class of displacements recorded in the tests was the distortion of the column center line. This was measured using a taut string line positioned about 1 inch away from the surface of a short side of the specimen, directly above the column center line marked on the specimen, Figure 2.33 and 2.34. A pulley and weight arrangement kept the string taut throughout the test. This string provided a straight-line reference frame between points A and B in Figure 2.33. Displacements were measured by sighting the string position against scales glued to the face of the column. The scales were oriented perpendicular to the column axis and were mounted at intervals over the height of the column. A mirror was mounted next to each scale to eliminate parallax in the readings. For Specimens 1M10 and 2M10 two string lines were used, one on each short face, and the readings were averaged. In the remaining tests, in the 1200 kip machine, it was possible to install only one string line. The accuracy of the string line readings was ± 0.02 inches.

2.7.3. *Strains*

Strains in longitudinal reinforcing bars were measured using electric resistance strain gages. The gage size was 1.5 mm wide by 5 mm long. Each gage was applied to a small smoothed area on the surface of a bar, then coated with a liquid plastic waterproofing compound. Lead wires were routed out of the concrete wall through small holes drilled in the exterior formwork.

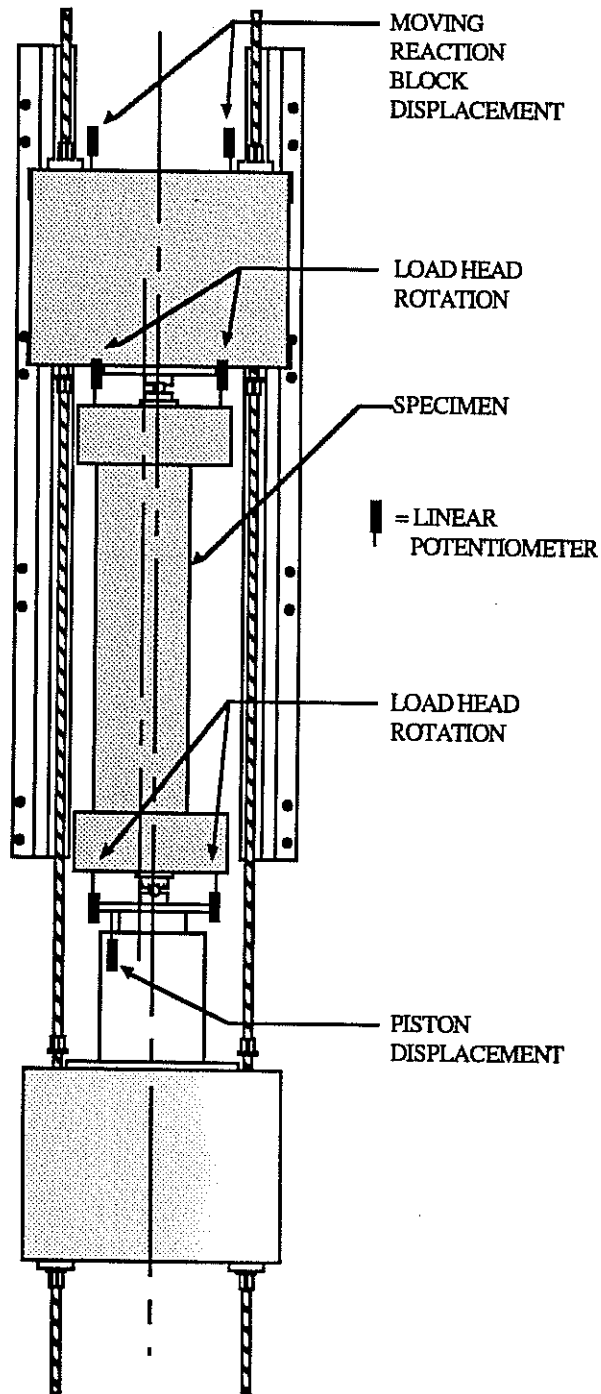


Figure 2.32: Load Head and Test Machine Displacements

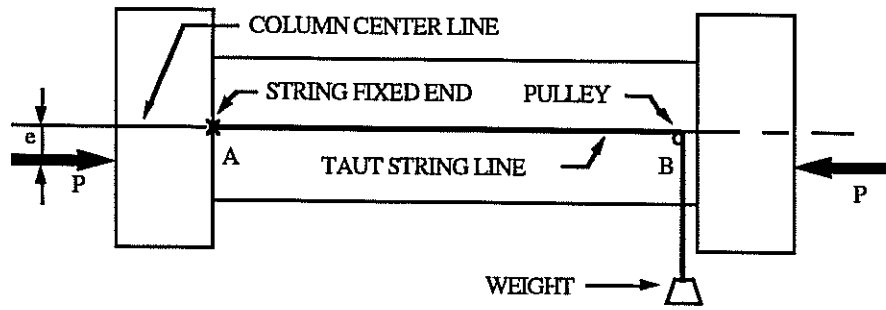


Figure 2.33: Taut String Line Schematic

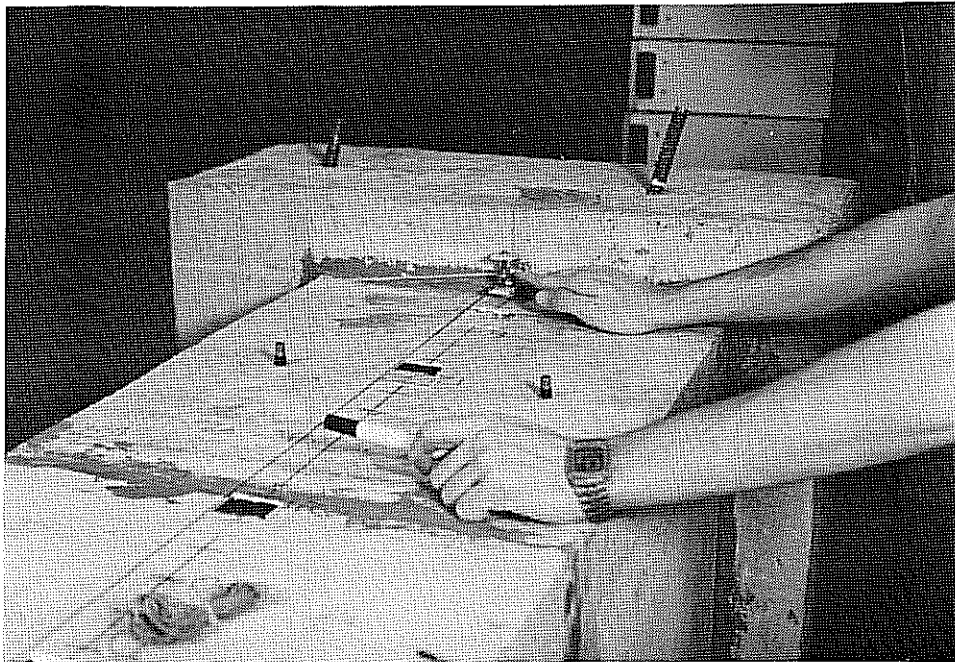


Figure 2.34: Taut String Line Installed on Specimen

Gages were located in each specimen as shown in Figures 2.5 to 2.10 and 2.35 to 2.42. In all cases a gage was placed on the side of the bar closest to the wall surface. This positioning was necessary to keep the gages from being damaged by the internal concrete vibrator.

The pattern of gage placement in each specimen was designed to measure three trends: a ring of gages near mid height of the specimen tested the hypothesis of plane sections remaining plane during bending; an array of gages over the compression face determined the distribution of longitudinal strains over that face; and two lines of gages near mid-height on the compression face on the inner and outer curtains of steel indicated strain gradients through the thickness of the wall. Not all twelve specimens were fitted with all three patterns of gages, but a sufficient number of gages was placed overall to gain the desired information.

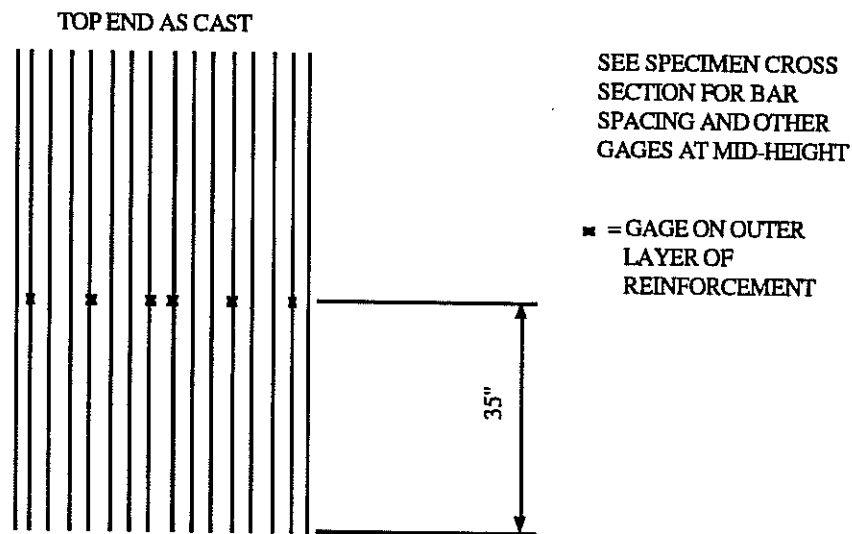


Figure 2.35: Gage Positions on Compression Face, Specimen 1M10

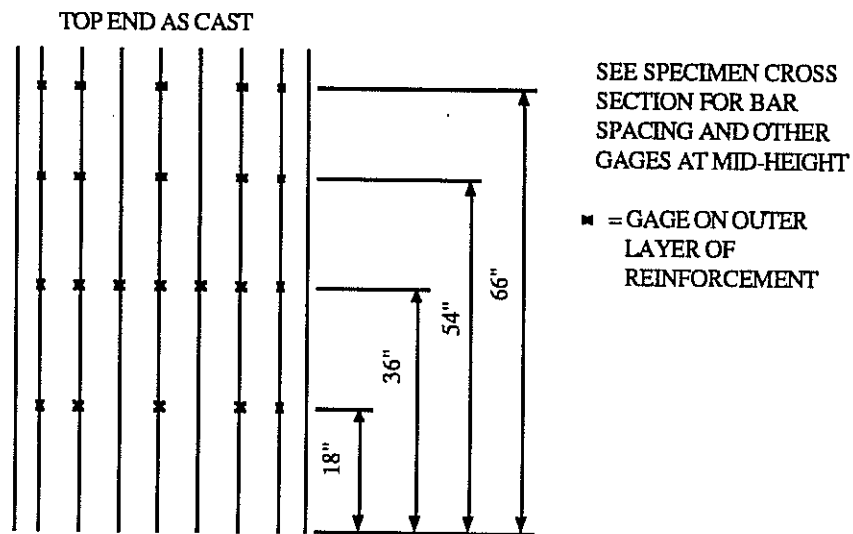


Figure 2.36: Gage Positions on Compression Face, Specimen 2M10

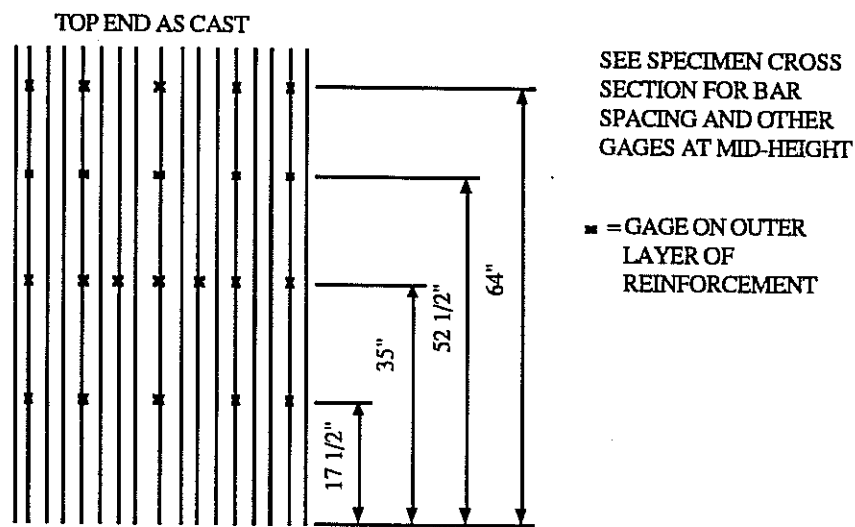


Figure 2.37: Gage Positions on Compression Face, Specimen 3M14

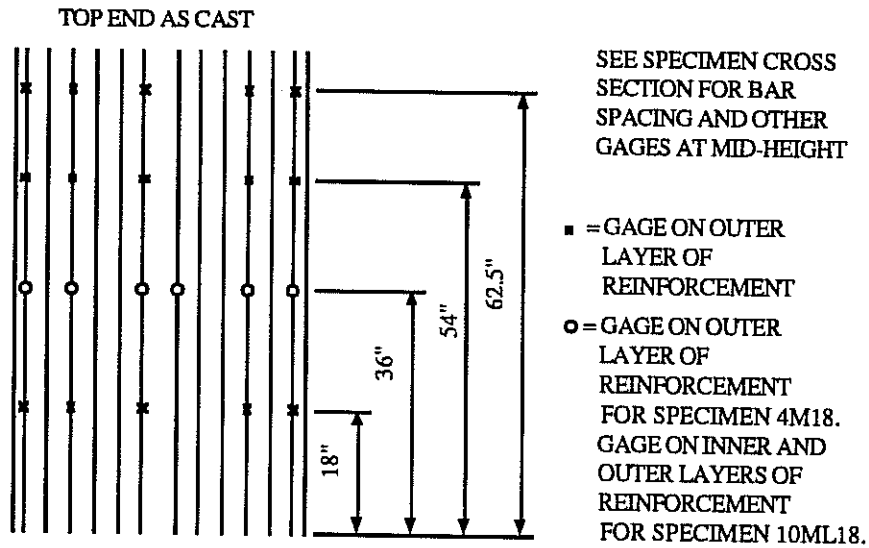


Figure 2.38: Gage Positions on Compression Face, Specimens 4M18 and 10ML18

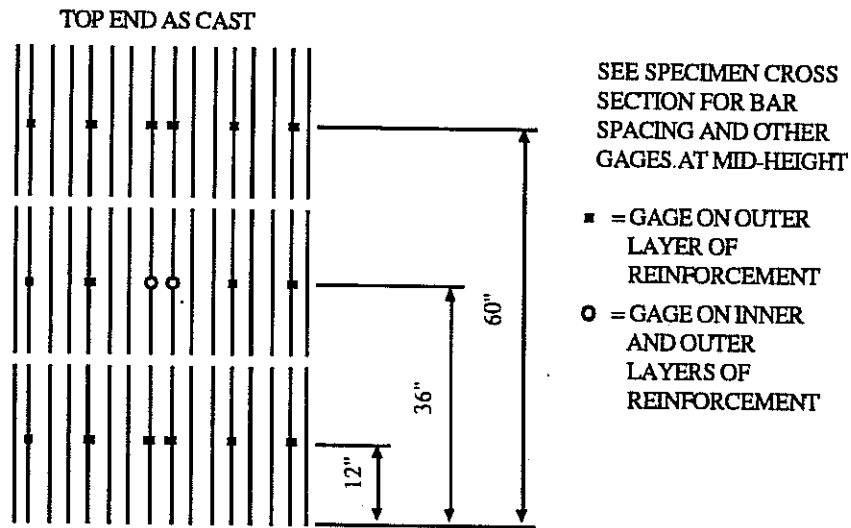


Figure 2.39: Gage Positions on Compression Face, Specimen 5S9

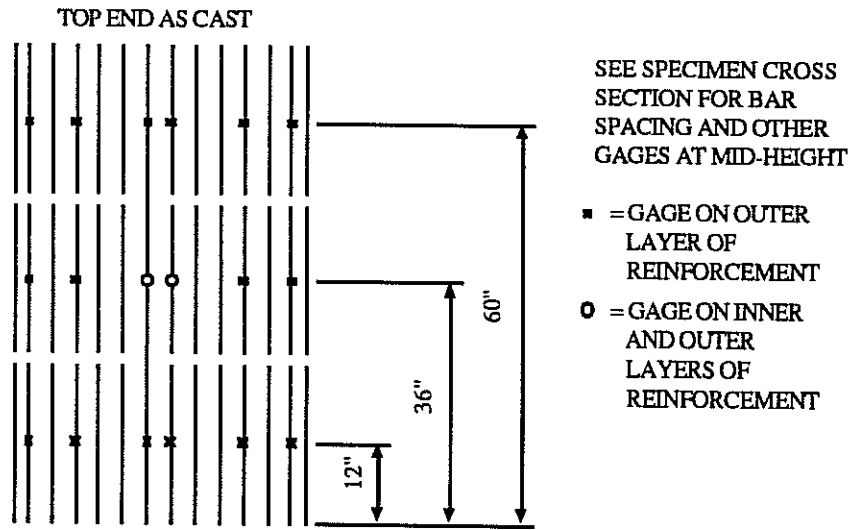


Figure 2.40: Gage Positions on Compression Face, Specimen 6S16

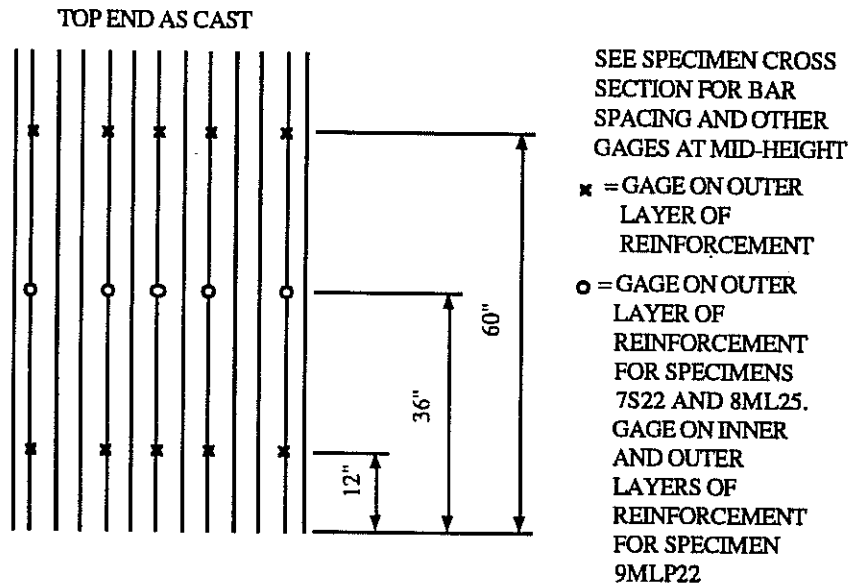


Figure 2.41: Gage Positions on Compression Face, Specs. 7S22, 8ML25, 9MLP22

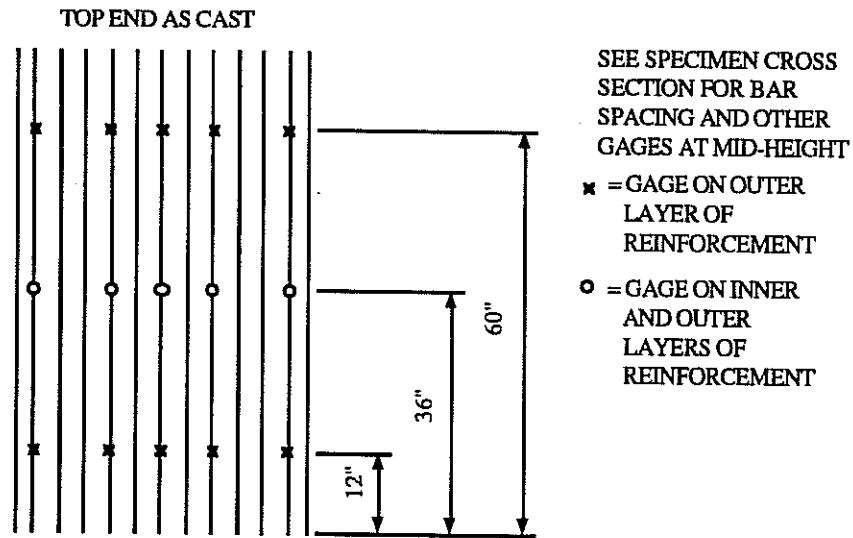


Figure 2.42: Gage Positions on Compression Face, Specimens 11ML34 and 12S29

2.7.4. Wall Thickness and Straightness Measurements

Because the buckling of a thin plate is sensitive to imperfections in plate thickness, accurate measurements were made of the thickness of the compression face of each specimen. For segmental specimens the wall thickness was measured before assembling the segments. Measurements were made with a pincer caliper near the top and bottom edge of each segment at three locations across the compression face. For monolithic and multiple-lift specimens wall thickness measurements were made after the specimen was tested. Using an impact hammer a slot was made in the compression face about 2 inches wide running along the center line of the face. Wall thickness measurements were made with a pincer caliper about 4 inches on either side of the slot at approximately ten locations over the height of the specimen. The accuracy of all wall thickness measurements was ± 0.02 inches. Figure 2.43 shows plots of average wall thickness of the compression face vs. distance above the base of the specimen. The location of the specimen failure is also indicated.

The straightness of the compression flange was measured using a taught string line. The line was stretched vertically and held against the inner face of the compression flange (inside the void, before the top solid load head was cast).

Variation from straightness of the inner surface of the wall was found to be no more than ± 0.06 inches from top to bottom. This high degree of straightness was achieved by careful construction of the inner box forms.

The worst possible combination of simultaneous errors in wall thickness and straightness would place the center plane of the wall 0.16 inches from its ideal location. In most locations, however, the error was probably no more than ± 0.05 inches.

2.8. Test Procedure

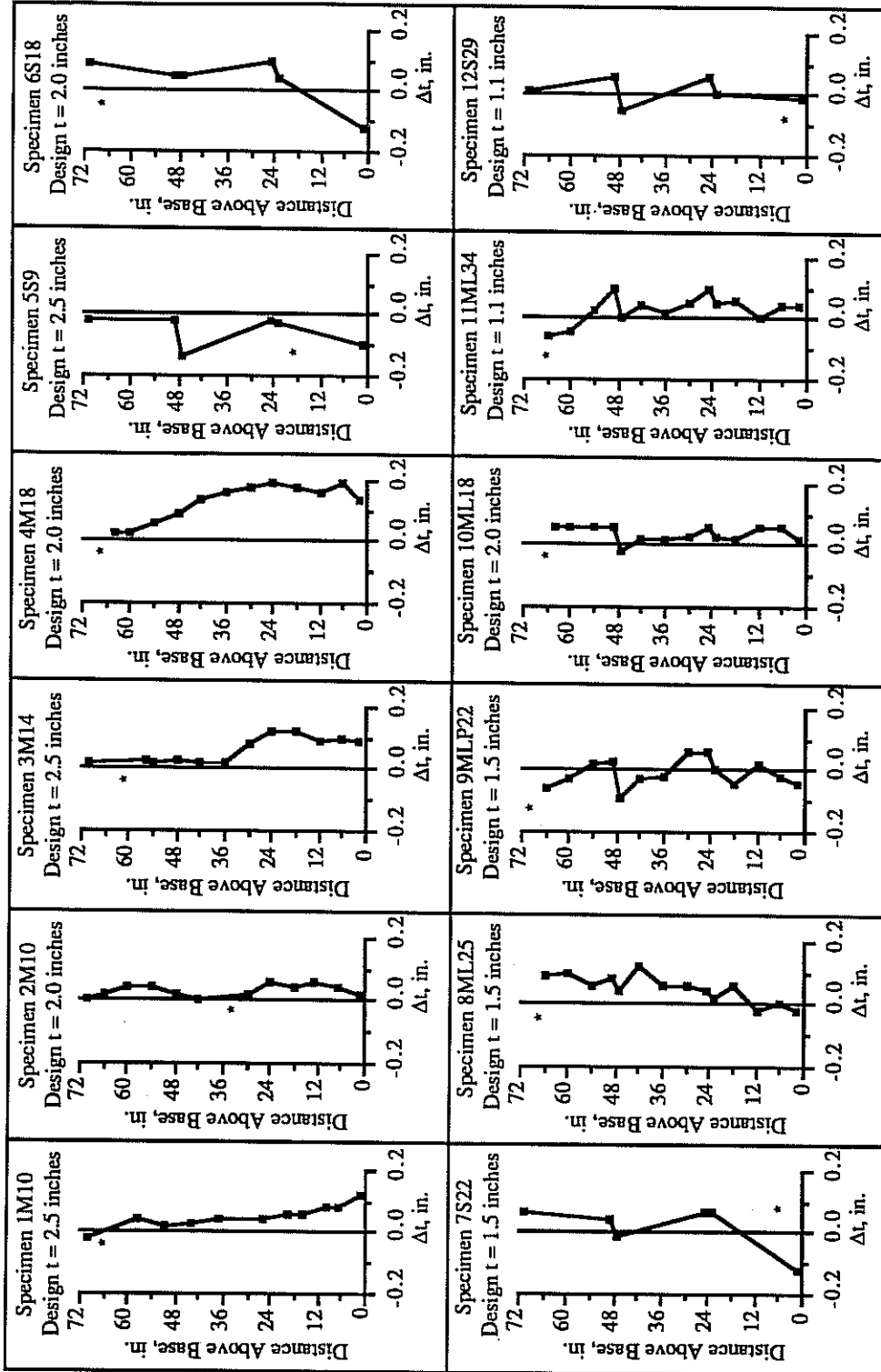
2.8.1. Data Acquisition System

Data from the strain gages, displacement transducers and pressure transducer was gathered electronically using a Hewlett Packard 3497A Control Unit driven by an IBM XT computer. From 35 to 65 instruments were read in each test at a scan rate of about 10 per second.

2.8.2. Steps in Testing

The first stage of each test was alignment of the test specimen in the test machine. Great care was taken to align the test specimen accurately, relative to the test machine center line, using surveying instruments. The maximum allowed misalignment of the longitudinal center line of the test specimen (plus the desired eccentricity) with respect to the longitudinal center line of the test machine was ± 0.10 inches in any direction. In most cases the accuracy was within ± 0.06 inches. Given the size of the specimens and test machines it was felt this was the best alignment accuracy that could practically be achieved.

After alignment the specimen was fixed in position by temporary restraining hardware. The pin bearings were then aligned at the ends of the specimen and a thin layer of hydrastone was placed between the pin bearing plates and the concrete load heads. The instruments were then installed and connected to the data acquisition system.



* Denotes approximate location of failure, distance above base of specimen.

Figure 2.43: Measured Deviation of Wall Thickness From Design Wall Thickness

Each specimen was loaded to failure according to the following procedure. First a "zero state" scan of all instruments was taken and initial taut string line readings were made. A load of 40 to 60 kips was applied, all temporary restraining hardware was removed, and an instrument scan was made. Loading of the specimen then proceeded in 40 kip steps, with an instrument scan taken just after each load step was applied. Cracks were marked with a black pen when they initially appeared on the surface of the specimen, and crack growth was marked about every 160 kips thereafter. Taut string line readings were also made at load intervals of about 160 kips. Photographs were taken of the initial test setup, at the initiation of cracking, at intervals after cracking, and after failure. Because of safety concerns crack readings and taut string line measurements were stopped when signs of imminent failure were observed.

The total time for loading to failure was between 79 and 151 minutes, depending on the specimen (see Table 3.1). Over this period the time intervals between load steps were fairly constant for a given specimen, although about five extra minutes were required at certain load steps to allow for taking photographs, marking cracks and reading the taut string line. The average rate of loading for each test was between 3 and 10 kips/minute.

The load at failure was determined in one of two ways. With many specimens failure occurred about 30 seconds after a load step was applied, that is, the specimen crept to failure under the applied load. Because of this delay it was possible to make a data scan immediately after the load step had been applied but before failure occurred. With other specimens failure occurred as a load step was being applied. In that case the failure load was determined by constant visual monitoring during loading of a calibrated hydraulic pressure dial gage. At previous load steps close agreement was observed between this dial gage and the electronic pressure transducer readings, so consistent measurements of failure loads were obtained by the two methods.

Chapter 3 Experimental Results

3.1. Overview

In this chapter the results of the experimental program are presented and discussed. First, some general observations are made regarding the accuracy and limitations of some of the test data. Second, results from the twelve hollow pier tests are presented and special characteristics of each test are noted. Finally, the results of all twelve tests are compared and various aspects of the experimental behavior are discussed.

3.2. Accuracy and Limitations of Test Data

The geometric tolerances followed in constructing and testing the specimens, and the accuracy of the instrumentation were described in Chapter 2. Below some practical limitations on strain gage data and specimen load head displacement measurements are discussed.

Strain gages were installed in the test specimens with the aim of measuring not only strains in the reinforcing bars, but also, by the assumption of compatibility between the steel and concrete, strains in the surrounding concrete. As is often the case with data obtained from strain gages mounted on reinforcing bars the measured strains in this test program were sometimes erratic. Several factors could be responsible for the observed inconsistencies. Strain gages are delicate instruments which sometimes do not perform well when embedded in concrete: moisture may penetrate the protective coating of a gage or damage to the surface of a gage may occur during casting or testing. Gages mounted on small-diameter reinforcing bars tend to come unglued when the bar is strained. Inhomogeneities and cracks in the surrounding concrete as well as residual stresses in reinforcing bars also contribute to erratic strain readings.

For these reasons any single gage cannot be relied on to give an accurate absolute reading of strain; however groups of gages viewed as a whole can indicate overall trends or relative magnitudes of strain. Taking this approach general information about strains can be gained from the test program in two areas:

observation of through-thickness strain gradients in the compression flanges of the specimens; and verification of the hypothesis that plane cross sections remain plane during loading. Unfortunately no strain patterns could be discerned in a third area, the distribution of longitudinal strains over the breadth and length of the compression flanges of the specimens. Two examples of the erratic strain distributions measured over the compression flanges are shown in Figures 3.1 and 3.2. Since useful data was not obtained from these gages they are not discussed further.

Four linear potentiometers were installed on specimens 8ML25 through 12S29 with the intention of measuring rotations of the specimen load heads, as shown in Figure 2.32. However, it was found that there was some distortion of these load heads during the tests, as evidenced by the typical load head crack patterns illustrated in Figures 3.6, 3.14 and 3.27. Because most specimens were loaded at very low eccentricities the rotations of the load heads were small. The maximum estimated load head rotation for specimens 8ML25 through 12S29 is 0.001 radians. This translates to a maximum linear potentiometer reading of 0.015 inches. However, spurious linear potentiometer readings introduced by load head distortions were estimated to be in the range of 0.04 to 0.12 inches. Thus load head distortion displacements overshadowed load head rotation displacements and accurate load head rotation measurements could not be obtained. For this reason load head rotation data are not presented.

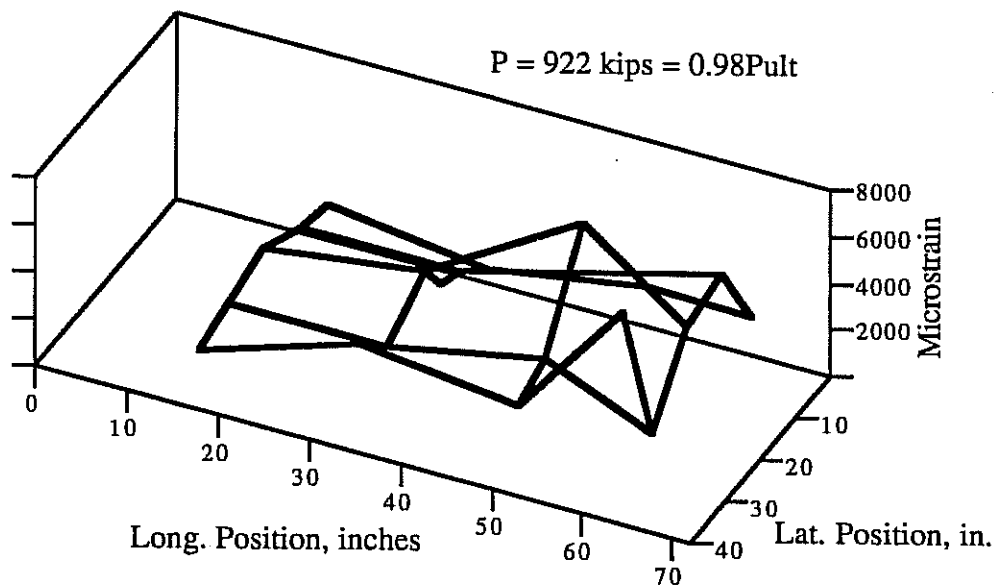


Figure 3.1: Specimen 3M14 Strain Distribution Over Compression Flange

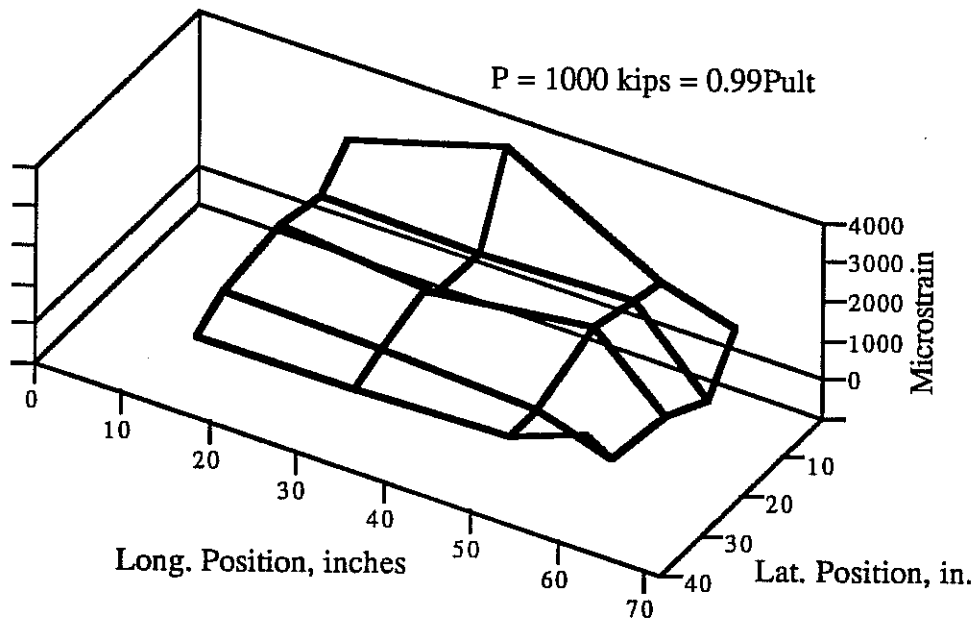


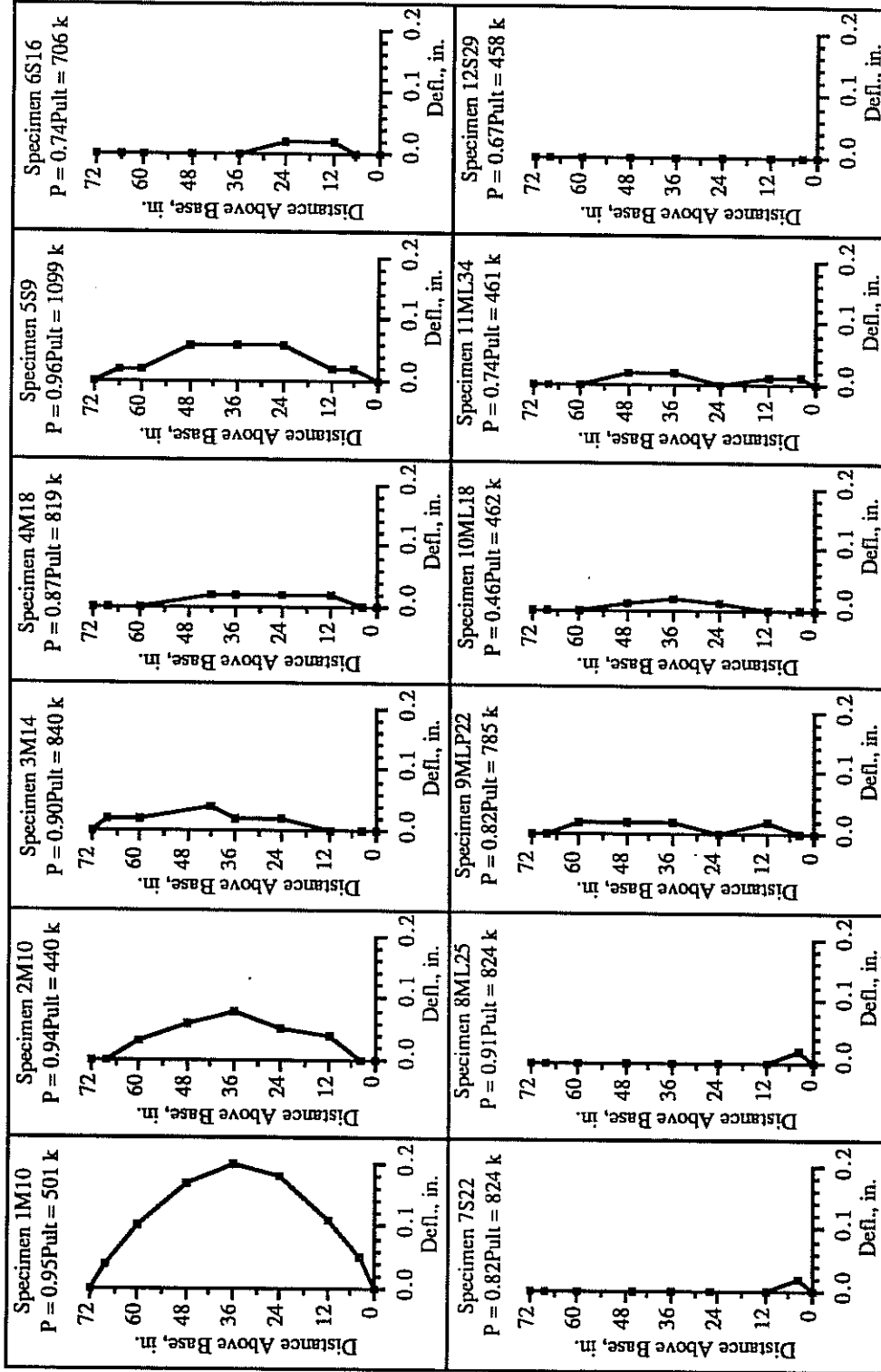
Figure 3.2: Specimen 10ML18 Strain Distribution Over Compression Flange

Specimen Number	Failure Load kips	Eccentricity inches	Failure Moment kip-in*	Failure Inches From Bottom	Time to Failure minutes	Average Load Rate kips/min.	String Line Reading at Mid-Height**		
							Reading inches	Load kips	Load / Pult
1M10	527	8.5	4590	64 - 70	144	3.7	0.20	501	0.95
2M10	470	0.62	331	32 - 38	159	3.0	0.08	440	0.92
3M14	938	1.0	975	56 - 66	202	4.6	0.04	840	0.90
4M18	938	2.75	2600	66 - 71	111	8.4	0.02	819	0.87
5S9	1138	0.75	922	16 - 24	128	8.9	0.06	1100	0.96
6S16	948	1.0	967	66 - 70	97	9.8	0.02	706	0.74
7S22	999	1.0	1020	1 - 6	120	8.3	0.02	824	0.82
8ML25	904	1.0	922	66 - 71	101	9.0	0.02	824	0.91
9MLP22	961	1.0	980	68 - 70	118	8.1	0.02	785	0.82
10ML18	1013	2.75	2810	64 - 70	101	10.0	0.02	462	0.46
11ML34	623	1.0	635	66 - 68	97	6.4	0.02	461	0.74
12S29	682	1.0	682	2 - 6	71	9.6	0.00	458	0.67

* Failure Moment = (Failure Load) x (Eccentricity + Maximum String Line Reading at Mid-Height)

** See explanatory note at the beginning of Section 3.3

Table 3.1: Summary of Test Results



Column center line deflections are shown for maximum load at which readings were taken. Accuracy = ±0.02 inches.

Table 3.2: Taut String Line Readings of Column Center Line Deflections

3.3. Test Results

The geometric and material properties of the twelve test specimens have been presented in Tables 2.1 and 2.2. Table 3.1 summarizes the main experimental data. Table 3.2 shows the column center line deflections obtained from taut string line readings. Results and discussions of each of the twelve tests are presented in sections 3.3.1 to 3.3.12.

The center line deflections are shown in Table 3.2 for the maximum load at which string line readings were taken. For most specimens the maximum load at which string line readings were taken was near the ultimate load, but with a few specimens this load was as little as 46% of the ultimate load. This was because string line readings had to be stopped for safety reasons when a specimen seemed to be giving signs that it was about to fail. Thus, the center line deflections shown in Table 3.2 represent the best available measurements for computing second order moments induced in the specimens. It can be seen that for most specimens the center line deflections, and consequently the second order moments, were small even near ultimate load. Thus, the lack of center line deflection measurements near ultimate load for some specimens does not result in a large error in the computed second order moments.

It should be noted that in the following discussions of experimental results the two wide flanges of the hollow rectangular test sections are referred to as the "compression" and "tension" flanges. This is merely a convenient way of naming the two flanges which does not necessarily reflect the true state of stress in the flanges. In most of the tests the eccentricity of the applied load was so small that no tensile stresses were induced in the "tension" flange.

3.3.1. 1M10 (Monolithic, 15" x 30", 2.5" walls, $X_u/t = 10.0$)

Figures 3.3 to 3.9 summarize the experimental results for specimen 1M10. The specimen failed explosively at a load of 527 kips. The mode of failure was crushing of the compression flange in a region between 64 and 70 inches above the bottom load head (as cast), as shown in Figures 3.3 and 3.5. These figures give the

impression that the only damage to the specimen was spalling of the outer layer of concrete cover. However, inspection of the specimen revealed that the compression flange was crushed completely through its thickness along a line roughly at the center of the spalled region.

Several narrow longitudinal cracks appeared in each load head at about 400 kips, and these grew in length until the failure load was reached (Figure 3.6). Lateral cracks appeared in the tension flange of the specimen at 175 kips. When the load reached 250 kips a lateral crack had formed at the locations of every layer of lateral reinforcement in the specimen (Figure 3.4). Specimen 1M10 was the only one of the twelve specimens which exhibited this type of lateral cracking. This was because it was the only specimen tested at an eccentricity large enough to induce tension stress in the "tension" flange.

No cracks appeared in the compression flange prior to failure (the cracks shown in Figures 3.3 and 3.5 were marked after failure).

The reinforcement details in this specimen all performed well. A few longitudinal bars were observed to be buckled outward between layers of lateral reinforcement after failure. Such buckling of longitudinal bars is to be expected since the concrete which surrounds and supports the bars is lost suddenly in an explosive failure.

Figure 3.7 shows the compression flange profile just prior to failure. The outward bulge of the face had the lowest magnitude of any of the twelve specimens.

Figure 3.8 shows the distribution of longitudinal strains over the cross section at mid-height. (Data is not shown for one corner gage which failed). The figure confirms the hypothesis that plane cross sections remained plane at all load levels, for this particular specimen.

The experimental moment-curvature curve for the specimen is plotted in Figure 3.9. After initial "settling in" of the instruments at low loads, the curve shows fairly linear behavior up to about 80% of the failure load.

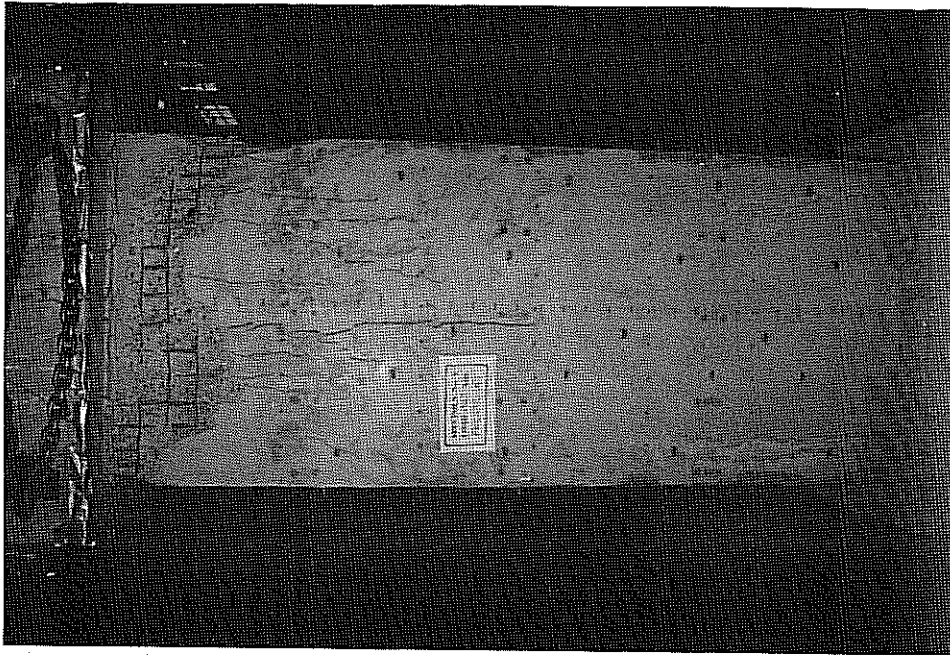


Figure 3.3: Specimen 1M10 Compression Flange

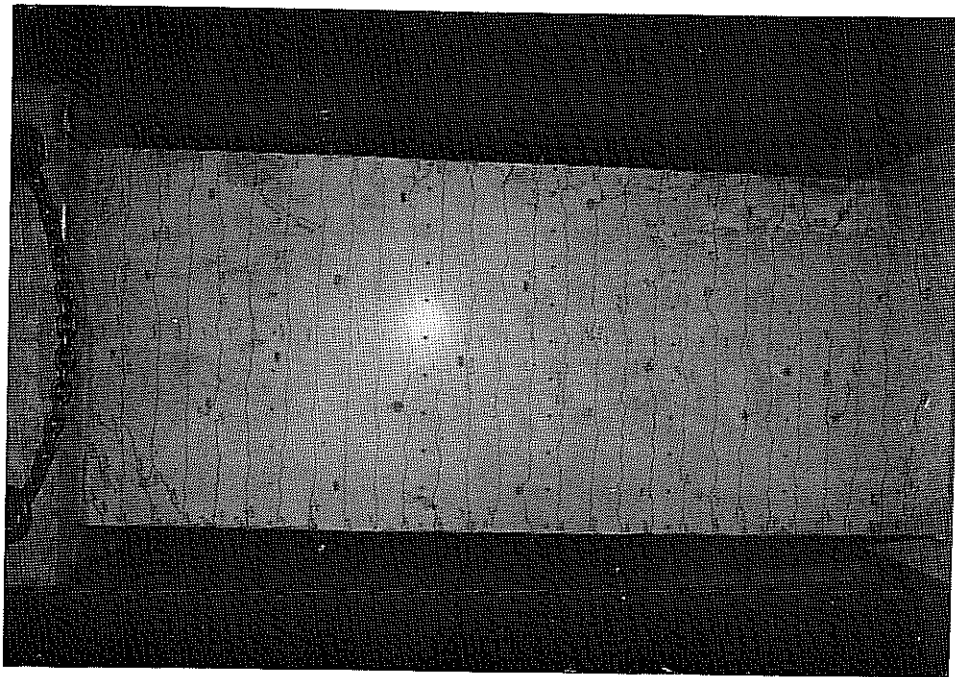


Figure 3.4: Specimen 1M10 Tension Flange

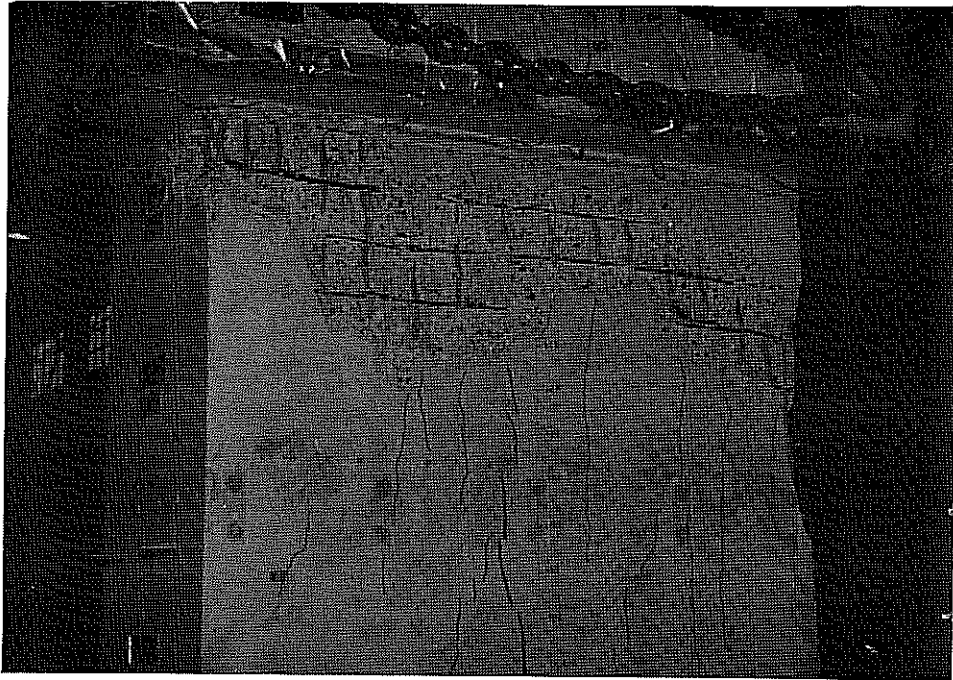


Figure 3.5: Specimen 1M10 Compression Flange Close-Up

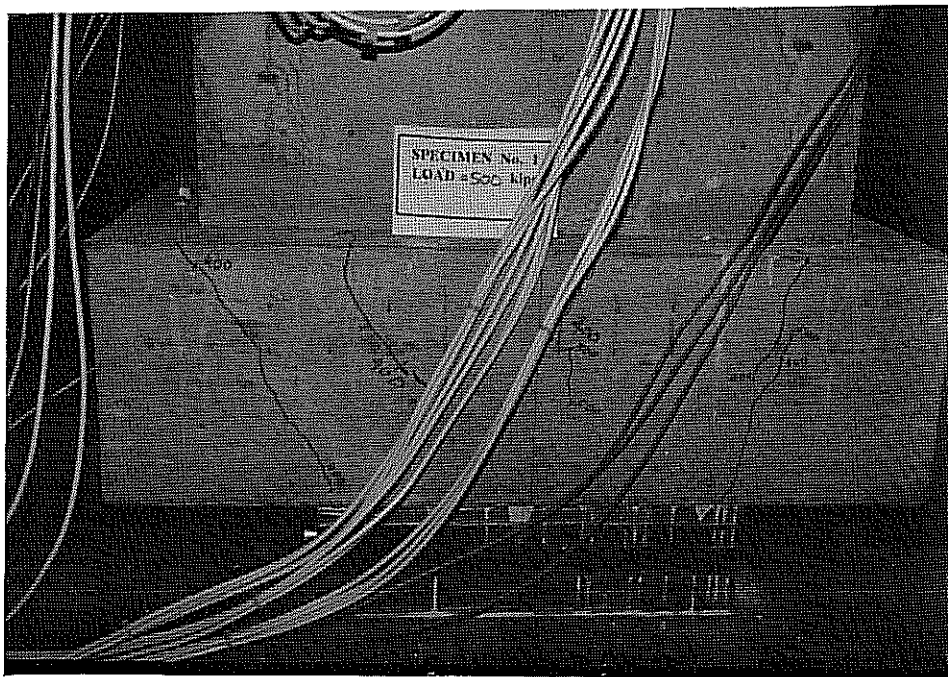


Figure 3.6: Specimen 1M10 Bottom Load Head

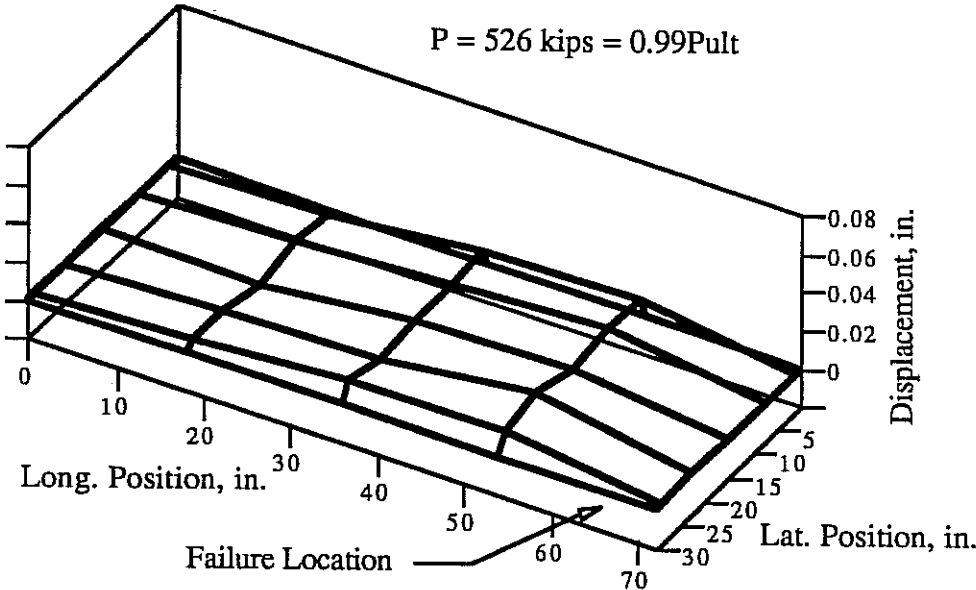


Figure 3.7: Specimen 1M10 Compression Flange Profile

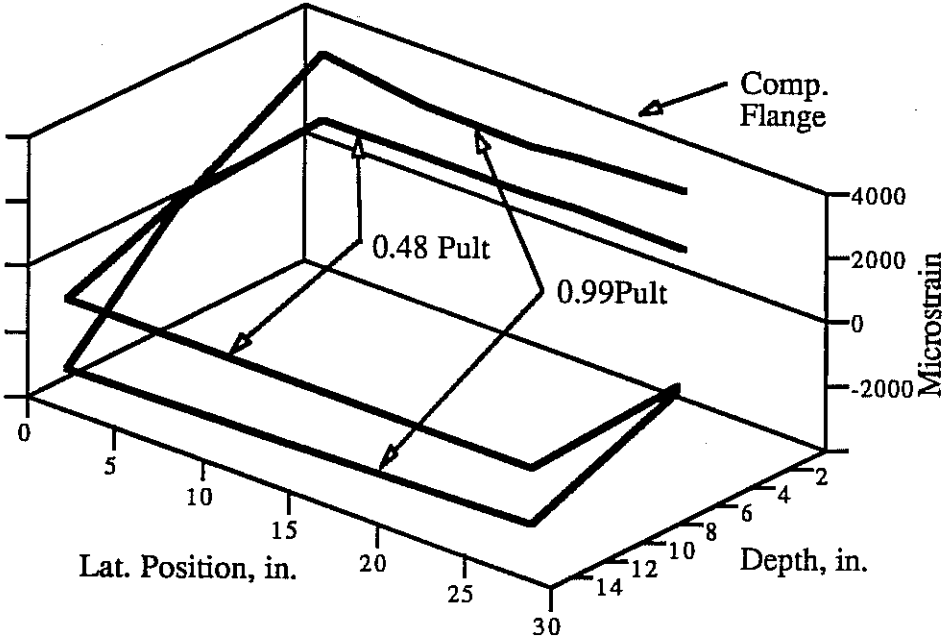


Figure 3.8: Specimen 1M10 Cross Section Strain Distribution

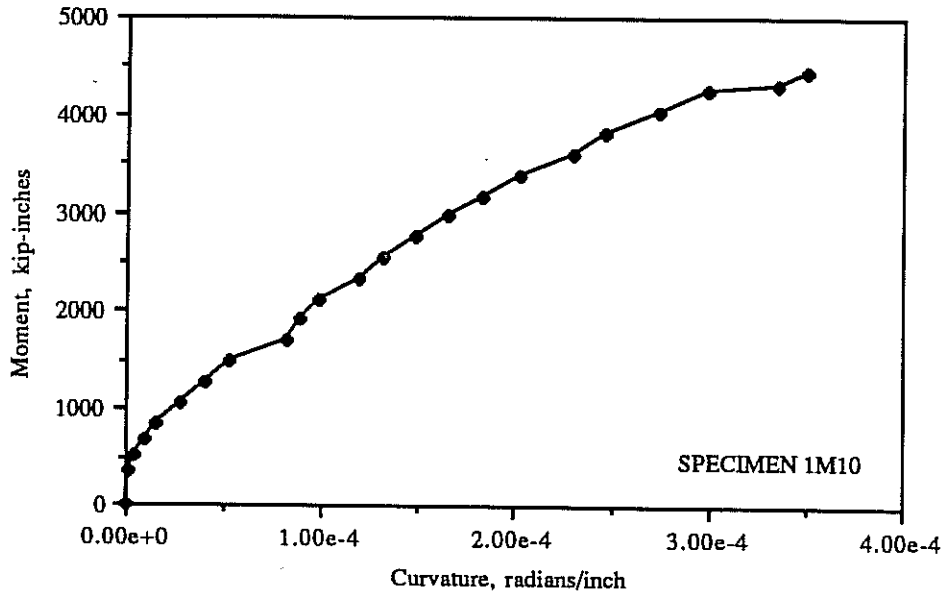


Figure 3.9: Specimen 1M10 Moment-Curvature Curve

3.3.2. 2M10 (Monolithic, 12" x 24", 2.0" walls, $X_u/t = 10.0$)

Results from the test on specimen 2M10 are shown in Figures 3.10 to 3.17. The specimen failed explosively near mid-height at a load of 470 kips (Figures 3.10 and 3.11). Failure was initiated by rupture of the compression flange accompanied by crushing in the side faces, as shown in Figure 3.11. A few minutes before failure the specimen sustained a momentary peak load of 480 kips when the desired target load was briefly exceeded. However failure occurred after about one minute of sustained loading at 470 kips.

A few small cracks were observed in the specimen load head at a load of 450 kips, as shown in Figure 3.14. Three longitudinal cracks appeared in the compression flange just prior to failure, as shown in Figure 3.10. These cracks were near the locations of longitudinal reinforcing bars. No cracks were observed in the "tension" flange before failure. The "tension" flange cracks indicated by dashed lines in Figure 3.12 were marked after failure.

Reinforcing details in this specimen performed well. Most longitudinal bars in the failure region buckled between layers of lateral reinforcement, as shown in Figure 3.13.

The compression flange profile plotted in Figure 3.15 is similar to that for specimen 1M10, but the magnitudes of the displacements are slightly greater.

Longitudinal compressive strains over the cross section are shown in Figure 3.16. (Data is not shown for one malfunctioning corner gage). At 50% of the ultimate load the strain distribution was very close to planar, but at ultimate load the compression flange strain profile was irregular.

The moment-curvature relationship for specimen 2M10, plotted in Figure 3.17, becomes very flat over the last few load steps preceding failure. This is consistent with the observation that the specimen crept to failure under a sustained load.

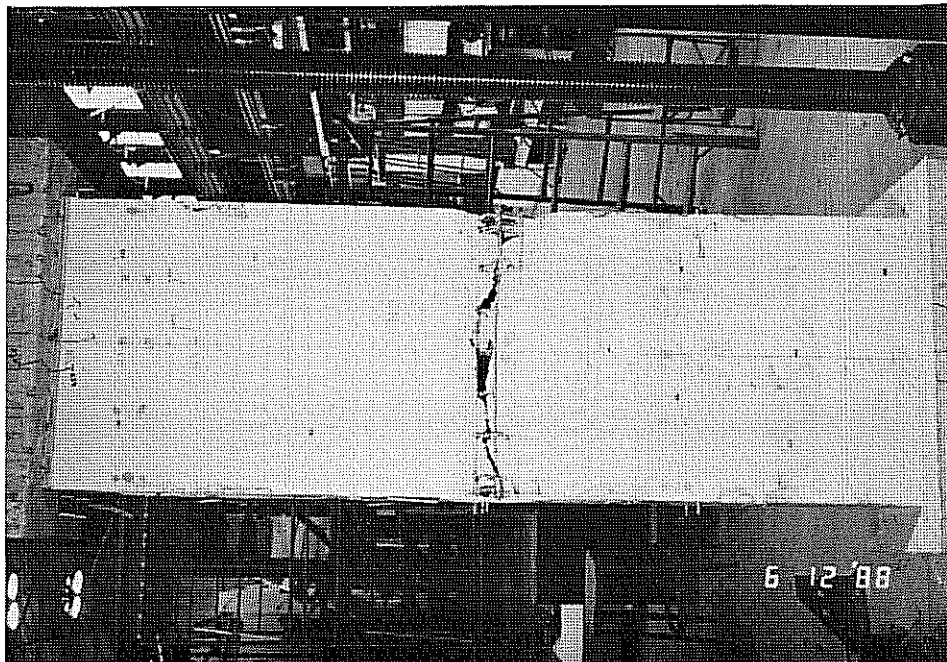


Figure 3.10: Specimen 2M10 Compression Flange



Figure 3.11: Specimen 2M10 Compression Flange Close-Up

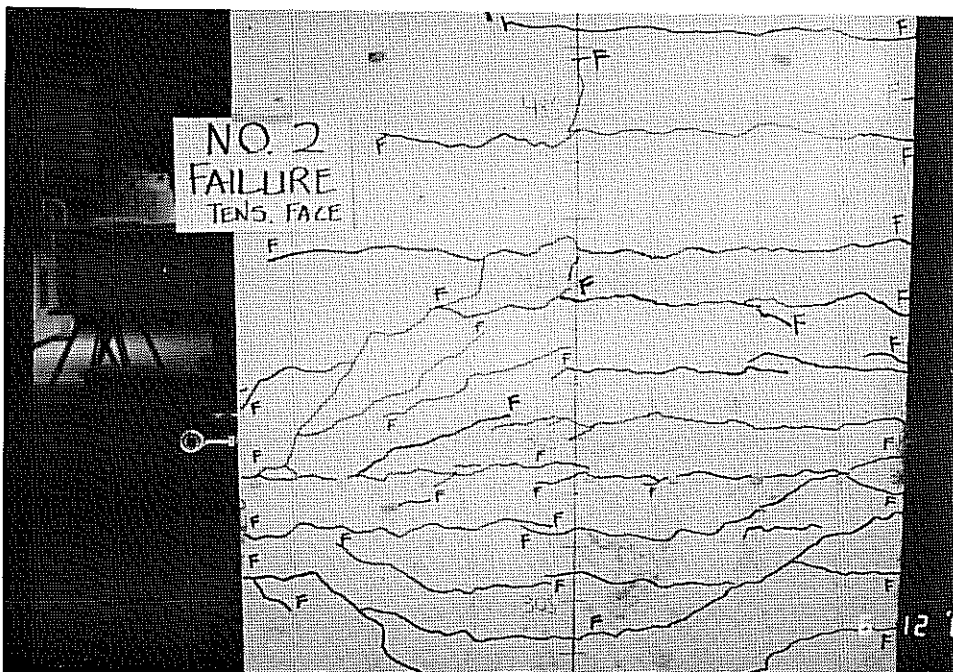


Figure 3.12: Specimen 2M10 "Tension" Flange

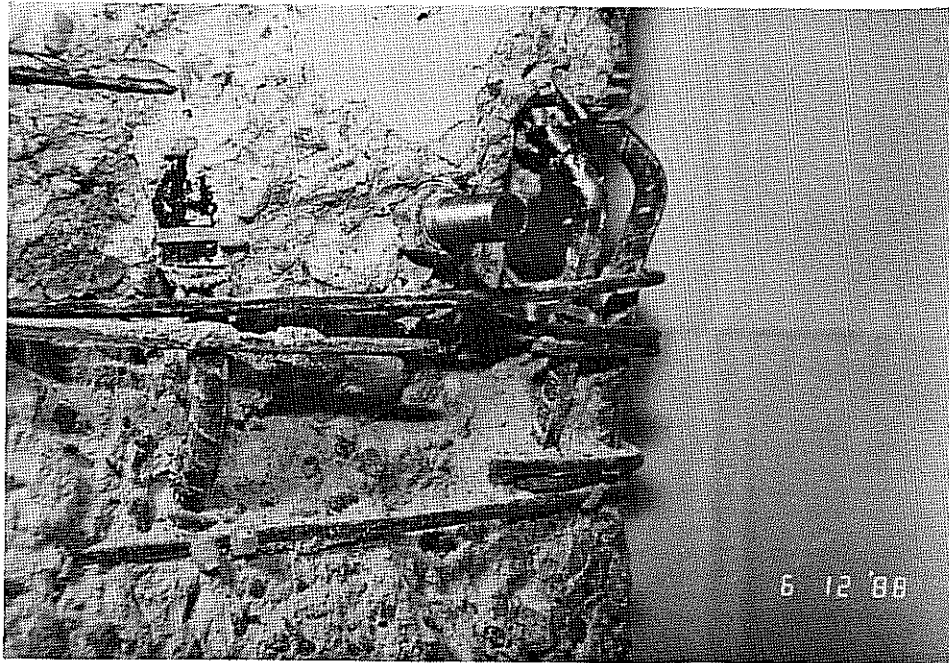


Figure 3.13: Specimen 2M10 Failure Region Close-Up

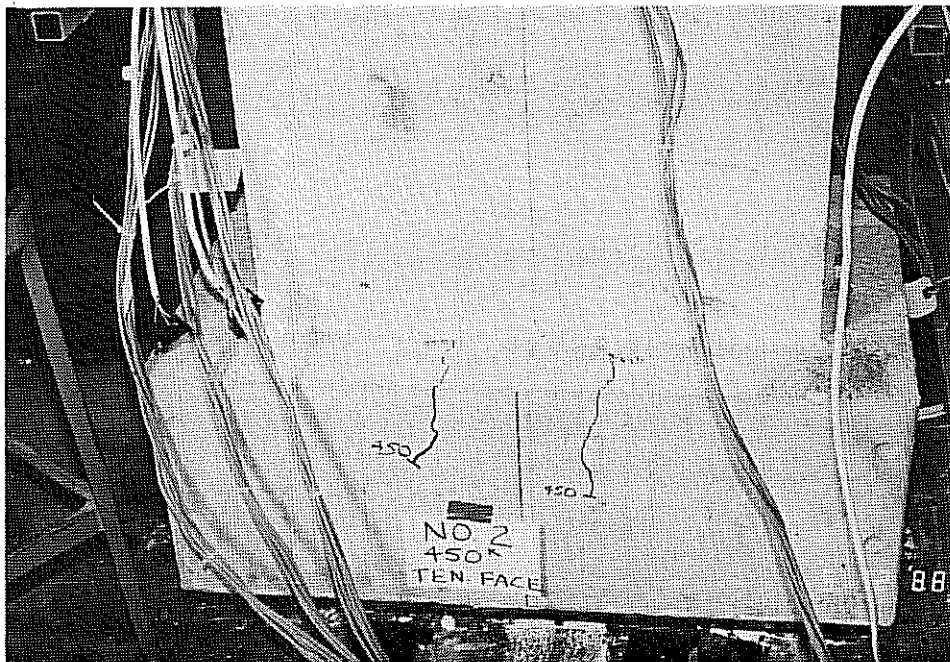


Figure 3.14: Specimen 2M10 Bottom Load Head

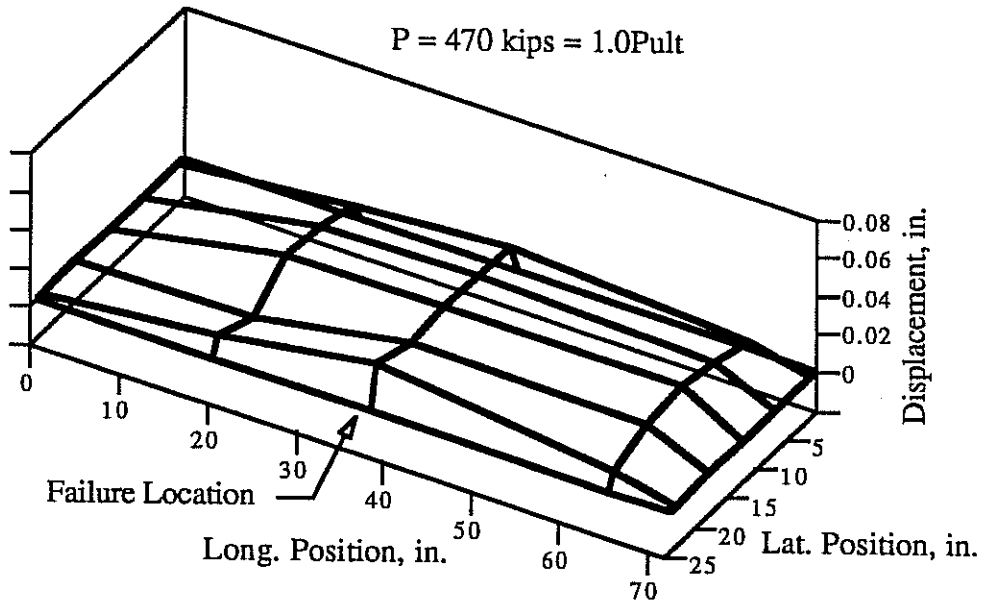


Figure 3.15: Specimen 2M10 Compression Flange Profile

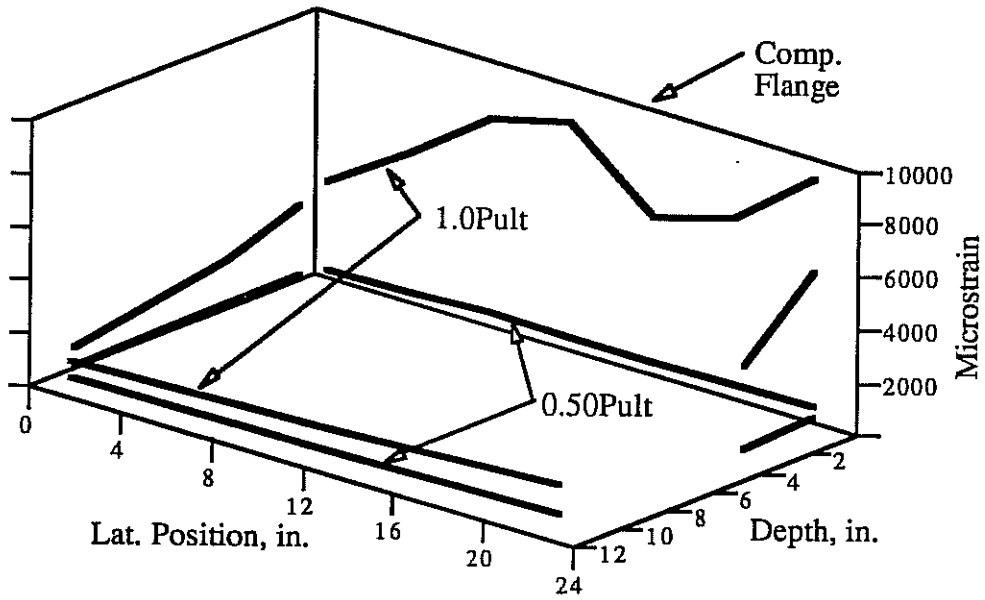


Figure 3.16: Specimen 2M10 Cross Section Strain Distribution

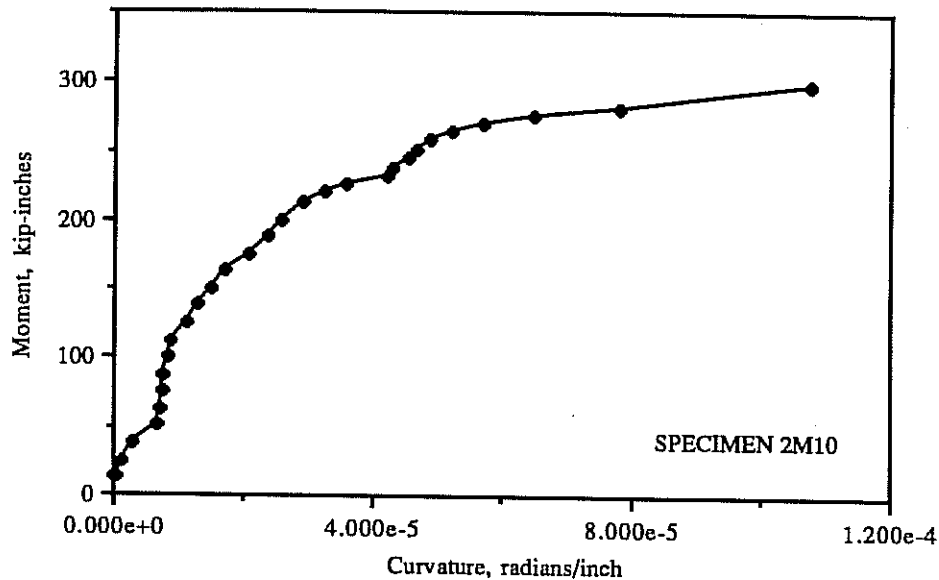


Figure 3.17: Specimen 2M10 Moment-Curvature Curve

3.3.3. 3M14 (Monolithic, 20" x 40", 2.5" walls, $X_U/t = 14.0$)

Experimental results for specimen 3M14 are illustrated in Figures 3.18 to 3.25. The specimen failed explosively at a load of 938 kips. The failure region was between 56 and 66 inches above the bottom load head (as cast). Crushing of the compression flange and side faces was extensive, as shown in Figures 3.18, 3.20, 3.21 and 3.22. The cross section underwent a large rotation in the failure region, as illustrated by the aerial view in Figure 3.22. This large rotation at failure was typical of all the specimens in the test program. The failure occurred while a load step was being applied to the specimen; that is, the specimen did not creep to failure under a sustained load.

Longitudinal cracks first appeared in the specimen load heads at a load of 280 kips, and continued to grow up to a load of about 640 kips. Longitudinal cracks appeared in the compression flange beginning at a load of 280 kips (Figure 3.18), and in the "tension" flange beginning at a load of 400 kips (Figure 3.19). The number of cracks forming in the compression and "tension" flanges was large compared to most other specimens in the test program. Cracks in the compression

and "tension" flanges generally formed at the locations of longitudinal reinforcing bars.

No particular problems were noted with the reinforcement details in this specimen, although crushing was so extensive in the failure region that it was difficult to determine the influence of reinforcement details on the failure.

In Figure 3.23 the compression flange profile is seen to have a general outward bulging shape just before failure. The magnitude of the displacements were relatively large compared to other specimens. The displacements were slightly greater near the two ends of the specimen.

Figure 3.24 shows that at 51% of the ultimate load the cross section compressive strain distribution was very close to planar. At 98% of the ultimate load the strains across the "tension" flange and the two side faces are planar, but the compression flange strains are erratic.

The moment-curvature plot in Figure 3.25 is fairly flat near the failure load, agreeing with the observed failure mode of creep to failure under sustained load.

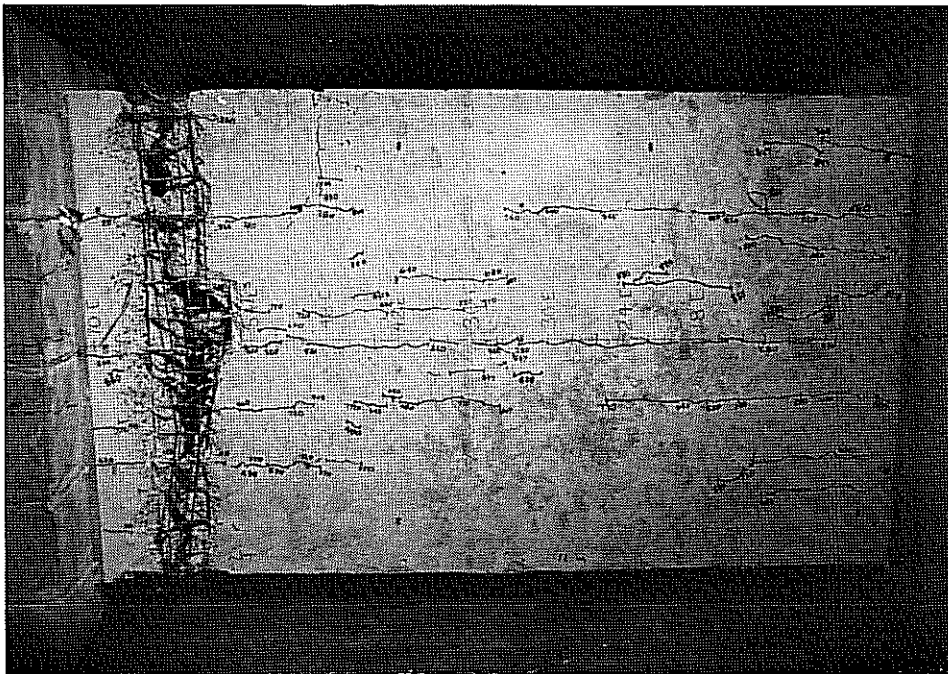


Figure 3.18: Specimen 3M14 Compression Flange

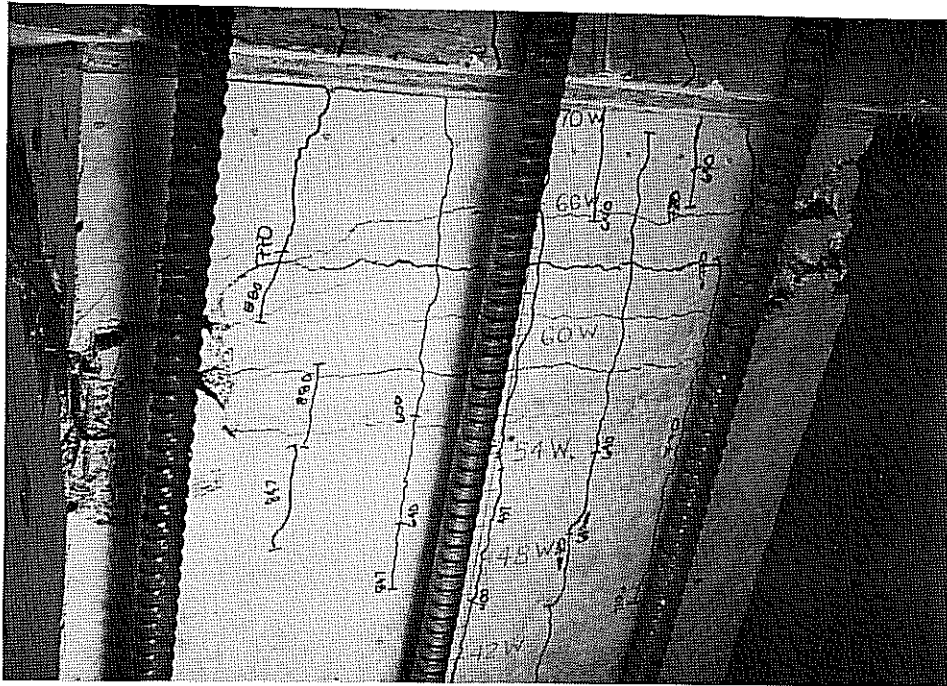


Figure 3.19: Specimen 3M14 Tension Flange

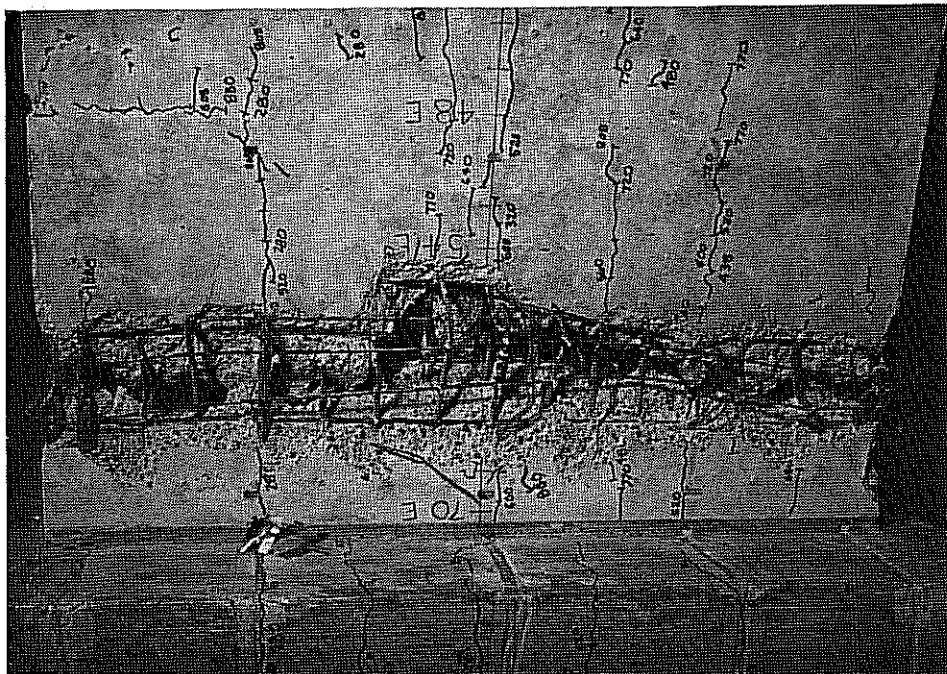


Figure 3.20: Specimen 3M14 Compression Flange Close-Up

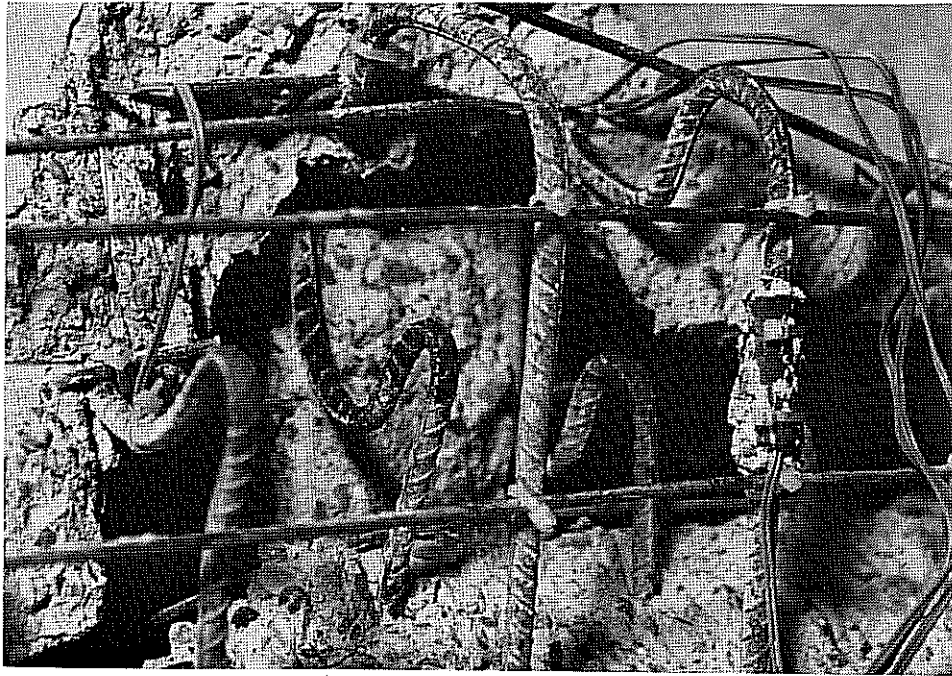


Figure 3.21: Specimen 3M14 Reinforcement in Failure Zone

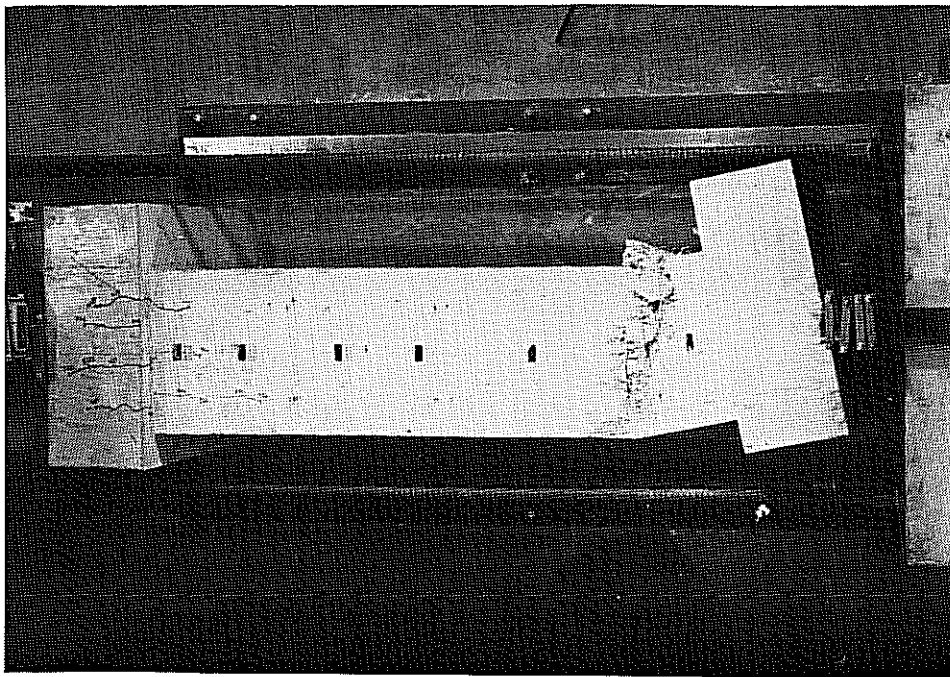


Figure 3.22: Specimen 3M14 Aerial View

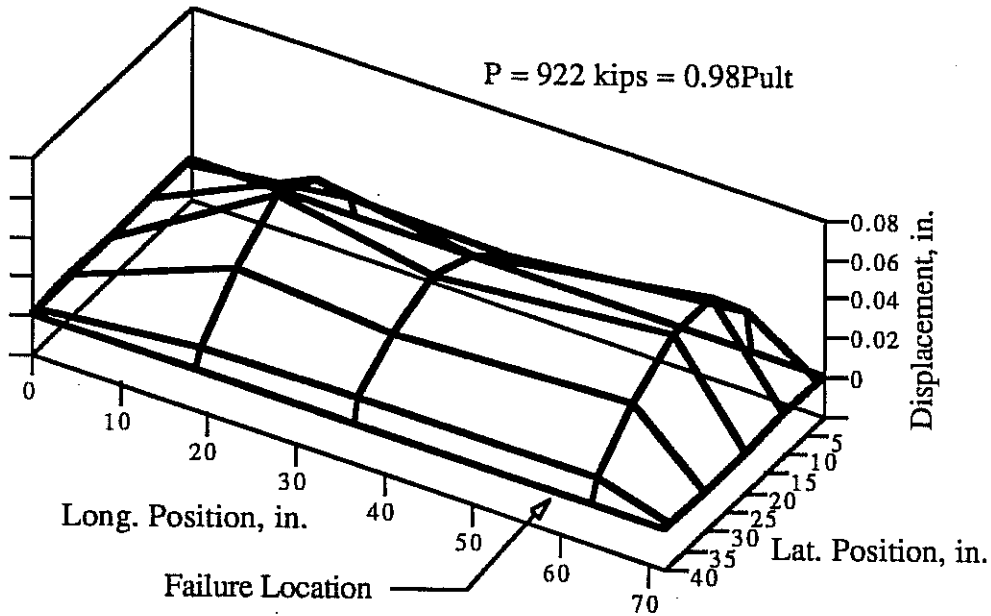


Figure 3.23: Specimen 3M14 Compression Flange Profile

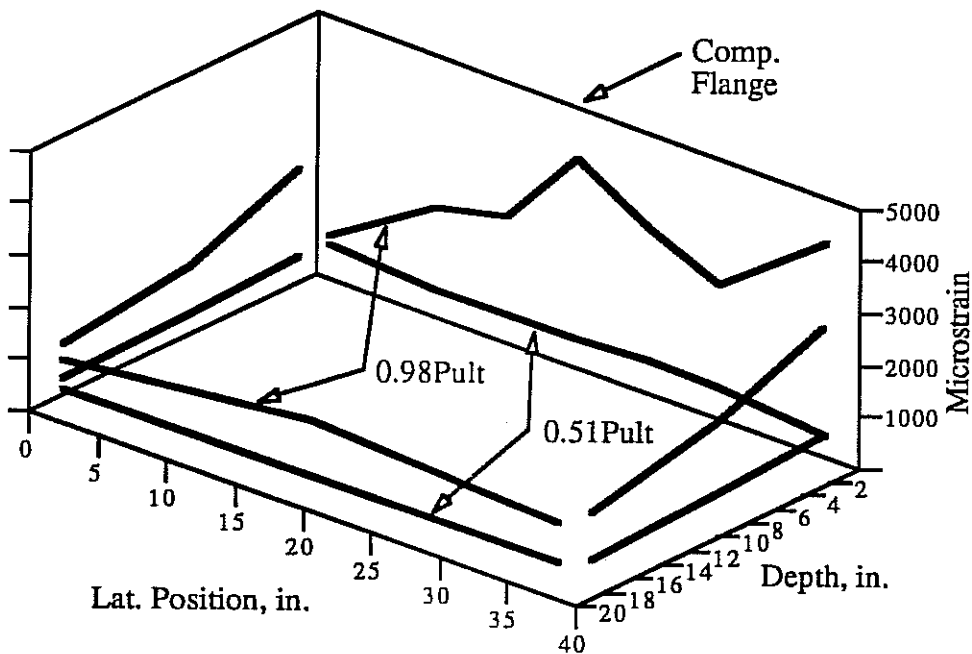


Figure 3.24: Specimen 3M14 Cross Section Strain Distribution

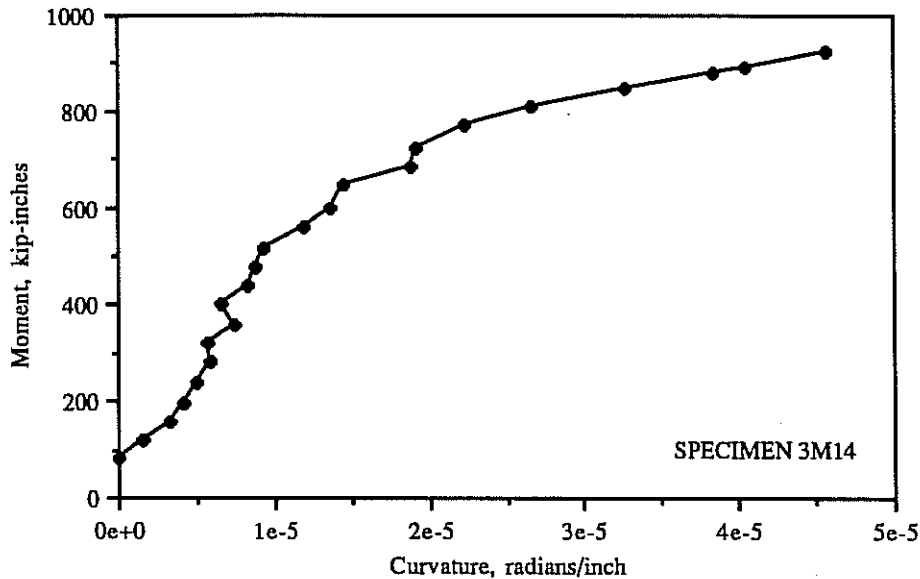


Figure 3.25: Specimen 3M14 Moment-Curvature Curve

3.3.4. 4M18 (Monolithic, 20" x 40", 2.0" walls, $X_u/t = 18.0$)

Figures 3.26 to 3.32 show the results of the test on specimen 4M18. The failure, which was explosive, occurred at a load of 938 kips. The specimen crept to failure after the last load step had been applied about two minutes. Just prior to failure faint "ticking" sounds were heard emanating from the specimen, but no other warning of imminent failure was observed. The location of the failure was near the top end of the specimen (Figures 3.26 to 3.29), occurring in a region between 66 and 71 inches above the bottom load head (as cast).

Cracks first appeared in the specimen load heads at a load of 458 kips. At the same load short longitudinal cracks formed in the "tension" flange near both ends of the specimen. Cracks first appeared in the compression flange, near the ends, at 496 kips. Cracks in the "tension" and compression flanges generally occurred at the locations of longitudinal reinforcing bars. The cracks shown by dashed lines in Figures 3.26 and 3.27 were marked after failure.

Reinforcement details in this specimen generally performed well, with one exception. The lap splices for lateral reinforcement on both the short faces of the

specimen separated and splayed outward at failure (Figure 3.29). This is to be expected, as the lap splices were not enclosed by any other reinforcement, and depended mainly on the concrete cover for their strength. Similar problems with this detail were observed in all subsequent specimens.

The compression flange profile in Figure 3.14 shows a fairly uniform bulging pattern just before failure, although displacements are higher near the ends than in the middle of the compression flange.

At low loads the strain distribution over the cross section, plotted in Figure 3.31, was close to planar. Near ultimate the strain distribution was less uniform, but still close to planar.

The moment-curvature curve plotted in Figure 3.32 is fairly steep and linear, which is not consistent with the observed creep failure mode of the specimen. Possibly some local phenomenon other than overall cross section failure was responsible for the collapse. Later inspection revealed that there was probably a weak zone of concrete near the top end of the specimen.

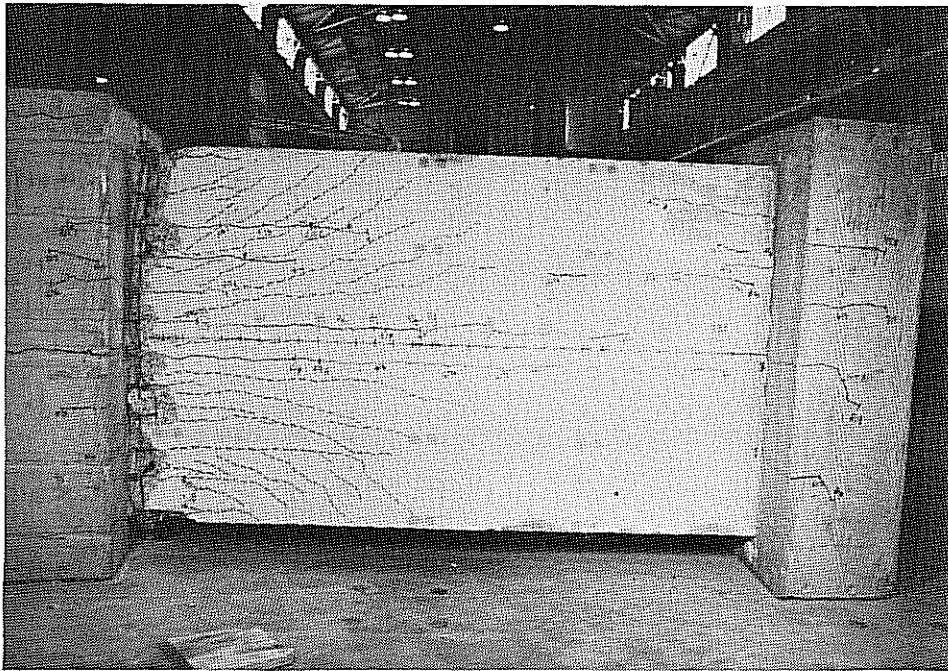


Figure 3.26: Specimen 4M18 Compression Flange

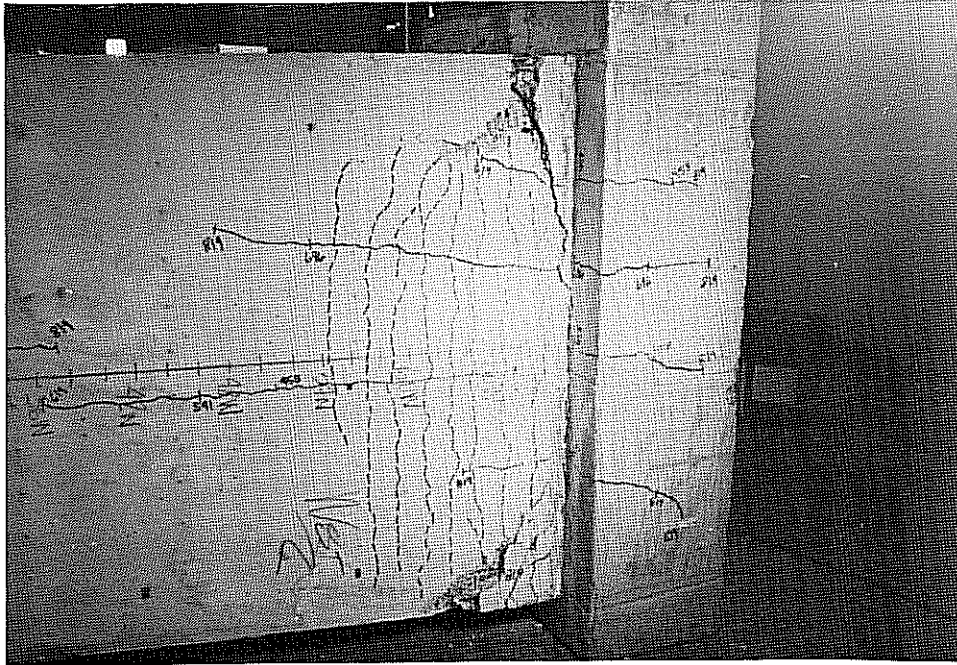


Figure 3.27: Specimen 4M18 "Tension" Flange



Figure 3.28: Specimen 4M18 Compression Flange Close-Up



Figure 3.29: Specimen 4M18 Side Face

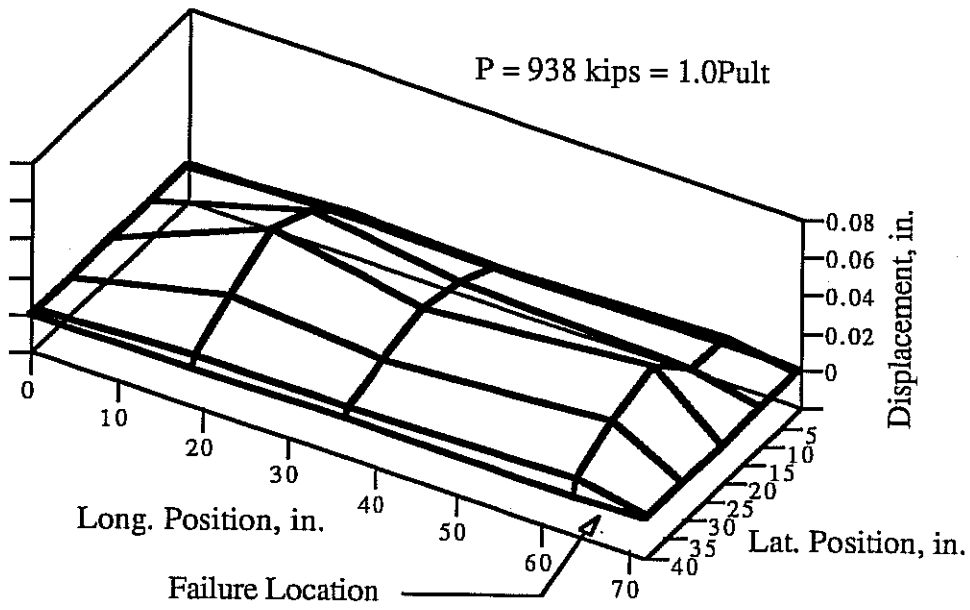


Figure 3.30: Specimen 4M18 Compression Flange Profile

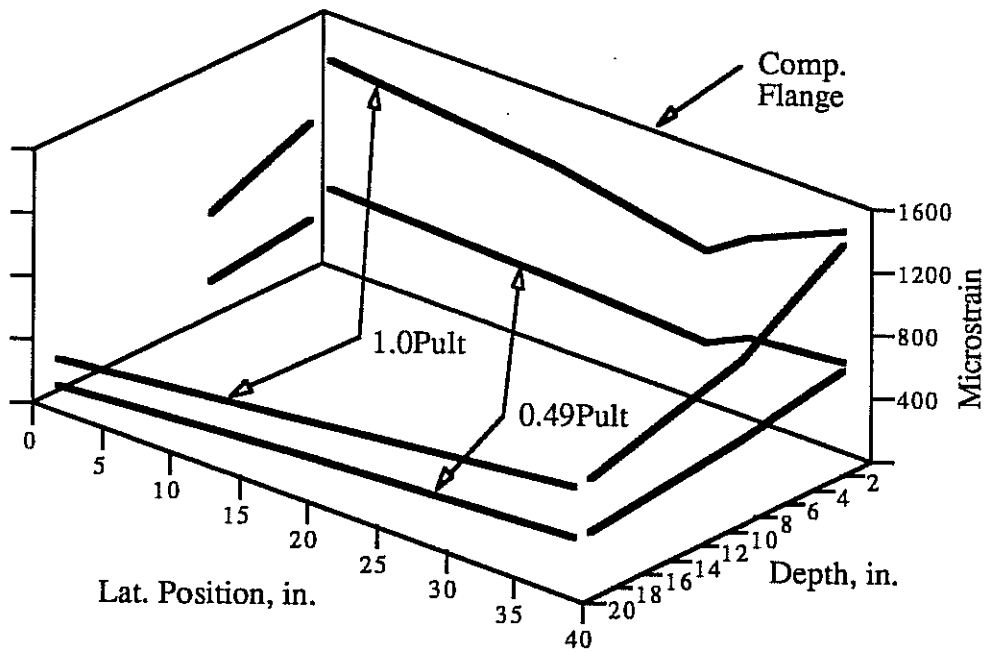


Figure 3.31: Specimen 4M18 Cross Section Strain Distribution

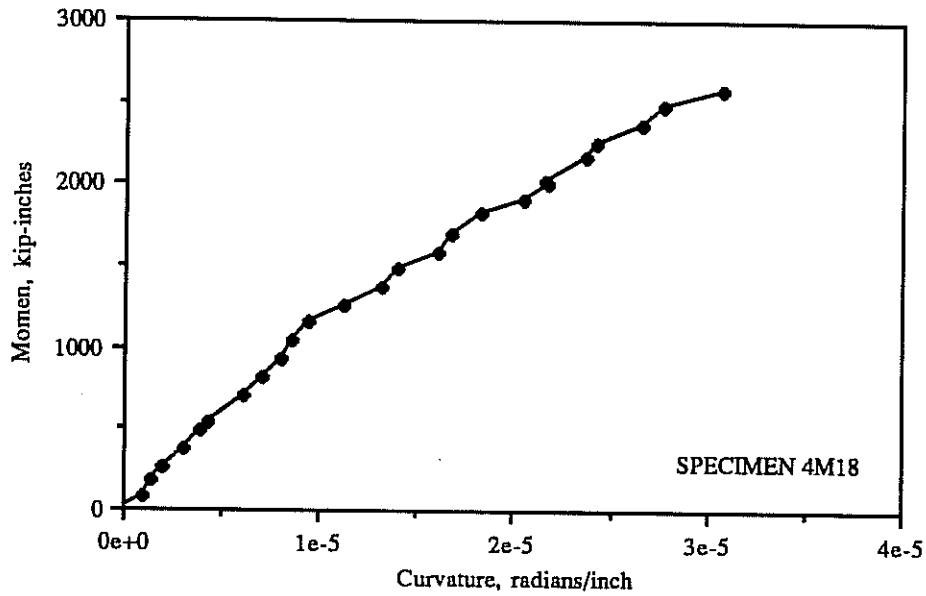


Figure 3.32: Specimen 4M18 Moment-Curvature Curve

3.3.5. 5S9 (Segmental, 15" x 30", 2.5" walls, $X_u/t = 8.8$)

Figures 3.33 to 3.39 show the experimental results from specimen 5S9. The failure was explosive and occurred at a load of 1138 kips. The location of the failure was at the joint between the middle and bottom segments of the specimen (Figures 3.34 to 3.36), between 16 and 24 inches above the bottom load head (as cast). Failure occurred about one minute after the final load step was applied, and was preceded by faint ticking sounds. The cross section underwent a large rotation at the failure region, as illustrated in Figure 3.33.

The primary region of crushing was in the top edge of the lower segment of the specimen, with the center segment remaining relatively intact. The bottom edge of the center segment was driven between the two curtains of reinforcing steel in the lower segment, as shown in Figures 3.35 and 3.36. In a follow-up investigation the outside concrete cover was chipped away from the specimen with an impact hammer and the locations of all reinforcement cross ties were established. It was found that cross ties were positioned in their designed locations throughout the specimen, except in the upper portions of the three segments. In those areas many of the cross ties had been loosened by the concrete vibrator during the casting operation and had fallen down into the formwork. (Since this was the first segmental specimen cast an adequate method of securing the ties had not been worked out). The largest number of cross ties were missing near the top edge of the bottom segment, where the failure occurred. It is likely, then, that a primary cause of failure was the lack of cross ties between curtains of reinforcement at the top edge of the bottom segment. This conclusion is further supported by the fact that failure occurred in the segment with the highest concrete strength; that is, the location of the failure was not determined by material weakness, but by some other defect.

Cracks first formed in the load heads at 666 kips (Figure 3.34), on the "tension" flange at 700 kips and on the compression flange at 861 kips. Cracks on the "tension" and compression flanges initiated near the ends of the specimen and progressed towards the center. These cracks were generally located near longitudinal reinforcing bars. Cracking on the "tension" and compression flanges prior to failure was not extensive compared to other specimens. The cracks indicated by dashed line

in Figures 3.34 to 3.36 were marked after failure.

Problems with a lack of cross ties in the bottom segment have been described above. Another reinforcement detail which performed poorly was the lap splices of lateral bars on the short faces of the specimen, as illustrated in Figure 3.36.

It was noted in Section 2.4.3 that the use of smooth plastic post-tensioning ducts in this specimen led to slipping of the post-tensioning bars within the ducts at failure (Figure 2.16). Both post-tensioning bars in the compression flange slipped in this manner. This indicates that the post-tensioning bars in the compression flange may not have acted integrally with the concrete cross section and may not have provided the full strength expected.

The epoxy used at the joints of the segmental specimen performed well. Cracks were observed to pass directly through the epoxy joints, demonstrating that the joints did not create planes of weakness.

The compression flange profile just before failure, plotted in Figure 3.37, was a uniformly shaped outward bulge. The deformations were small compared to most other specimens.

At low loads the strain distribution over the cross section, shown in Figure 3.38, was close to planar. Just before failure the strain distribution was erratic. The two side face gages near the edges of the compression flange appeared to malfunction during the test.

The moment-curvature plot in Figure 3.39 approaches a horizontal slope just before failure. This agrees with the observed failure mode of creep to failure under a sustained load.

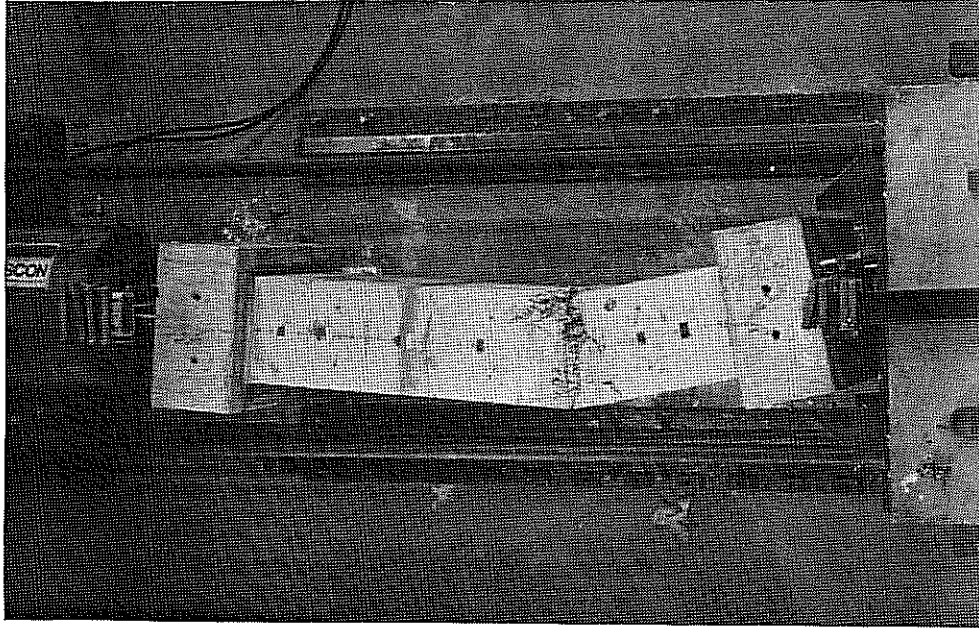


Figure 3.33: Specimen 5S9 Aerial View

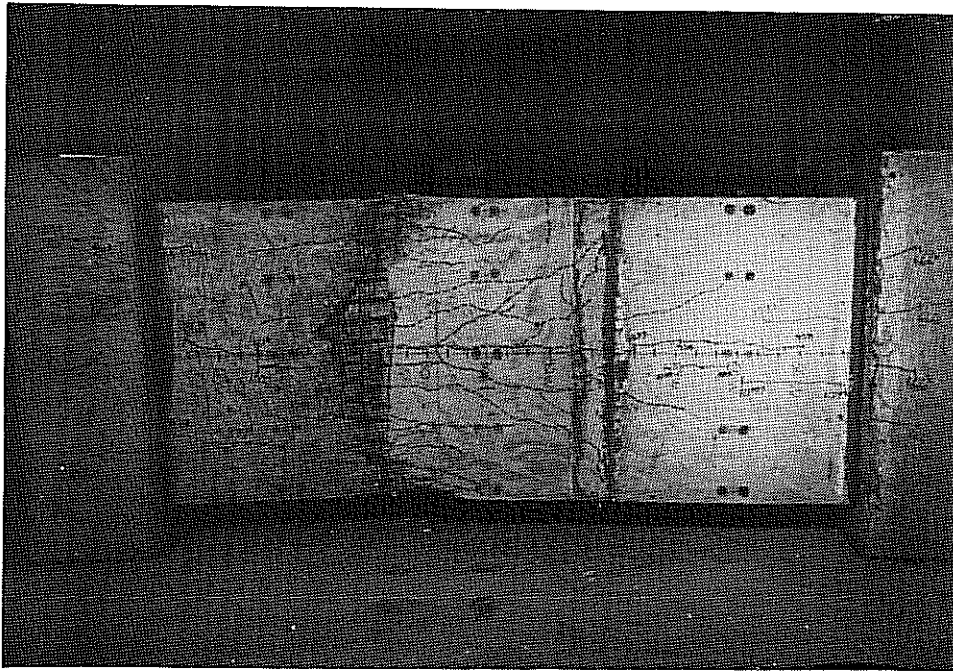


Figure 3.34: Specimen 5S9 Compression Flange

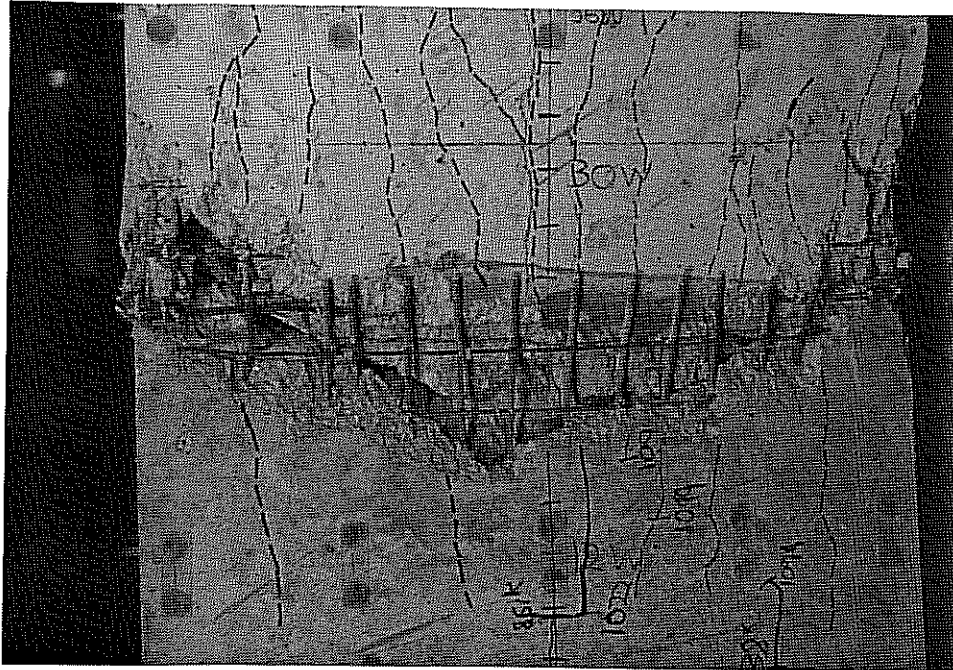


Figure 3.35: Specimen 5S9 Compression Flange Close-Up

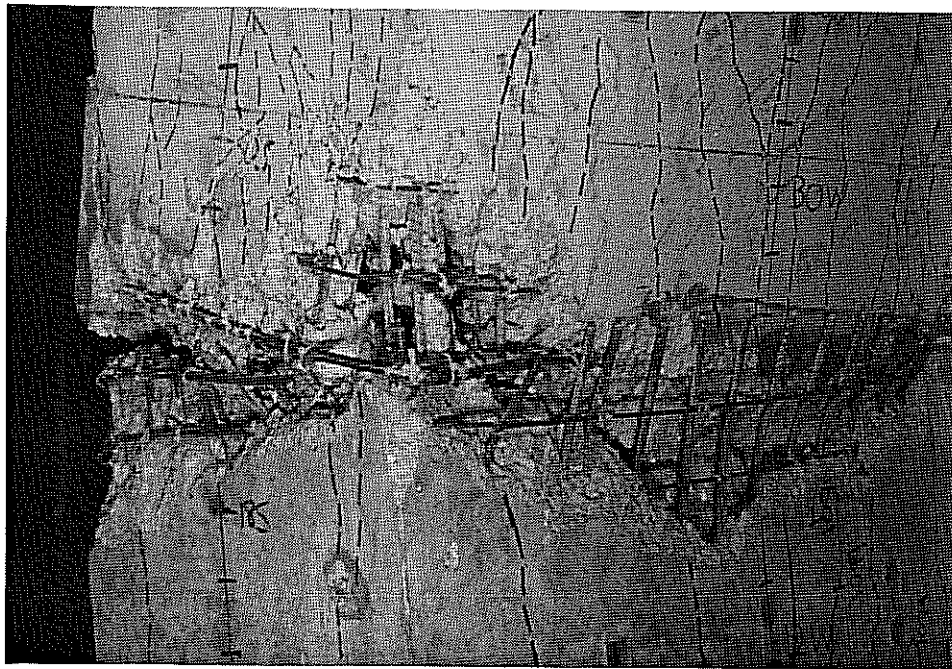


Figure 3.36: Specimen 5S9 Side Face Close-Up

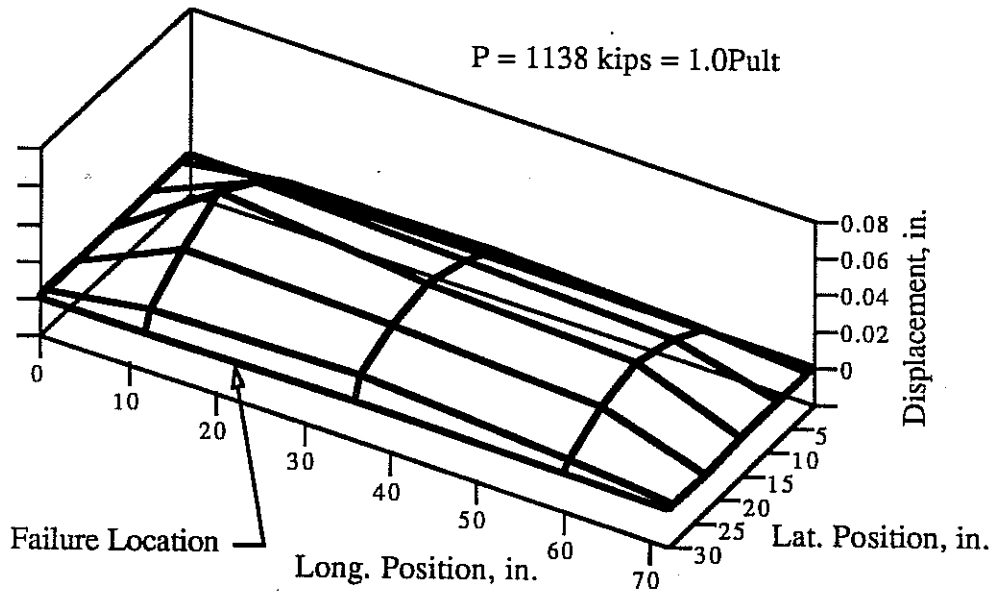


Figure 3.37: Specimen 5S9 Compression Flange Profile

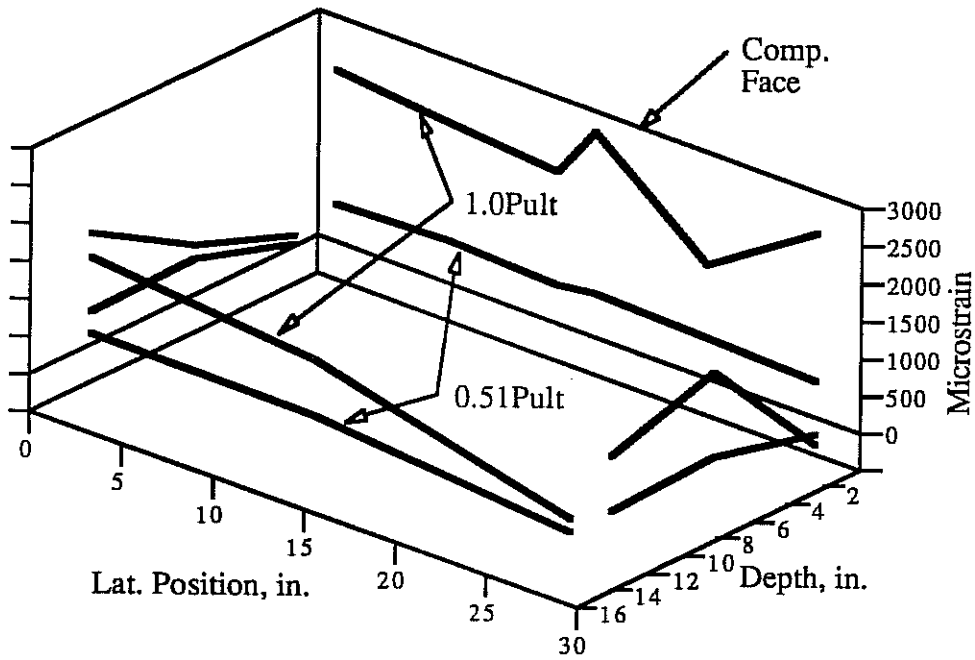


Figure 3.38: Specimen 5S9 Cross Section Strain Distribution

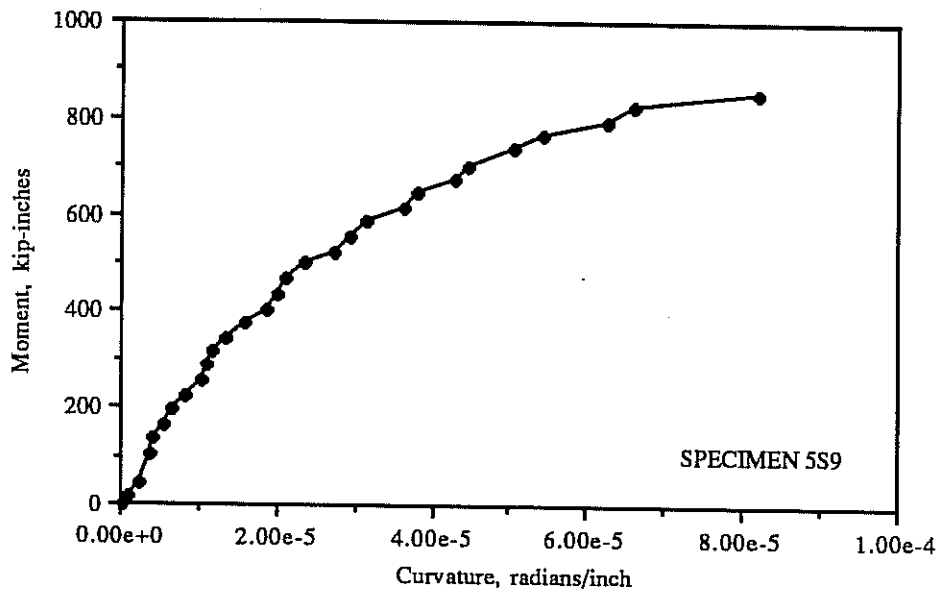


Figure 3.39: Specimen 5S9 Moment-Curvature Curve

3.3.6. 6S16 (Segmental, 20" x 40", 2.0" walls, $X_u/t = 15.5$)

Figures 3.40 to 3.48 show the experimental results from Specimen 6S16. The specimen failed explosively at a load of 948 kips. Failure occurred as the last load step was being applied; that is, the specimen did not creep to failure. Faint cracking sounds were heard immediately before failure. The rupture zone was located near the top of the specimen (as cast) 66 to 70 inches above the bottom load head (Figures 3.40 and 3.42).

Cracking of the specimen load heads was first observed at a load of 502 kips. These cracks were generally narrow and short and they did not grow significantly during the remainder of the test. Longitudinal cracks in the "tension" flange also appeared at 502 kips. These generally began near the ends of the specimen and grew toward the center (Figure 3.41). Longitudinal cracks first appeared in the compression flange at 586 kips (Figures 3.40 and 3.42). Longitudinal cracks generally formed near the locations of longitudinal reinforcing bars. At failure a wide transverse crack opened up in the "tension" flange due to the large rotation of the cross section in the failure zone. The crack was located about one inch below the joint between the top segment and the top load head. In Figure 3.43 this crack

appears to be a separation of the epoxy joint, when in fact the entire crack passed through concrete. The location of this crack was probably dictated by the position of the ends of the longitudinal reinforcing bars, located 0.75 inches from the epoxy joint.

The reinforcement details of this specimen performed well, with the exception of the lap splices of the lateral reinforcement on the two short faces (Figure 3.44).

Both post-tensioning bars in the compression flange slipped in their ducts at failure, as shown in Figure 3.45. This occurred despite the fact that an improved method of forming the ducts was used to reduce the possibility of slipping (as explained in Section 2.4.3). Slipping probably occurred for two reasons. First, the failure was located very near the end of the specimen, so the "development length" of the grouted post-tensioning bars in compression was only equal to the thickness of the solid load head, or 12 inches. At failure large compressive forces were transferred to the post-tensioning bars and the development length was insufficient to prevent slipping. Second, 1 inch diameter bars were used in this specimen, while 0.625 inch diameter bars were used in all other post-tensioned specimens. The 0.625 inches diameter bars were observed to buckle at the failure region in most other specimens. However, the 1 inch diameter bars used in this specimen were much stiffer, tending to slip in the ducts rather than buckle.

The epoxy performed well in this specimen. As mentioned above a large transverse crack formed in the "tension" flange at failure near an epoxy joint (Figure 3.43). Since the crack did not form in the epoxy, but in the adjacent concrete it can be concluded that the tensile strength of the epoxy exceeded the tensile strength of the concrete.

The compression flange profile just prior to failure is shown in Figure 3.46. It is interesting to note that there was a region of relatively large deformations near the bottom of the specimen, yet failure occurred near the top, where deformations were small. This indicates that failure was probably not induced by bulging of the compression flange for this particular specimen.

Longitudinal compressive strain distributions over the cross section are plotted in Figure 3.47. At lower loads the strain distribution was close to planar. Near ultimate the strain distribution is very irregular. One gage near the center of the compression

flange gave erratic readings during the test.

The moment-curvature data for the specimen is plotted in Figure 3.48. Near failure the slope of the curve is not close to horizontal, which is consistent with the specimen failing as a load step was applied, rather than creeping to failure under a constant load. The moment-curvature plot is rather jagged, compared to other moment curvature plots from the test program. This is explained by the irregular readings obtained from one of the potentiometers used to measure curvature in this test. The plunger of the potentiometer was probably not seated evenly against the curvature measurement frame, or there was insufficient plunger spring pressure. Since the curvature measurements are sensitive to small errors in potentiometer readings, one irregular potentiometer can result in a jagged moment-curvature plot.

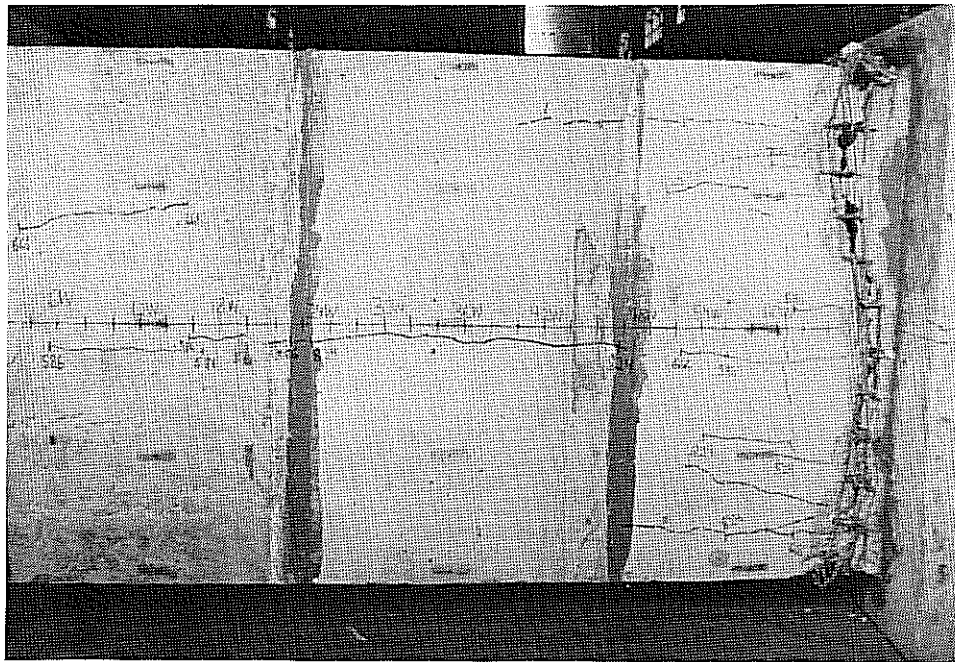


Figure 3.40: Specimen 6S16 Compression Flange

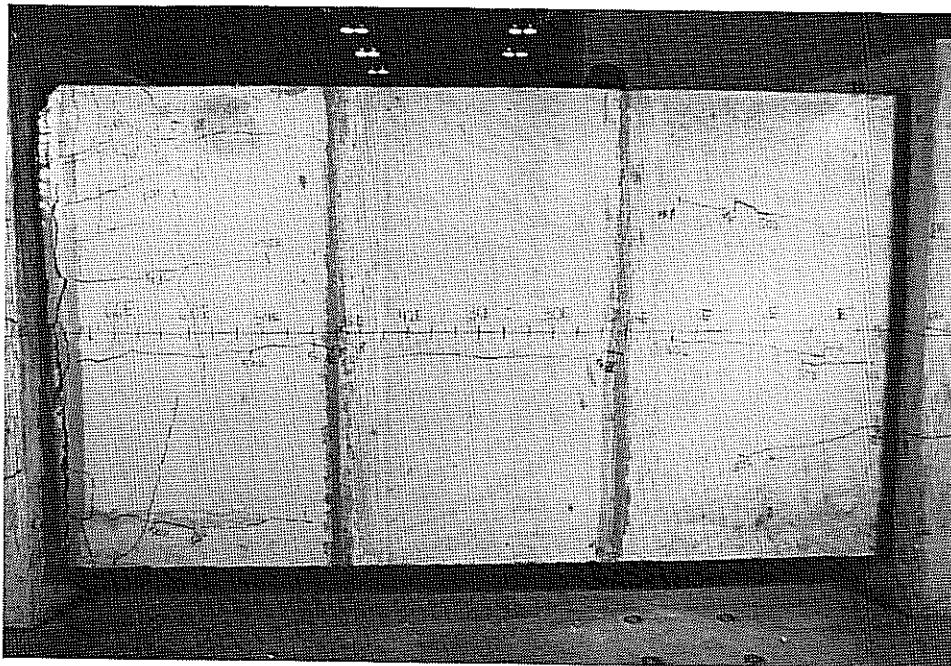


Figure 3.41: Specimen 6S16 "Tension" Flange

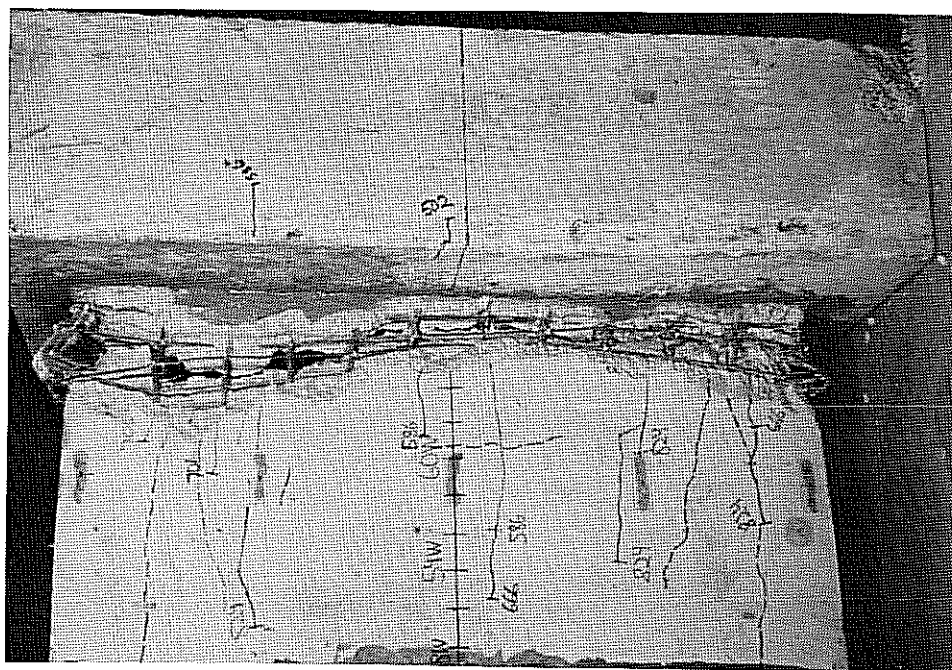


Figure 3.42: Specimen 6S16 Compression Flange Close-Up

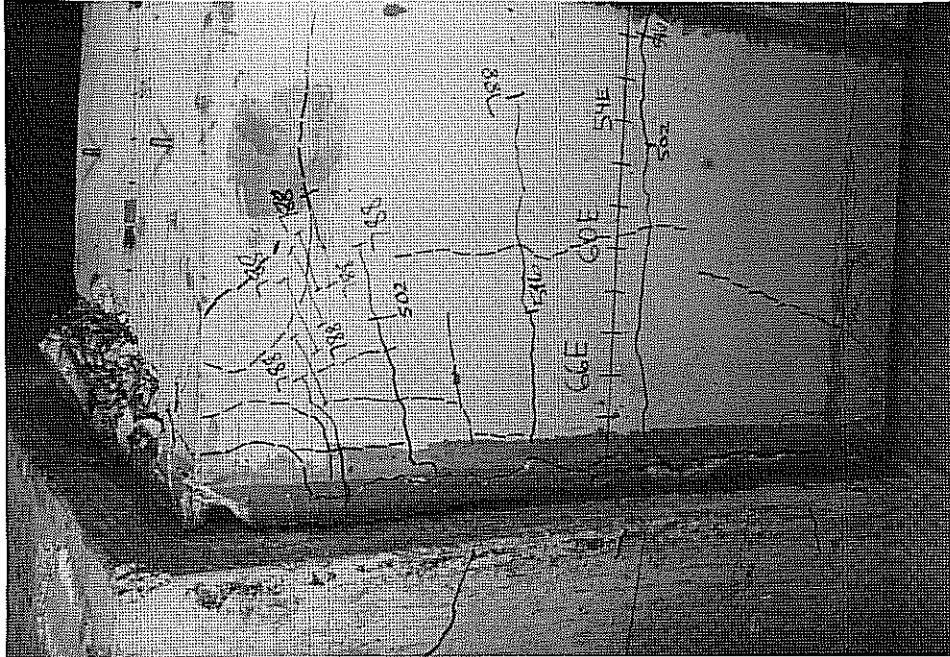


Figure 3.43: Specimen 6S16 "Tension" Flange Close-Up

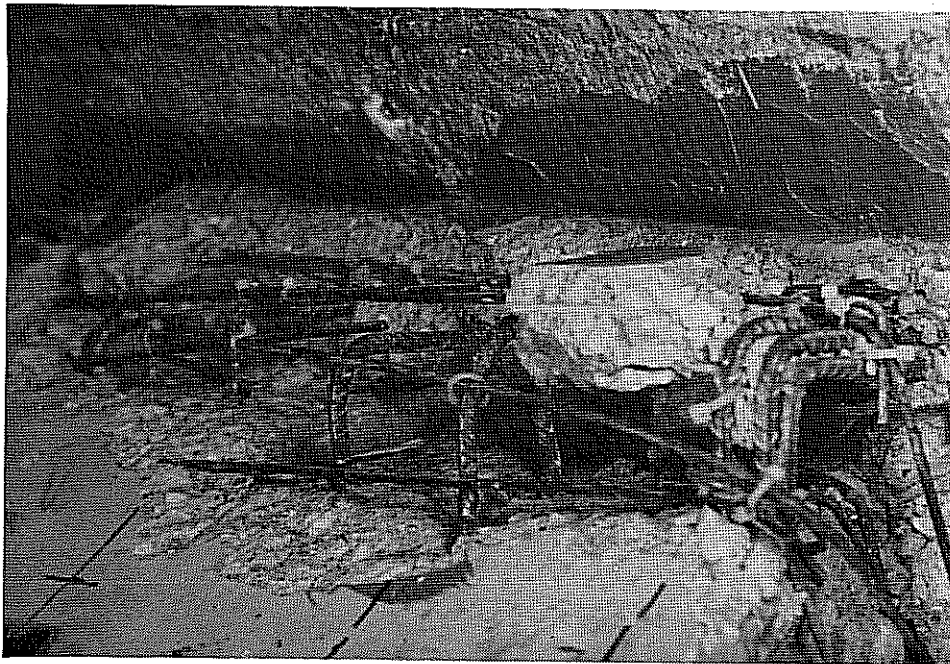


Figure 3.44: Specimen 6S16 Side Face Close-Up

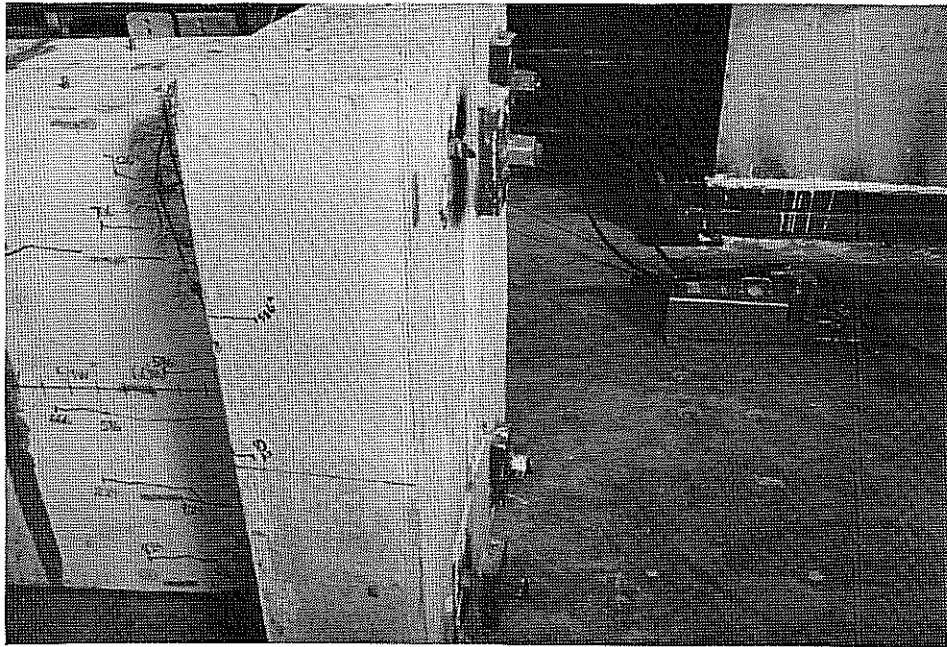


Figure 3.45: Specimen 6S16 Post-Tensioning Anchorages

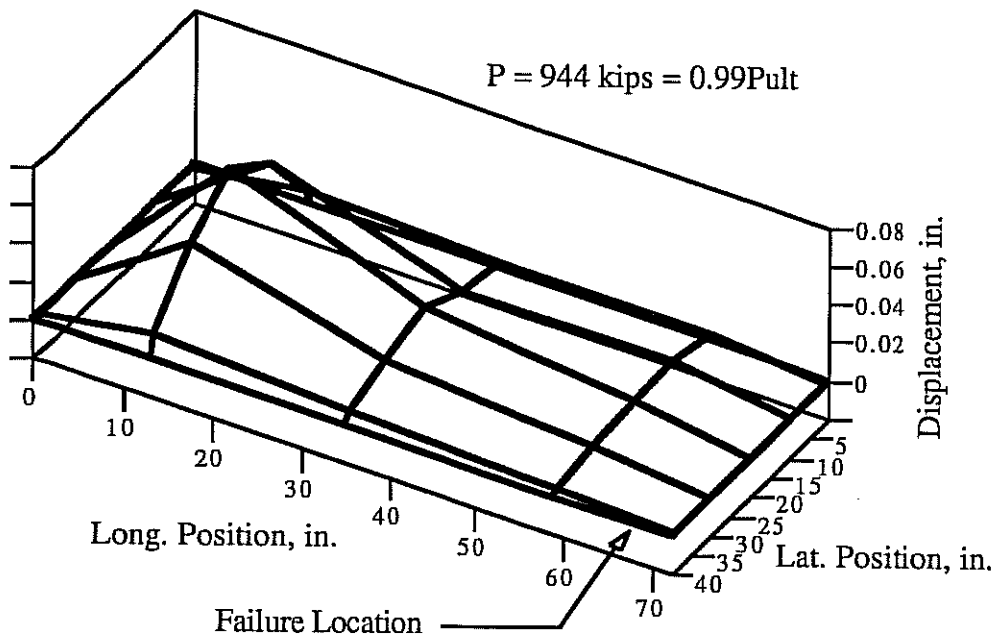


Figure 3.46: Specimen 6S16 Compression Flange Profile

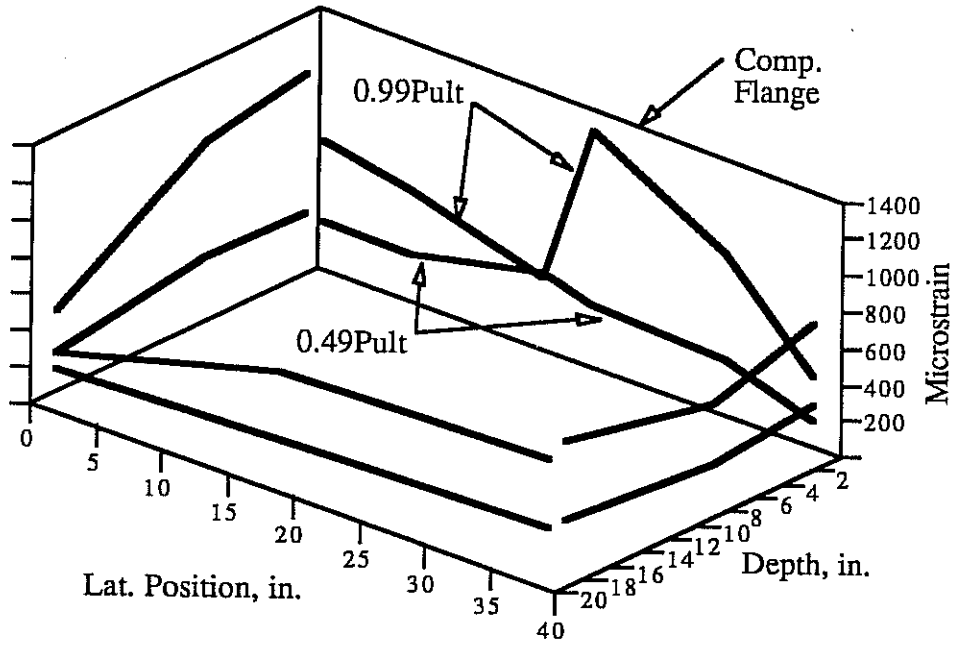


Figure 3.47: Specimen 6S16 Cross Section Strain Distribution

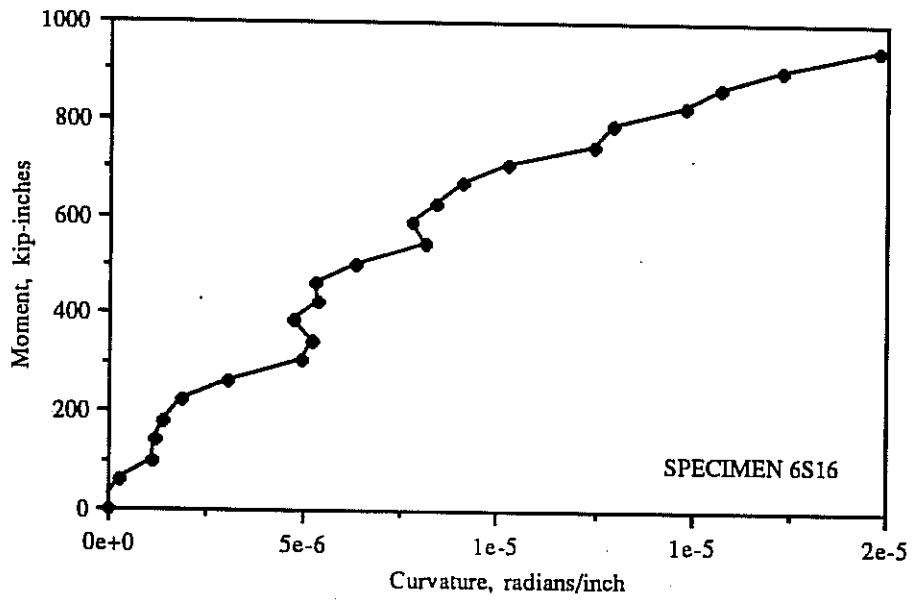


Figure 3.48: Specimen 6S16 Moment-Curvature Curve

3.3.7. 7S22 (*Segmental, 20" x 40", 1.5" walls, $X_w/t = 21.7$*)

Figures 3.49 to 3.57 show the experimental results for specimen 7S22. The failure was explosive and occurred at a load of 999 kips. The location of the failure was near the bottom of the specimen (Figures 3.49 to 3.51), occurring in a band 1 to 6 inches above the bottom load head (as cast).

Small cracks first appeared in the specimen load heads at a load of 302 kips. There was less load head cracking for this specimen than with most other specimens. Longitudinal cracks first formed in the compression flange at a load of 423 kips, and in the "tension" flange at a load of 744 kips. The extent of cracking in the "tension" and compression flanges was minor compared to other specimens. Cracks tended to be located near longitudinal reinforcing bars. In Figures 3.50 and 3.51 the cracks indicated by dashed lines were marked after failure.

The interior of the specimen was inspected after failure, and a crack pattern was observed on the inside surface of the load head, as shown in Figure 3.53. This crack pattern is consistent with the cracks typically observed on the sides of the load heads (for example see figures 3.6, 3.14 and 3.27), which indicate tensile stresses on the face of the load head closest to the hollow test section. Such tensile stresses could be caused by "dishing" deformation of the load head. The load head is loaded near its center on one face by a bearing plate, and is supported around the periphery of the opposite face by the walls of the hollow cross section.

Both post-tensioning bars in the compression flange buckled inward at the failure zone. The bars also fractured on the outer face of the bend, as illustrated in Figure 3.52. The fracturing was probably caused by the high rate of deformation at failure and the sharp radius of the bend.

Reinforcement details performed well in this specimen, except for the lateral bar splices on the two short faces of the specimen, as shown in Figure 3.54. It is doubtful that inward buckling of the post-tensioning bars (Figure 3.52) could have been prevented by the addition of more diagonal ties in the haunch regions.

The epoxy of this specimen performed well. As with specimen 6S16 a large lateral crack formed at failure near an epoxy joint on the "tension" flange (Figure 3.50). The crack formed in the concrete rather than the epoxy, indicating the tensile strength of the epoxy was greater than the tensile strength of the concrete.

The compression flange profile near failure, plotted in Figure 3.55, indicates larger displacements near the ends of the specimen than near the center. Failure occurred in the region of highest displacements.

At low loads the cross section strain distribution, plotted in Figure 3.57, was nearly planar. Near ultimate loads the strain distribution was close to planar, with the exception of two gage readings.

The specimen did not creep to failure under a sustained load, even though the slope of the moment-curvature plot, shown in Figure 3.57, is close to horizontal near the ultimate load. Apparently there was just sufficient bending stiffness remaining near the ultimate load to prevent creep failure. The moment curvature plot is somewhat irregular. As was discussed in connection with specimen 6S16 the curvature measurements were very sensitive to errors in potentiometer readings. The irregularities in Figure 3.57 could result from potentiometer reading errors as small as 0.002 inches. Such small errors might have been caused by something as minor as accidentally touching the curvature measurement frame while marking concrete cracks during the test.



Figure 3.49: Specimen 7S22 Compression Flange

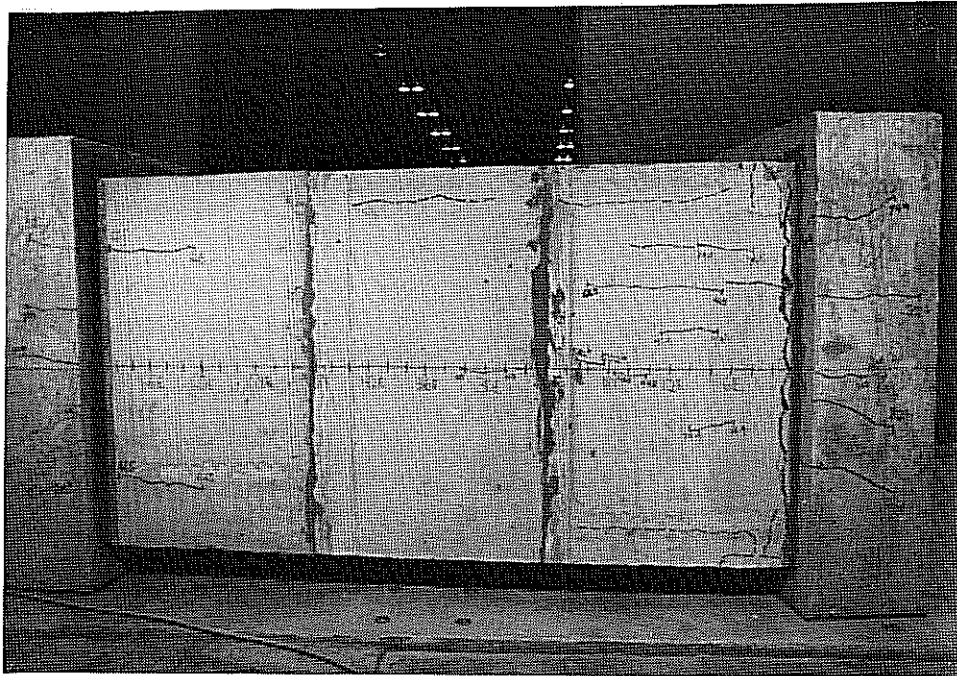


Figure 3.50: Specimen 7S22 "Tension" Flange

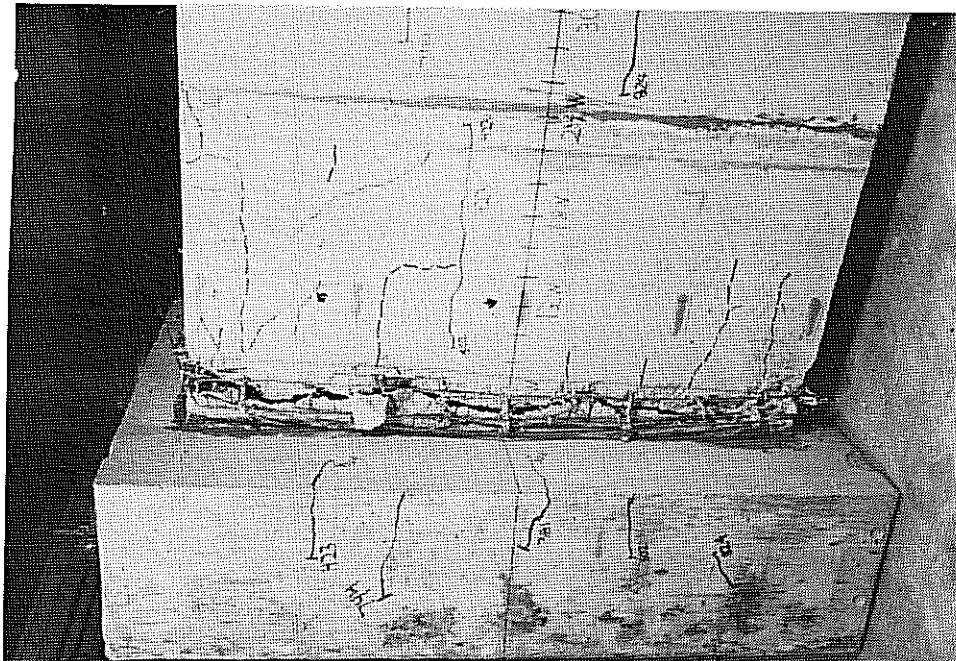


Figure 3.51: Specimen 7S22 Compression Flange Close-Up



Figure 3.52: Specimen 7S22 Interior View of Post-Tensioning Bar

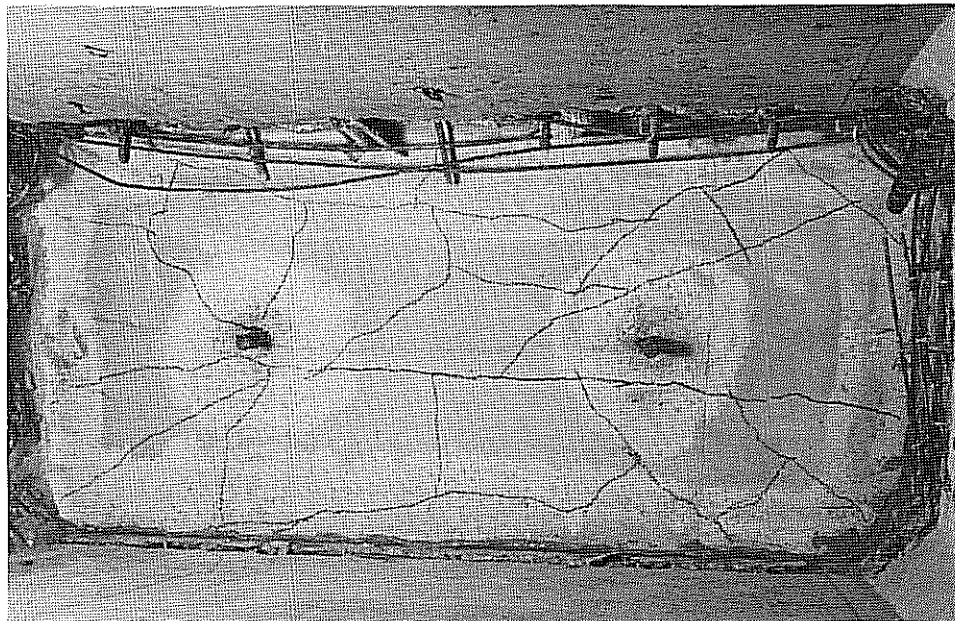


Figure 3.53: Specimen 7S22 Interior View of Load Head



Figure 3.54: Specimen 7S22 Side Face Close-Up

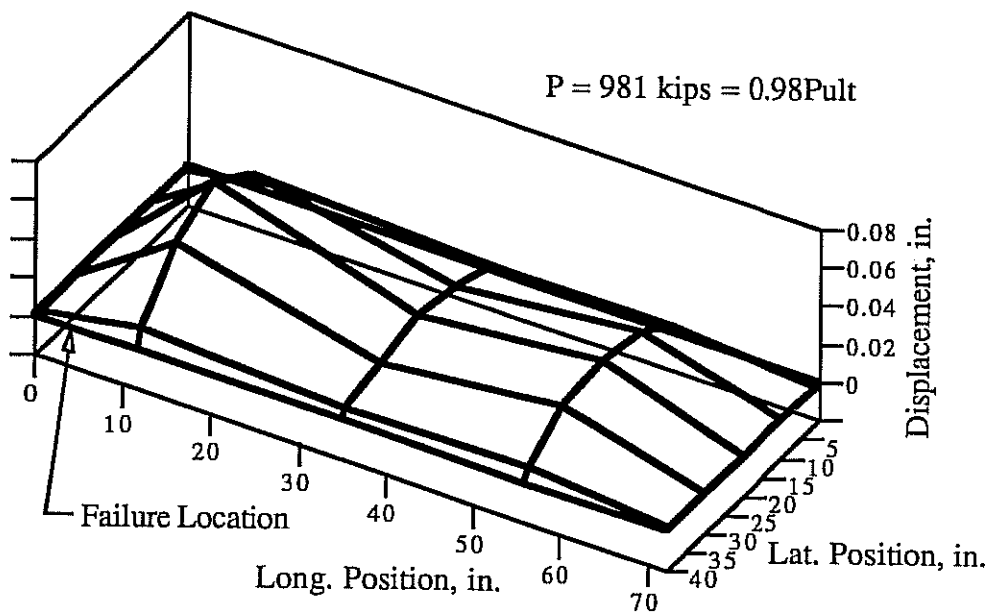


Figure 3.55: Specimen 7S22 Compression Flange Profile

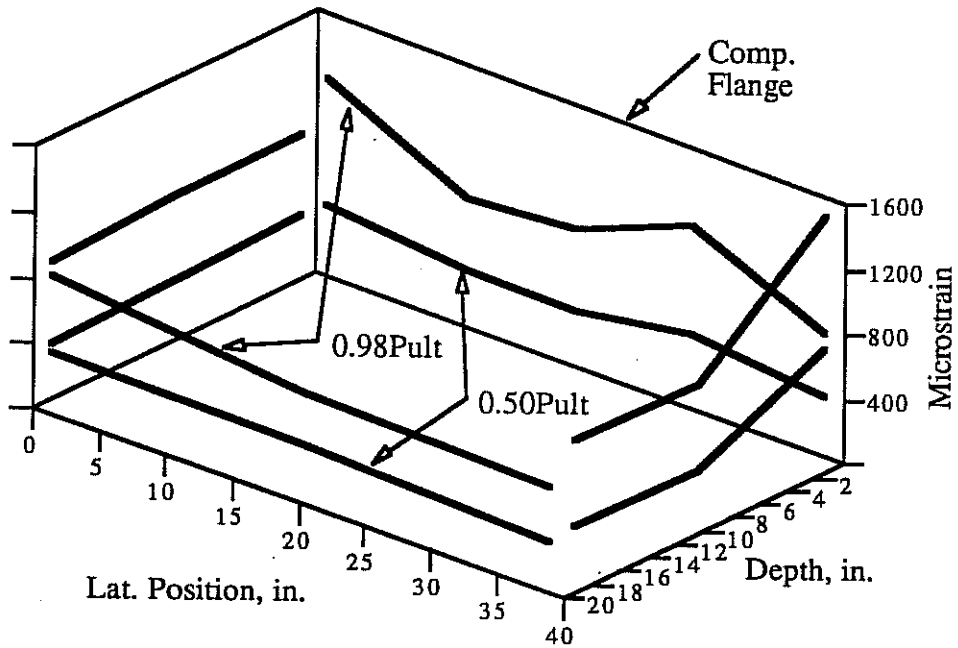


Figure 3.56: Specimen 7S22 Cross Section Strain Distribution

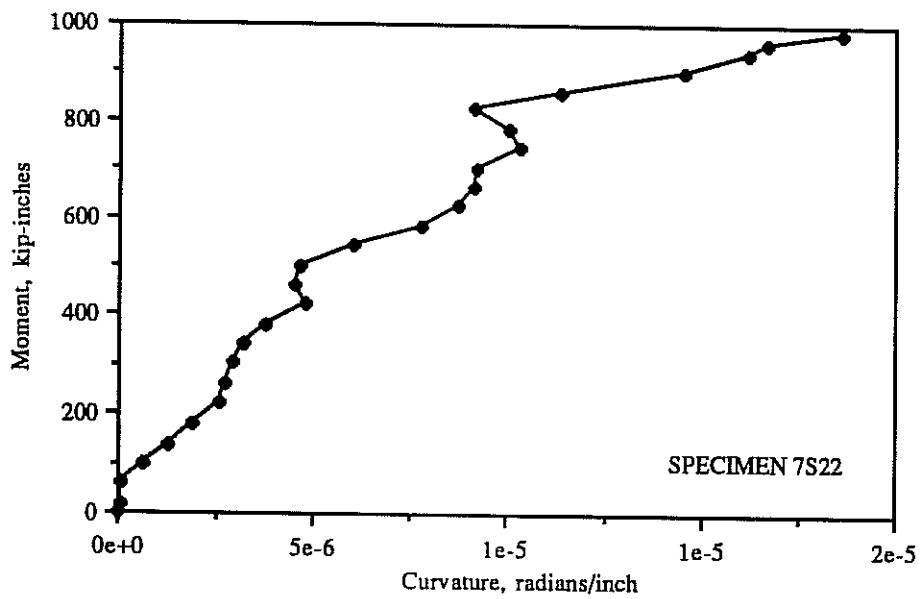


Figure 3.57: Specimen 7S22 Moment-Curvature Curve

3.3.8. *8ML25 (Multiple-Lift, 20" x 40", 1.5" walls, $X_u/t = 24.7$)*

Experimental results from specimen 8ML25 are shown in Figures 3.58 to 3.66. The specimen failed explosively at a load of 904 kips. The failure region was located near the top end of the specimen (as cast) between 66 and 74 inches above the bottom load head (Figures 3.58, 3.60 and 3.61). The specimen crept to failure under sustained load about one minute after the last load step was applied. No ticking sounds or other signs of imminent collapse were noted prior to failure.

Cracks first appeared in the specimen load heads at a load of 300 kips. Short longitudinal cracks formed on both the "tension" and compression flanges at a load of 502 kips. Cracking in the "tension" and compression flanges prior to failure was limited to the two end thirds of the specimen, with the majority of the cracks occurring in the bottom one-third. Cracks tended to form near longitudinal reinforcing bars. The cracks indicated by dashed lines in Figures 3.58 to 3.60 were marked after failure. The cross section underwent a large rotation in the failure zone, as shown in Figure 3.61.

No problems were encountered with reinforcement details in this specimen, other than the lateral reinforcement lap splices shown in Figure 3.62.

The displaced shape of the compression flange just prior to failure, plotted in Figure 3.63, indicates a uniformly shaped bulge with slightly higher displacements near the failure region.

The strain distributions over the cross section, shown in Figure 3.64, are nearly planar both at low loads and near the ultimate load.

Figure 3.65 shows the experimental moment-curvature curve for the specimen. The slope of the curve approaches horizontal near ultimate load. However, the curve is not quite flat enough at its peak to be consistent with the observed behavior of creep to failure under sustained load. Possibly some local phenomenon contributed to the failure, such as buckling of the compression flange.

The load-axial shortening curve of the specimen is shown in Figure 3.66. The curve is nearly linear over most of the load range.

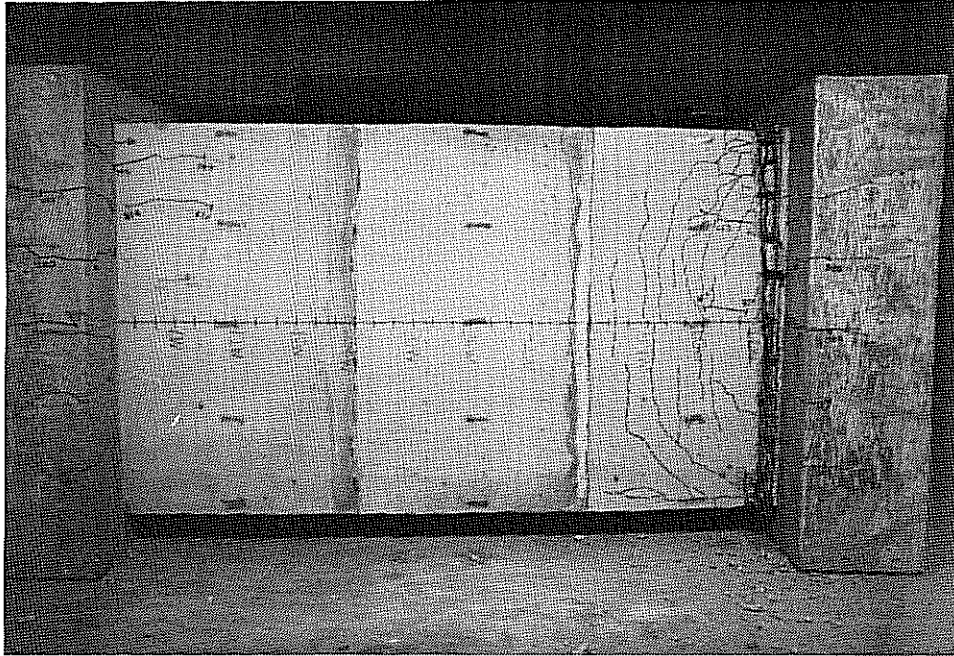


Figure 3.58: Specimen 8ML25 Compression Flange

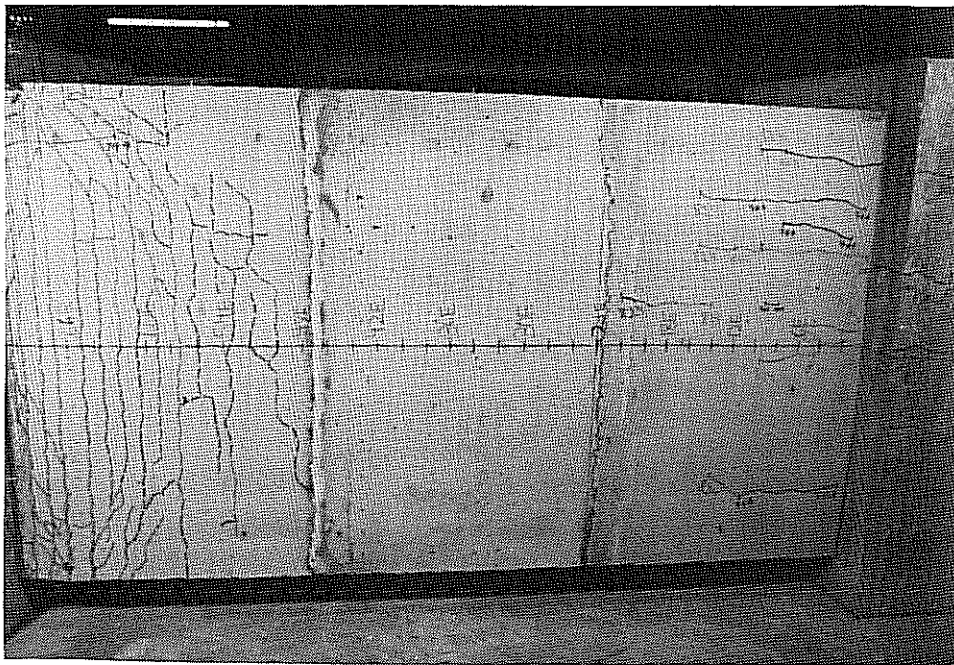


Figure 3.59: Specimen 8ML25 "Tension" Flange

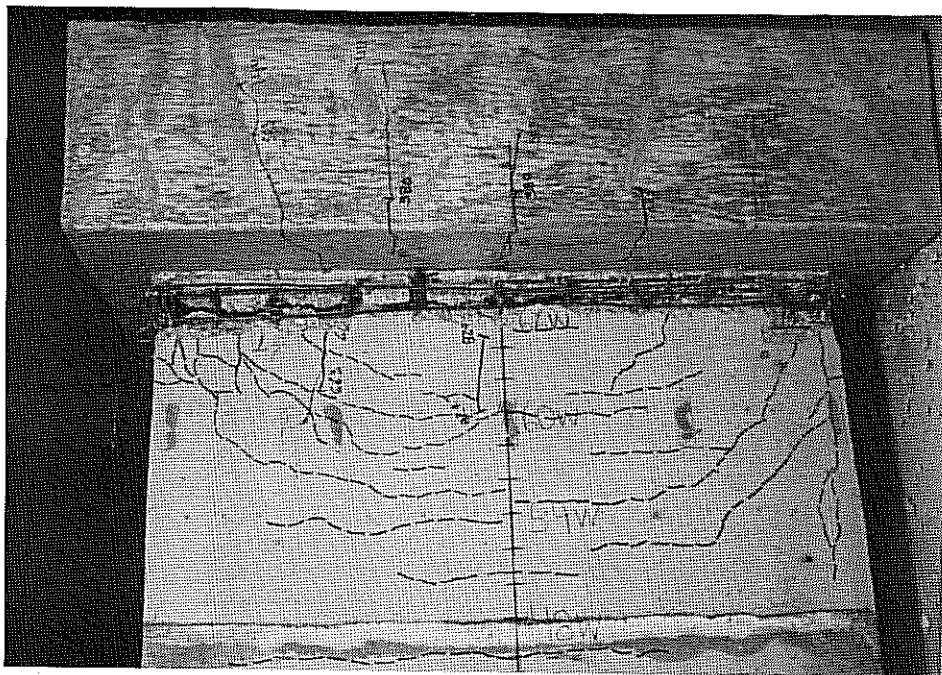


Figure 3.60: Specimen 8ML25 Compression Flange Close-Up

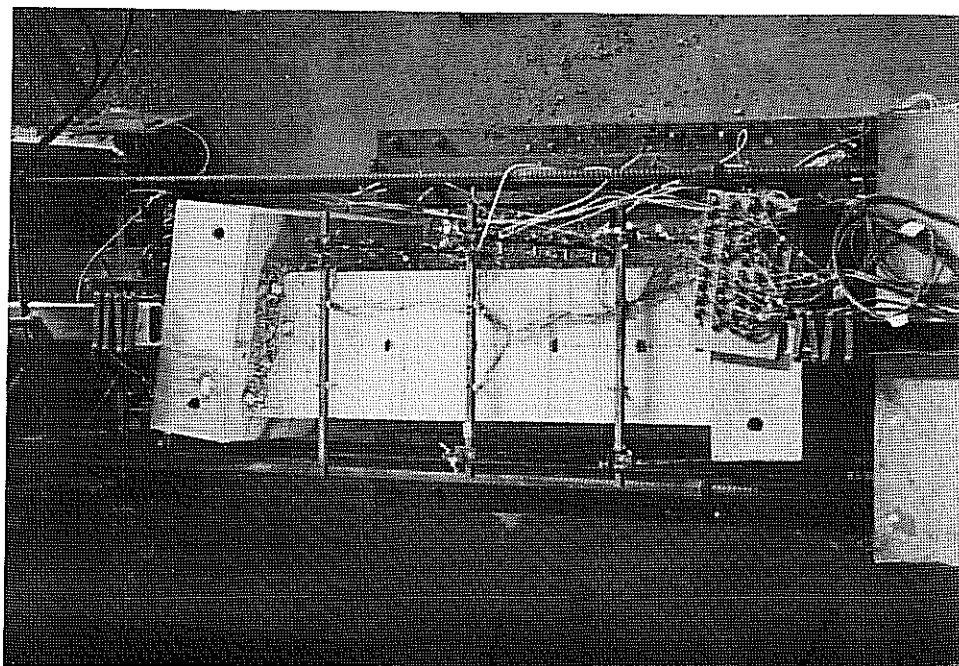


Figure 3.61: Specimen 8ML25 Aerial View

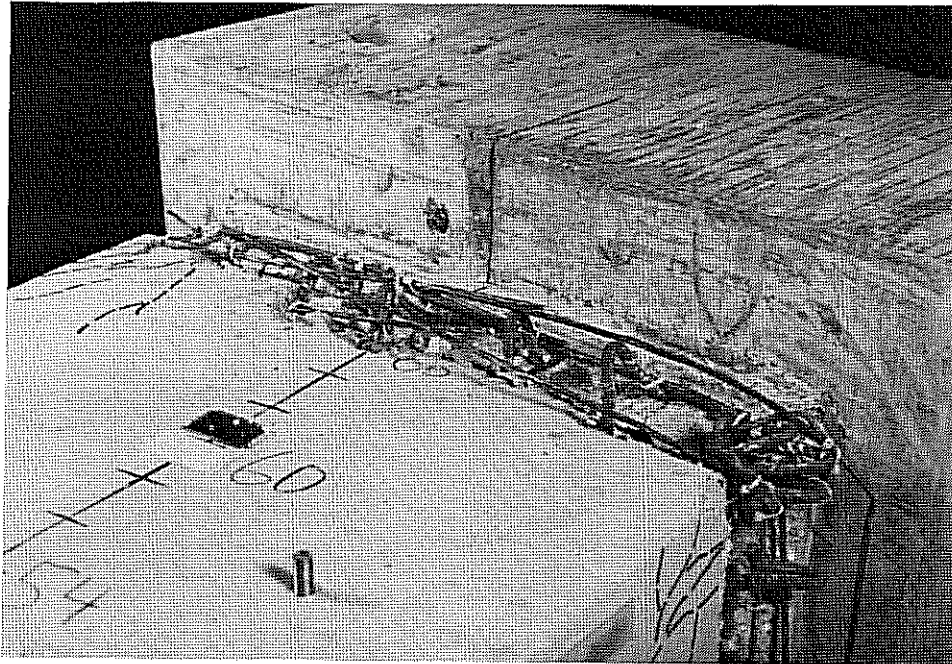


Figure 3.62: Specimen 8ML25 Side Face Close-Up

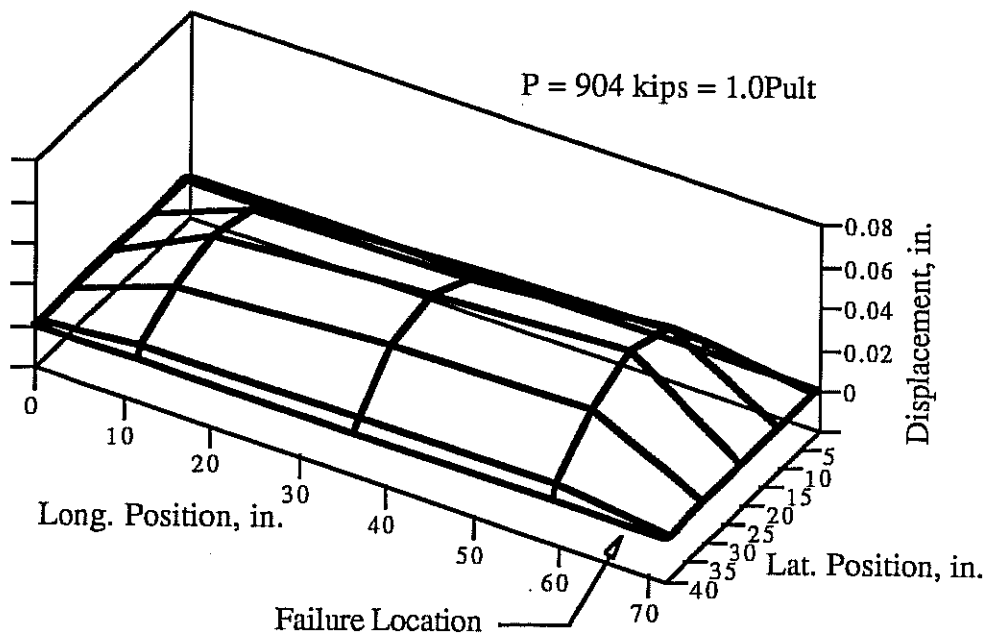


Figure 3.63: Specimen 8ML25 Compression Flange Profile

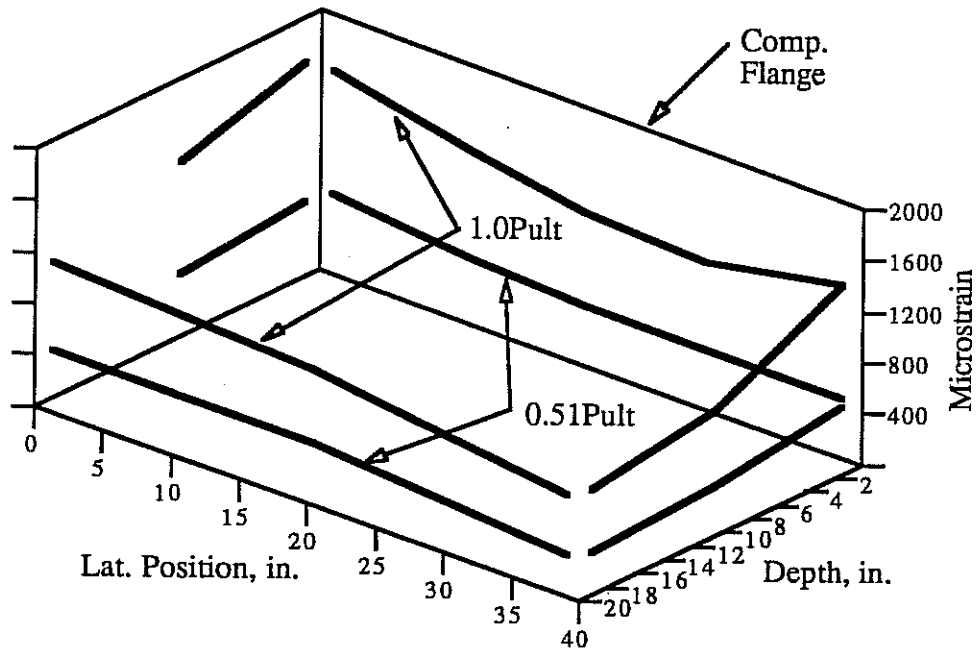


Figure 3.64: Specimen 8ML25 Cross Section Strain Distribution

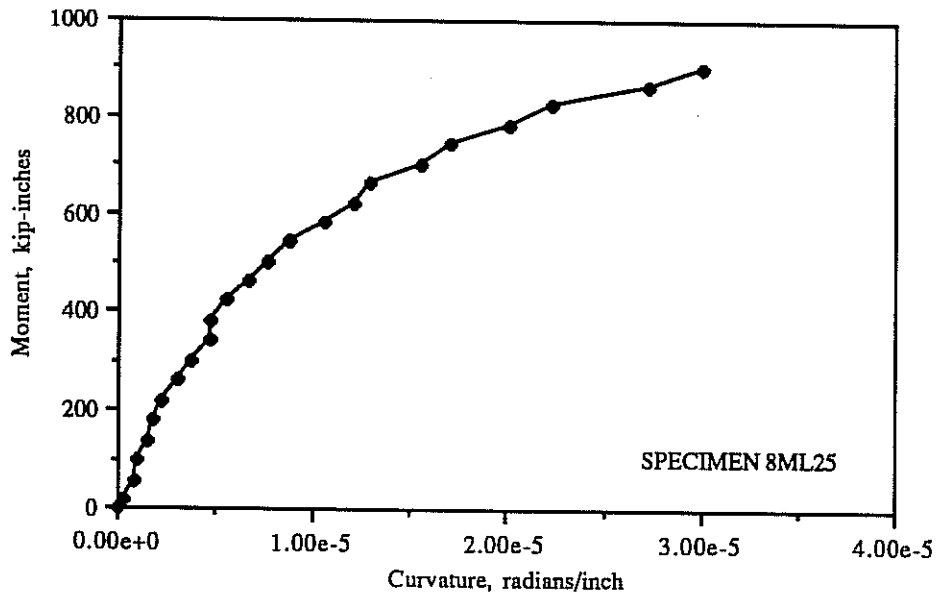


Figure 3.65: Specimen 8ML25 Moment-Curvature Curve

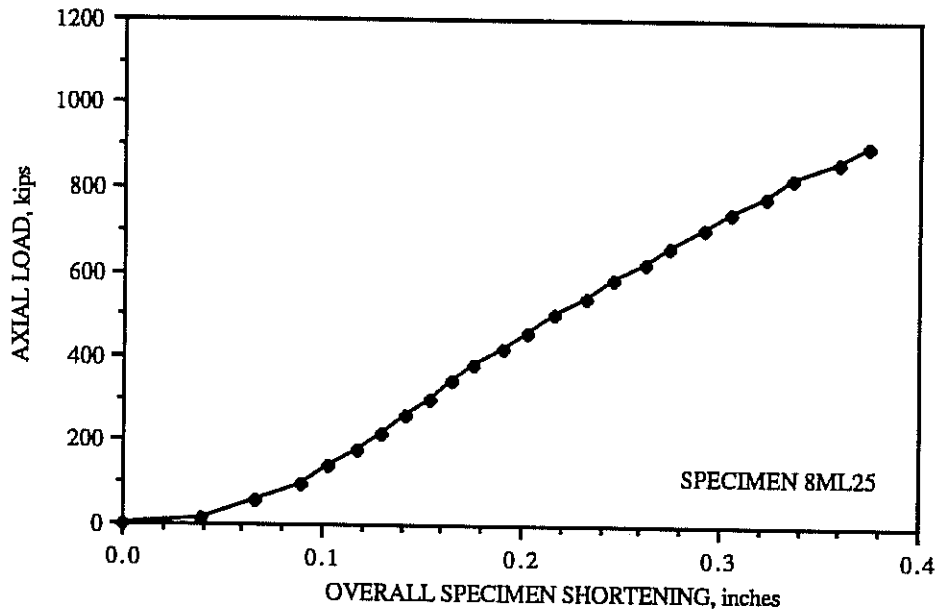


Figure 3.66: Specimen 8ML25 Axial Shortening Curve

3.3.9. 9MLP22 (Multiple-Lift, P.T., 20" x 40", 1.5" walls, $X_{ll}/t = 21.7$)

Figures 3.67 to 3.76 illustrate the experimental results for specimen 9MLP22. The failure, which was explosive, occurred at 961 kips. The failure was located near the top end of the specimen (as cast), 68 to 70 inches above the bottom load head (Figures 3.67 and 3.69). An unusual feature of the failure was that the compression flange was pushed outward about two inches near the failure zone (Figure 3.69).

The first cracks in the specimen load heads formed at a load of 260 kips. Longitudinal cracks appeared in both the "tension" and compression flanges of the specimen at a load of 505 kips. Cracking of the "tension" and compression flanges of the specimen was minor compared to most specimens tested, and most of the cracking occurred near the ends of the specimen. Cracks tended to form at the locations of longitudinal reinforcing bars. The cracks shown by dashed line in Figures 3.67 to 3.69 were marked after failure.

The post-tensioning bars of this specimen behaved in a similar manner to the bars of specimen 7S22. Both bars in the compression flange buckled inward at failure. One bar fractured at the outer face of the bend, as shown in Figure 3.70.

Reinforcement details in this specimen performed well, except for the lateral bar

splices on the short faces of the specimen (Figure 3.71).

The compression flange profile just before failure is plotted in Figure 3.72. Displacements near the ends of the specimen were greater than near the middle. This displacement pattern is characteristic of several specimens.

The longitudinal strain distribution over the cross section is plotted in Figure 3.73. It can be seen that the strain distribution at 49% of ultimate load is very close to planar, while the strain distribution near ultimate is somewhat irregular. The corner gage at depth coordinate 1.1 inches and lateral position coordinate 0.25 inches appeared to be giving erratic readings at strains over about 1000 microstrains.

For this specimen, and all subsequent specimens, a row of strain gages was installed on the inner and outer layers of reinforcing steel in the compression flange near mid-height. This permitted observation of through-thickness strain gradients in the compression flange. Figure 3.74 shows a plot of data from these gages at 49% and 99% of ultimate load. At the lower load it can be seen that the strain distribution is uniform across the width of the flange and that inner bars have higher strains than outer bars. This is contrary to the expected result, as outer bars are further from the neutral axis of the specimen.

The inconsistency could be explained by plate bending of the compression flange. Figure 3.72 indicates that the compression flange bulges outward as the specimen is loaded. This creates a local strain gradient through the thickness of the wall contrary to the strain gradient caused by overall bending of the specimen. The combined effect of overall specimen bending strains and local plate bending strains is larger strains in the inner layer of reinforcement than in the outer layer. The difference is even more pronounced near ultimate load, as shown by the upper curves in Figure 3.74. At 99% of ultimate load the strains indicated by the separate lines of inner and outer gages in Figure 3.74 are irregular, but all of the inner bar gage readings are higher than the outer bar gage readings.

The slope of the moment-curvature curve plotted in Figure 3.75 is not quite horizontal near the ultimate load. This is consistent with the specimen failing as load was being applied, rather than creeping to failure under a constant load.

The load-axial shortening curve for the specimen is plotted in Figure 3.76. The curve is somewhat nonlinear at low loads, but is nearly linear at higher loads.

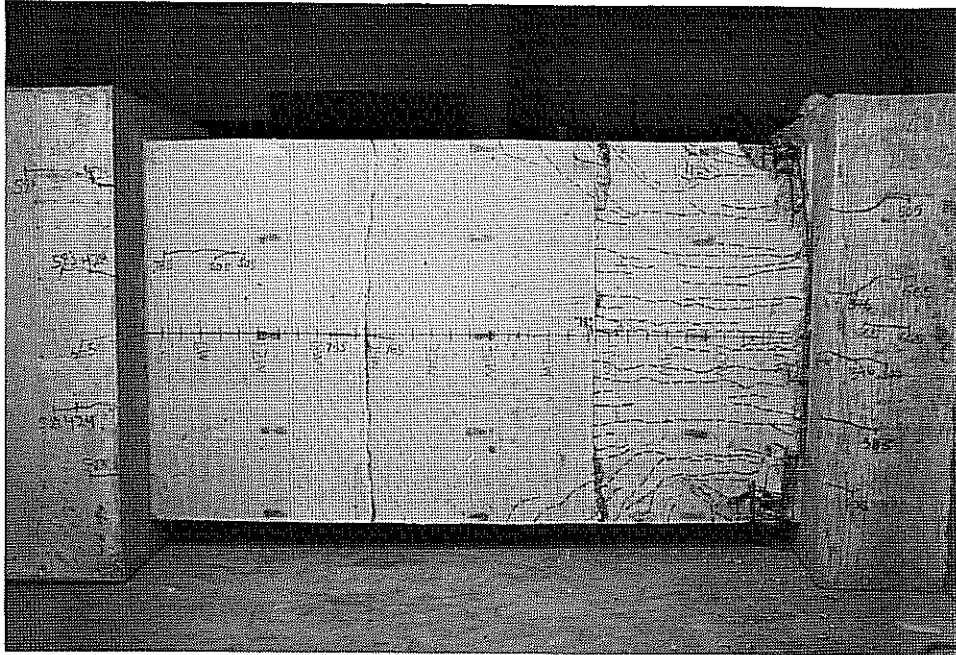


Figure 3.67: Specimen 9MLP22 Compression Flange

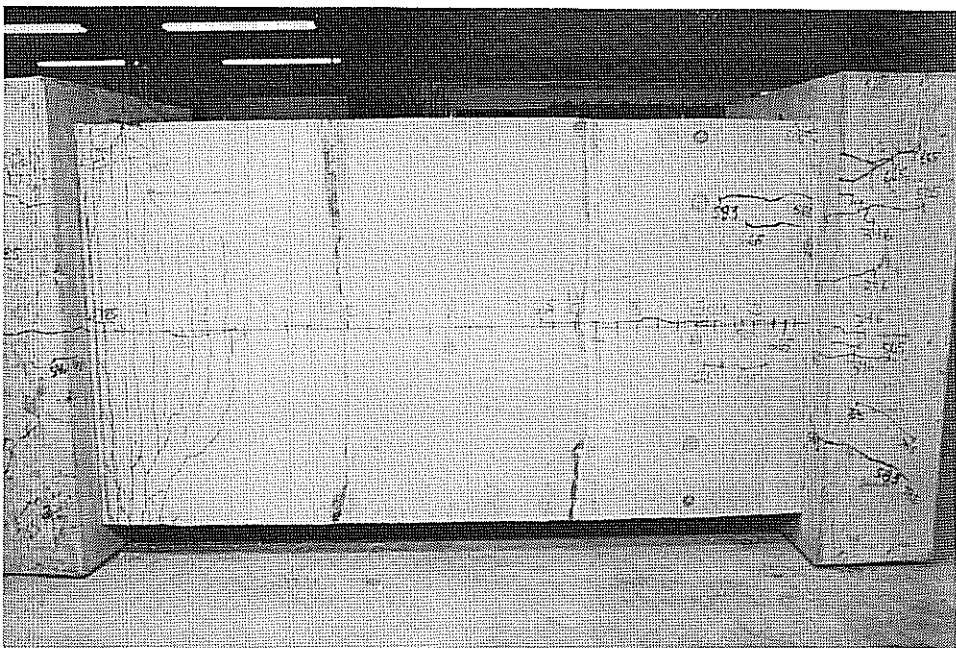


Figure 3.68: Specimen 9MLP22 "Tension" Flange

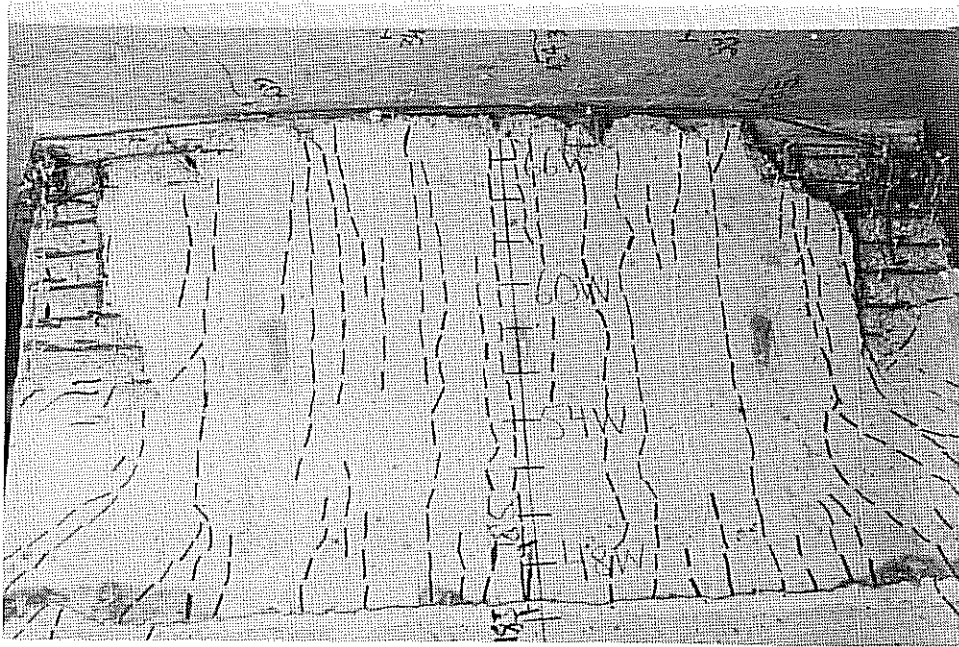


Figure 3.69: Specimen 9MLP22 Compression Flange Close-Up



Figure 3.70: Specimen 9MLP22 Interior View of Post-Tensioning Bar

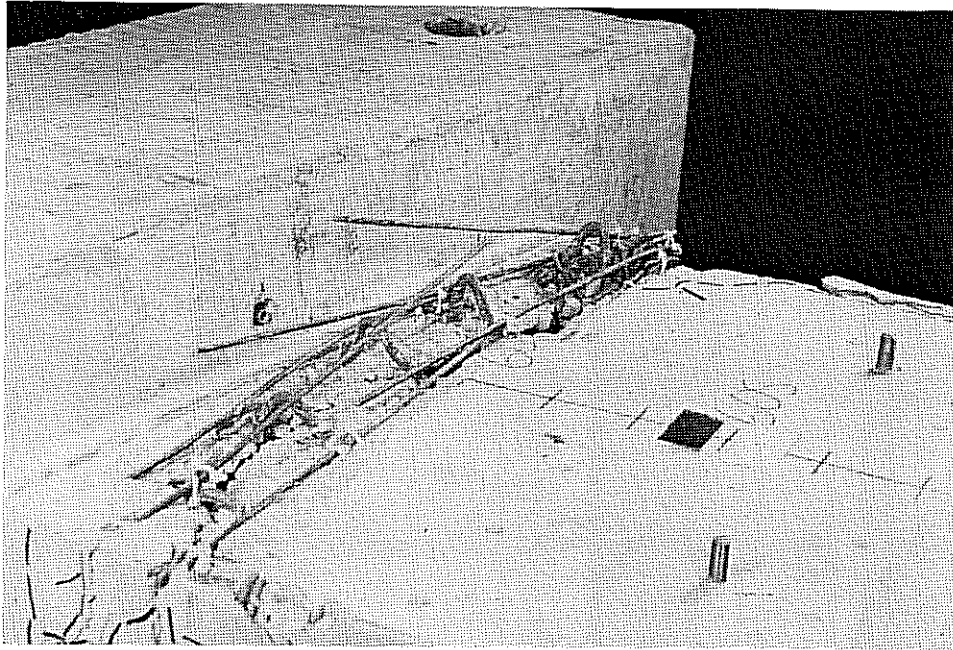


Figure 3.71: Specimen 9MLP22 Side Face Close-Up

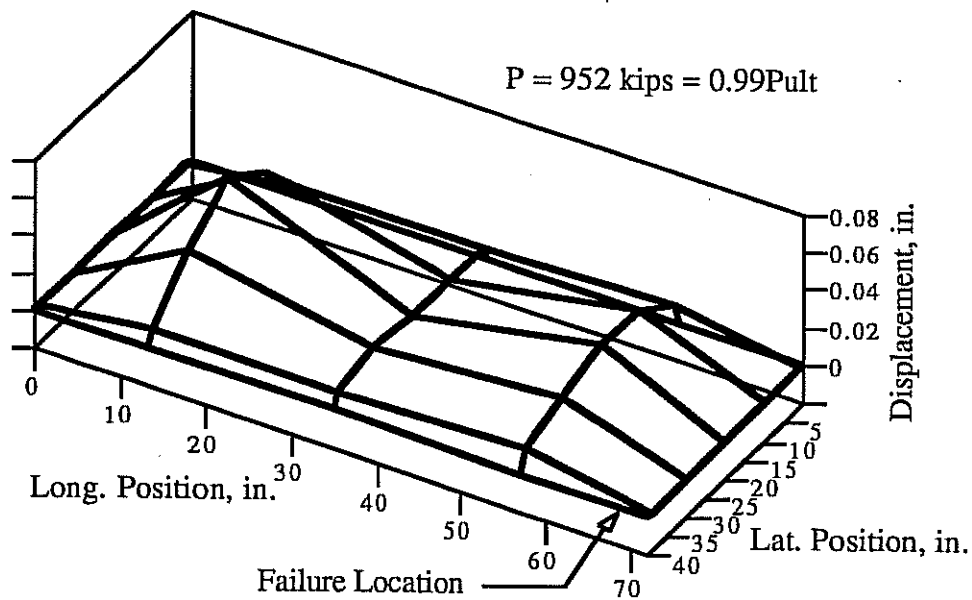


Figure 3.72: Specimen 9MLP22 Compression Flange Profile

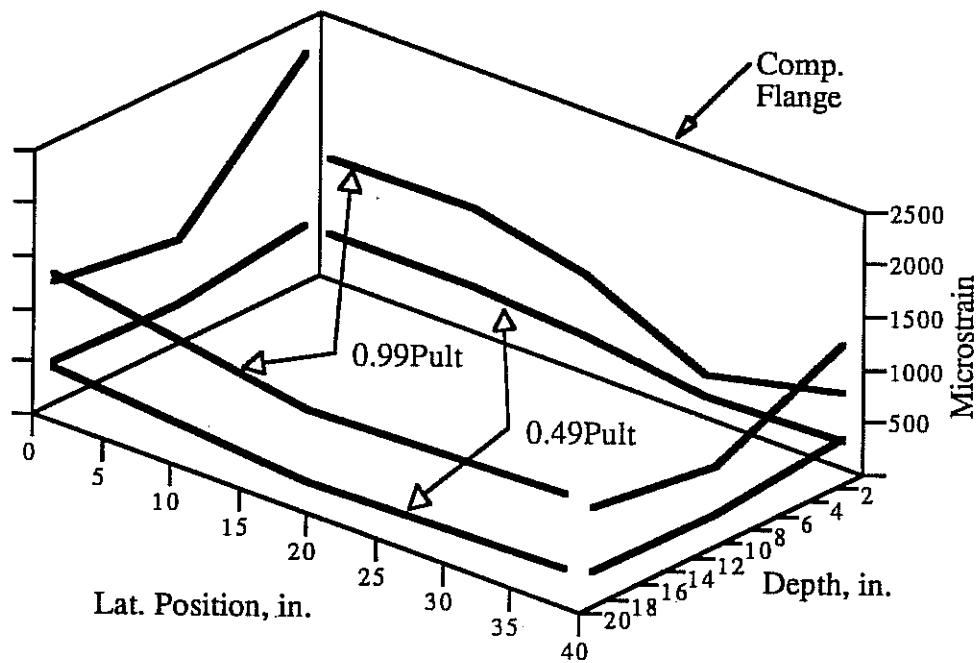


Figure 3.73: Specimen 9MLP22 Cross Section Strain Distribution

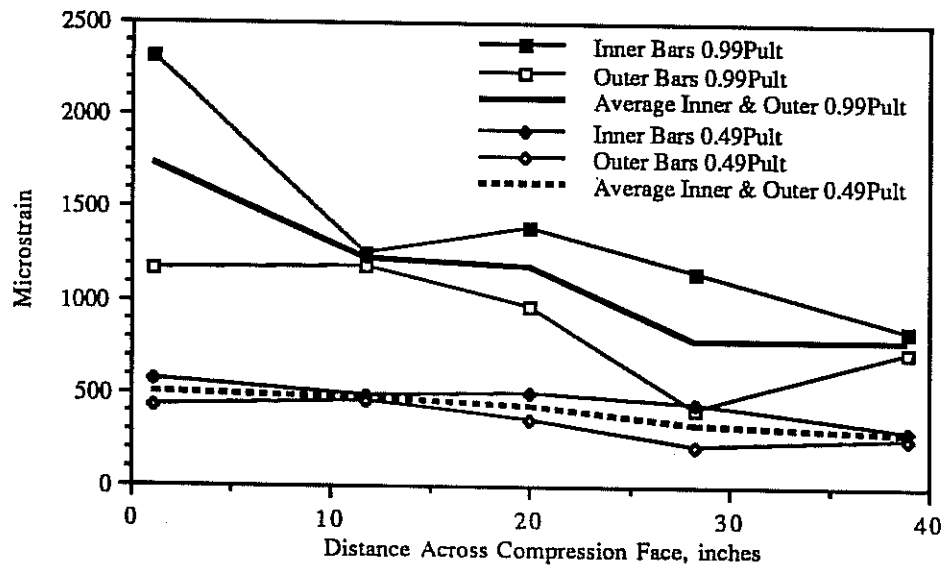


Figure 3.74: Specimen 9MLP22 Compression Flange Strains at Mid-Height

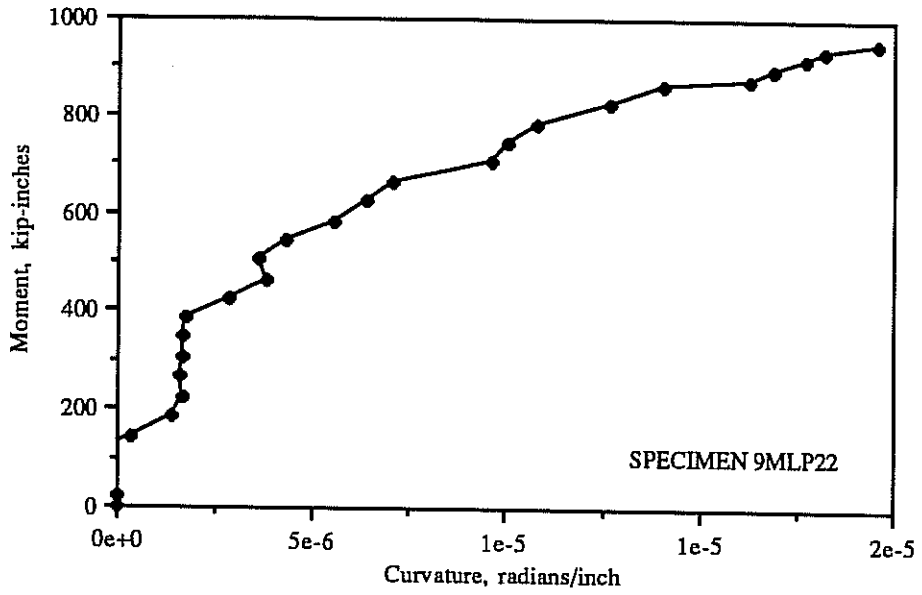


Figure 3.75: Specimen 9MLP22 Moment-Curvature Curve

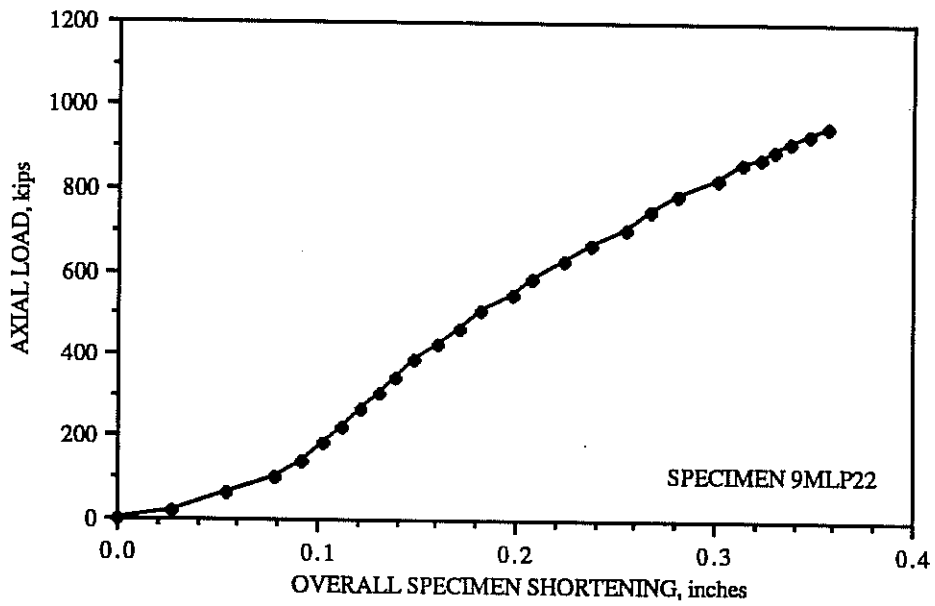


Figure 3.76: Specimen 9MLP22 Axial Shortening Curve

3.3.10. 10ML18 (*Multiple-Lift, 20" x 40", 2.0" walls, $X_u/t = 18.0$*)

The experimental results for Specimen 10ML18 are illustrated in Figures 3.77 to 3.86. The specimen failed explosively at a load of 1013 kips. Over about the last 500 kips of applied load faint ticking sounds were heard emanating from the specimen. The specimen failed as a load step was being applied, rather than creeping to failure under a sustained load. The location of the failure was near the top of the specimen (as cast), between 64 and 70 inches above the bottom load head (Figures 3.77, 3.79 and 3.81). An interesting feature of this specimen is that the compression flange was pushed inward about two inches near the failure zone, as shown in Figure 3.81.

Cracks first appeared in the load heads at a load of 300 kips. The extent of load head cracking in this specimen was small compared to most other specimens. The first longitudinal crack in the compression flange formed at a load of 380 kips. This crack was near the top end and was unusually long, about 36 inches, compared to the first cracks of other test specimens. At 462 kips the first cracks appeared in the "tension" flange. Cracks in the compression and "tension" flanges tended to form near the locations of longitudinal reinforcing bars. The cracks indicated by dashed lines in Figures 3.77, 3.78, 3.79 and 3.81 were marked after failure.

All reinforcement details performed well in this specimen, with the exception of the lateral bar splices on both short faces, shown in Figure 3.80.

The compression flange profile near failure, illustrated in Figure 3.82, shows unusually high displacements compared to other specimens in the test program. Displacements were higher near the ends of the specimen than near the middle.

The longitudinal strain distribution over the cross section at 49% and 99% of ultimate load are plotted in Figure 7. (Data is not shown for one malfunctioning gage on the compression flange). At both the low and high load levels the strain distributions were close to planar.

Strains in the inner and outer reinforcing bars of the compression flange are plotted in Figure 3.84. (Data from on defective outer bar gage is not shown). At low load the inner and outer bar strain gage readings were practically equal, and the distribution of strains across the width of the flange was nearly linear. Near ultimate load the strain readings were more erratic, but most outer bars had larger strain

readings than inner bars. The irregularities across the width of the flange could be partly attributed to degradation of the strain gages at higher strains.

The moment-curvature plot for the specimen is shown in Figure 3.85. The slope at the peak of the curve is not horizontal, which is consistent with the specimen failing as load was applied, rather than creeping to failure under sustained load.

The load-axial shortening curve for the specimen is plotted in Figure 3.86. The curve is initially nonlinear, but becomes nearly linear at high loads.

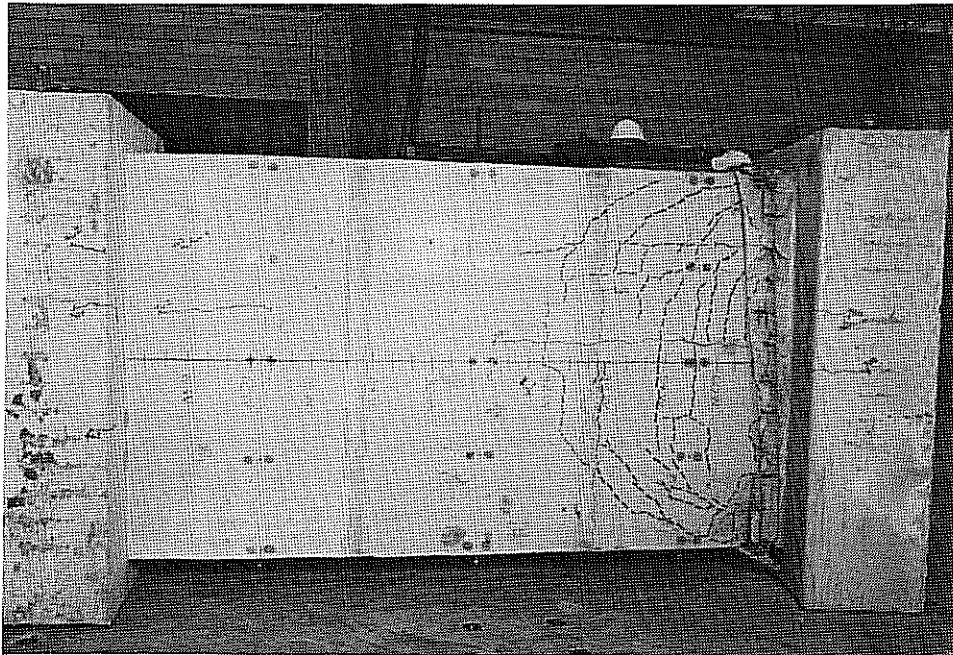


Figure 3.77: Specimen 10ML18 Compression Flange

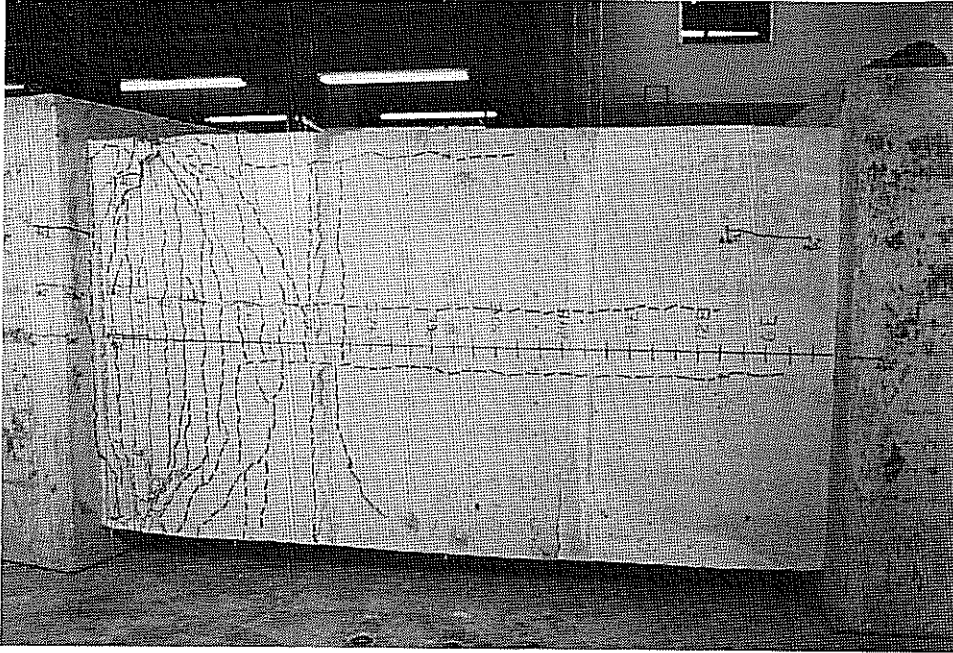


Figure 3.78: Specimen 10ML18 "Tension" Flange

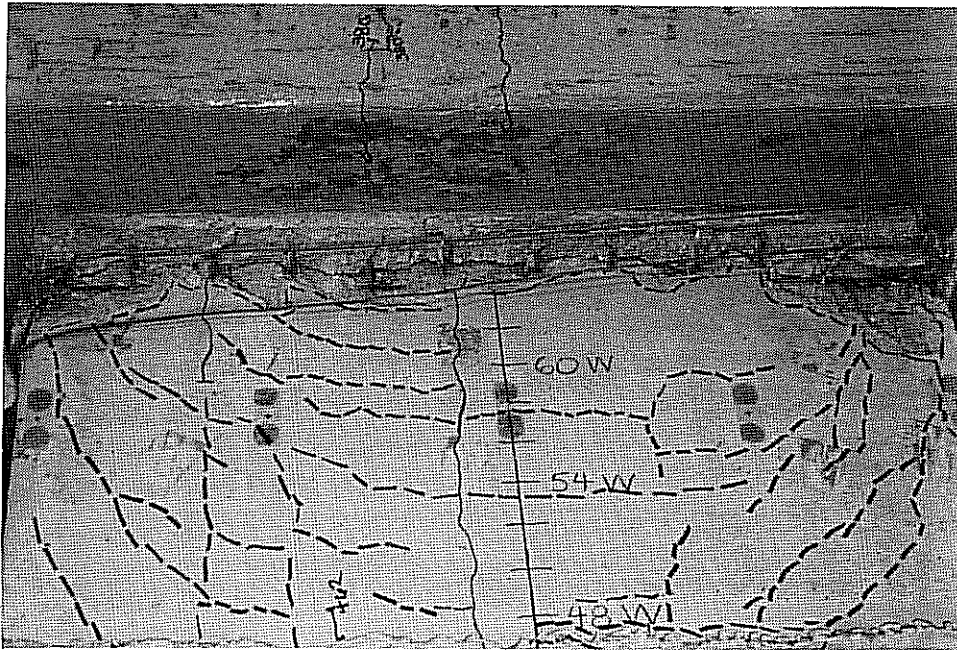


Figure 3.79: Specimen 10ML18 Compression Flange Close-Up

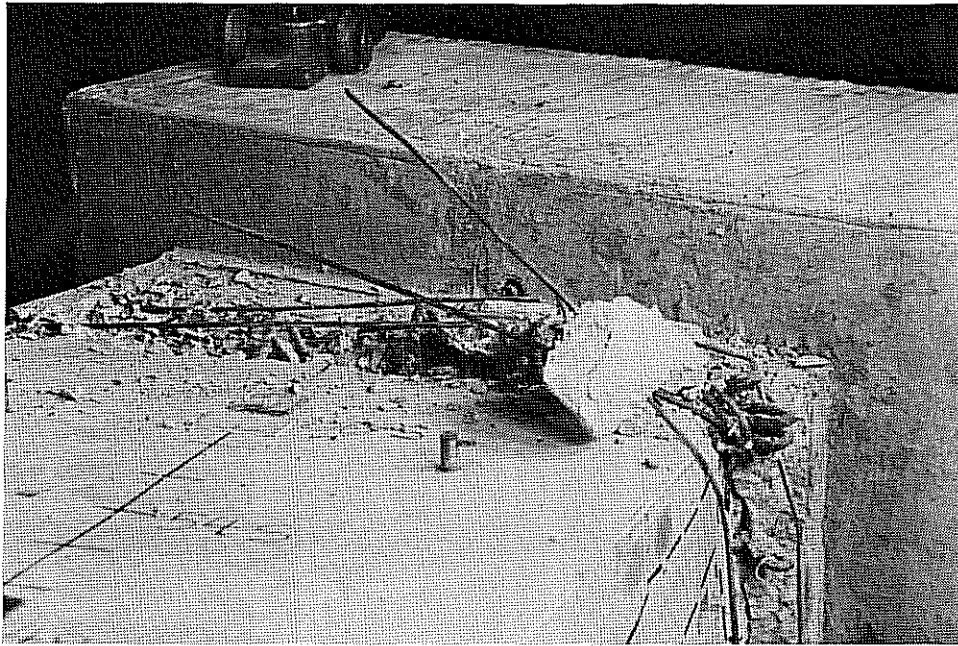


Figure 3.80: Specimen 10ML18 Side Face Close-Up

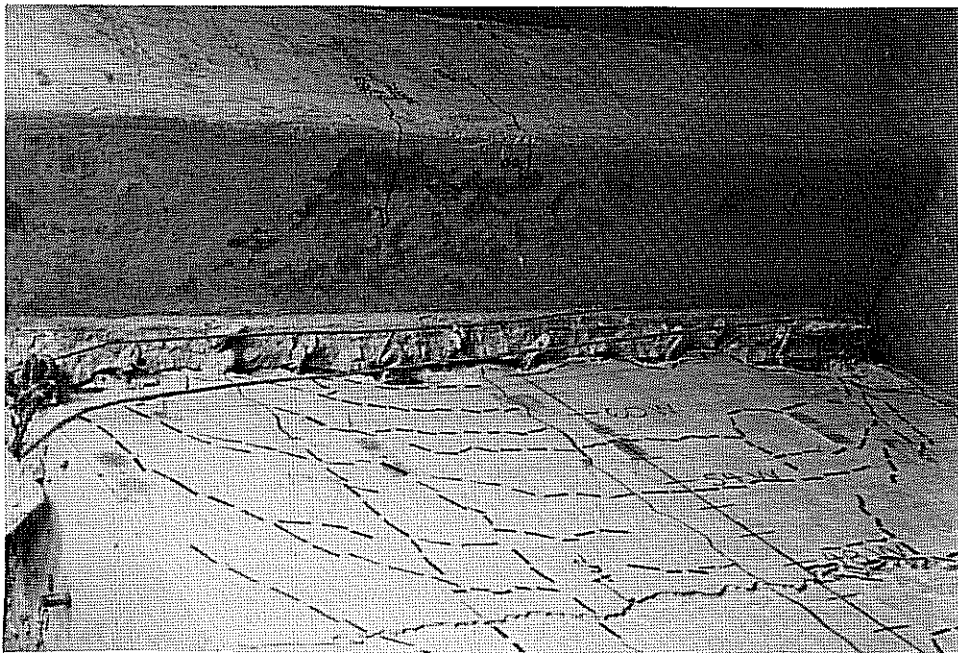


Figure 3.81: Specimen 10ML18 Compression Flange Displacement at Failure

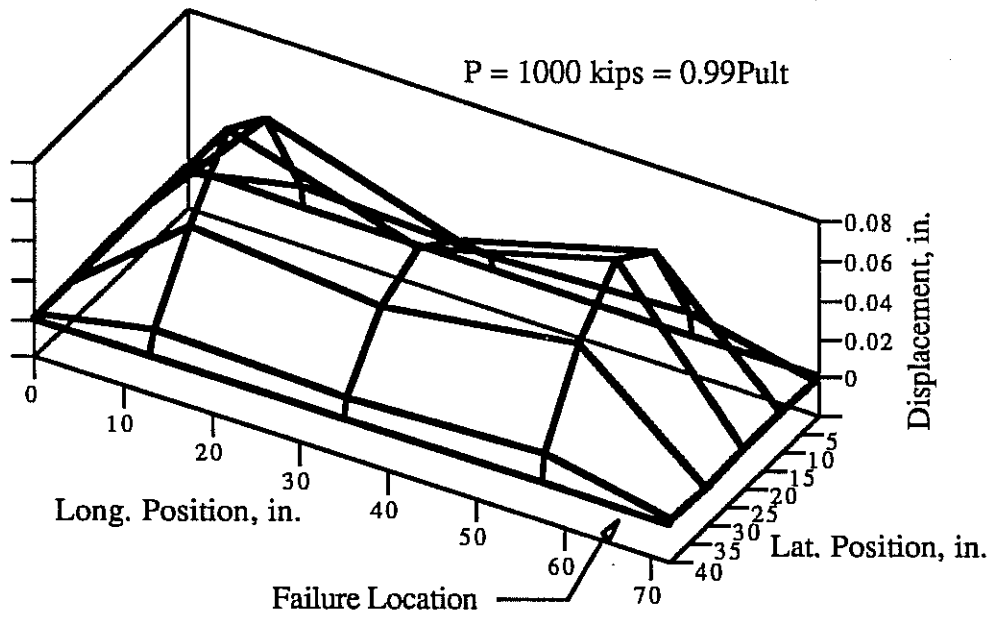


Figure 3.82: Specimen 10ML18 Compression Flange Profile

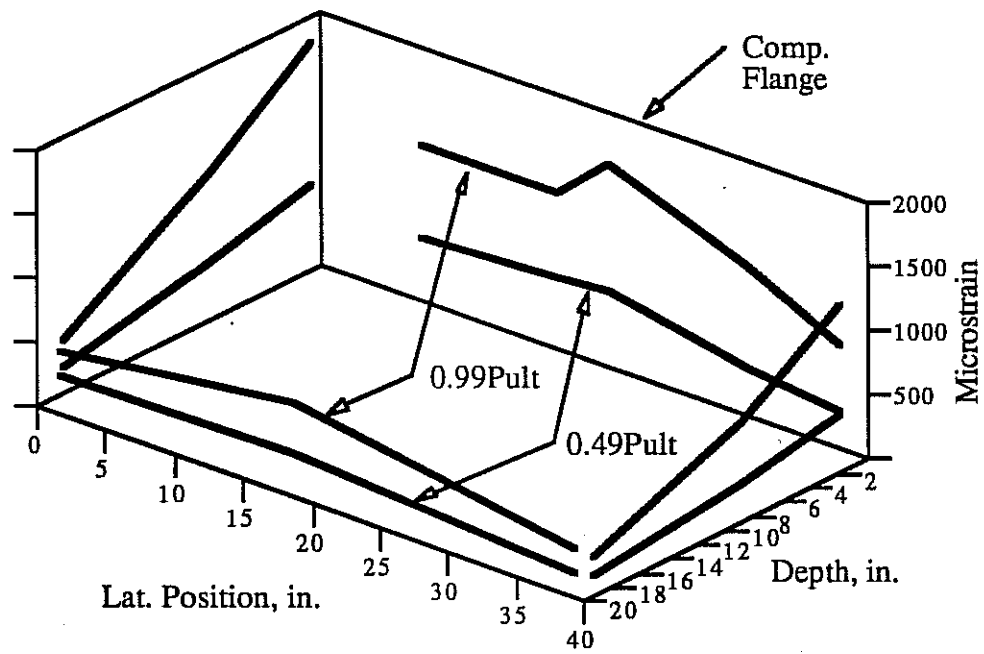


Figure 3.83: Specimen 10ML18 Cross Section Strain Distribution

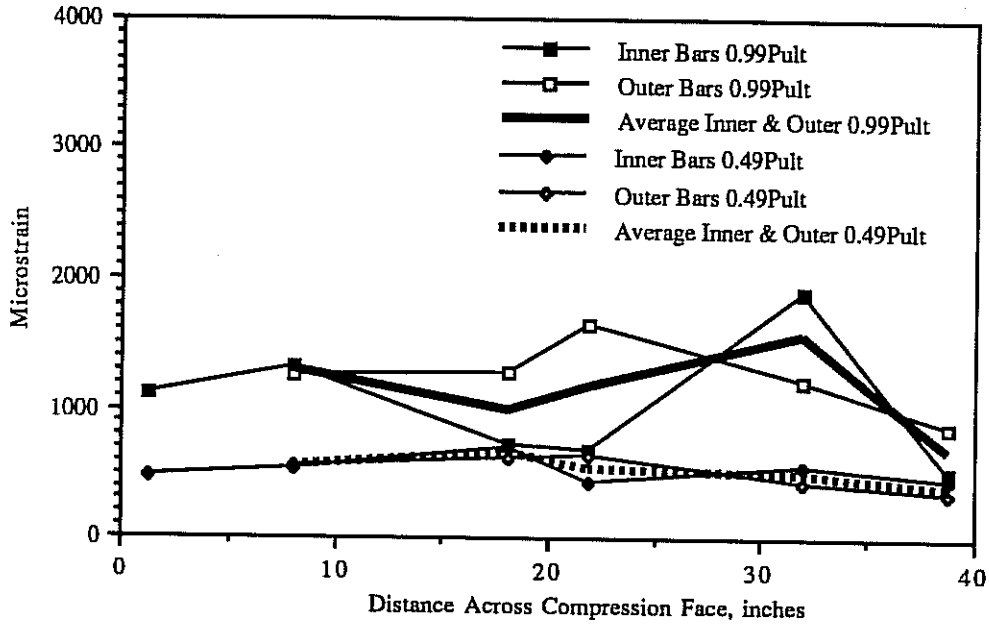


Figure 3.84: Specimen 10ML18 Compression Flange Strains at Mid-Height

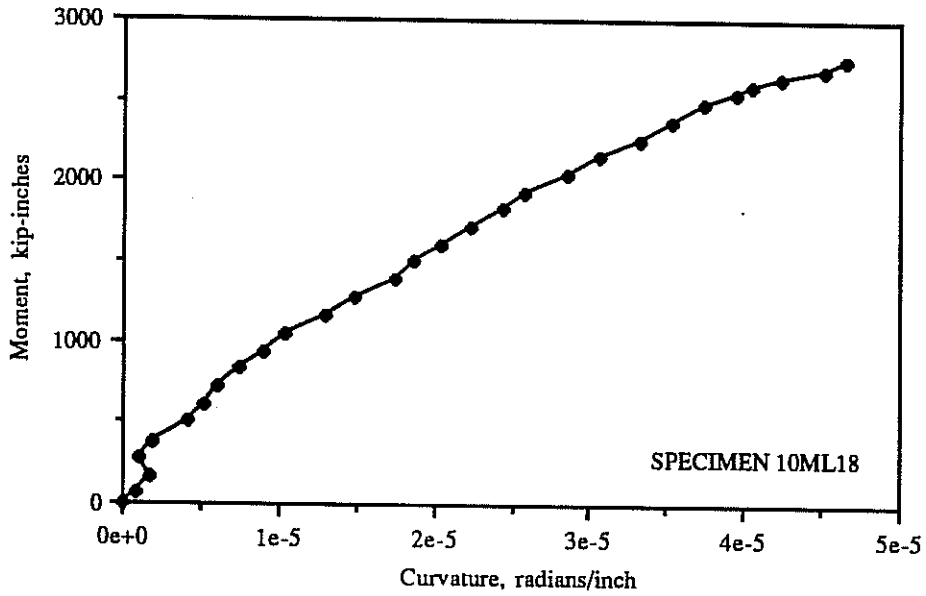


Figure 3.85: Specimen 10ML18 Moment-Curvature Curve

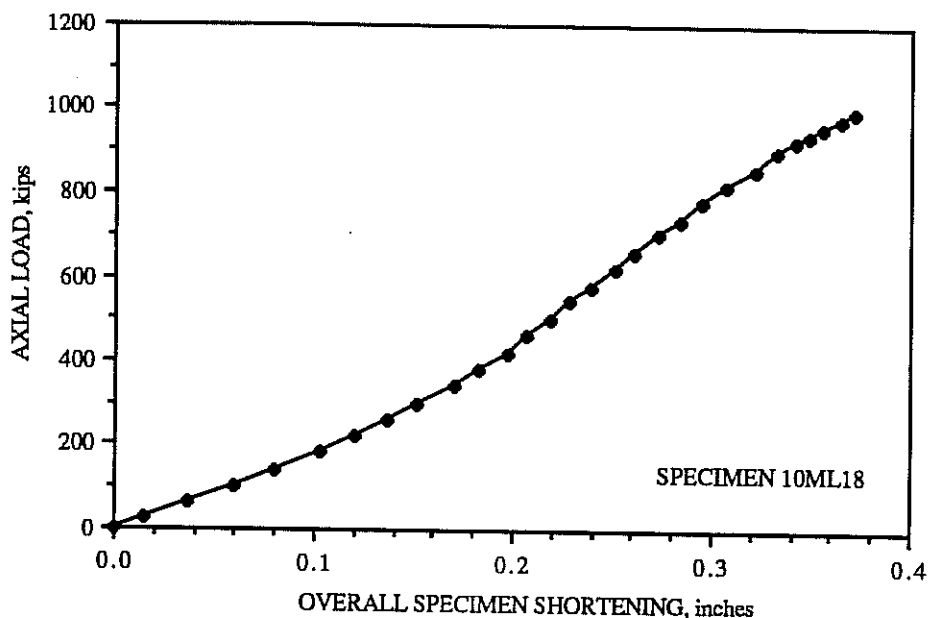


Figure 3.86: Specimen 10ML18 Axial Shortening Curve

3.3.11. 11ML34 (Multiple-Lift, 20" x 40", 1.1" walls, $X_{u/t} = 33.6$)

Figures 3.87 to 3.96 show the experimental results for specimen 11ML34. The failure, which was explosive, occurred at a load of 623 kips. The specimen crept to failure about 10 seconds after the final load step had been applied. The location of the failure was near the top of the specimen (as cast) between 66 and 68 inches above the bottom load head (Figures 3.87, 3.89 and 3.90). Near the failure zone the compression flange displaced inward about two inches, as shown in Figures 3.89 and 3.90.

First cracking of the specimen load heads occurred at a load of 343 kips. Longitudinal cracks appeared in both the compression and "tension" flanges at a load of 422 kips. Cracking in the compression and "tension" flanges was confined mainly to the regions near the ends of the specimen. Cracks tended to form at the locations of longitudinal reinforcing bars. The cracks indicated in Figures 3.87 to 3.90 by dashed lines were marked after failure.

No problems were observed with reinforcement details, other than the lateral reinforcement lap splices on the side faces of the specimen (Figure 3.91).

The compression flange profile just prior to failure is plotted in Figure 3.92. It is interesting to note that the compression flange assumed a double curvature shape at failure. Similar plots of the compression flange shape were made for other values of compressive load. It was found that the compression flange had a similar shape throughout the load history; that is, the compression flange did not snap through from one mode shape to another. This was the only specimen which exhibited a doubly-curved compression flange; it was also the specimen with the highest value of wall slenderness ratio.

Figure 3.93 shows the distribution of strains over the cross section at 48% and 100% of ultimate load. At the lower value of load the strain distribution was nearly planar. Near ultimate load the strain distribution was somewhat irregular, but close to planar.

The through-thickness strain gradient data, plotted in Figure 3.94, clearly indicates greater compressive strains in the inner layer of bars than in the outer layer at both low and high loads. Although the lines of strain gages were located near the center node of the doubly-curved displaced shape of the compression flange (Figure 3.92) there was still some outward bulging of the flange at that location. This bulging is probably responsible for the compressive strains in the inner bars being greater than in the outer bars.

The experimental moment-curvature plot is shown in Figure 3.95. The slope of the curve tends toward zero at higher loads, but does not reach zero at the ultimate load. This is not consistent with the observed failure mode of creep to failure under sustained load. Possibly failure was caused by some phenomenon other than overall material failure of the cross section, such as local buckling of the compression flange.

The load-axial shortening plot shown in Figure 3.96 is nearly linear over the entire load range.

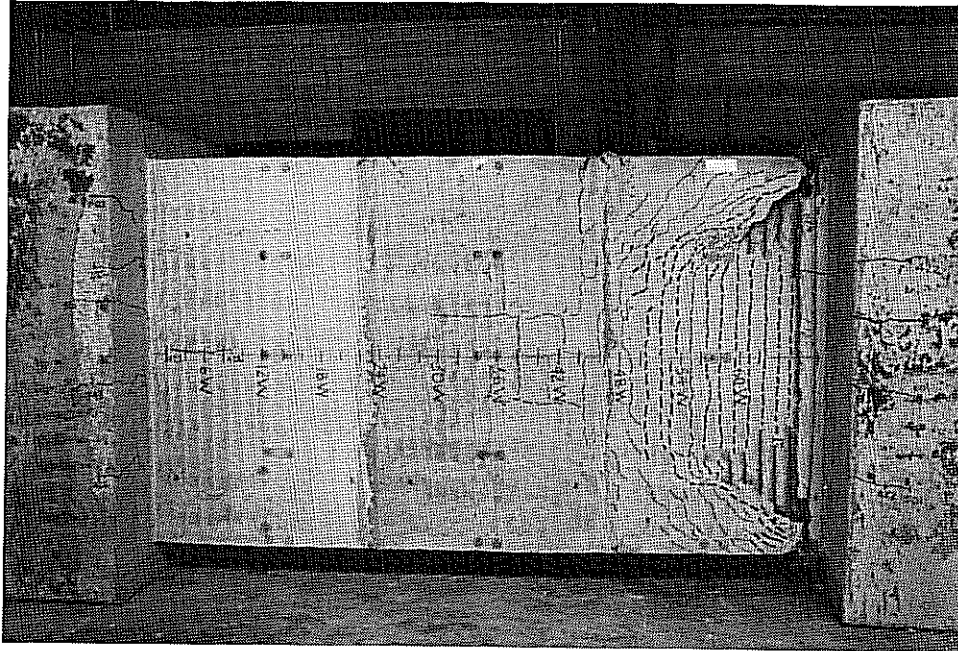


Figure 3.87: Specimen 11ML34 Compression Flange

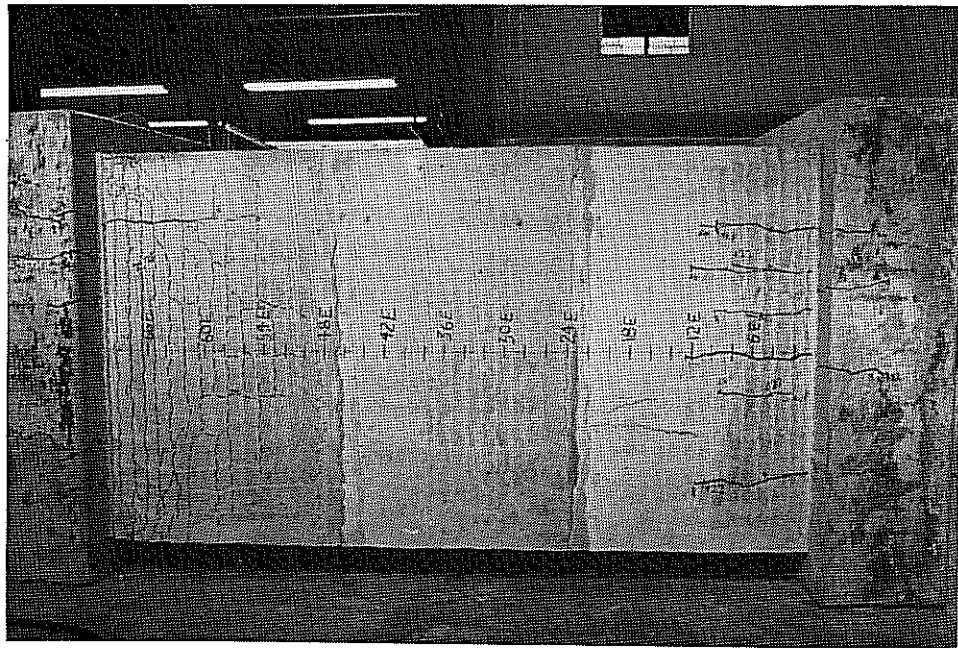


Figure 3.88: Specimen 11ML34 "Tension" Flange

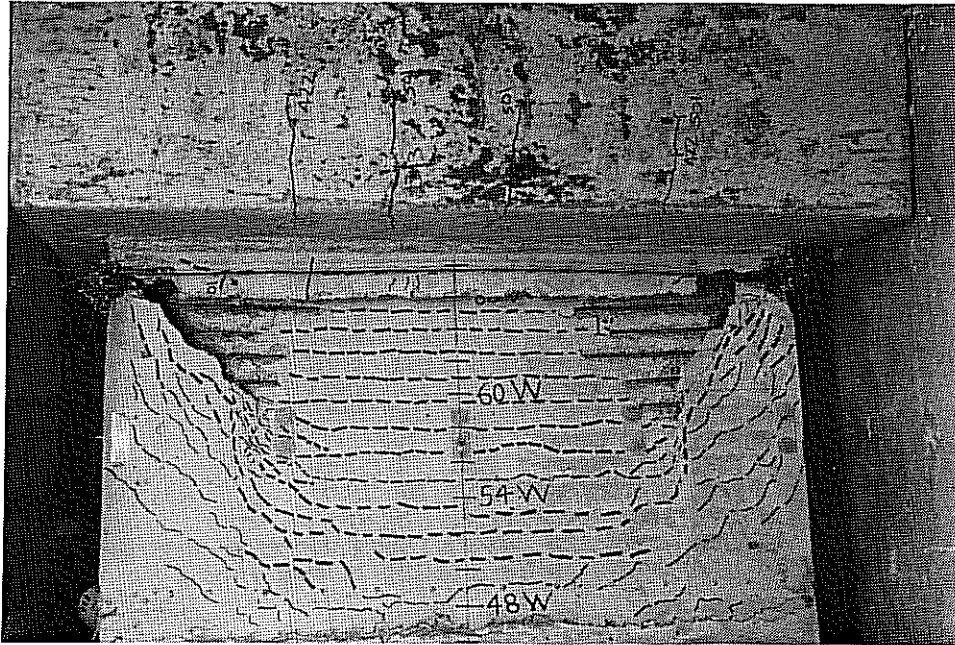


Figure 3.89: Specimen 11ML34 Compression Flange Close-Up

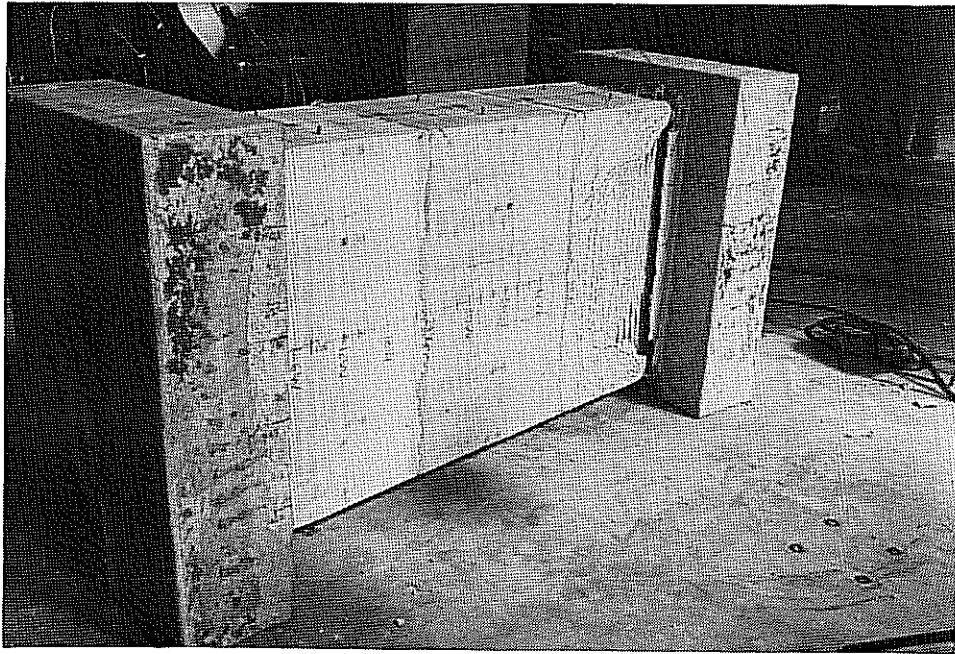


Figure 3.90: Specimen 11ML34 Compression Flange Displacement at Failure

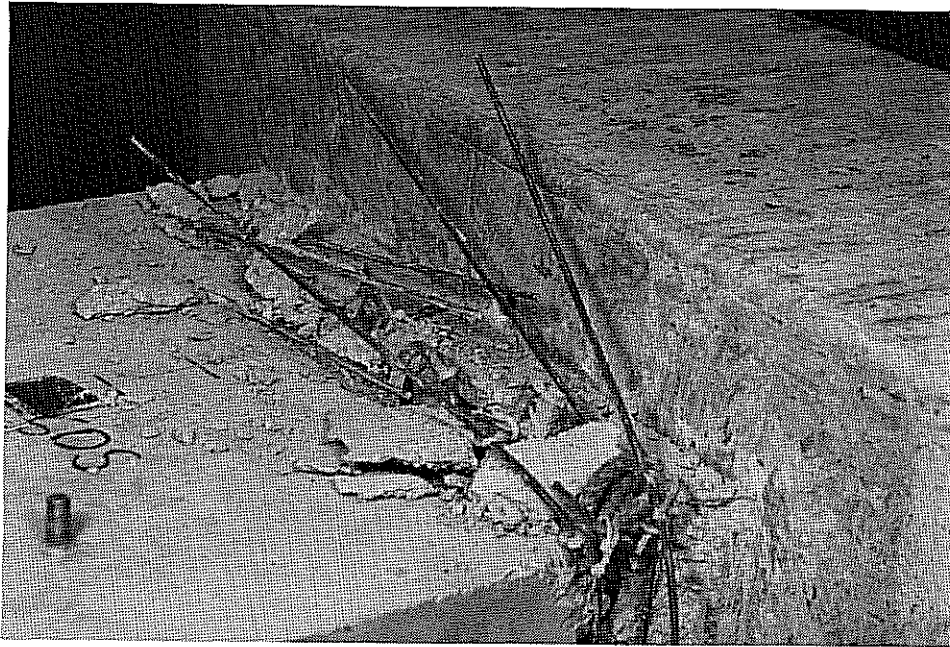


Figure 3.91: Specimen 11ML34 Side Face Close-Up

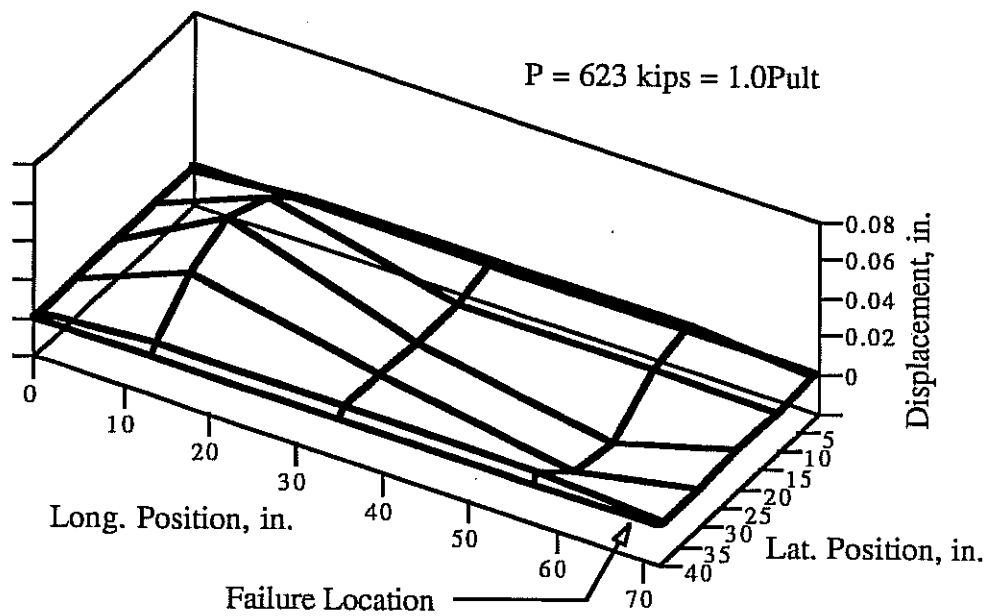


Figure 3.92: Specimen 11ML34 Compression Flange Profile

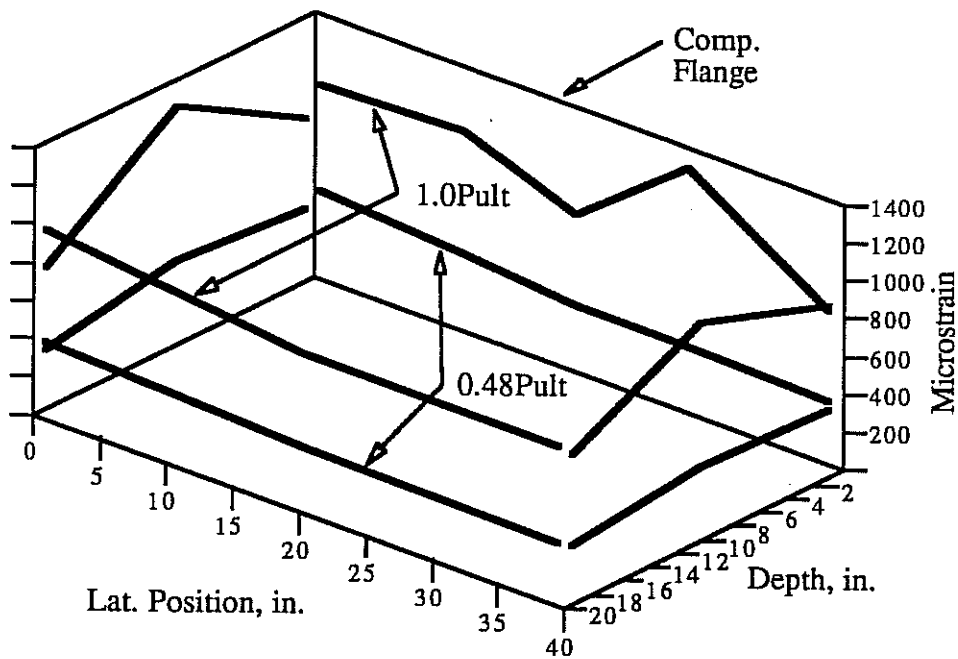


Figure 3.93: Specimen 11ML34 Cross Section Strain Distribution

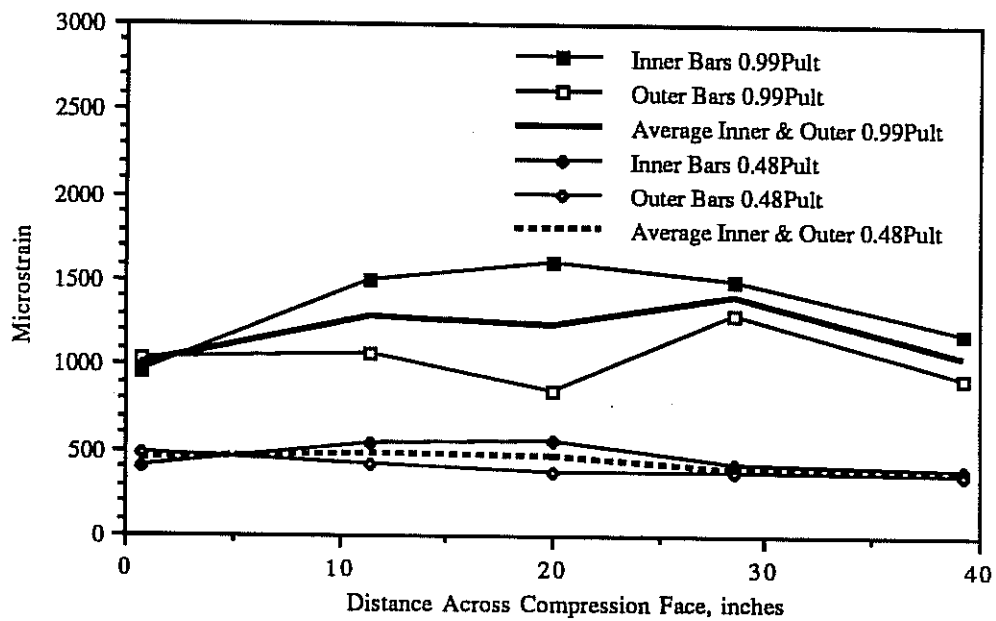


Figure 3.94: Specimen 11ML34 Compression Flange Strains at Mid-Height

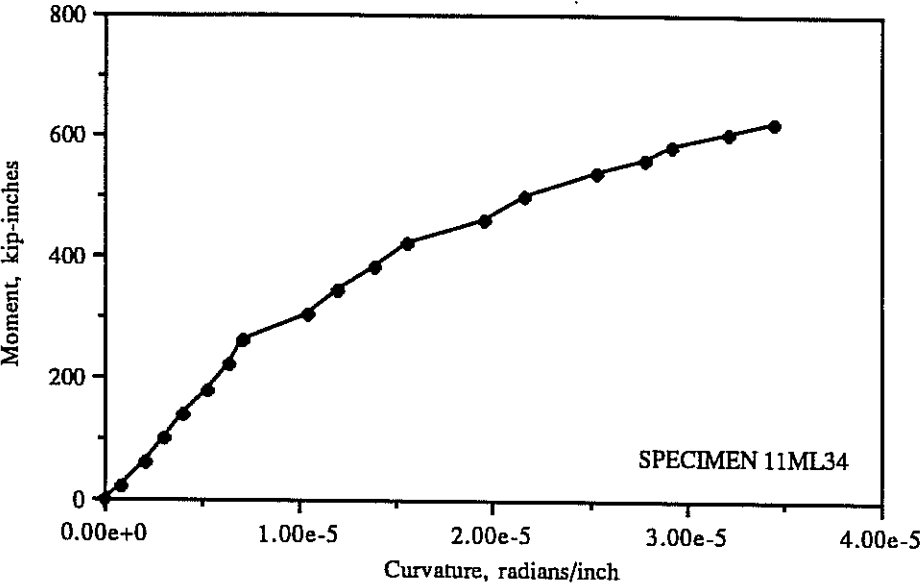


Figure 3.95: Specimen 11ML34 Moment-Curvature Curve

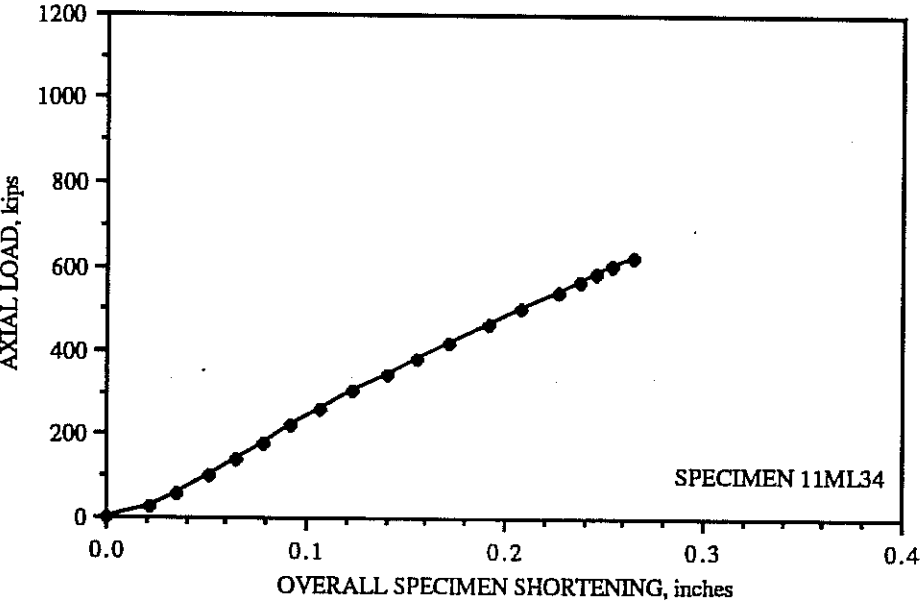


Figure 3.96: Specimen 11ML34 Axial Shortening Curve

3.3.12. 12S29 (Segmental, 20" x 40", 1.1" walls, $X_u/t = 29.3$)

Experimental data from specimen 12S29 is shown in Figures 3.97 to 3.108. The specimen failed explosively at a load of 682 kips, about 10 seconds after the last load step was applied. Between about 460 kips and the failure load the specimen emitted occasional faint ticking sounds. The failure zone was located near the bottom of the specimen (as cast) between 2 and 6 inches above the bottom load head (Figures 3.97 and 3.99). A notable feature of the failure was that the compression flange moved outward about two inches at failure, as shown in Figures 3.99 and 3.100. (Figure 3.100 is an interior view of the specimen).

Cracks first appeared in the specimen load heads at a load of 300 kips. At 458 kips short longitudinal cracks were observed in both the compression and "tension" flanges. These cracks were grouped near the ends of the specimen, and none grew more than 14 inches in length. Cracks generally formed near longitudinal reinforcing bars. The cracks indicated by dashed lines in Figures 3.97 to 3.99 were marked after failure.

Reinforcement details performed adequately in this specimen, except for the lateral bar lap splices on the side faces (Figure 3.103).

One post-tensioning bar in the compression flange slipped in its duct at failure (Figure 3.102), while the other bar in the compression flange buckled inward (Figure 3.101). The bar that buckled inward did not fracture, as similar bars did in specimens 7S22 and 9MLP22. The post-tensioning bar which slipped probably did so because only a 12 inch development length was available through the thickness of the load head.

The epoxy performance was satisfactory for this specimen. Although the failure region was in close proximity to an epoxy joint the failure did not pass through the joint, indicating the epoxy did not create a plane of weakness.

The compression flange profile just before failure is shown in Figure 3.104. It can be seen that out-of-plane displacements were large near the ends of the specimen and small near the center. The failure region occurred in the area of largest out-of-plane displacements.

Figure 3.105 shows the measured distribution of longitudinal strains over the cross section at 50% and 100% of the ultimate load. At the lower load the strain

distribution was nearly planar. At ultimate load the strain distribution was somewhat irregular.

Strains in the inner and outer layers of bars at mid-height on the compression flange are plotted in Figure 3.106. On the right side of the diagram outer bars have higher compressive strains than inner bar, while the opposite is true on the left side. Since just one malfunctioning gage on either the left or right side of the diagram would lead to opposite interpretations of this data, little can be concluded from the figure.

The experimental moment-curvature curve is plotted in Figure 3.107. The slope of the curve gradually decreases as the ultimate load is approached. However, the slope of the curve is not zero at the failure point, which conflicts with the observed creep to failure mode of the specimen. Possibly some local phenomenon was responsible for the failure, such as buckling of the compression flange.

The load-axial shortening curve for the specimen is plotted in Figure 3.108. The curve is initially nonlinear at low loads, and is nearly linear at higher loads.

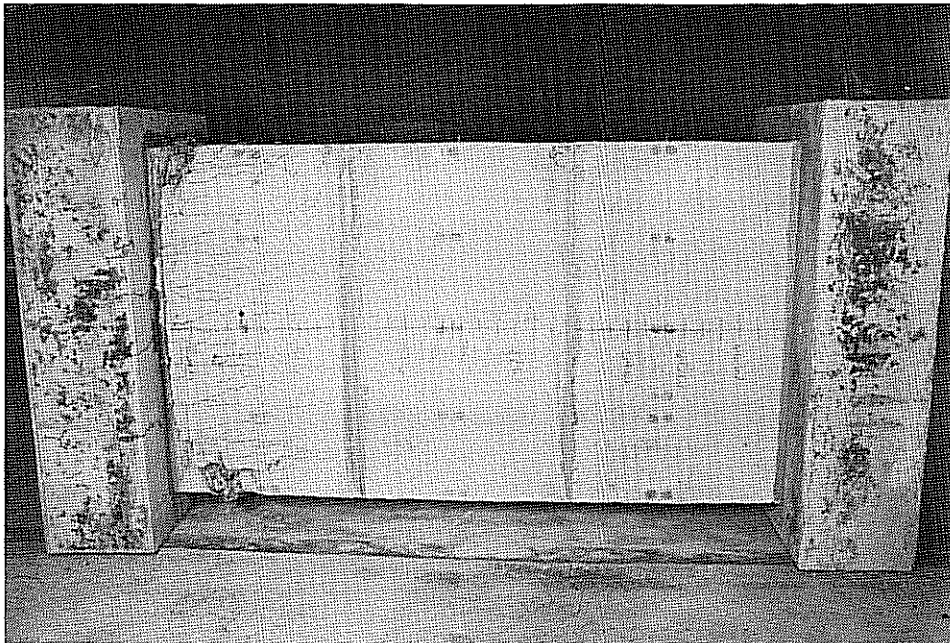


Figure 3.97: Specimen 12S29 Compression Flange

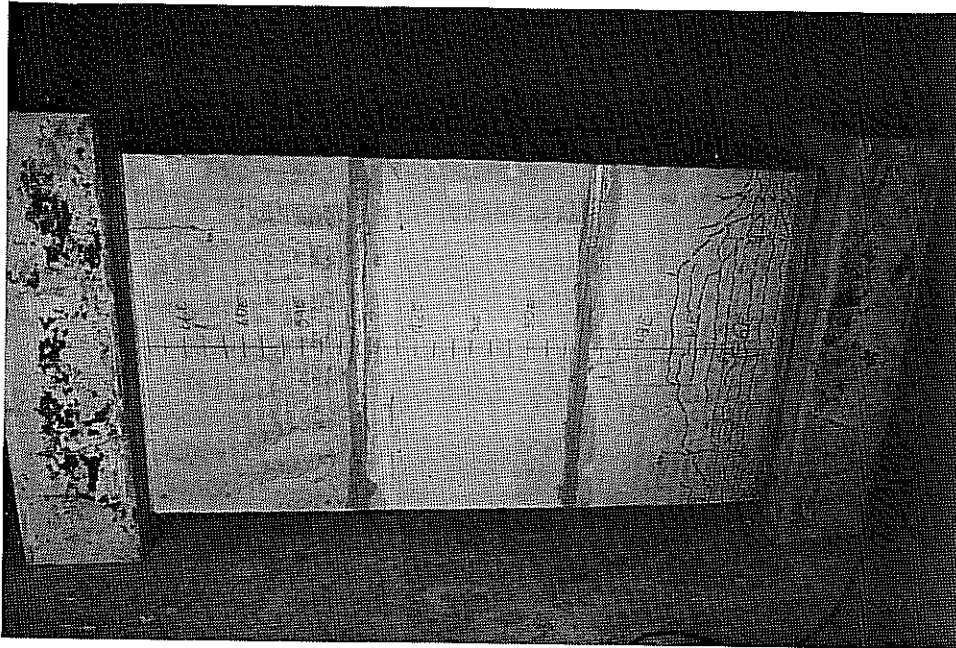


Figure 3.98: Specimen 12S29 "Tension" Flange

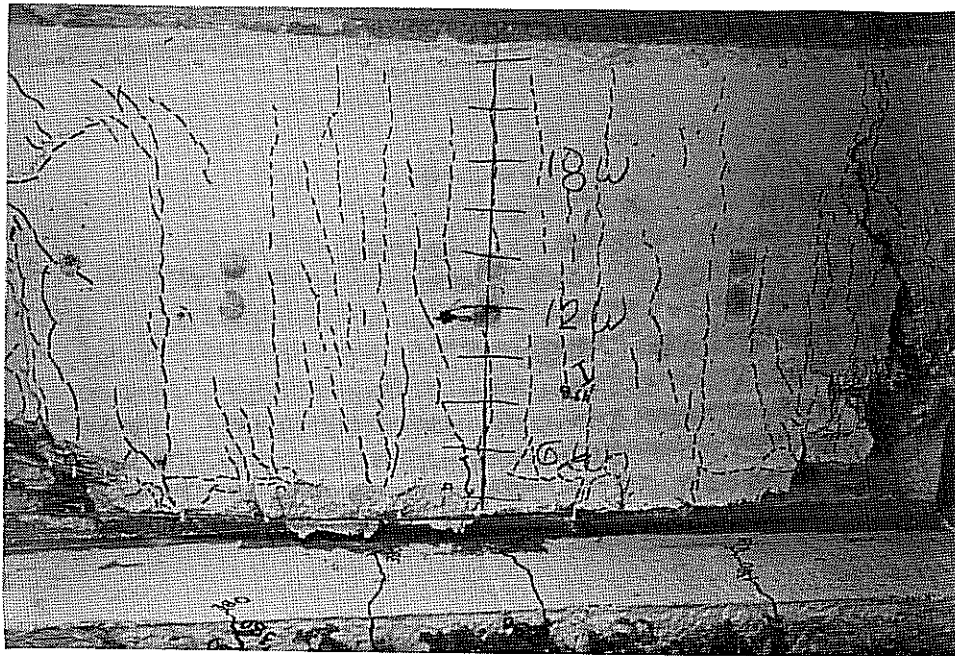


Figure 3.99: Specimen 12S29 Compression Flange Close-Up



Figure 3.100: Specimen 12S29 Interior View of Failure Region



Figure 3.101: Specimen 12S29 Interior View of Post-Tensioning Bar

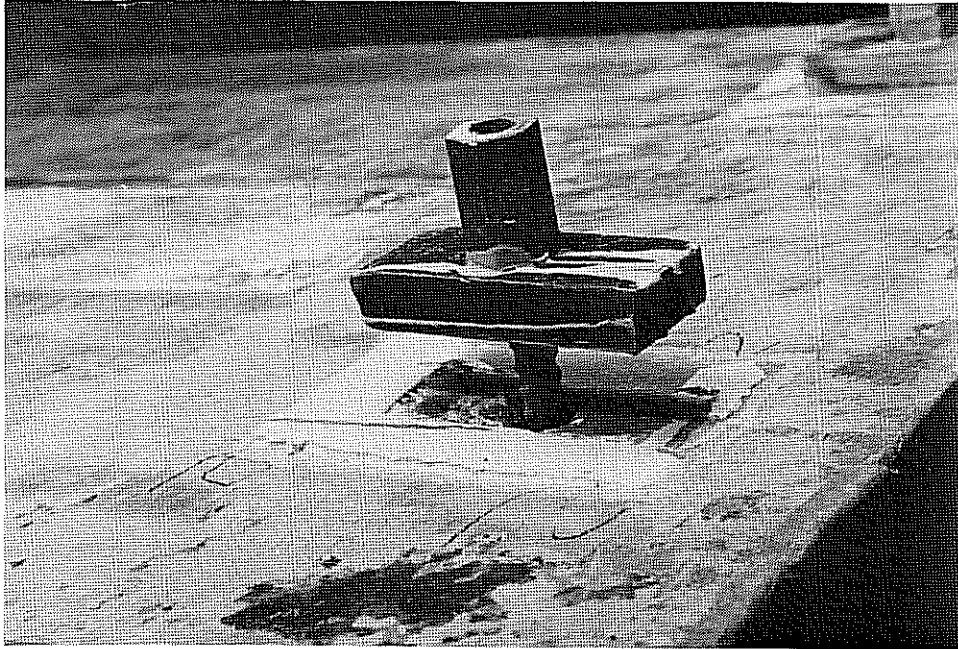


Figure 3.102: Specimen 12S29 Post-Tensioning Anchorage



Figure 3.103: Specimen 12S29 Side Face Close-Up

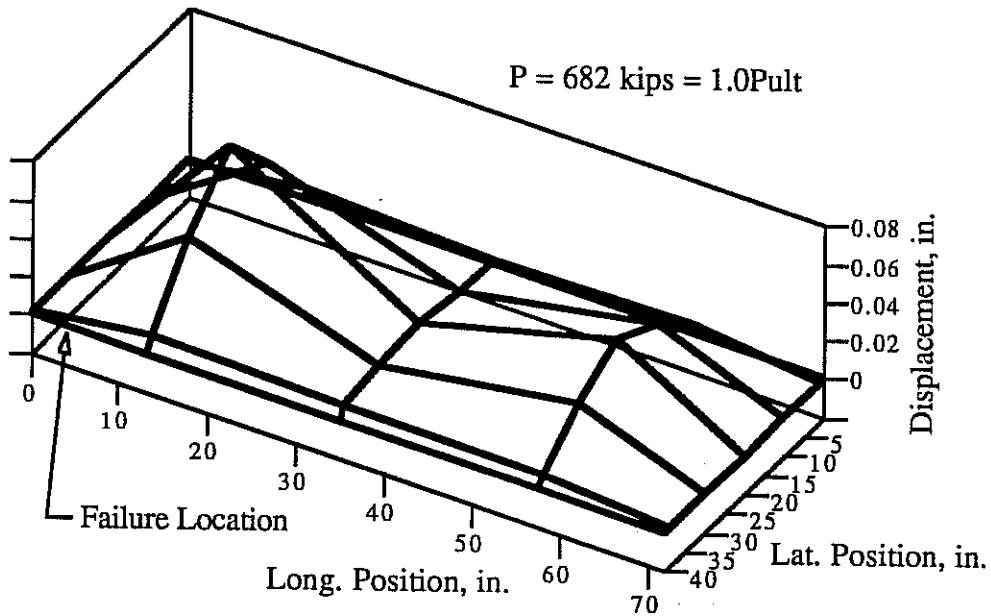


Figure 3.104: Specimen 12S29 Compression Flange Profile

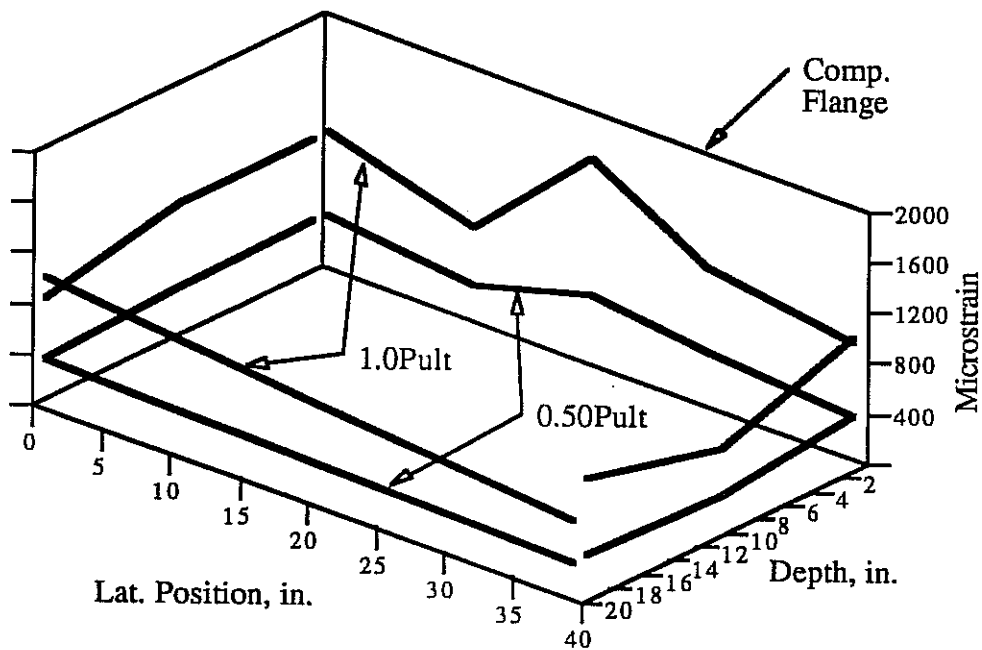


Figure 3.105: Specimen 12S29 Cross Section Strain Distribution

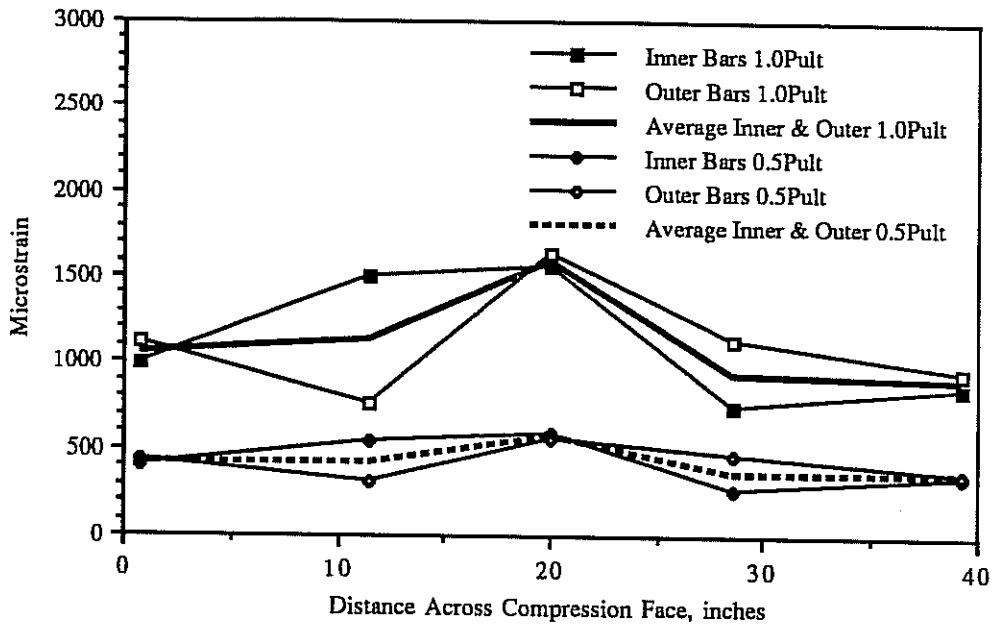


Figure 3.106: Specimen 12S29 Compression Flange Strains at Mid-Height

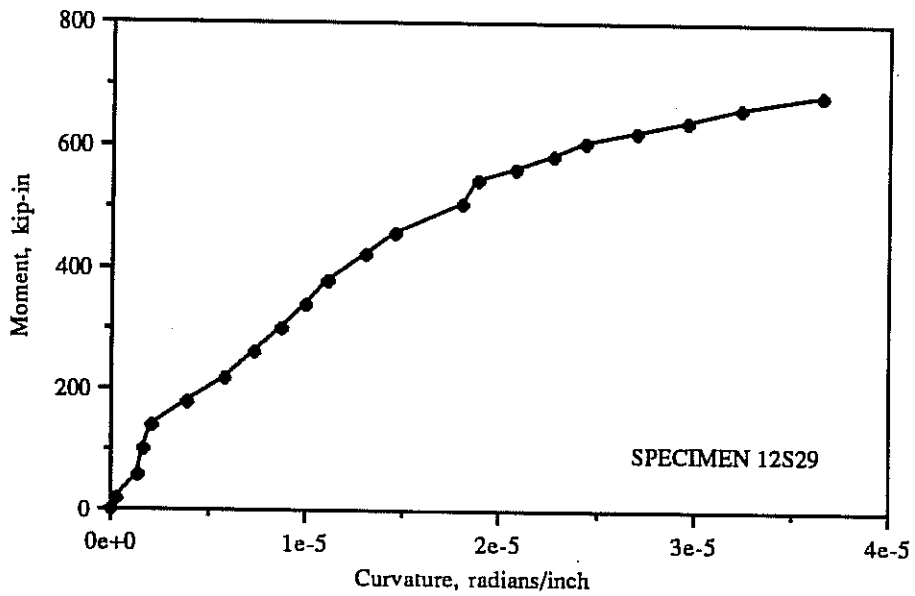


Figure 3.107: Specimen 12S29 Moment-Curvature Curve

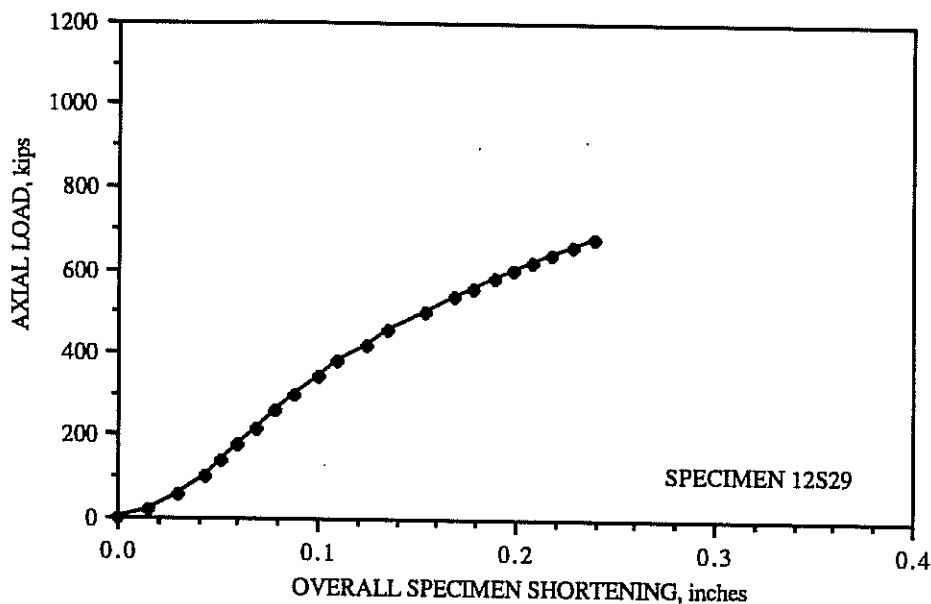


Figure 3.108: Specimen 12S29 Axial Shortening Curve

3.4. Discussion of Experimental Results

In this section the results of the twelve hollow pier tests are compared and discussed. The discussion is organized in thirteen subtopics, each focusing on a separate aspect of the experimental behavior.

3.4.1. Compression Flange Behavior

Two characteristics of compression flange behavior were measured in the test program: the compression flange profile, and the through-thickness variation of longitudinal strains. Compression flange profiles just prior to failure are illustrated in Sections 3.3.1 to 3.3.12. Strains in the inner and outer layer of reinforcement in the compression flanges of the last four specimens are illustrated in Sections 3.3.9 to 3.3.12.

All but one of the compression flange profiles show an outward bulge shape with single curvature. (The reasons for some of the bulge shapes being irregular are discussed below). Specimen 11ML34 has a compression flange profile with double curvature. Since this was the specimen with the largest value of wall slenderness

ratio it is possible that the unique profile shape is related to local buckling of the thin flange. The local buckling characteristics of the compression flanges of the test specimens are explored analytically in Chapters 4 and 5.

Several of the specimens had compression flange profiles with greater displacements near the ends of the flange than in the center (Figures 3.23, 3.30, 3.55, 3.72, 3.82 and 3.104). These local end bulges are probably due to distortions of the solid specimen load heads. As the specimens were loaded the load heads assumed a slightly "dished" shape because they were loaded at the center of one face and supported near the edges of the opposite face by the walls of the hollow cross section. The distortion induced a rotational displacement along the short edges of the four plates which make up the hollow cross section. This accounts for the tendency of bulging to be greater near the ends of many specimens than near the center. This also accounts for the observed outward, rather than inward, bulging of all compression flanges.

Distortion of the specimen load heads also induced a region of higher stresses near the center of each short edge of the four plates making up the hollow cross section. The effects of these stress concentrations on crack patterns of the specimens are discussed in section 3.4.4.

Longitudinal compressive strains in the inner layer of reinforcing bars were in several cases greater than in the outer layer (see Figures 3.74, 3.94 and 3.106). This trend is contrary to what would normally be expected, since the outer layer of reinforcement is further from the neutral axis of the specimen than the inner layer. The difference can be explained by the observed non-planar action of the compression flange in all specimens. The outward bulging of the compression flange induced a strain gradient through the thickness of the flange which counteracted the normal strain gradient imposed by overall bending of the specimen.

3.4.2. Axial Shortening Behavior

All five available axial shortening curves (specimens 8ML25 to 12S29) have nearly the same overall slope. This is somewhat surprising, since the five specimens had cross section areas ranging from 130 to 224 square inches.

The measured overall axial shortening curves include an unknown component

due to distortion of the load heads. Using some of the measurements of the test machine and specimen displacements it is possible to make a rough estimate of the contribution of load head distortion to overall axial shortening of the specimen. At maximum load this contribution is estimated to be 0.1 to 0.2 inches, while the actual axial shortening of the hollow test section is estimated to be about 0.08 to 0.1 inches. Thus, load head distortions, rather than shortening of the hollow test section, dominate the load-axial shortening diagrams. Since the load heads were all similarly constructed this would account for the similar slopes of the diagrams.

3.4.3. Center Line Deformations

Because most specimens were tested at low eccentricities the observed center line deflections were small (see Table 3.2). The deflected shapes near ultimate load were all symmetric, within the experimental error of ± 0.02 inches.

In computing the maximum applied moment at failure second-order effects were taken into account by adding the maximum observed center line deflection to the eccentricity of the applied load (see the footnote to Table 3.1).

Second order moments for all specimens, except 2M10, amounted to less than 7.5% of the total applied moment, but second order moments for specimen 2M10 were 11.2% of the total applied moment. Thus specimen 2M10 probably failed exactly at mid-height because of the relatively large second-order moments at that location.

3.4.4. Cracking

Two main types of cracks were observed in the specimens prior to failure: longitudinal cracks in the specimen load heads and longitudinal cracks in the compression and "tension" flanges of the hollow test section.

Load head cracks always appeared at lower loads than cracks in the flanges of the hollow test section. The load head cracks were first visible on the side faces of the load heads, and they initiated at the edges of the load heads closest to the hollow test section (see for example Figures 3.14 and 3.60). These cracks usually extended through about half the thickness of the load heads and sometimes they extended through the full thickness. The pattern of cracking indicates that each load head

assumed a slightly "dished" shape during loading, with the convex side nearest the hollow test section and the concave side nearest the loading plate.

The longitudinal cracking patterns observed in the hollow test sections were related to the distortions of the load heads. Because the load heads did not remain perfectly rigid during loading the applied stresses along the short edges of the compression and "tension" flanges were not uniform; that is, a region of higher stresses was created near the center of each short edge.

Work by Guyon⁹⁴ on anchorage zone stresses in post-tensioned beams is helpful in relating load head distortions to the observed crack patterns in the compression and "tension" flanges of the specimens. Figure 3.109 shows the transverse stress isobars set up when a concentrated or partial distributed load is applied to the edge of a plate of finite width. It can be seen that a zone of tensile stresses is formed at the center of the plate a short distance from the point of application of the load. This agrees well with the observed cracking behavior of the compression and "tension" flanges of the specimens, as longitudinal cracks tended to initiate in that region. Note on the right side of Figure 3.109 that even when a distributed load is spread over half the width of the plate a tensile zone is created.

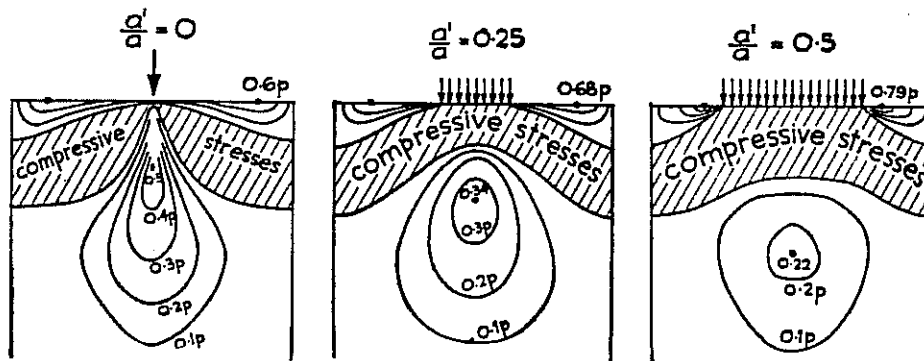


Figure 3.109: Transverse Stress Isobars in an Edge-Loaded Plate⁹⁴

Figure 3.110 shows the value of maximum transverse tensile stress as a function of the ratio of the loaded width of the plate to the total width of the plate. The tensile strength of concrete in direct tension is roughly 4 times the square root of the compressive strength⁹⁵. Thus for the specimens tested in this study the calculated

concrete tensile strength ranged between about 4% and 7% of the ultimate compressive strength. In the test program longitudinal cracks in the compression and "tension" flanges of the specimens initiated at an average load of 55% of the ultimate load. It can be assumed approximately, then, that at first cracking the longitudinal compressive stresses in the flanges of the test specimen were about 50% of the ultimate crushing strength of the concrete. This implies that the transverse tensile stresses at first cracking were roughly 8% to 14% of the longitudinal compressive stress (i.e. 4% to 7% of the ultimate crushing strength of the concrete, or 8% to 14% of half the crushing strength).

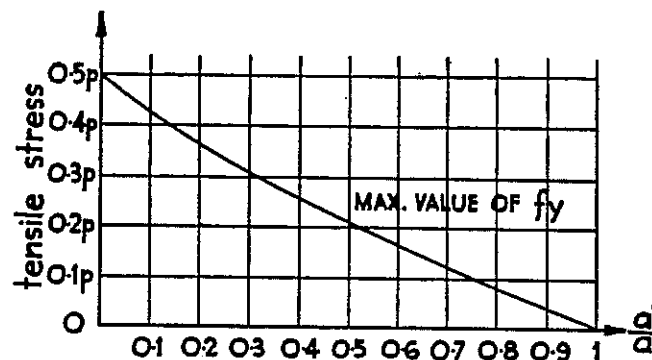


Figure 3.110: Maximum Transverse Tensile Stress vs. Extent of Loaded Area⁹⁴

Referring to Figure 3.110 it can be seen that when the maximum transverse tensile stress in the plate is 0.08p to 0.14p the partial distributed load covers 65% to 80% of the edge of the plate. While this approach is approximate, it gives a rough idea of how the compressive forces were distributed over the width of the compression and "tension" flanges in the test specimens.

It is interesting to note that for three of the test specimens (4M18, 5S9 and 6S16) the first longitudinal cracks in the "tension" flange appeared at a lower load than the first cracks in the compression flange. Cracks were expected to appear first in the compression flange because it was more highly stressed. No specific reason for this behavior is known, but random variations in concrete tensile strength may have permitted cracking to occur first on the "tension" face. This is probably the case,

since the loads for first cracking in the compression and "tension" flanges are fairly close together for all three specimens.

3.4.5. Location of Failure

The twelve specimens of the test program can be divided into two groups: those which failed near the middle of the specimen and those which failed near the ends.

Specimens 2M10 and 5S9 both failed near the middle of the specimen. The reasons for the failure of each of these are discussed in section 3.4.3 and 3.4.9. Specimen 2M10 failed almost exactly at mid-height because second order moments were relatively large for that specimen, creating the maximum total moment near mid-height. Specimen 5S9 failed at the top edge of the bottom segment because cross ties between the two layers of reinforcement in the compression flange were missing in that location.

The remaining ten specimens failed near one end. Eight specimens failed near the top end and two near the bottom end (see Table 3.1). Two conditions are probably responsible for the failures being located near an end. First, a zone of weaker concrete forms at the top of vertically cast columns due to the upward migration of free water in fresh concrete - the so-called "water gain" effect. Second, it has been established through observation of crack patterns that load head distortions created non-uniform stress distributions at the interface between the load heads and the hollow test sections. Specifically, there was probably a region of higher stress near the center of each short edge of the compression and "tension" flanges, as discussed in Section 3.4.4.

While the water gain effect and load head distortion probably influenced the locations of failures, they were not the only factors determining the ultimate failure load. Other contributing factors have been considered in this study, including wall slenderness (Section 3.4.6), reinforcement details (Section 3.4.9), methods of construction (Section 3.4.12) and post-tensioning effects (Section 3.4.13).

3.4.6. Wall Slenderness Ratio

The wall slenderness ratio of the twelve specimens varied between 8.8 and 33.6. The influence of wall slenderness ratio on three aspects of the observed specimen

behavior are discussed below.

The profiles of the compression flanges of the specimens all had the same general shape of a single outward bulge, with the exception of specimen 11ML34. For specimen 11ML34 the compression flange profile had two bulges, one inward and one outward, as shown in Figure 3.92. Since the compression flange of specimen 11ML34 had the highest wall slenderness ratio of any specimen it is likely that the double bulge flange shape was related to local buckling of the compression flange. Compression flange profiles are discussed in more detail in Section 3.4.1, and local wall buckling is investigated analytically in Chapter 4.

The appearance of the failure zone tended to be different for specimens with low and high wall slenderness ratios. Specimens 10ML18, 11ML34 and 12S29 had wall slenderness ratios of 18.0, 33.6 and 29.3, respectively. At failure the compression flanges of these three specimens displaced either inward or outward at failure, as shown in Figures 3.81, 3.90 and 3.100. With all other specimens the compression flange remained essentially in its original plane after failure. This indicates that non-planar action of the compression flange may have played a role in the failure of specimens with high wall slenderness ratios.

The experimental moment-curvature relationships for monolithic and multiple-lift specimens are plotted in Figure 3.111, and for segmental specimens in Figure 3.112. (The moment-curvature relationship for specimen 1M10 is omitted from Figure 3.111 because the specimen was loaded at a much larger eccentricity than the other monolithic and multiple-lift specimens). It can be seen from the two figures that wall slenderness ratio has no apparent effect on the moment-curvature behavior of monolithic (and multiple-lift) or segmental specimens. That is, as the wall slenderness ratio increases there is no consistent change in the moment-curvature relationships shown in the two figures.

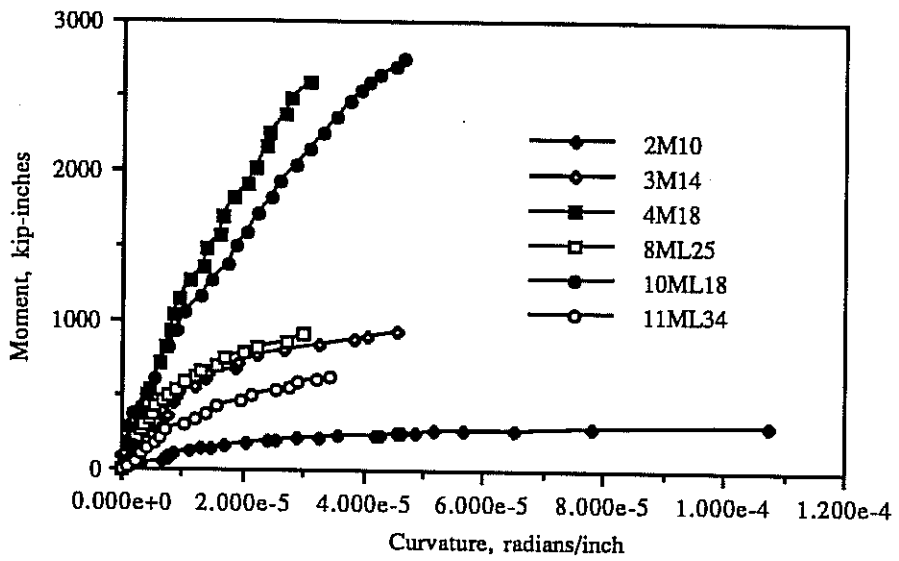


Figure 3.111: Moment-Curvature Data for Monolithic and Multiple-Lift Specimens

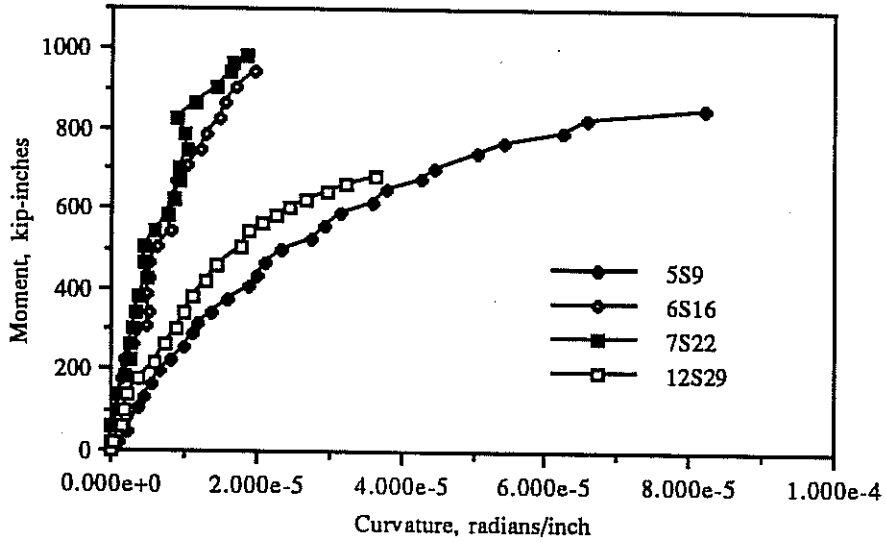


Figure 3.112: Moment-Curvature Data for Segmental Specimens

3.4.7. Plane Sections Remain Plane

A ring of strain gages near mid-height of the test specimens was used to determine the distribution of longitudinal strains over the cross section. One of the fundamental assumptions of the analytical model developed in this study is that cross sections which are originally plane before loading remain plane during loading. The ring of strain gages at mid-height was intended to test this assumption.

The experimental results plotted in Sections 3.3.1 to 3.3.12 show that at 50% of the ultimate load all specimens had strain distributions which were very close to planar. At ultimate load several of the specimens (1M10, 4M18, 8ML25 and 12S29) had strain distributions which were slightly irregular, but were still close to planar. The remaining specimens had strain distributions at ultimate which tended to be planar, but had large local aberrations on one or more faces. Several explanations for the aberrations are possible. First, some strain gages may have been operating improperly at higher strains due to the gages coming unglued from the bar or due simply to the useful range of the gages being exceeded. Second, the gages may have been working properly, but the strains in the reinforcing bars may not have been representative of the strains in the surrounding concrete. Longitudinal cracks often formed at the location of longitudinal reinforcing bars, so some bars may not have acted integrally with the surrounding concrete. Finally, the gages may have given valid readings of strains in the cross section, indicating that, in fact, at high loads plane sections did not remain plane.

It is likely that all three of the above explanations are valid to some extent in accounting for the observed non-planar strain distributions at high loads. Taken as a whole, though, the experimental evidence indicates that plane sections did not remain entirely plane at high loads. The extent of the deviation from a true planar strain distribution is not accurately known, but based on the observed strain distributions it appears the maximum deviations are on the order of 25% of the expected planar distribution.

Most observed deviations from a planar strain distribution were localized and occurred in the compression flange of the specimen. However, there is no pattern to the locations of the deviations within the flange, such as tending to occur near the center of the flange or near the edges. There also does not appear to be any

systematic relationship between the wall slenderness ratio of the compression flange and the magnitude of deviation from a planar strain distribution. This indicates that the deviations are probably not strongly related to plate bending. Rather, the deviations are more likely the result of redistributions of stresses caused by cracking in the hollow test section, or imperfect loading of the hollow test section by the cracked load head.

While the hypothesis of plane sections remaining plane appears to be true for some of the tests specimens, it is only approximately valid for the remaining specimens. Nonetheless the assumption of plane sections remaining plane is incorporated in the analytical model developed in this study, recognizing that the model may only approximately reflect the true strain distribution in the cross section.

3.4.8. Post-Tensioning Bars

The only problem observed with post-tensioning bars in the test specimen was the tendency of the bars to slip through the post-tensioning ducts in the load heads at failure. In specimen 5S9 this slipping can be attributed to the use of plastic ducts with smooth side walls. In other specimens slipping was probably the result of insufficient development length for the post-tensioning bars in compression. Failures often occurred near one end of a specimen, which left only 12 inches of development length in compression (the thickness of the solid load head).

The problem observed with post-tensioning bars in the test specimens may have a counterpart in full-size structures. Hollow segmental bridge piers are often built with solid top caps to provide a region for transfer of loads from the bridge superstructure to the hollow pier section. If the pier design is based on the ultimate strength limit state then the possibility of failure of the hollow section just below the solid pier cap should be considered. In that case the requirements for the development length in compression of the post-tensioning bars within the pier cap should be checked.

3.4.9. Reinforcement Details

The failure mode of specimen 5S9 demonstrates the importance of providing cross ties in segmental construction. The unintentional omission of cross ties near

the top of one segment in specimen 5S9 resulted in splitting of the segment wall along its center plane (Figure 3.35). Similar failures were not observed for any of the monolithic or multiple-lift specimens, although in those specimens no cross ties were missing.

In all test specimens cross ties were placed in a "checkerboard" pattern at every-other intersection of a longitudinal and lateral reinforcing bar. Additional cross ties were placed in the test specimens at likely locations of stress concentrations: at the top and bottom edges of all segments in segmental specimens; and at the top and bottom edges of monolithic and multiple-lift specimens (Figure 2.4). The cross tie spacing in the test specimens is equivalent to a spacing of about 20 to 24 inches longitudinally and 10 to 42 inches laterally in a full size structure. Cross tie spacings in recent hollow pier designs (Figure 2.2) average about 24 inches longitudinally and 24 inches laterally. Apparently it is not current design practice to provide additional cross ties at the top and bottom edges of pier segments, except at the locations of post-tensioning anchorages.

The corner reinforcement detail adopted for the test specimens was two overlapping "hairpin" bars, as shown in Figure 2.3. This detail performed well in confining the concrete at the corner regions of all specimens. It also has the advantage of ease of construction.

In the haunched regions of segmental specimens special diagonal corner ties were used. These ties incorporated a 90° hook at each end, as shown in Figure 2.3. While the 90° hook presented some minor difficulties during construction, the tie design was observed to perform well in confining the post-tensioning ducts in the corner regions of all post-tensioned specimens.

A reinforcement detail which performed poorly was the lap splices in lateral reinforcing bars on the side faces of the specimens (see for example Figures 3.29, 3.44 and 3.62). At failure the splices separated because they were not adequately confined by other reinforcement. Two improvements to this detail are possible. First, lap splices of lateral reinforcing bars in the middle of walls could be avoided altogether. Instead, lateral bars which run the full width of the wall should be used, with hooks or 90° bends at each end (see the first, third and sixth examples in Figure 2.2). This detail presents some problems with construction tolerances because the

distance between hooks or 90° bends in the reinforcing bars must be accurately controlled. Second, if lap splices must be used in lateral reinforcing bars then the splice region should be enclosed by the hooks of wall cross ties. These ties should be provided along the length of the splice wherever longitudinal bars and lateral bars intersect.

3.4.10. Reinforcement Ratio

The reinforcement ratios of the test specimens varied from 0.015 to 0.026. No systematic difference in failure mode or crack patterns were observed for specimens near the high or low ends of this range.

Reinforcement ratios for prototype piers and pylons are sometimes lower than the 0.015 lower limit of the test series (see Section 2.3.1). However, the most lightly reinforced sections generally have only a single layer of reinforcement in each wall. Sections with two layers of steel in each wall usually have reinforcement ratios of 0.01 or greater. Since all of the test specimens had two layers of reinforcement in each wall no conclusions can be drawn from the experiments about very lightly reinforced sections with only a single layer of reinforcement. It appears that if a cross section has two layers of reinforcement in each wall and the reinforcement ratio lies in the practical range of 0.01 to 0.025 then the reinforcement ratio has no discernable affect on the behavior of the cross section (except for the normally computed variations in stiffness and strength).

3.4.11. Concrete Strength

The influence of concrete strength on the specimen behavior can be determined by comparing specimens 3M14 and 4M18. The two specimens have similar geometric properties but concrete strengths of 3540 and 7700 psi, respectively.

Both specimens failed in similar ways and at similar locations (Figures 3.18 to 3.22 and 3.26 to 3.29), although the extent of crushing was greater for the lower strength specimen. The compression flange shapes before failure had similar shapes (Figures 3.23 and 3.30) but the magnitude of the bulge was greater for the lower strength specimen. More extensive longitudinal cracking prior to failure was observed in the lower strength specimen, and the onset of cracking occurred at a

lower percentage of ultimate load for the lower strength specimen.

The most pronounced difference between the specimens was in the moment-curvature behavior. As shown in Figure 3.113 the moment-curvature relationship for the lower strength specimen is nonlinear, with a slope tending toward zero at failure, while the moment curvature relationship for the higher strength specimen is nearly linear up to failure. This difference in moment-curvature behavior reflects the different shapes of the stress-strain curves for low and high strength concretes. Low strength concretes have stress-strain curves with rounded ascending branches and long, gradually sloped descending branches. This results in softening of the moment-curvature curve at high moments as high stresses and strains are reached in the cross section. On the other hand, high strength concretes have stress-strain curves with nearly linear ascending branches and short steep descending branches. This results in nearly linear moment-curvature relationships up to failure, and rupture of the cross section follows soon after a maximum stress of f'_c is reached.

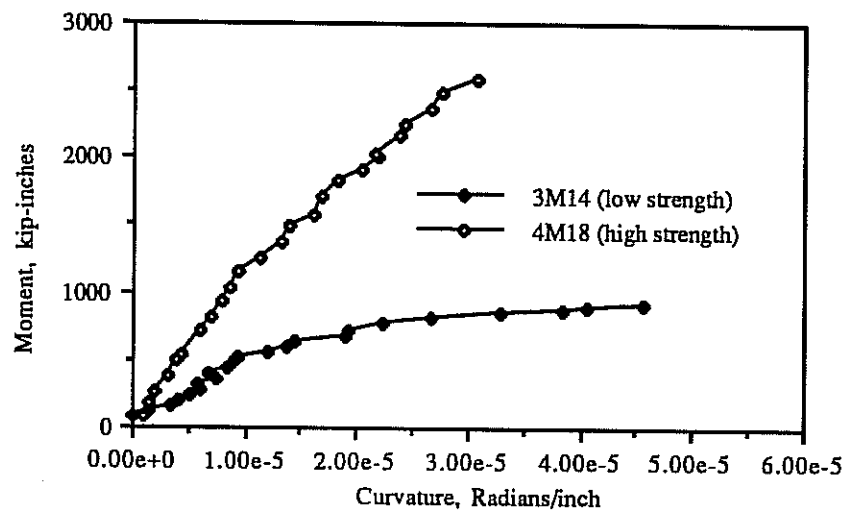


Figure 3.113: Moment-Curvature Data for Specimens 3M14 and 4M18

The greater stiffness and more linear moment-curvature behavior offered by high strength concrete sections are distinct advantages when second-order effects are considered. Bridge piers and pylons are often tall and slender, so second order deflections and moments can be significant considerations in design. While high

strength concrete may not be essential as a requirement for strength of the pier or pylon it may be helpful from the standpoint of stiffness.

3.4.12. Method of Construction

The influence of the method of construction on specimen behavior was studied by constructing three types of specimens: "monolithic" specimens, for which the entire hollow test section was cast in a single lift; "multiple-lift" specimens, which were similar to monolithic specimens except that they were cast in three lifts; and "segmental" specimens, for which three separate segments were made, epoxied together and post-tensioned. Monolithic and multiple-lift specimens are compared first, then monolithic and multiple-lift specimens are compared to segmental specimens.

The only difference observed between monolithic and multiple-lift specimens was that the water gain effect (the migration of water toward the top of the fresh concrete in vertically-cast columns) was possibly more pronounced in monolithic specimens than in multiple-lift specimens. This was determined by comparing specimens 4M18 and 10ML18, which were nearly identical except that 4M18 was constructed with a single monolithic lift and 10ML18 was constructed with multiple lifts. Specimen 4M18 failed at a load well below the expected ultimate load (calculated using the procedure described in Chapter 4), while specimen 10ML18 failed very near the expected ultimate load. This would follow from the fact that specimen 4M18 required a 72 inch tall lift and more extensive vibration of the fresh concrete than specimen 10ML18, which had only 24 inch lifts.

The experimental moment-curvature relationships for monolithic and multiple-lift specimens are shown in Figure 3.111. (Data from specimen 1M10 is not shown because the specimen was loaded at a much larger eccentricity than other specimens). No systematic differences in the moment-curvature behavior of the two types of specimens is observed.

Several pairs of specimens can be compared to determine the differences in behavior between segmental specimens and monolithic or multiple-lift specimens: 5S9 and 1M10; 4M18 and 6S16; 7S22 and 8ML25; and 12S29 and 11ML34. The observed cracking patterns for the pairs of specimens are illustrated in Sections 3.3.1

to 3.3.12. There is no apparent difference between the cracking patterns of segmental and monolithic or multiple-lift specimens. Compression flange profiles are also illustrated in Sections 3.3.1 to 3.3.12. The construction method appears to have no influence on compression flange profiles. The location of failure for each specimen is shown in Table 3.1. The only two specimens which failed near the bottom end (as cast) were segmental specimens 7S22 and 12S29; the corresponding multiple-lift specimens 8ML25 and 11ML34 failed near the top end. This indicates that the water gain effect is perhaps less pronounced for segmental construction.

Moment-curvature plots for the pairs of segmental and monolithic or multiple-lift specimens are shown in Figures 3.114 and 3.115. (Because the scale of the moment-curvature diagram of specimen 1M10 is much greater than for other specimens, the comparison between 1M10 and 5S9 is plotted separately). The extreme difference in the moment-curvature plots for specimens 1M10 and 5S9 is due to the different eccentricities at which the two specimens were tested. Both specimens had roughly the same cross section, but specimen 1M10 was tested at an eccentricity of 8.5 inches and specimen 5S9 was tested at an eccentricity of only 0.75 inches. It is interesting to note that the curvature at failure for the segmental post-tensioned specimen is much less than for the monolithic specimen. However, the large magnitude of the difference in failure curvature is probably due to the different loading eccentricities. Specimens 4M18 and 6S16 are compared in Figure 3.115. As with specimens 1M10 and 5S9 the differences in moment-curvature behavior are mainly due to the different eccentricities at which the specimens were loaded. Specimen 4M18 was loaded at an eccentricity of 2.75 inches and specimen 6S16 was loaded at an eccentricity of 1.0 inches. The curvature at failure for the post-tensioned specimen is lower, but again, this may be due to different loading eccentricities. Specimens 7S22 and 8ML25 were tested at the same eccentricity of 1.0 inch. Figure 3.115 shows that specimen 7S22, the segmental specimen, failed at a lower curvature than 8ML25. Specimens 11ML34 and 12S29 were tested at the same eccentricity of 1.0 inch. The two moment-curvature plots, shown in Figure 3.115, are almost identical. In this case the curvature at failure is higher for the segmental specimen than for the monolithic specimen. This indicates that it may not be universally true that segmental, post-tensioned hollow concrete compression

members fail at lower curvatures than monolithic hollow concrete compression members. Based on the limited experimental data presented here no definitive conclusion can be made. However, if there is any reduction in curvature at failure for segmental post-tensioned members, the reduction is probably not large enough to influence the choice of construction method (monolithic vs. segmental) for a particular hollow pier or pylon.

In summary, the experimental results indicate that there were almost no differences between the behavior of segmental, monolithic or multiple-lift specimens which could be attributed to the method of construction. The only systematic differences observed were that the single-lift monolithic specimens were more prone to fail at their top end, and that segmental post-tensioned specimens possibly fail at a somewhat lower curvature than monolithic specimens.

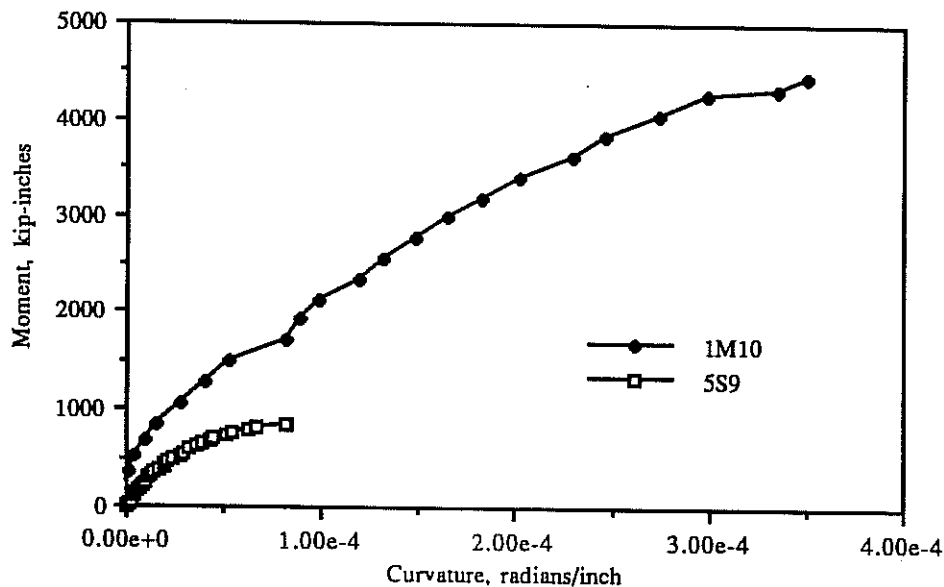


Figure 3.114: Moment-Curvature Data for Specimens 1M10 and 5S9

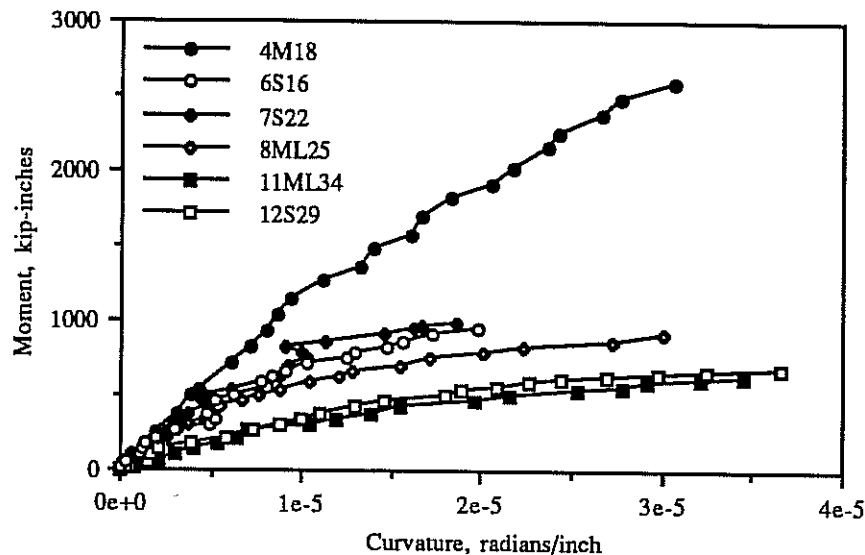


Figure 3.115: Moment-Curvature Data for Monolithic and Segmental Specimens

3.4.13. Post-Tensioning Effects

Specimens 8ML25 and 9MLP22 can be compared to investigate the effects of post-tensioning on specimen behavior (as distinct from the effects of segmental vs. monolithic construction). Specimen 8ML25 was cast in three lifts with continuous longitudinal reinforcement, and was not post-tensioned. Specimen 9MLP22 was similar to 8ML25, but it was post-tensioned. While specimen 9MLP22 does not represent realistic construction practice, as non-segmental piers and pylons are not post-tensioned, it provides a means of comparing directly a post-tensioned and a non-post-tensioned specimen which are constructed in the same way.

The figures in Sections 3.1.8 and 3.1.9 show that both specimens behaved nearly the same with respect to crack patterns, failure location and compression flange profile. The only observed difference was in the moment-curvature behavior. Figure 3.116 shows the moment-curvature data from the two specimens. The curve for specimen 9MLP22 is slightly steeper than for 8ML25 and specimen 9MLP22 failed at a lower value of curvature than 8ML25. The greater stiffness of specimen 9MLP22 is caused by the greater total area of reinforcing steel, including post-tensioning steel, in that specimen (3.42 square inches in 8ML25 and 4.52 square

inches in 9MLP22). Specimen 9MLP22 failed at a lower curvature because of the initial concrete strains imposed on 9MLP22 by post-tensioning forces. These initial strains decreased the strain range available to resist externally applied loads, so the curvature at failure was smaller than for specimen 8ML25.

This would explain the differences in moment-curvature behavior between segmental post-tensioned specimens and monolithic non-post-tensioned specimens, as discussed above in Section 3.4.12. The segmental specimens tended to fail at somewhat lower curvatures than the monolithic specimens not because of the segmental construction, but because of the post-tensioning forces required to hold the segments together.

Thus the effects of post-tensioning on test specimen behavior appear to be relatively minor. Crack patterns and failure modes were similar for specimens 8ML25 and 9MLP22. Bending stiffness may be increased slightly with post-tensioned construction because of the presence of post-tensioning bars; however, the curvature at failure may be smaller for post-tensioned construction because of the initial concrete strains imposed by post-tensioning forces.

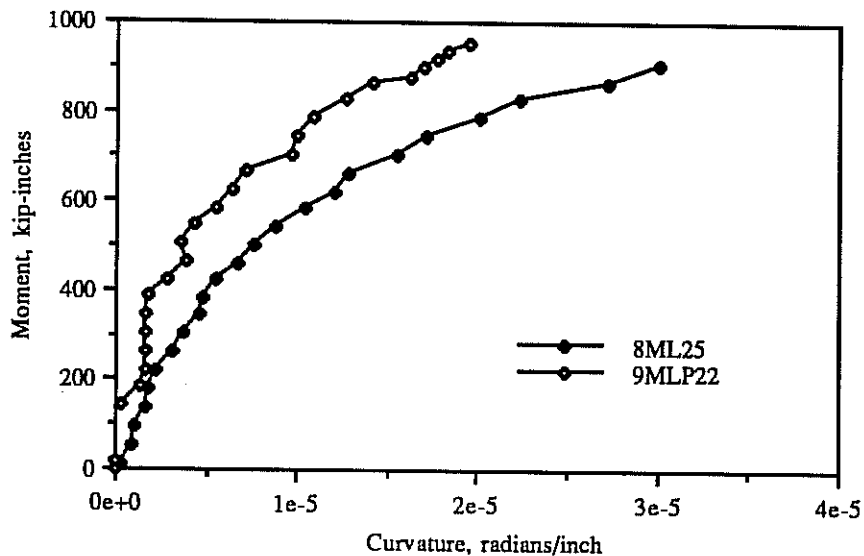


Figure 3.116: Moment-Curvature Data for Specimens 8ML25 and 9MLP22

Chapter 4

Analytical Model

4.1. Overview

As part of this study an analytical model was developed which predicts the capacity of a short, reinforced concrete column with a hollow, thin-walled rectangular cross section, subject to simultaneous axial load and uniaxial bending about the weak axis. The model has two components: a plate buckling analysis, which predicts the critical buckling stress for the thin compression flange of a cross section; and a section capacity analysis, which predicts the overall capacity of the column, including the effects of post-tensioning and local buckling of the compression flange. The model was implemented in two computer programs, PLCRST and HOLMP. The development of the analytical model is described below, and the flow charts, user's guides and source codes for the computer programs are given in Reference 141. The programs run on personal computers with a math coprocessor chip. Sample runs of the program are shown in the Appendix. Comparisons between the results of the experimental program and the analytical model are made in Chapter 5.

4.2. Notation

The following notation is used throughout this chapter.

a	= Length of plate
A_c	= Area of concrete
A_{ps}	= Area of post-tensioning steel
A_s	= Area of non-post-tensioned (discontinuous) reinforcing steel
b	= Width of plate (wide flange of rectangular cross section)
b_f	= Width of plate (narrow flange of rectangular cross section)
D	= Plate flexural rigidity per unit width (see Equation 4.2)
e	= Eccentricity of applied load
E_0	= Initial tangent modulus of elasticity of concrete
E_s	= Modulus of elasticity of steel
E_t	= Instantaneous tangent modulus of elasticity of concrete
f_c	= Concrete test cylinder peak compressive stress

f_{cr}	= Buckling stress of plate (See Equation 4.1)
f_y	= Yield stress of non-post-tensioned (discontinuous) reinforcing steel
h	= Thickness of plate
k	= Plate buckling coefficient
k_3	= Peak stress reduction factor for Hognestad constitutive model
m	= Number of longitudinal half waves in buckled plate
M	= Bending moment applied externally to the cross section
P	= Axial load applied externally to the cross section
P_0	= Axial load capacity of a concentrically loaded column
\bar{z}	= Distance of centroid of reinforcement layer from center of plate
ϵ_4	= Maximum concrete strain at extreme fiber of cross section
ϵ_{cr}	= Buckling strain of plate
ϵ_0	= Concrete test cylinder strain at peak compressive stress
ϵ_u	= Maximum attainable concrete strain in Hognestad model = 0.0038
ν	= Poisson's ratio
ρ	= Reinforcement ratio
Φ	= Curvature of column

4.3. Constitutive Models

Constitutive models are required for the three materials making up the cross section: concrete, non-post-tensioned reinforcing steel and post-tensioning steel. The constitutive relationships adopted for the plate buckling and section capacity analytical models are described below.

4.3.1. Concrete Constitutive Model

Four formulations of the uniaxial compression stress-strain curve for concrete were investigated for use in the analytical model. The most well-known of these curves is the one developed by Hognestad^{96,97,98,99}. The Hognestad curve consists of a parabolic ascending branch and a linear descending branch, as shown in Figure 4.1. The other three constitutive models, by Wang et al.¹⁰⁰, Carreira and Chu¹⁰¹, and Desayi and Krishnan¹⁰² incorporate more complex curves or combinations of curves to represent the stress-strain behavior of concrete.

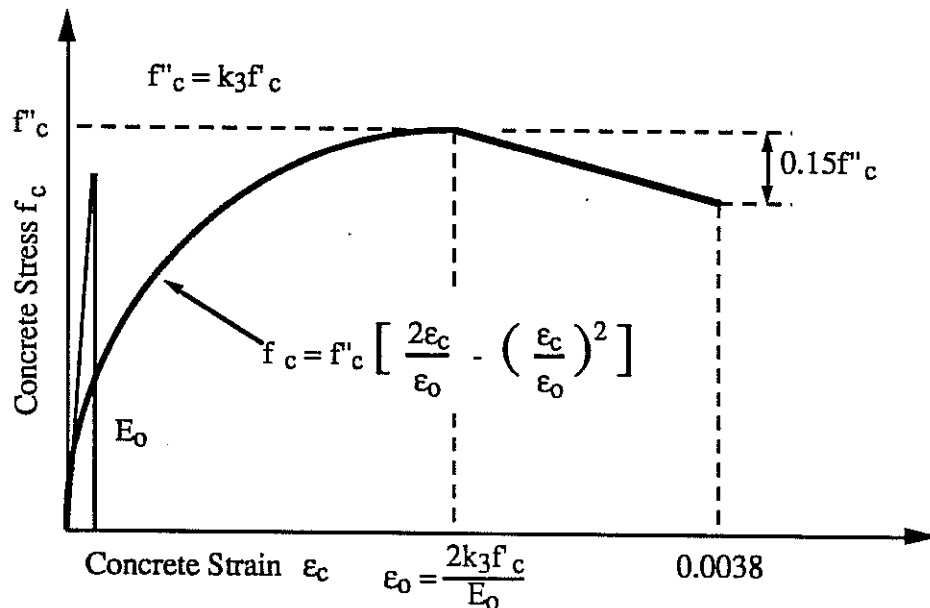


Figure 4.1: Hognestad Constitutive Model

As described in Section 2.4.1.5 experimental stress-strain curves were obtained from cylinders made from the same concrete as the hollow pier specimens. The four constitutive models were compared with the experimental stress-strain curves. It was found that the model which matched the experimental stress-strain curves most consistently, particularly on the ascending branch of the curve, was the Hognestad formulation. In some cases the other three constitutive models matched the descending branch of the experimental stress-strain curve better than the Hognestad model; however at the same time these models often over- or under-estimated the initial stiffness of the ascending branch. Since it was felt that it is more important to accurately model the ascending branch of the stress-strain curve than the descending branch, and since the Hognestad curve provided an excellent match to the ascending branch as well as a fairly good match to the descending branch, the Hognestad model was chosen for use in this study. In Figure 2.13 the Hognestad stress-strain curve is compared to each of the experimental stress-strain curves. It can be seen that the Hognestad model is a good predictor of the experimental stress-strain behavior.

To further verify the adequacy of the Hognestad model the interaction diagrams for several hollow pier specimens were computed using the analytical method

described in this chapter. The specimens were analyzed using both the Hognestad constitutive model and the more complicated constitutive model developed by Wang et. al.¹⁰⁰. The chief merit of the Wang model is that it is a better predictor of the descending branch of the stress-strain curve. However because of its complexity it requires greater computational time. It was found that there was very little difference between the column interaction diagrams obtained using the Hognestad and Wang models - on the order of 1 or 2%. Thus the complex Wang model was not found to offer any advantage over the simple Hognestad model.

The Hognestad constitutive model requires only two input parameters: peak stress, f'_c ; and a peak stress reduction factor, k_3 . The peak stress reduction factor accounts for several factors, chiefly the casting position of the member, and is discussed further in Section 5.2. The value of E_o was computed from the following formula.

$$E_o = 1 \times 10^6 + 40,000\sqrt{f'_c} \quad (f'_c \text{ and } E_o \text{ in psi}).$$

This formula has been shown¹⁰³ to be a better predictor of E_o over a wider range of concrete strengths than the more familiar formula of Pauw¹⁰⁴:

$$E_o = 57,000\sqrt{f'_c} \quad (f'_c \text{ and } E_o \text{ in psi}).$$

In the Hognestad model the strain at peak stress, ϵ_o , is related to f'_c and E_o by the equation

$$\epsilon_o = \frac{2k_3f'_c}{E_o}$$

The value of ultimate strain, ϵ_u , was taken as 0.0038, as suggested by Hognestad.

4.3.2. *Non-Post-Tensioned Reinforcing Steel Constitutive Model*

The stress-strain curve of the longitudinal reinforcing bars was assumed to be elastic-perfectly plastic. This agrees well with the observed stress-strain behavior of

the bars (Figure 2.14), except that strain hardening after yield is conservatively neglected. Based on the bar tension tests performed, the yield stress of the steel, f_y , was taken as 75.1 ksi, and the modulus of elasticity 29,000 ksi.

4.3.3. *Post-Tensioned Steel Constitutive Model*

The post-tensioning bars were assumed to behave elastically up to a yield stress of 138 ksi (123 ksi for the 1 inch diameter bars). After yielding the bars were assumed to behave plastically, which conservatively neglects strain hardening effects. The modulus of elasticity of the bars was taken as 29,000 ksi.

4.4. Plate Buckling Model

4.4.1. *Calculation of Buckling Stress*

The compression flange of the hollow cross section is treated as a thin, rectangular plate subjected to uniformly distributed loads along two edges, as shown in Figure 4.2.

The two short edges of the plate are shown as simply supported, even though there is some rotational restraint provided along the short edges of the compression flange in the hollow pier test specimens. The simply supported boundary condition was chosen for two reasons. First, neglecting the rotational restraint along the short edges is a conservative assumption, since the buckling load of a rectangular plate with simply-supported short edges is less than that of a plate with restrained short edges. Since the degree of rotational restraint is unknown for the short edges of the compression flanges (because of load head rotations and distortions) the conservative assumption of simply supported edges was adopted. Second, the difference in buckling stress between the case of simply supported short edges and built-in short edges is small. Figure 4.4 illustrates the buckling coefficients, k , (which are proportional to the buckling stresses) for elastic plates with various combinations of boundary conditions and length-to-width ratios, a/b . The two boundary conditions of interest in the present study are cases 1 and 3 in Figure 4.4. It can be seen that for plates with a/b greater than about 2 the difference in buckling stress between the cases of fixed and simply supported short edges is less than 15%. For values of a/b greater

than about 5 the difference becomes negligible. Although the information shown in Figure 4.3 is for linear elastic plates, similar results can be expected for nonlinear plates.

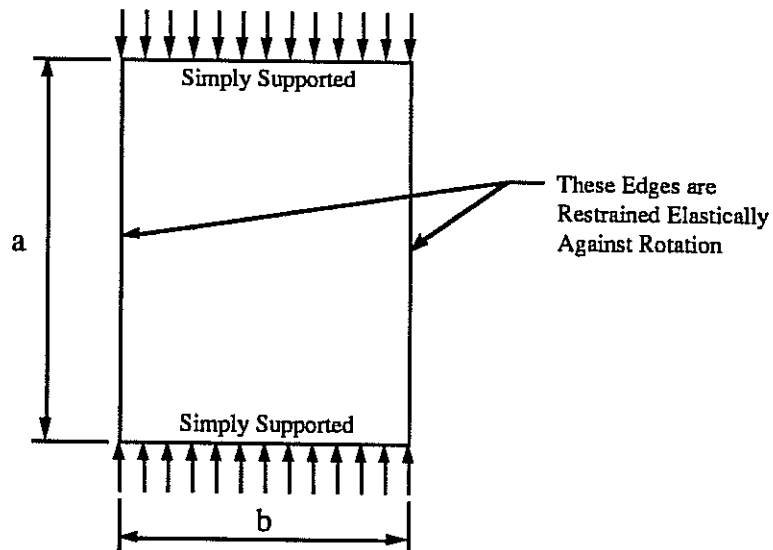


Figure 4.2: Compression Flange of Hollow Rectangular Cross Section

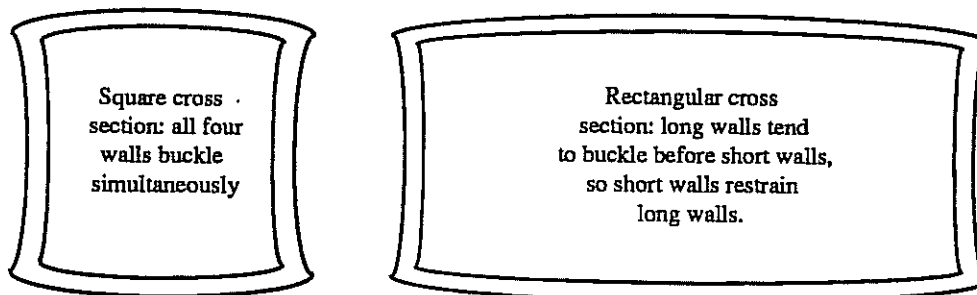


Figure 4.3: Local Wall Buckling in a Square and Rectangular Cross Section

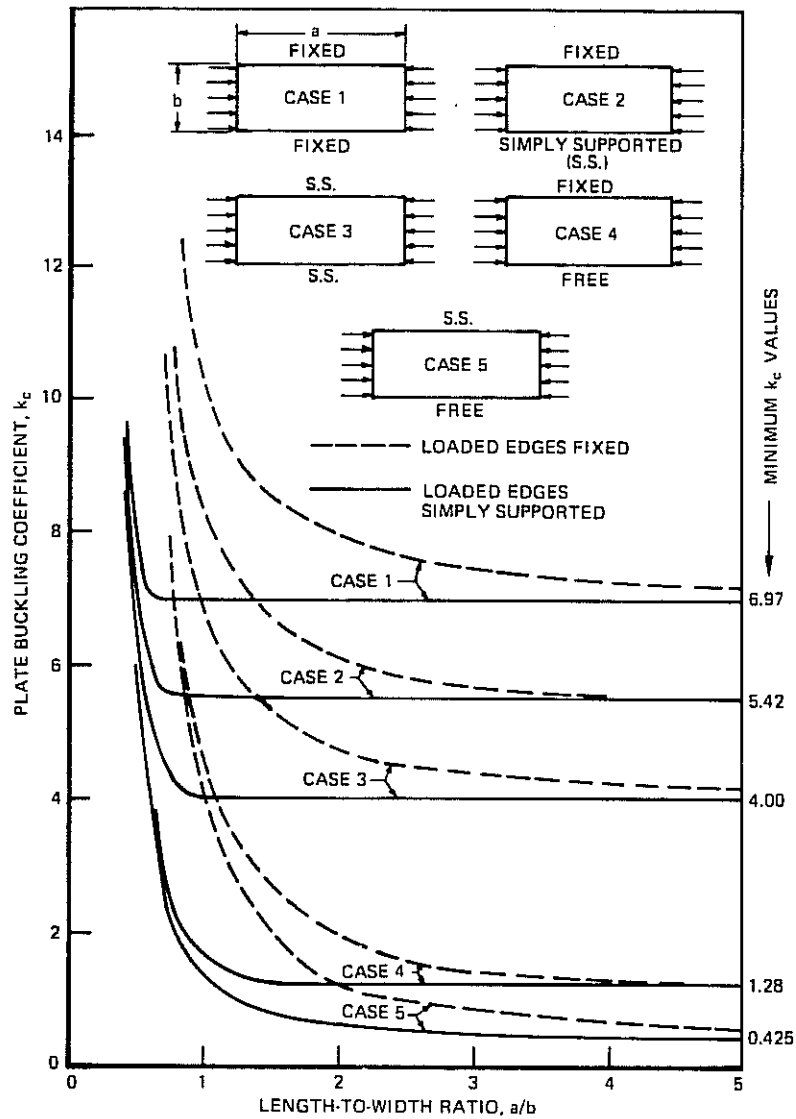


Figure 4.4: Buckling Coefficients, k_c , for Various Boundary Conditions¹⁰⁵

The two long edges of the compression flange of the cross section are shown in Figure 4.2 as being elastically restrained against rotation. The degree of rotational restraint depends on the relative plate bending stiffnesses of the four walls of the cross section. If the cross section is square and loaded concentrically, then all four plates of the cross section will buckle at the same load, as illustrated in Figure 4.3. The boundary conditions along the long edges of each of the four plates will be

simply supported, since none of the plates acts to restrain rotation of the edges of adjacent plates. However, if the cross section is rectangular then the wide plates will tend to buckle at a lower load than the narrow plates, as shown in Figure 4.3. The narrow plates will restrain rotation of the edges of the wide plates, increasing the buckling load of the wide plates.

In classical elastic plate buckling theory¹⁰⁶ the length-to-width ratio a/b and boundary conditions of the plate are taken into account by a single buckling coefficient, k . The critical buckling stress, f_{cr} , of a plate according to this theory is

$$f_{cr} = \frac{k\pi^2 D}{hb^2} \quad (\text{Eqn. 4.1})$$

where

$$D = \frac{E_0 h^3}{12(1 - \nu^2)} \quad (\text{Eqn. 4.2})$$

and

b = Plate width

h = Plate thickness

E_0 = Modulus of elasticity

ν = Poisson's ratio.

In an earlier phase of this study⁴⁶ the buckling coefficient k was derived for a plate with the boundary conditions shown in Figure 4.2. Similar results were obtained by Stowel et al.^{13,14,15,16}, who presented their findings in tabular form. The derivation of k is complicated by the fact that the side flanges of the cross section, which provide the rotational restraint to the long edges of the compression flange, are themselves subject to in-plane stresses. The more highly stressed the side flanges are, the less rotational restraint they are able to provide to the compression flange. Therefore, the compression flange cannot be treated simply as an isolated plate with rotational springs of constant stiffness along its long edges, but must be treated as part of an assembly of plates, all subject to in-plane stresses. For a concentrically loaded rectangular section with all walls of equal thickness the buckling coefficient of a wide flange was found to be given by the transcendental equation

$$\begin{aligned}
& 2\alpha\beta (1 - \cos\beta b \cosh\alpha b) + (\alpha^2 - \beta^2) \sin\beta b \sinh\alpha b = \\
& -\frac{1}{r^2} (\alpha^2 + \beta^2)^2 \sin\beta b \sinh\alpha b + 2\frac{\beta}{r} (\alpha^2 + \beta^2) \cos\beta b \sinh\alpha b \\
& - 2\frac{\alpha}{r} (\alpha^2 + \beta^2) \sin\beta b \cosh\alpha b \quad \text{(Eqn. 4.3)}
\end{aligned}$$

where
$$\alpha = \sqrt{\frac{m^2\pi^2}{a^2} + \sqrt{k \frac{m^2\pi^4}{a^2b^2}}}$$

and
$$\beta = \sqrt{-\frac{m^2\pi^2}{a^2} + \sqrt{k \frac{m^2\pi^4}{a^2b^2}}}$$

m = Number of longitudinal half-waves in the buckled flange

a = Plate length

b = Width of wide flange in cross section

$$r = 4 \frac{S_f^{\text{II}}}{(D/b)_f} \frac{1}{(1+C)} \frac{1}{b_f}$$

b_f = Width of narrow flange (side face) of cross section

$$\frac{S_f^{\text{II}}}{(D/b)_f} = \frac{\left(\frac{\alpha b}{2}\right)^2 + \left(\frac{\beta b}{2}\right)^2}{\frac{\alpha b}{2} \tanh \frac{\alpha b}{2} + \frac{\beta b}{2} \tan \frac{\beta b}{2} + \frac{\alpha b}{2} \coth \frac{\alpha b}{2} - \frac{\beta b}{2} \cot \frac{\beta b}{2}}$$

$$C = \frac{\left(\frac{\alpha b}{2} \tanh \frac{\alpha b}{2} + \frac{\beta b}{2} \tan \frac{\beta b}{2}\right) - \left(\frac{\alpha b}{2} \coth \frac{\alpha b}{2} - \frac{\beta b}{2} \cot \frac{\beta b}{2}\right)}{\frac{\alpha b}{2} \tanh \frac{\alpha b}{2} + \frac{\beta b}{2} \tan \frac{\beta b}{2} + \frac{\alpha b}{2} \coth \frac{\alpha b}{2} - \frac{\beta b}{2} \cot \frac{\beta b}{2}}$$

The expressions for $\frac{S_f^{\text{II}}}{(D/b)_f}$ and C are evaluated for the narrow flange (side face) of the cross section.

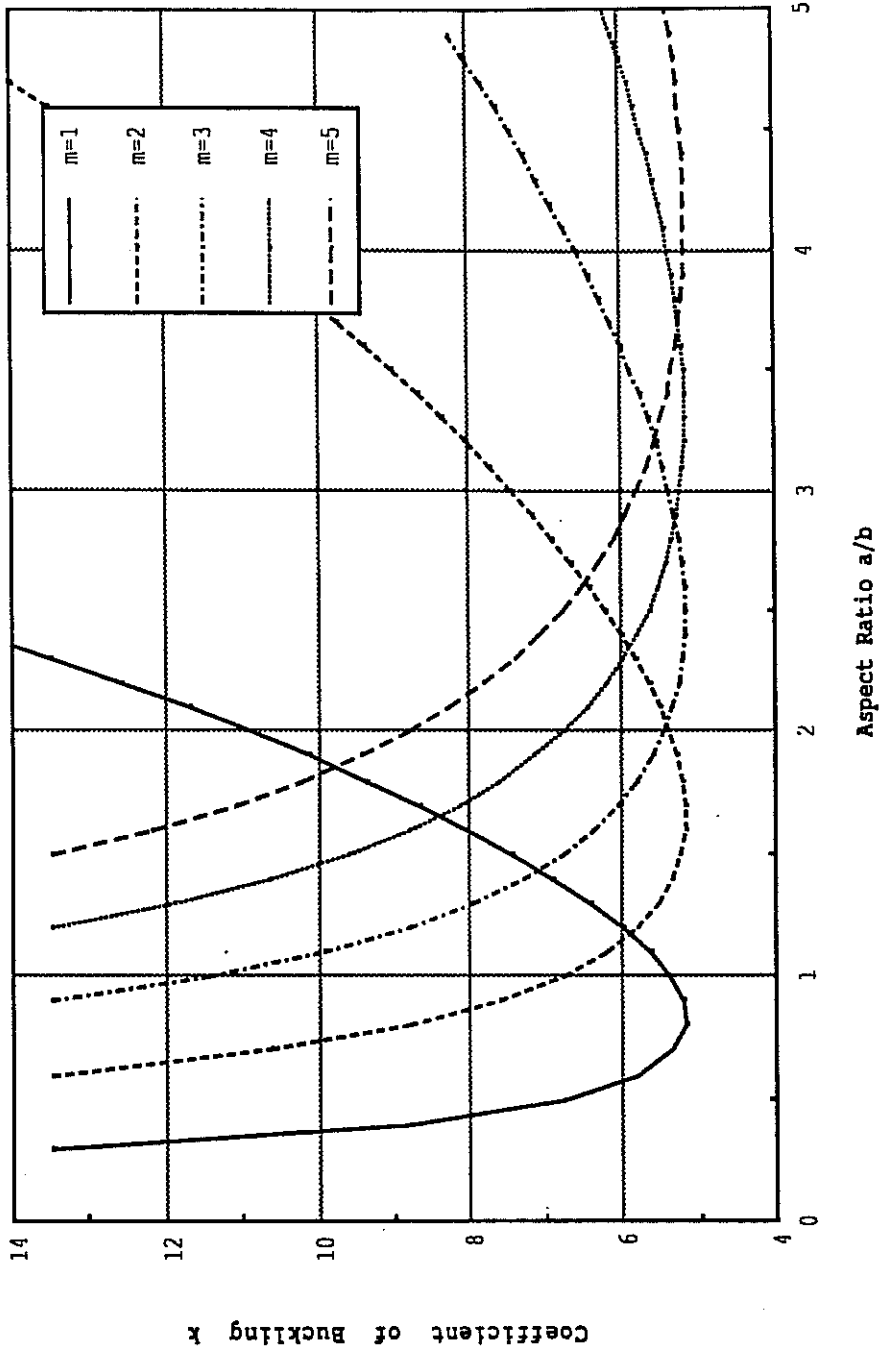


Figure 4.5: Typical Family of Curves Defining k and m for Plate With Long Edges Elastically Restrained Against Rotation (From Ref. 46)

Equation 4.3 must be solved iteratively for k , given fixed values of a/b , b_f/b and m . A family of curves can be generated for a range of integral values of m and a fixed value of b_f/b , giving k as a function of a/b . An example of such a family of curves is illustrated in Figure 4.5⁴⁶. For a fixed value of a/b the curve giving the lowest value of k determines the buckling coefficient and number of half waves for the wide flange of the cross section. Once the buckling coefficient is established, the buckling stress of the wide flange can be computed by Equation 4.1.

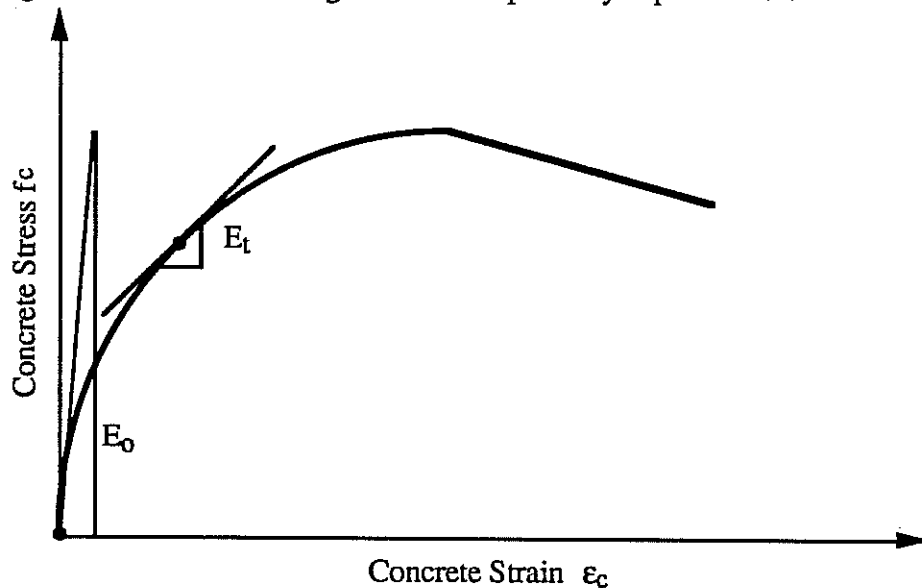


Figure 4.6: Definitions of Initial and Tangent Concrete Moduli

Two modifications must be made to the elastic buckling theory described above in order to adapt the theory for use with reinforced concrete plates: material nonlinearities must be taken into account, and the influence of reinforcement on the bending stiffness of the plate must be considered.

As discussed in Section 1.6.3, material nonlinearities of the concrete can be approximately accounted for in the analysis by substituting the instantaneous tangent modulus of the concrete, E_t , for the constant initial tangent modulus E_0 (Figure 4.6). While other, more rigorous, treatments of inelastic plate buckling are available¹⁴⁰, the relatively simple tangent modulus approach has been shown by others^{33,34,35,36,37} to adequately model the buckling behavior of thin concrete plates.

The presence of reinforcing steel can be accounted for approximately by

modifying the flexural rigidity of the plate. The flexural rigidity term in the plate buckling model, D , is given by Equation 4.2. This term can be expanded to include the contribution of reinforcing steel.

$$D = D_c + D_s \quad (\text{Eqn. 4.4})$$

D_c is given by Equation 4.2 with the constant modulus E_o replaced by the instantaneous tangent concrete modulus E_t . D_s can be derived by considering a unit width strip of plate. If the strip contains two layers of reinforcement, then

$$\begin{aligned} D_s &= E_s I_s && (\text{Eqn. 4.5}) \\ &\approx E_s (A_{s1} \bar{z}_1^2 + A_{s2} \bar{z}_2^2) \\ &= E_s h (\rho_{s1} \bar{z}_1^2 + \rho_{s2} \bar{z}_2^2) \end{aligned}$$

- where
- E_s = Modulus of elasticity of steel
 - A_{si} = Area of steel in layer i per unit width of plate
 - \bar{z}_i = Distance of centroid of layer i from center plane of plate
 - ρ_{si} = Reinforcement ratio of each layer per unit width of plate
 - h = Plate thickness.

If two identical layers of reinforcement are located equal distances from the center plane of the plate, then

$$D_s = E_s \rho_s h \bar{z}^2$$

- where
- ρ_s = Total reinforcement ratio per unit width of the plate
 - \bar{z} = Distance of the centroid of each steel layer from the center plane of the plate.

The term D_s is only necessary when the steel is stressed in the elastic range. Once the steel has yielded $E_s = 0$ so $D_s = 0$.

4.4.2. Plate Buckling in an Eccentrically Loaded Cross Section

It should be noted that the plate buckling coefficient, k , was derived assuming the plate is part of a rectangular cross section which is loaded concentrically. If the cross section is loaded eccentrically then the boundary conditions on the compression

flange (the flange with the greatest tendency to buckle) change because the states of stress in the other three plates of the cross section are different. Fortunately the concentric loading case is the most conservative case to consider when predicting the critical buckling stress of the compression flange. Suppose a load P_1 is applied concentrically to a rectangular cross section, inducing a uniform compressive stress σ_1 in all four of the plates making up the cross section. Furthermore, suppose that σ_1 is just large enough to induce buckling of the compression flange of the cross section (and the "tension" flange in this case, since all flanges are stressed equally). Now suppose a load P_2 is applied eccentrically which is less than P_1 , but induces the same stress σ_1 in the compression flange. In this case the compression flange will not buckle at the stress of σ_1 because the other three flanges of the cross section are carrying a lower level of stress than when the concentric load P_1 was applied. At a lower level of stress the three flanges are further from their own buckling loads so they are better able to restrain the edges of the compression flange against rotation, and prevent buckling. Furthermore, when an eccentric load is applied the stress distributions in the two side flanges are no longer uniform, but vary linearly across the width of the flanges. This introduces a new class of buckled shape with buckling coefficients higher than the case of uniformly distributed stress¹⁰⁷. Thus the compression flange buckling stress derived for the case of a concentrically loaded column provides a lower bound on the compression flange buckling stress for eccentrically loaded columns.

4.4.3. *Verification of Plate Buckling Model*

The plate buckling model described above was verified in an earlier part of the study⁴⁶ by comparing the results of the model with the results from tests on slender, simply-supported concrete plates performed by Swartz^{35,36,37} and by Ernst^{33,34}. (These are the best available sets of experimental data for verifying the plate buckling model, as explained in Section 1.6.3).

The results of the analytical model are compared with the test results of Swartz in Figure 4.7. The analytical model gives a conservative prediction of the experimental failure stress in almost every case, with the prediction becoming more conservative at higher wall slenderness ratios. One reason that the theoretical predictions tend to be

conservative is that perfect, simply supported boundary conditions are assumed in the analytical model. In the tests such ideal edge conditions cannot be achieved, so some rotational edge restraint is provided, increasing the failure stress. The thinner plates in the test series are probably more sensitive to unintentional edge rotational restraint. This is why the theoretical failure stresses become more conservative at higher wall slenderness ratios. Since it is not possible to quantify the degree of edge rotational restraint provided in the tests, a precise comparison between the analytical model and test results cannot be made. However, it appears that in general the analytical model provides a good prediction of the test results obtained by Swartz.

The agreement between the analytical model and the test results of Ernst do not, at first, appear to be very good, as shown by the solid circles in Figure 4.8. The solid circles represent the ratio of the average experimental failure stress (the failure load divided by the cross-sectional area of the plate) to the calculated failure stress. It can be seen that the theory apparently gives non-conservative predictions of the failure stress in almost all cases. Ernst measured strains on the surfaces of the plates he tested. He found that there were large strain gradients through the thickness of the plates, and attributed the strain gradients to nonuniformity of the applied load and to accidental eccentricities. Since the plates tested were very thin (0.5 to 1.5 inches) it is possible that if the buckling stress was reached locally on one surface of the plate then the plate would fail. In Figure 4.8 the open circles represent the maximum observed experimental stress on either surface of the plate divided by the theoretical buckling stress. It can be seen that in this case the agreement between theory and experiment is fairly good, with the theory giving generally conservative predictions.

This finding, that the maximum stress in the plate, rather than the average stress, may determine the buckling load, is significant from the point of view of development of the overall section capacity model. When the hollow rectangular column section is subject to overall bending a strain gradient is set up through the depth of the cross section, inducing a local strain gradient with the same slope through the thickness of the compression flange (Figure 4.9). Thus, when checking for local buckling of the compression flange the maximum extreme fiber strain (ϵ_4 in Figure 4.9), rather than the average strain in the flange, should be compared with the computed buckling strain of the flange.

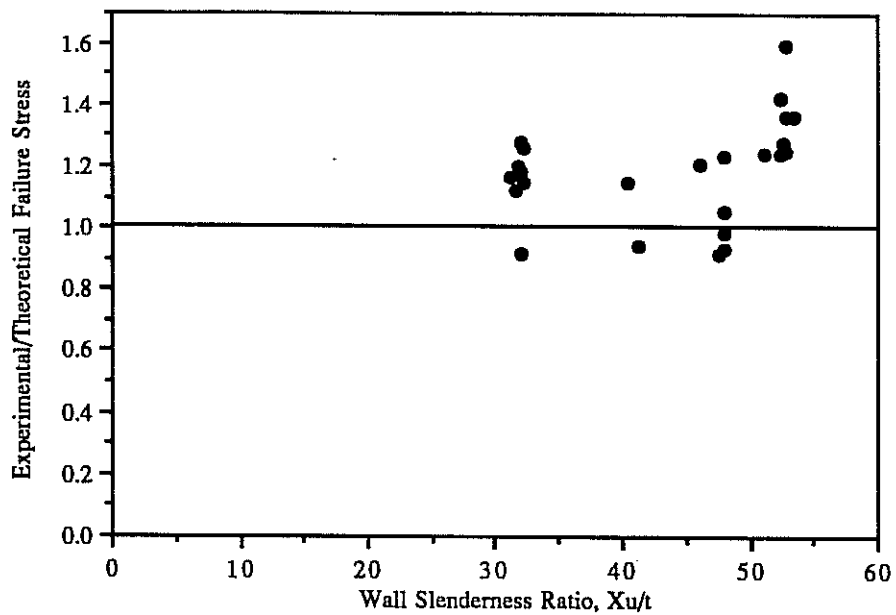


Figure 4.7: Comparison of Plate Buckling Model With Experiments of Swartz

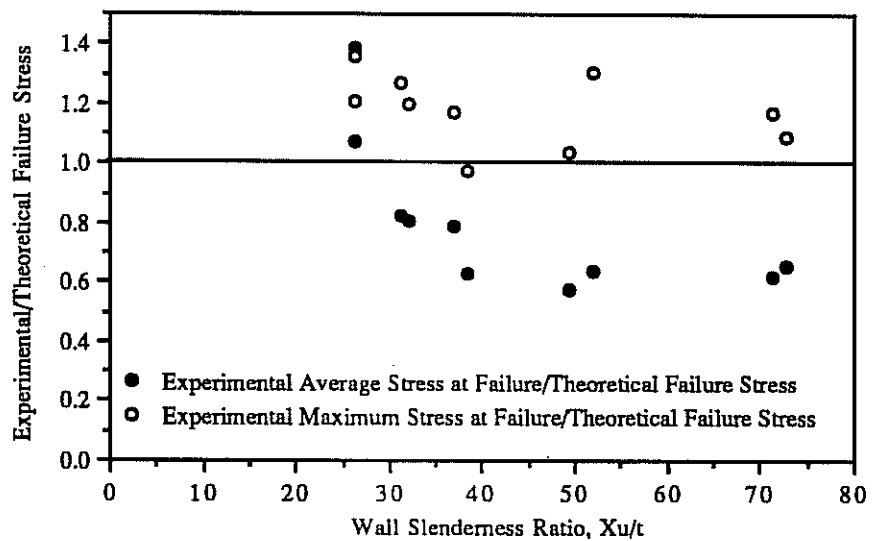


Figure 4.8: Comparison of Plate Buckling Model With Experiments of Ernst

4.4.4. *Computer Program PLCRST*

The plate buckling model described above has been implemented in a computer program called PLCRST⁴⁶. The flow chart for the program, a user's guide and the source code are given in Reference 141. The buckling stress obtained from PLCRST is used as part of the input data for a separate program HOLMP, described below. HOLMP computes the axial load-moment interaction diagram for a hollow rectangular section, and includes the effects of local compression flange buckling.

4.5. *Section Capacity Model*

An analytical model was developed to calculate the strength of a short reinforced concrete column with hollow rectangular cross section subject to simultaneous axial load and uniaxial bending moment about the weak axis. The model allows for the presence of post-tensioning tendons grouted inside ducts running within the walls of the cross section. The cross section capacity may be limited by material failure or by local buckling of the compression flange. Overall, or Euler, buckling of tall, slender columns is not considered, although the interaction between local flange buckling and overall column buckling is discussed in Section 5.5.2. All four walls of the cross section must have the same thickness.

4.5.1. *Computing P and M for a Given Strain Distribution*

A fundamental assumption of the section capacity model is that cross sections which are plane before the column is loaded remain plane after loading (the Bernoulli-Navier hypothesis). A typical planar strain distribution is shown in Figure 4.9. Given any such planar distribution the axial load and bending moment acting on the cross section can be computed by numerical integration. The cross section is divided into a number of strips parallel to the axis of bending. Each strip may contain an area of concrete A_{ci} , an area of non-post-tensioned reinforcing steel A_{si} , and an area of post-tensioning steel A_{psi} . Knowing the strain distribution over the cross section the stress at the centroid of each area A_{ci} , A_{si} and A_{psi} can be computed. Axial load is then computed by summing the products of all stresses times related areas. Bending moment is computed by summing the product of stress times area times distance to the centroid of the cross section for each element of the cross section. If the section

is post-tensioned then the initial strains induced by post-tensioning forces must be added to the planar strain distribution induced by external loads before stresses are computed.

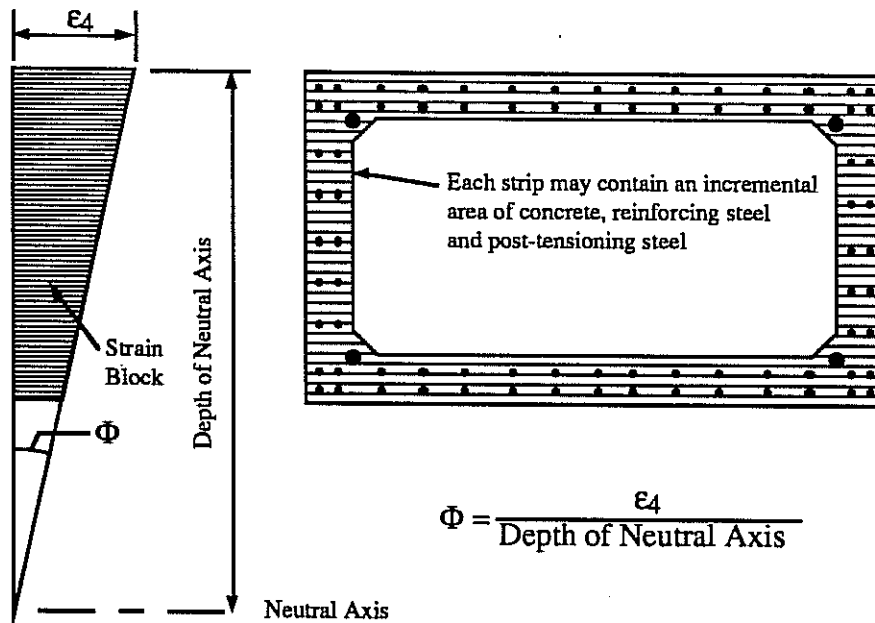


Figure 4.9: Cross Section Strain Distribution

4.5.2. Computing the Axial Load - Moment Interaction Diagram

The following procedure is used to obtain the axial load-moment interaction diagram for the ultimate strength of a given column, shown in Figure 4.10.

A value of ultimate axial load P is first selected. It is desired to compute the corresponding value of ultimate bending moment, M , lying on the interaction diagram. (The value of P is, of course, between zero and P_0 , the axial capacity of the concentrically loaded column). Figure 4.9 illustrates that when the strain distribution over the cross section is planar, M is a function of two variables: the curvature of the cross section, Φ , and the concrete strain at the extreme fiber of the cross section, ϵ_4 .

Examining Figure 4.9 it appears that many orientations of the planar strain distribution which correspond to the assumed axial load P are possible. That is, there are many possible values of Φ and ϵ_4 corresponding to P , so no unique value of M is determined. However, Breen¹⁰⁸ has shown that for any given pair of values of P

and Φ there exists a unique value of ϵ_4 . Thus, for any given load P , a range of values of Φ may be assumed and the corresponding unique values of ϵ_4 computed. This is accomplished by iterating on ϵ_4 until the calculated value of P agrees with the assumed value of P . Then, since Φ and ϵ_4 determine M , the value of M corresponding to each unique P - Φ - ϵ_4 set can be computed. The result is a series of unique sets of P , Φ , ϵ_4 and M .

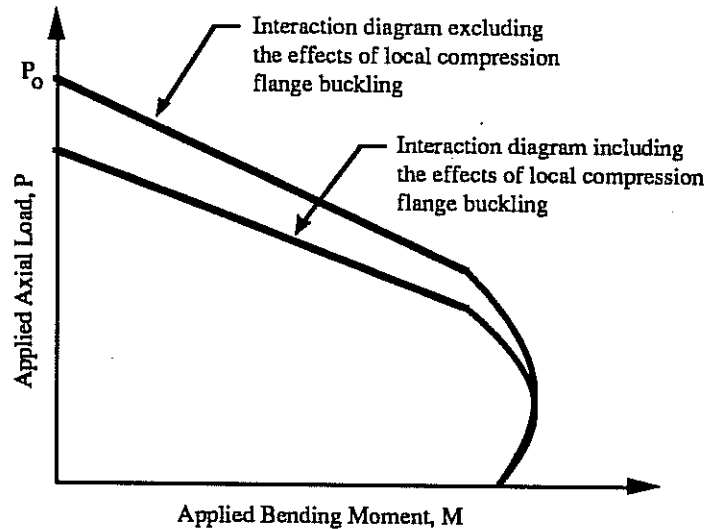


Figure 4.10: Typical Interaction Diagram

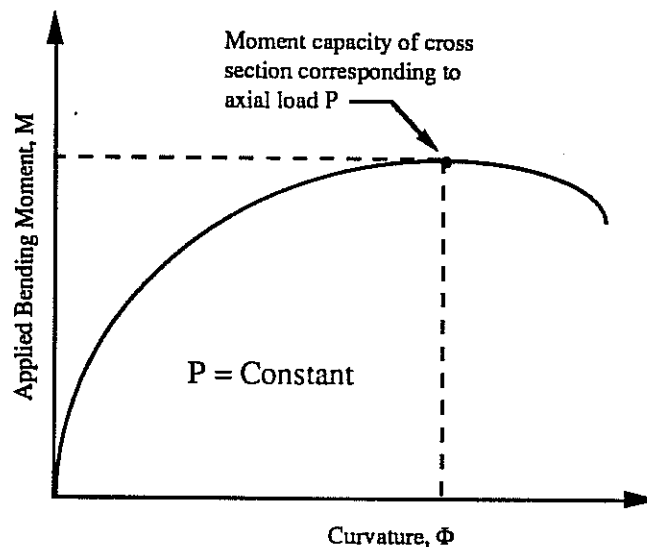


Figure 4.11: Typical Moment-Curvature Diagram for Constant P

The next step is to construct a curve of moment vs. curvature for the assumed value of P (Figure 4.11). Fowler¹⁰⁹ has demonstrated that the maximum value of M on this curve corresponds to the moment capacity of the cross section subject to the axial load P . The pair of values of M and P determined in this way represents just one point on the column interaction diagram. The entire interaction diagram can be constructed by repeating the above procedure for assumed values of P varying over the range 0 to P_0 .

The possibility of local buckling of the compression flange of the cross section can also be included in the analysis. When iterating on ϵ_4 , strains no larger than the buckling strain of the compression flange, ϵ_{cr} , are permitted. When the moment-curvature curve (for a constant value of P) is searched for the maximum value of M , the value of ϵ_4 corresponding to maximum M is also checked. If it is found that the value of ϵ_4 is less than ϵ_{cr} , then the strength of the cross section is determined by material failure rather than local buckling; if ϵ_4 equals ϵ_{cr} , then the strength of the cross section is determined by local buckling of the compression flange. The lower curve in Figure 4.10 illustrates the typical effect of local compression flange buckling on the shape of the interaction diagram.

4.5.3. Computer Program HOLMP

The above procedure has been implemented in a computer program called HOLMP. The flow chart for the program, a user's guide and the source code are given in Reference 141. One value required for the input data of HOLMP is the buckling stress of the compression flange of the cross section. This can be obtained from the program PLCRST, described in Section 4.4. For a given cross section HOLMP computes two interaction diagrams: one including and one excluding the effects of local buckling of the compression flange (Figure 4.10). In this way the influence of local wall buckling on the strength of the column can be studied.

Chapter 5

Model Verification and Design Recommendations

5.1. Overview

In order to verify the analytical model developed in this study the model was used to generate predictions of the results of laboratory tests on concrete compression members with hollow rectangular cross sections. The available body of experimental data is described in Section 1.6.2. Besides the present study, apparently only three other test programs on hollow rectangular columns have been performed. Jobse and Moustafa^{27,28} tested two segmental box columns with wall slenderness ratio of 32 in combined compression and uniaxial bending. Poston et al.²⁶ performed combined compression and biaxial bending tests on single- and multiple-cell hollow columns with maximum wall slenderness ratio of 7.6. Procter²⁵ tested small-scale concentrically loaded stub columns with maximum wall slenderness ratio of 7.5.

The plate buckling model developed in this study, as implemented in the program PLCRST, is used to determine the critical buckling stresses of the most slender wall in all the hollow cross sections of the test specimens described above. The value of critical buckling stress is then used as part of the input data for the program HOLMP, which computes the capacity of the cross section, taking wall slenderness effects into account.

Based on the the experimental and analytical results obtained in this study recommendations for the design of hollow concrete compression members with slender walls can be made. These recommendations are presented and discussed in the last portion of this chapter.

5.2. Input Data for Analytical Model

Most input parameters for the plate buckling and section capacity models developed in this study are well defined. For example, the geometry of the cross section and the material properties of the non-post-tensioned and post-tensioned reinforcement are known fairly accurately. However, there are four parameters which are less certain or open to interpretation: the value of concrete compressive strength, f'_c ; the value of the peak stress reduction factor in the concrete constitutive

model, k_3 ; the value of the maximum or limiting extreme fiber concrete compressive strain to be used in design; and the area of non-post-tensioned, discontinuous, reinforcement which should be considered in the analysis of segmentally constructed members. For the purposes of this study the general approach taken in choosing values for these four parameters was that the parameters should reflect the assumptions normally made in design practice. In this way the observed strengths of the specimens could be compared with the strengths that would normally be calculated by a designer, and suggestions could be made for improvements in design practice. Each of the four parameters and its range of possible values is discussed below.

Concrete compressive strength, f_c , is usually determined in the United States by performing compression tests on 6 inch diameter by 12 inch long concrete cylinders. The methods of fabrication and testing concrete cylinders are specified in the American Society for Testing and Materials standards C192¹¹⁰ and C39¹¹¹. It is generally assumed that the concrete compressive strengths obtained from such cylinder tests are representative of the strength of concrete in structural members. However, there may be significant differences between the state of stress in a concrete test cylinder and the state of stress in a structural member due to differences in confining stresses, strain gradients, the presence of reinforcing steel, and rate of loading.

Fortunately, from the point of view of the analysis of hollow concrete compression members, the state of stress in a concrete compression strength test cylinder is similar to the state of stress in the wall of a hollow concrete compression member. Generally a uniaxial state of stress exists in both the test cylinder (except in the regions near the end caps) and the wall of a hollow compression member. There is no strain gradient through the thickness of a concrete test cylinder and strain gradients through the walls of hollow sections are generally small. Test cylinders contain no reinforcing steel, while the walls of hollow concrete sections are only lightly reinforced, usually containing 0.5% to 2% steel in the cross section.

Perhaps the main difference between concrete test cylinders and the walls of hollow concrete compression members is the rate of loading. To explore this difference two types of cylinder tests were performed in the test program of this

study: a standard "fast" cylinder test, taking 1.5 to 3.5 minutes to load from zero stress to peak stress; and a "slow" cylinder test, taking from 18 to 56 minutes to load from zero stress to peak stress (see Section 2.4.1.5 and Table 2.2). The compressive strengths from the "slow" tests were found to average 6% lower than the compressive strengths of the "fast" tests. The time from zero load to failure of the hollow pier specimens was between 71 and 202 minutes (Table 3.1), so the "slow" cylinder tests were probably more representative of the concrete compressive strength in the hollow pier specimens than the "fast" cylinder tests. Nonetheless, the standard "fast" cylinder test compressive strengths were used in analyzing the test specimens for two reasons: first, the intention of the analysis was to reflect standard design practice, and it is standard practice to use cylinder strengths from such "fast" tests; and second, the presence of about 1.5% reinforcement in the walls of most hollow concrete sections and the small amount of confinement this reinforcement provides tend to offset the reduction in concrete compressive strength caused by the slower rate of loading of hollow concrete sections.

The peak stress reduction factor, k_3 , in the Hognestad concrete constitutive model (Section 4.3.1) was originally intended to account for observed differences between concrete cylinder strength, f'_c and the apparent concrete compressive strength, f''_c , which was back-calculated from tests on various types of concrete members¹¹².

$$f''_c = k_3 f'_c$$

For both flexural and compression members Hognestad suggested a value of $k_3 = 0.85$. This value appears to have been derived from a combination of empirical evidence and a general consensus of professional opinion. Later work by Petersons¹¹³ and by Fowler¹¹⁴ provided a more rational basis for $k_3 = 0.85$ for columns. It was found by both authors that the strength of vertically-cast columns decreases near the top of the column due to the upward migration of water in the fresh concrete. By taking core samples at various heights of columns Petersons found that near the top of vertically-cast columns k_3 varied between 0.73 and 0.99, with an average value of 0.87. Based on tests of both vertically- and horizontally-cast columns, Fowler recommended $k_3 = 0.85$ for vertically-cast columns. Since $k_3 = 0.85$ seems to be the most generally accepted value for vertically-cast columns, that

was the value used in analyzing the test specimens.

The value of the maximum or limiting extreme fiber concrete compressive strain to be used in design is specified in both the *ACI Building Code Requirements for Reinforced Concrete*¹¹⁵ and the *AASHTO Standard Specifications for Highway Bridges*¹¹⁶ as 0.003. This is a conservative design limit which may not necessarily reflect the maximum compressive strain attainable in the member. Actual maximum compressive strains of up to 0.017 at failure have been observed under certain conditions^{117,118}. It was determined in Section 4.3.1 that the Hognestad constitutive model is a good predictor of the stress-strain curve of the concrete used in the test specimens of this study. This was established by comparing the Hognestad model with experimental stress-strain curves obtained from cylinder tests. Therefore, in developing the analytical model of this study it was assumed that the Hognestad stress-strain curve represents the actual constitutive behavior of the concrete. However, building code limits on maximum allowable design strain arbitrarily truncate this curve at a strain of 0.003.

While it might seem that arbitrarily limiting maximum extreme fiber compressive strains to 0.003 could lead to a significant under-prediction of column strength, in fact the value of extreme fiber compressive strain has been found to have little influence on the computed strength of the cross section. Using the analytical model developed in this study it was determined that the computed capacity of the hollow pier specimens was essentially unaffected by the value of maximum strain in the range 0.003 to 0.0038. Hognestad¹¹⁹ also observed that in general the calculated strength of most concrete members is relatively insensitive to the assumed value of ultimate strain for values of ultimate strain of 0.003 or greater. Thus, from the point of view of computation of strength, it is inconsequential whether the Hognestad constitutive curve is truncated by design code limitations at a strain of 0.003, or is carried out to the strain of 0.0038 originally recommended by Hognestad. In keeping with current design code provisions the ultimate strain used in analyzing the test specimens was limited to 0.003. A further discussion of ultimate compressive strains and failure criteria is presented in Section 5.5.3.

It is current design practice to calculate the strength of segmentally constructed piers and pylons neglecting the presence of all non-post-tensioned longitudinal

reinforcement. This is because the non-post-tensioned reinforcement is discontinuous at the joints between segments, creating planes of weakness at those locations. In calculating the strength of the segmentally constructed test specimens two analyses were made: the first analysis followed current design practice and neglected all non-post-tensioned reinforcement, providing a lower-bound estimate of capacity; the second analysis included all non-post-tensioned reinforcement, providing an upper-bound estimate of capacity.

5.3. Plate Buckling Model

5.3.1. *Computed Buckling Stresses of Compression Flanges*

The program PLCRST was used to compute the plate buckling stress for the most slender wall of each of the test specimens from the test programs of the present study, Jobse and Moustafa^{27,28}, Poston et al.²⁶ and Procter²⁵. The input parameters for the program and the computed buckling stresses are shown in Table 5.1. The width of each plate was determined as shown in Figure 1.4. For segmentally constructed specimens the concrete strength of the actual segment in which the failure was located in the hollow pier test was used in computing the buckling stress of the compression flange. Also, for segmentally constructed specimens the buckling stress of the compression flange was calculated assuming all non-post-tensioned reinforcement was continuous over the height of the flange. This was done because even though the non-post-tensioned reinforcement is discontinuous at joints between segments it contributes to the plate bending stiffness over most of the plate. (In computations of section strength non-post-tensioned reinforcement is neglected because it is discontinuous at joints between segments).

Table 5.1 shows that for flanges with wall slenderness ratio less than about 18 the buckling stress of the flange is nearly equal to the peak stress of the stress-strain curve, k_3f_c (see Figure 4.1). For plates with wall slenderness ratio in the range 18 to 34 the buckling stress is 99% to 81% of k_3f_c . These observations should not be interpreted as meaning plates with wall slenderness ratios less than 18 cannot buckle. Instead, such plates can buckle, but the buckling stress is nearly the same as the crushing stress of the concrete. Viewed from the perspective of failure strain, the

buckling strain of the plate is nearly the same as the strain at peak stress, ϵ_o (Figure 4.1). This distinction becomes important when a plate is considered as a component of a hollow, thin-walled compression member. The role of wall slenderness and plate buckling in determining overall section capacity is discussed in Section 5.5.3.3.

5.3.2. *Concrete Plate Buckling Parameter Study*

In an earlier phase of this study Tran⁴⁶ performed an analytical parameter study of slender rectangular concrete plates restrained elastically against rotation along the long edges and subject to uniformly distributed in-plane loads along the short edges (Figure 4.2). Tran made use of the plate buckling program PLCRST to study the influence of several factors on plate buckling: plate length-to-width ratio, wall slenderness ratio, concrete strength, reinforcement content, and edge restraint. The main conclusions of this parameter study are summarized here, as they are relevant to the behavior of hollow concrete sections with slender walls.

The ranges of parameters studied by Tran were as follows. The wall length-to-width ratio was varied from 0.3 to 20. The range of wall slenderness ratio (width - to-thickness) was varied from 5 to 120. The range of concrete strength was 3,000 to 10,000 psi. The reinforcement content of the plate was varied between 0.2% and 6%. The ratio of width of the plate to the width of the side flange plates (which characterizes edge restraint) was varied between 1 and 5. The thicknesses of all four walls of the cross section were assumed to be equal.

Tran found that plates with length-to-width ratios greater than 3 have the same buckling stress as a plate with length-to-width ratio equal to 3, all else being equal. Furthermore, the buckling stress calculated for a length-to-width ratio of 3 (or greater) will be the minimum buckling stress for the plate. This means that for most hollow piers and pylons, which are generally tall, the length of the member has no effect on the critical buckling stress of the compression flange. If the length-to-width ratio of the compression flange is less than 3 then the buckling stress can be conservatively calculated assuming a length-to-width ratio equal to 3 (or greater).

Specimen Number	Plate Dimensions, in.			Flange Width*	ρ %	\bar{z}^{**} in.	f_y ksi	$k_3 F_c$ psi	f_{cr} psi	$\frac{f_{cr}}{k_3 F_c}$	$\frac{X_u}{t}$
	Length	Width	Thick.								
Present Study 1M10	72	25	2.55	10	1.79	0.5	75.1	6680	6680	1.00	10.0
Present Study 2M10	72	20	2.03	8	1.17	0.25	75.1	2690	2690	1.00	10.0
Present Study 3M14	72	35	2.56	15	1.38	0.5	75.1	3010	3010	1.00	14.0
Present Study 4M18	72	36	2.13	16	1.24	0.25	75.1	6490	6490	0.99	18.0
Present Study 5S9	72	22	2.46	7	1.76	0.5	75.1	5800	5800	1.00	8.8
Present Study 6S16	72	31	2.07	11	1.18	0.25	75.1	4110	4100	1.00	15.5
Present Study 7S22	72	32.5	1.57	12.5	1.30	0.375	75.1	5880	5820	0.99	21.7
Present Study 8ML25	72	37	1.55	17	1.49	0.375	75.1	5360	5320	0.99	24.7
Present Study 9MLP22	72	32.5	1.49	12.5	1.37	0.375	75.1	5490	5470	1.00	21.7
Present Study 10ML18	72	36	2.04	16	1.29	0.25	75.1	5680	5630	0.99	18.0
Present Study 11ML34	72	37.8	1.16	17.8	1.95	0.188	75.1	4470	4250	0.95	33.6
Present Study 12S29	72	33	1.16	13	1.74	0.188	75.1	3980	3880	0.97	29.3
Jobse and Moustafa 1	180	48	1.5	48	0.72	0	60***	7380	6110	0.83	32.0
Jobse and Moustafa 2A	180	48	1.5	48	0.72	0	60***	8400	6790	0.81	32.0
Poston et al. 1	72	19	2.5	3	1.00	0.53	61.1	3540	3540	1.00	7.6
Poston et al. 2	72	8.25	2.5	3	0.92	0.53	61.1	3660	3660	1.00	3.3
Poston et al. 3	72	4.7	2.5	3	0.81	0.53	61.1	4250	4250	1.00	1.9
Procter 1	9.8	6.21	0.83	2.28	0	0	—	5170	5170	1.00	7.5
Procter 2	9.8	5.83	1.02	1.90	0	0	—	5170	5170	1.00	5.7
Procter 3	9.8	5.39	1.24	1.46	0	0	—	5170	5170	1.00	4.3
Procter 4	9.8	5.03	1.42	1.10	0	0	—	5170	5170	1.00	3.6
Procter 5	9.8	4.61	1.63	0.68	0	0	—	5170	5170	1.00	2.9
Procter 6	9.8	4.29	1.79	0.36	0	0	—	5170	5170	1.00	2.4

* Width of side flanges of cross section **Distance of centroids of reinforcement layers from center plane of plates *** Assumed value

Table 5.1: Computed Flange Buckling Stresses

Tran found that the two parameters wall slenderness ratio and concrete strength are linked in their effect on the buckling stress of the plates. For a given concrete strength, f_c , the buckling stress of the plate is nearly equal to f_c for wall slenderness ratios below a certain value. For wall slenderness ratios above this value the buckling stress is less than f_c . Figure 5.1 shows the typical relationship between wall slenderness ratio, concrete strength and buckling stress. It can be seen that for high concrete strengths of 8,000 to 10,000 psi the wall slenderness ratio at which the buckling stress begins to decrease is about 15. For low concrete strengths of 3,000 to 5,000 psi the wall slenderness ratio at which the buckling stress begins to decrease is about 25. This finding is significant from a design standpoint. If higher strength concretes are used for hollow concrete piers and pylons in an effort to increase strength and stiffness and to decrease weight, then wall slenderness effects will be more pronounced at lower values of wall slenderness ratio than if lower strength concretes were used. In other words, for a given cross section the higher the concrete strength, the more susceptible the compression flange of the cross section is to buckling at a stress lower than f_c .

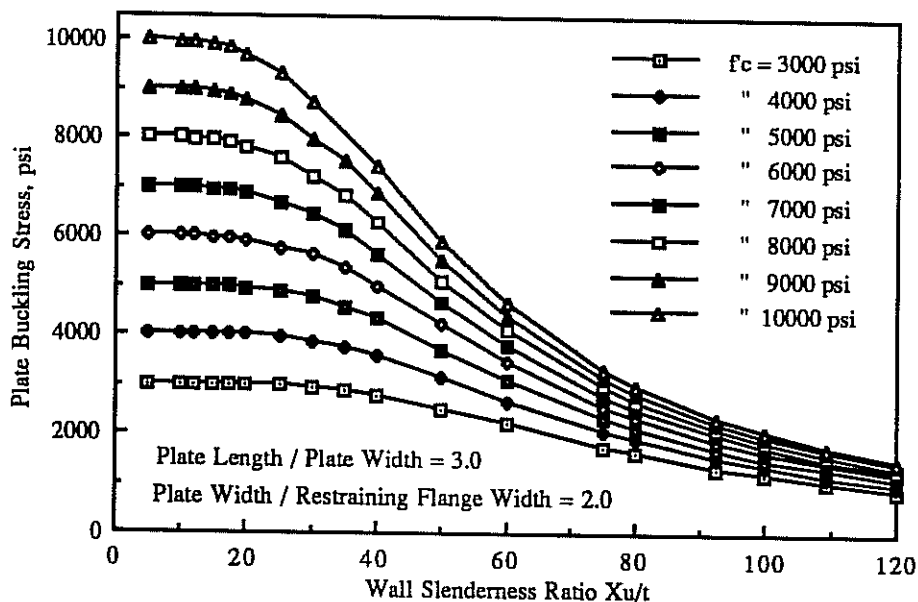


Figure 5.1: Effect of Concrete Strength on Plate Buckling Stress⁴⁶

Tran determined that reinforcement content plays a relatively minor role in determining the buckling stress of the plate with reinforcement ratios in the practical range of 0.5% to 2% and wall slenderness ratios up to 40. In all cases the addition of reinforcement is beneficial in that the reinforcement increases the buckling stress of the plate. However, the buckling stress of the reinforced plate is only on the order of 0.1% to 2.5% greater than the buckling stress of an unreinforced plate. This result is based on the assumption that there are two layers of reinforcement in the plate, one near each face. If the reinforcement lies in one plane at the center of the plate then the reinforcement has virtually no effect on the buckling stress. Thus, in the design of hollow piers and pylons it is generally ineffective to increase the reinforcement ratio as a means of increasing the buckling stress of a slender wall. The minor influence of reinforcement on the plate buckling stress was confirmed experimentally by Swartz^{31,32,33}, who tested plates with reinforcement ratios between 0.2% and 1.0%. It was found that the reinforcement content had very little influence on the observed failure load. The only benefit of increasing reinforcement was that plates with more reinforcement exhibited larger lateral deformations before failure.

The aspect ratios of practical hollow rectangular pier and pylon cross sections — the wide dimension of a cross section divided by the narrow dimension — almost always lie in the range of 1 to 5 (See Table 1.1). As discussed in Section 4.4.1 the degree of rotational restraint provided along the long edges of the wide flange of the cross section is a function of the cross section aspect ratio. Thus the aspect ratio of the cross section influences the buckling stress of the wide flange. The higher the aspect ratio the more restrained are the edges of the plate. For the minimum aspect ratio of 1 (a square cross section) and the worst case of a concentrically loaded cross section, the rotational restraint on the long edges of the plate is zero. That is, the long edges of the plate are simply supported (Figure 4.3). As the aspect ratio increases, so does the rotational restraint on the long edges of the wide flange, increasing the buckling stress of the flange. For very large values of cross section aspect ratio the boundary conditions on the long edge of the plate approach full fixity.

Tran studied the buckling stress of the wide flange of a rectangular cross section with respect to variations in cross section aspect ratio between 1 and 5 and variations in wall slenderness from 5 to 40. The thicknesses of all four walls of the cross

section were assumed to be the same. Tran found that in these ranges of cross section aspect ratio and wall slenderness ratio the rotational restraint provided to the long edges of the wide flange increased the buckling stress of the flange by only 0.3% to 7.2% over the simply supported edge condition. From a design standpoint this means that calculations of the critical buckling stress of most practical flanges may be simplified, without excess conservatism, by assuming simply supported boundary conditions along the long edges of the flange. As was discussed in Section 4.4.1 it is also possible to assume simply supported boundary conditions along the short edges of the flange without excess conservatism, provided the length-to-width ratio of the flange is greater than about 3. Thus a reasonable but conservative estimate of the buckling stress for most practical compression flanges can be calculated assuming simply supported boundary conditions on all four edges of the flange. (It should be born in mind, however, that while boundary conditions may be simplified for design purposes material nonlinearities must still be taken into account). In the present study the more realistic and complex plate boundary conditions of partial fixity along the long edges of the plate are considered in the interest of obtaining an accurate, rather than conservative, prediction of test specimen capacity.

5.4. Section Capacity Model

The buckling stress of the compression flange of each specimen from the four experimental studies was determined using the program PLCRST, as described above in Section 5.3.1. This buckling stress was then used in the program HOLMP to compute the capacity of the cross section. The computed capacity of each specimen is the calculated ultimate axial load and ultimate moment corresponding to the eccentricity at which the test specimen was loaded. That is, the observed failure point and the calculated failure point fall on the same line of constant eccentricity on the axial load-moment interaction diagram, as illustrated in Figure 5.2. (In the tests the eccentricity was not actually constant because of small additional eccentricities introduced by lateral deformations of the column center line. Therefore, in comparing the calculated and observed capacities the eccentricity which included the measured second order column center line deflections, as listed in Table 3.1, were

used. In most cases this second order correction was only a few percent).

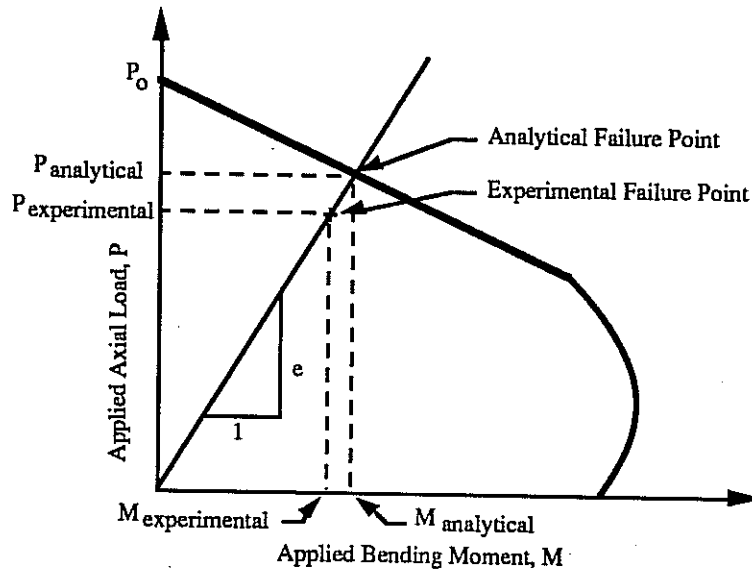


Figure 5.2: Method of Comparing Observed and Calculated Capacities

The computed and experimental capacities of the specimens are shown in Table 5.2. Results for the tests of Poston et al. are not shown in Table 5.2 because the tests in that study were loaded in biaxial bending and HOLMP allows only uniaxial bending. However the analytical results for Poston's specimens from the finite strip program BIMPHI are shown in Figure 1.6. In Table 5.3 the analytical capacities and experimental capacities shown in Table 5.2 are compared numerically. Table 5.4 shows the averages and standard deviations for the data in Table 5.3. The overall implications of the results shown in these three tables are discussed in Section 5.5. However, prior to that general discussion, the experimental results of individual tests are compared with the analytical model in Sections 5.4.1 through 5.4.4 below.

Specimen Number	Wall Slenderness Ratio	Experimental Results		HOLMP Excl. Local Buckling Excl. Non-Post-Tensioned Reinf. in Segmental Specs.		HOLMP Incl. Local Buckling Excl. Non-Post-Tensioned Reinf. in Segmental Specs.		HOLMP Excl. Local Buckling Incl. Non-Post-Tensioned Reinf. in Segmental Specs.		HOLMP Incl. Local Buckling Incl. Non-Post-Tensioned Reinf. in Segmental Specs.	
		P kips	M kip-in	P kips	M kip-in	P kips	M kip-in	P kips	M kip-in	P kips	M kip-in
1M10	10.0	527	4590	536	4653	537	4653	536	4653	537	4653
2M10	10.0	470	331	411	289	376	266	411	289	376	266
3M14	14.0	938	975	961	997	917	945	961	997	917	945
4M18	18.0	938	2600	1248	3456	1231	3397	1248	3456	1231	3397
5S9	8.8	1138	922	979	790	970	784	1242	1001	1232	994
6S16	15.5	948	967	885	900	857	867	1103	1122	1035	1047
7S22	21.7	999	1020	863	878	841	851	1074	1096	1046	1061
8ML25	24.7	904	922	1011	1032	997	1010	1011	1032	997	1010
9MLP22	21.7	961	980	1007	1026	995	1005	1007	1026	995	1005
10ML18	18.0	1013	2810	1112	3076	1088	3000	1112	3076	1088	3000
11ML34	33.6	623	635	713	724	636	646	713	724	636	646
12S29	29.3	682	682	442	441	424	423	666	654	579	575
Jobse 1	32	1614	7910	2078	10148	1583	7692	2184	10660	1678	8152
Jobse 2A	32	1346	27190	1493	30080	1132	22690	1558	31300	1188	23840
Procter 1	7.5	91	0	110	0	110	0	110	0	110	0
Procter 2	5.7	125	0	126	0	126	0	126	0	126	0
Procter 3	4.3	139	0	142	0	142	0	142	0	142	0
Procter 4	3.6	162	0	154	0	154	0	154	0	154	0
Procter 5	2.9	163	0	166	0	166	0	166	0	166	0
Procter 6	2.4	166	0	175	0	175	0	175	0	175	0
Procter 7	0	187	0	183	0	183	0	183	0	183	0

Table 5.2: Experimental and Computed Capacities of Test Specimens

Specimen Number	Wall Slenderness Ratio	Ratio of Observed Failure Load to Calculated Failure Load, <u>Excluding</u> Local Buckling and <u>Excluding</u> Non-Post-Tensioned Reinforcement in Segmental Specimens	Ratio of Observed Failure Load to Calculated Failure Load, <u>Including</u> Local Buckling and <u>Excluding</u> Non-Post-Tensioned Reinforcement in Segmental Specimens	Ratio of Observed Failure Load to Calculated Failure Load, <u>Excluding</u> Local Buckling and <u>Including</u> Non-Post-Tensioned Reinforcement in Segmental Specimens	Ratio of Observed Failure Load to Calculated Failure Load, <u>Including</u> Local Buckling and <u>Including</u> Non-Post-Tensioned Reinforcement in Segmental Specimens
1M10	10.0	0.98	0.98	0.98	0.98
2M10	10.0	1.14	1.25	1.14	1.25
3M14	14.0	0.97	1.02	0.97	1.02
4M18**	18.0	0.75	0.76	0.75	0.76
5S9	8.8	1.16	1.17	0.92	0.92
6S16	15.5	1.07	1.11	0.86	0.92
7S22	21.7	1.16	1.19	0.93	0.96
8ML25	24.7	0.89	0.91	0.89	0.91
9MLP22	21.7	0.95	0.96	0.95	0.96
10ML18	18.0	0.91	0.93	0.91	0.93
11ML34	33.6	0.87	0.98	0.87	0.98
12S29**	29.3	1.54	1.61	1.02	1.18
Jobse 1	32	0.78	1.02	0.74	0.96
Jobse 2A	32	0.90	1.19	0.86	1.13
Poston 1*	7.6	1.00	1.00	1.00	1.00
Poston 2*	3.3	1.00	1.00	1.00	1.00
Poston 3*	1.9	1.00	1.00	1.00	1.00
Poston 4*	0	1.00	1.00	1.00	1.00
Procter 1**	7.5	0.83	0.83	0.83	0.83
Procter 2	5.7	0.99	0.99	0.99	0.99
Procter 3	4.3	0.98	0.98	0.98	0.98
Procter 4	3.6	1.05	1.05	1.05	1.05
Procter 5	2.9	0.98	0.98	0.98	0.98
Procter 6	2.4	0.95	0.95	0.95	0.95
Procter 7	0	1.02	1.02	1.02	1.02

* Data from program BIMPHI, see Figure 1.6 ** Outlying points, as discussed in Section 5.5.1

Table 5.3: Ratios of Experimental to Computed Capacities of Test Specimens

Specimens From Table 5.3 That Are Included in Statistical Calculations	Ratio of Observed Failure Load to Calculated Failure Load, <u>Excluding</u> Local Buckling and <u>Excluding</u> Non-Post-Tensioned Reinforcement in Segmental Specimens	Ratio of Observed Failure Load to Calculated Failure Load, <u>Including</u> Local Buckling and <u>Including</u> Non-Post-Tensioned Reinforcement in Segmental Specimens	Ratio of Observed Failure Load to Calculated Failure Load, <u>Excluding</u> Local Buckling and <u>Including</u> Non-Post-Tensioned Reinforcement in Segmental Specimens	Ratio of Observed Failure Load to Calculated Failure Load, <u>Including</u> Local Buckling and <u>Including</u> Non-Post-Tensioned Reinforcement in Segmental Specimens
	All Wall Slenderness Ratios from 0 to 34	Average = 0.99 Std. Dev. = 0.09	Average = 1.03 Std. Dev. = 0.09	Average = 0.95 Std. Dev. = 0.08
Only Wall Slenderness Ratios from 0 to 14	Average = 1.02 Std. Dev. = 0.06	Average = 1.03 Std. Dev. = 0.08	Average = 1.00 Std. Dev. = 0.05	Average = 1.01 Std. Dev. = 0.08
Only Wall Slenderness Ratios from 15 to 34	Average = 0.94 Std. Dev. = 0.12	Average = 1.04 Std. Dev. = 0.11	Average = 0.88 Std. Dev. = 0.06	Average = 0.97 Std. Dev. = 0.07
All Wall Slenderness Ratios from 0 to 34	Average = 0.99 Std. Dev. = 0.15	Average = 1.04 Std. Dev. = 0.16	Average = 0.94 Std. Dev. = 0.09	Average = 0.99 Std. Dev. = 0.10
Only Wall Slenderness Ratios from 0 to 14	Average = 1.00 Std. Dev. = 0.08	Average = 1.02 Std. Dev. = 0.09	Average = 0.99 Std. Dev. = 0.07	Average = 1.00 Std. Dev. = 0.09
Only Wall Slenderness Ratios from 15 to 34	Average = 0.98 Std. Dev. = 0.23	Average = 1.07 Std. Dev. = 0.23	Average = 0.88 Std. Dev. = 0.08	Average = 0.97 Std. Dev. = 0.12
	Incl. Outlying Data Points*			
	Excl. Outlying Data Points*			

* Three outlying data points are discussed in Section 5.5.1

Table 5.4: Statistical Data for Ratios of Experimental to Computed Capacities of Test Specimens

5.4.1. Computed Capacities of Test Specimens of Present Study

5.4.1.1. Specimen 1M10 (Monolithic, 15" x 30", 2.5" walls, $X_u/t = 10.0$)

Figure 5.3 shows the interaction curve generated by HOLMP for specimen 1M10. The dashed line indicates the solution obtained when local compression flange buckling is neglected, and the solid line is the solution when local buckling is considered. The figure shows that the local wall buckling has virtually no effect on the behavior of this specimen. It can be seen that the experimental failure point agrees very well with the analytical solutions.

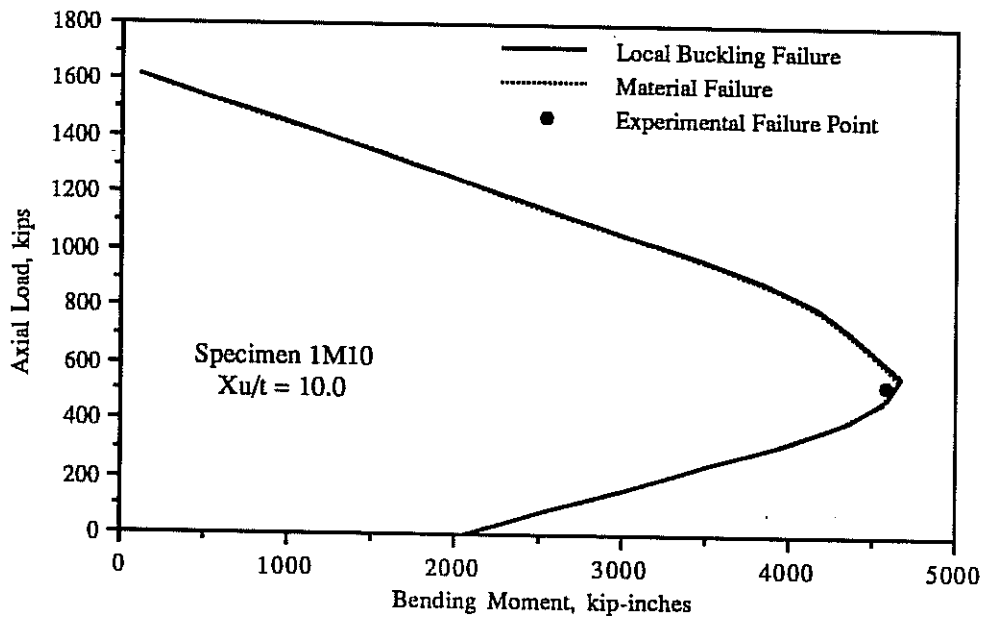


Figure 5.3: Interaction Diagrams for Specimen 1M10

5.4.1.2. Specimen 2M10 (Monolithic, 12" x 24", 2.0" walls, $X_u/t = 10.0$)

The interaction diagrams for material failure and local buckling failure of specimen 2M10 are shown in Figure 5.4. The effects of wall slenderness are greater for this specimen than for specimen 1M10, even though both specimens have the same wall slenderness ratio. This is because the local wall buckling strain of specimen 1M10 was almost exactly the same as the concrete compression failure

strain of 0.003, while the local wall buckling strain of specimen 2M10 was 0.00172, much less than the concrete compression failure strain of 0.003.

The experimental failure point falls above both the material failure and local failure interaction diagrams. No definitive reason is known for the conservative prediction of strength, but two factors were probably influential. The first reason has to do with the testing machine used to load the concrete test cylinders. This machine operates at two load ranges, and automatically switches from the low to high load range during testing, creating a sudden jump in load from 90 to 95 kips. Coincidentally the concrete test cylinders for specimen 2M10 failed somewhere in this range, so the normal cylinder testing machine could not be used for this specimen. Instead, another test machine was used which was not designed specifically for testing cylinders, and which was not as recently calibrated as the first machine. Consequently the strength of the cylinders for specimen 2M10 is not as accurately known as with all other specimens, which may account partially for the underprediction of strength. Second, specimen 2M10 was loaded at the lowest eccentricity of any of the twelve specimens, 0.62 inches. The maximum permitted error in alignment of the test specimen in the machine was ± 0.10 inches (see section 2.8.2), so the bending moment at failure for this specimen could be as much as 15% lower than reported. If this were the case, the experimental failure point would be shifted to the left in Figure 5.4, closer to the predicted strength curves.

5.4.1.3. Specimen 3M14 (Monolithic, 20" x 40", 2.5" walls, $X_U/t = 14.0$)

Figure 5.5 shows the local wall buckling and material failure interaction curves for specimen 3M14. The two curves are fairly close together near the top of the diagram. The experimental failure point falls between the two curves, slightly closer to the local buckling failure curve.

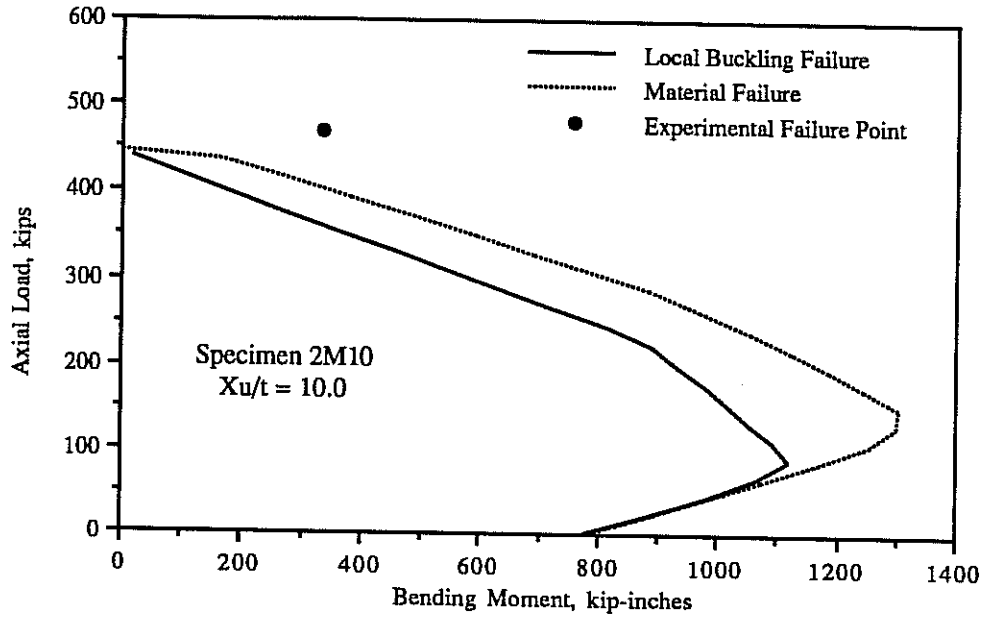


Figure 5.4: Interaction Diagrams for Specimen 2M10

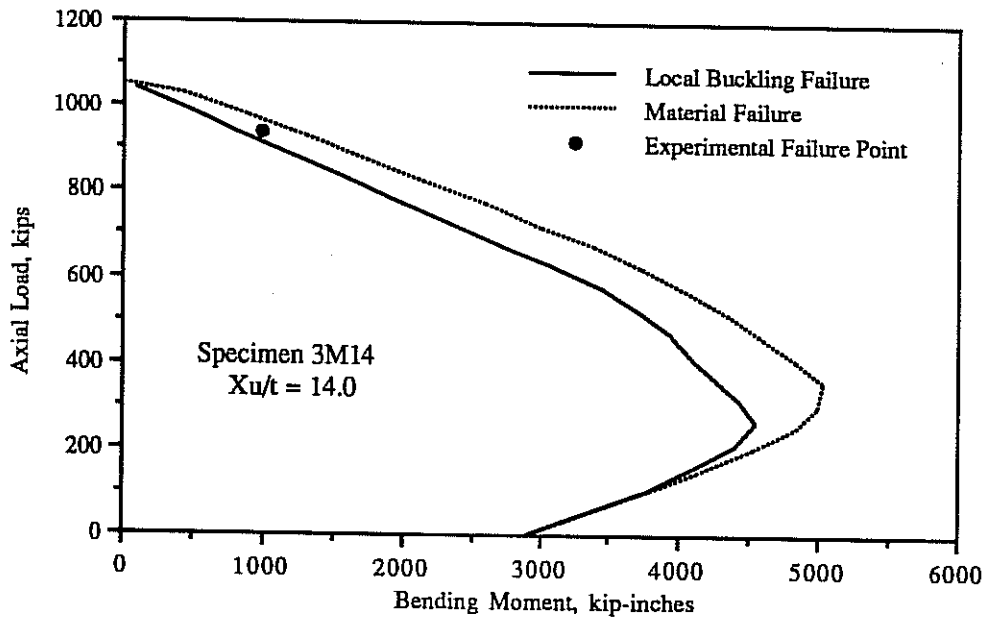


Figure 5.5: Interaction Diagrams for Specimen 3M14

5.4.1.4. Specimen 4M18 (Monolithic, 20" x 40", 2.0" walls, $X_U/t = 18.0$)

The buckling failure and material failure interaction curves are very close together for specimen 4M18, as shown in Figure 5.6. This is because the buckling strain of the flange and the concrete failure strain have nearly the same value. The experimental failure point is well below both curves, indicating some local weakness may have existed in the cross section. The most probable source of this weakness was the water gain effect - the migration of water toward the top of the fresh concrete during casting. Specimen 4M18 presented the most difficult casting conditions of any of the twelve specimens. The walls of the specimen were only 2 inches thick, 72 inches high, and were cast in a single lift. Because of the congested reinforcement cage the concrete had to be vibrated thoroughly to insure consolidation. About an hour after the walls of the specimen were cast bleed water was observed at the top edges of the walls. While a small amount of bleed water was normally observed with all the specimens of the test program, an excessive amount was noted with specimen 4M18. The additional water in the concrete near the top of the specimen raised the water-cement ratio and decreased the strength of the concrete. This conclusion is further supported by the observation that failure occurred very near the top of the specimen (Figures 3.26 and 3.28).

Thus the weakness of specimen 4M18 can be attributed to the unusual casting conditions encountered in fabricating the small scale test specimen. Since similar conditions do not exist in the fabrication of full-size structures (to scale the fabrication of the walls of specimen 4M18 would be equivalent to casting walls 10 inches thick and 30 feet high in a single lift) the problems encountered with specimen 4M18 should not carry over to prototype piers and pylons.

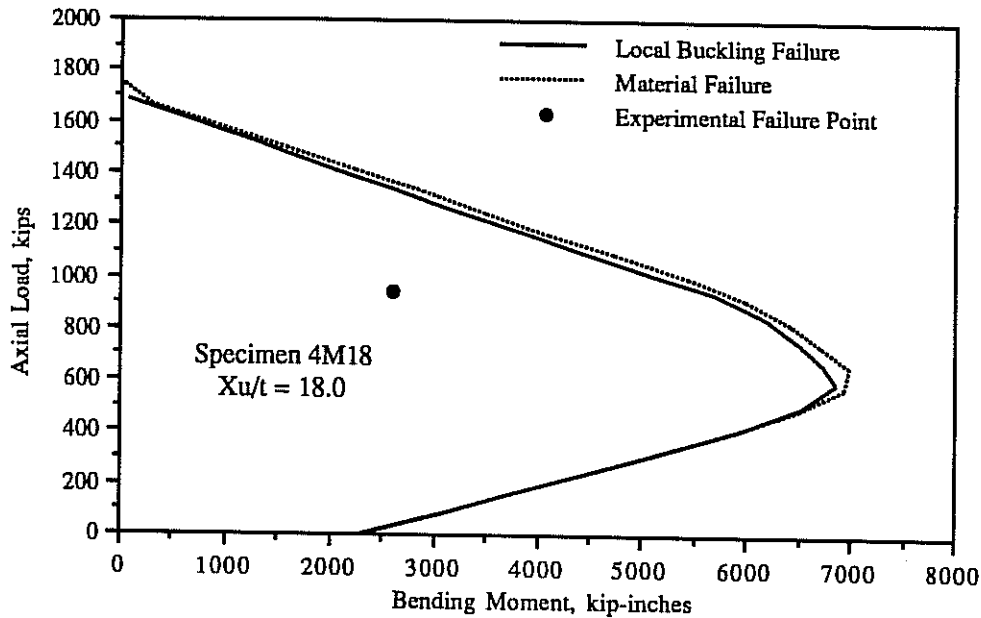


Figure 5.6: Interaction Diagrams for Specimen 4M18

5.4.1.5. Specimen 5S9 (Segmental, 15" x 30", 2.5" walls, $X_u/t = 8.8$)

Four interaction curves are shown for specimen 5S9 in Figure 5.7. The two upper curves are the local buckling failure and material failure interaction curves calculated assuming the non-post-tensioned reinforcement runs continuously over the length of the specimen. The two lower curves are the local buckling and material failure interaction curves calculated neglecting all non-post-tensioned reinforcement, because the non-post-tensioned reinforcement is discontinuous at the joints between segments. (In computing the buckling stress of the compression flange, using the program PLCRST, the non-post-tensioned reinforcement was included because it contributes to the plate bending stiffness of the flange over most of the height of the flange).

It can be seen that the experimental failure point falls between the two sets of curves, indicating that the specimen gained some strength from the presence of the non-post-tensioned reinforcement, but not as much strength as if the reinforcement was continuous.

It should be recalled that specimen 5S9 failed at the location of a joint between

two segments (Section 3.3.5). The failure was initiated by splitting of the compression flange down its center plane due to the absence of reinforcement cross ties near the top edge of one segment. It appears from the analysis shown above that the absence of the cross ties did not adversely affect the overall strength of the specimen, provided the strength is computed neglecting all non-post-tensioned (discontinuous) reinforcement. However, the wall splitting behavior observed with specimen 5S9 is undesirable: wall splitting presents an additional, but unnecessary failure mode; the splitting strength of the wall cannot be accurately predicted; and wall splitting is a localized, inherently brittle type of failure. Thus, even though specimen 5S9 exhibited sufficient strength, when compared to the analytical model, the unexpected failure mode of the specimen was unsatisfactory.

5.4.1.6. Specimen 6S16 (Segmental, 20" x 40", 2.0" walls, $X_U/t = 15.5$)

Figure 5.8 shows four computed interaction diagrams for specimen 6S16. The upper two curves include the effects of non-post-tensioned (discontinuous) reinforcement, and the lower two curves neglect the effects of non-post-tensioned reinforcement. As with specimen 5S9 the experimental failure point falls between the two sets of curves. The strength of the specimen was apparently improved by the presence of non-post-tensioned reinforcement, but the strength was less than would be calculated if the reinforcement was continuous.

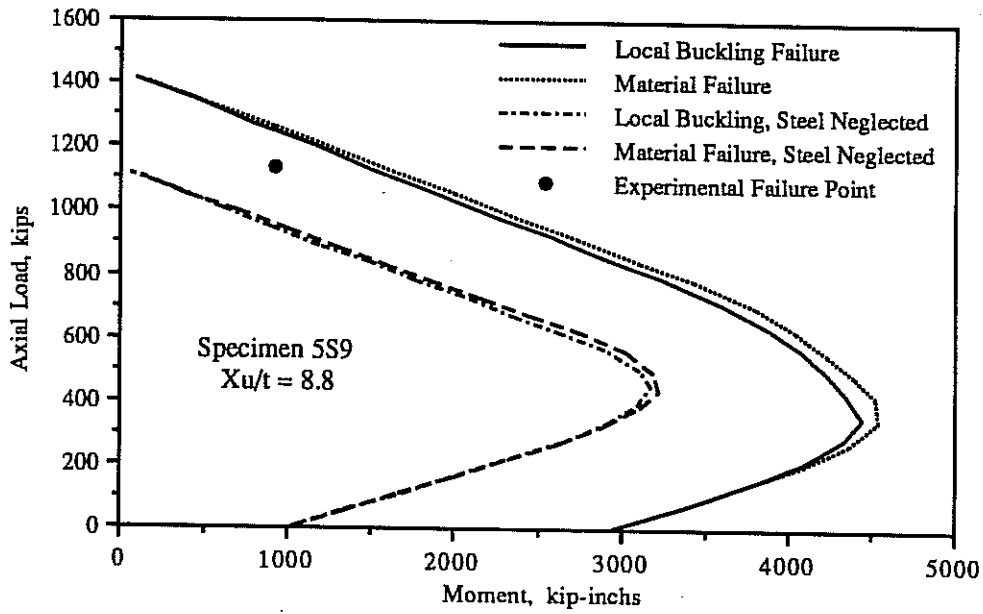


Figure 5.7: Interaction Diagrams for Specimen 5S9

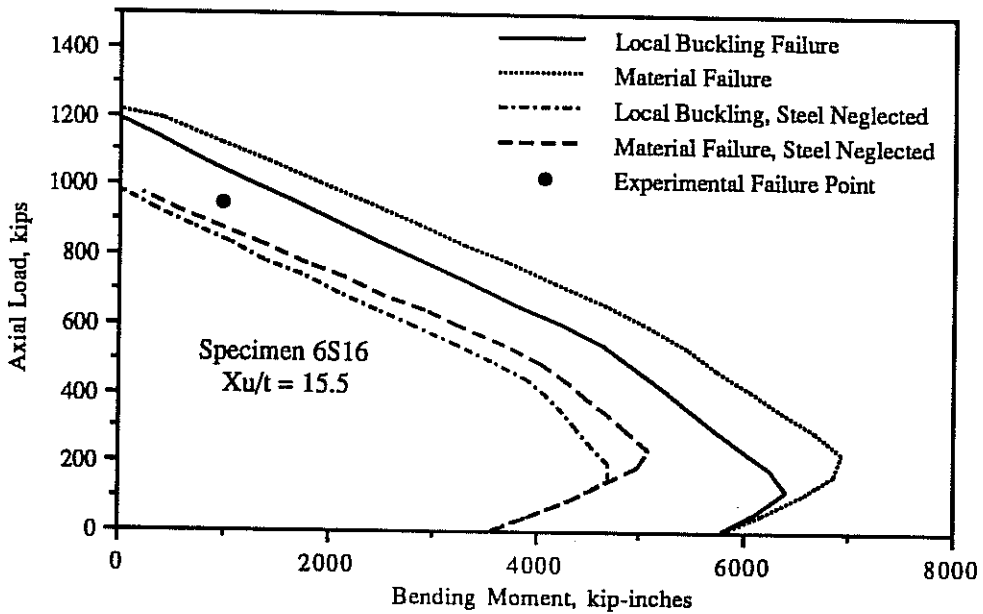


Figure 5.8: Interaction Diagrams for Specimen 6S16

5.4.1.7. Specimen 7S22 (Segmental, 20" x 40", 1.5" walls, $X_U/t = 21.7$)

In Figure 5.9 it can be seen that specimen 7S22 behaved similarly to 5S9 and 6S16, exhibiting a capacity somewhere between the strength calculated including non-post-tensioned (discontinuous) reinforcement, and the strength calculated neglecting non-post-tensioned reinforcement. In this case the strength was fairly close to the curve which includes the presence of non-post-tensioned reinforcement.

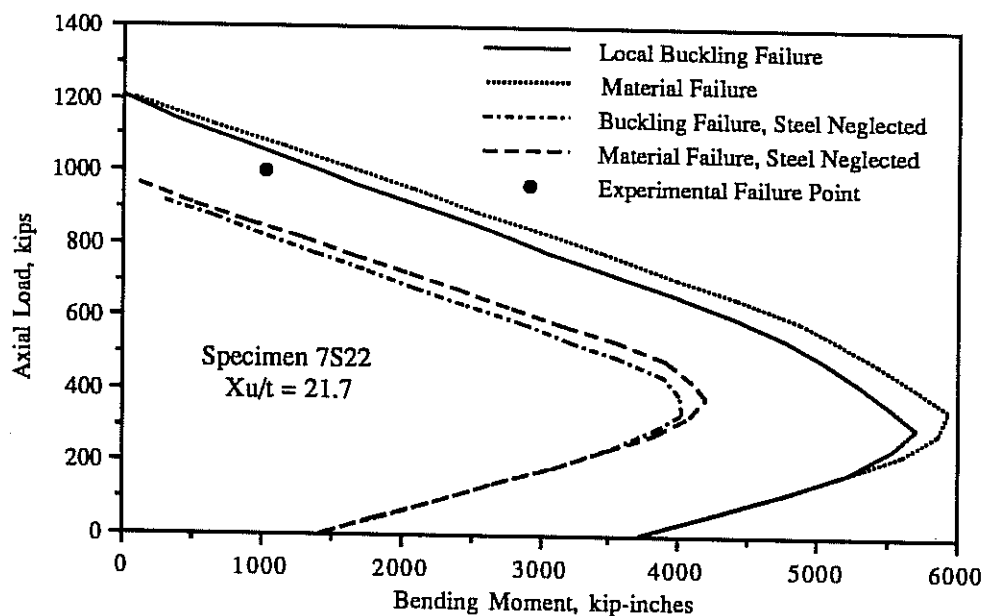


Figure 5.9: Interaction Diagrams for Specimen 7S22

5.4.1.8. Specimen 8ML25 (Multiple-Lift, 20" x 40", 1.5" walls, $X_U/t = 24.7$)

Figure 5.10 shows the analytical and experimental results for specimen 8ML25. The experimental failure point falls about 9% below the analytical solution, even if the effects of local wall buckling are included. No specific reason is known for the reduced strength, other than normally expected variations in concrete strength. It is possible that the water gain effect was not adequately accounted for by the factor $k_3 = 0.85$ in the Hognestad constitutive model.

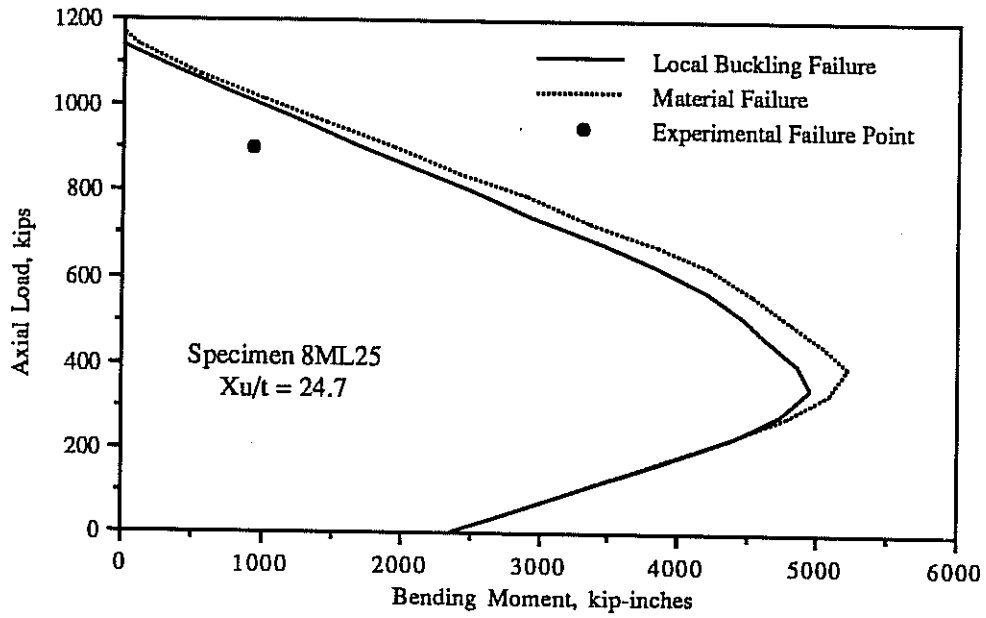


Figure 5.10: Interaction Diagrams for Specimen 8ML25

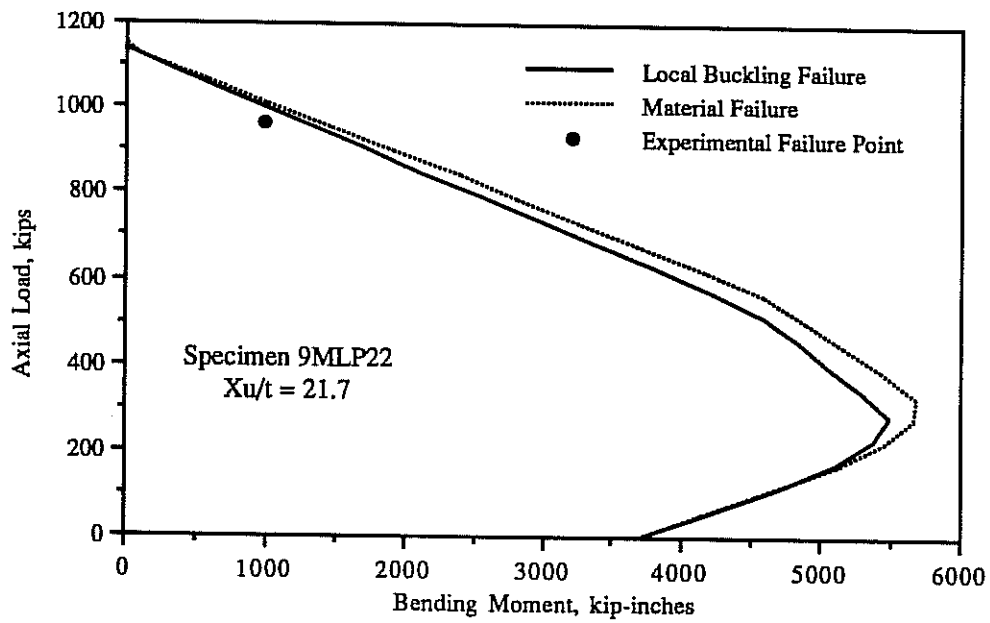


Figure 5.11: Interaction Diagrams for Specimen 9MLP22

5.4.1.9. Specimen 9MLP22 (Multiple-Lift, Post-Tensioned, 20" x 40",
1.5" walls, $X_u/t = 21.7$)

The analytical solutions and experimental failure point for specimen 9MLP22 are shown in Figure 5.11. There is good agreement between the experimental failure point and the analytical solution which includes the effects of local wall buckling.

5.4.1.10. Specimen 10ML18 (Multiple-Lift, 20" x 40", 2.0" walls, $X_u/t = 18.0$)

Figure 5.12 shows the analytical and experimental results for specimen 10ML18. There is fairly good agreement between the experimental failure point and the analytical solution which includes the effects of local wall buckling, although the experimental point is about 7% lower than the calculated strength. This difference can probably be attributed to normally expected variations in concrete strength. It is also possible that the water gain effect reduced the concrete strength near the top end of the specimen, since that is where the failure occurred. The factor $k_3 = 0.85$ in the Hognestad constitutive model may not have adequately compensated for the water gain effect in this case.

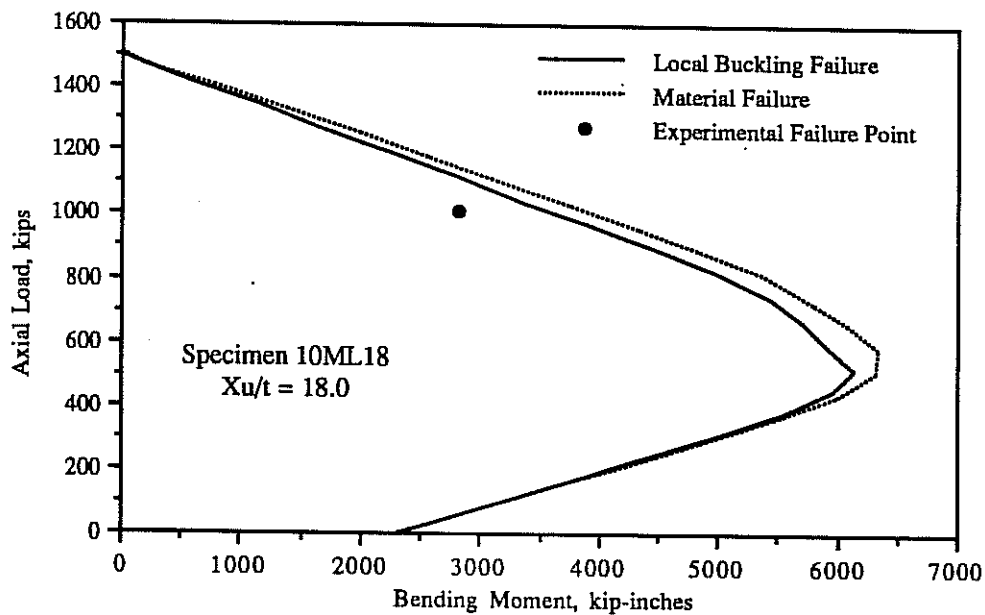


Figure 5.12: Interaction Diagrams for Specimen 10ML18

5.4.1.11. Specimen 11ML34 (Multiple-Lift, 20" x 40", 1.1" walls, $X_u/t = 33.6$)

In Figure 5.13 it can be seen that wall slenderness effects significantly reduced the calculated strength of specimen 11ML34. The experimental failure point is in very good agreement with the strength calculated including the effects of local wall buckling.

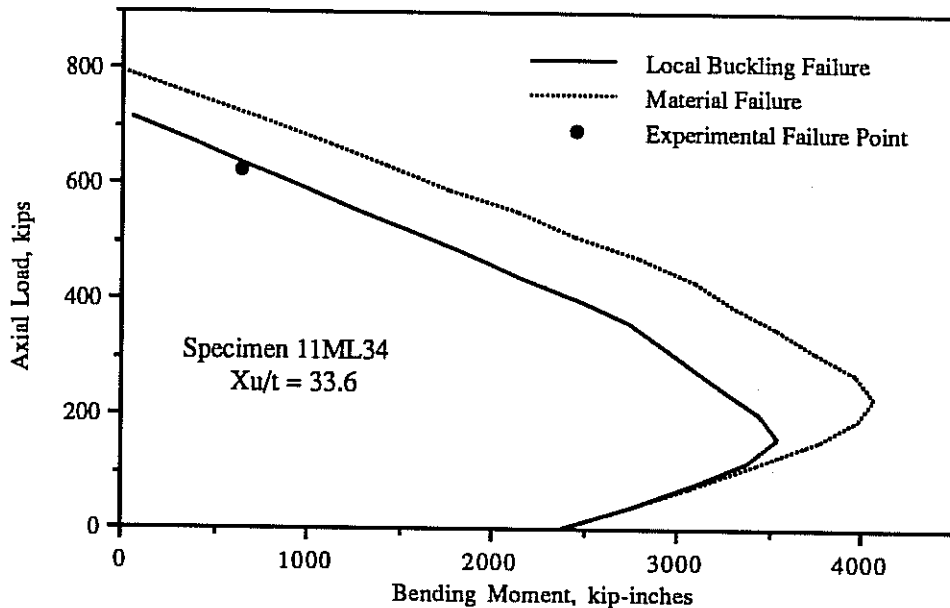


Figure 5.13: Interaction Diagrams for Specimen 11ML34

5.4.1.12. Specimen 12S29 (Segmental, 20" x 40", 1.1" walls, $X_u/t = 29.3$)

Figure 5.14 shows the analytical and experimental results for specimen 12S29. The experimental result falls above even the highest analytical prediction, that is, the strength calculated neglecting local wall buckling and including the presence of non-post-tensioned (discontinuous) reinforcement. The location of the failure zone in the test specimen provides a clue as to why the observed strength was so high. Specimen 12S29 failed very near the bottom end (as cast), whereas most other specimens in the test program failed near the top end (see Table 3.1). This indicates that the water gain effect probably did not reduce the strength of the specimen, as the water gain effect would create a weak zone near the top of the specimen, rather than the bottom. It seems likely that water gain was minimized in specimen 12S29. It

was the last specimen cast and casting techniques had been refined to the point that minimal vibration of the concrete was required.

If the water gain effect was not a factor in reducing the strength of specimen 12S29, then the reduction factor k_3 in the Hognestad constitutive model should have a value of 1.0 instead of 0.85. This would raise the predicted strength in Figure 5.14 by about 15%, and the experimental failure point would agree more closely with the analytical solutions. The experimental failure point would fall between the solution which includes non-post-tensioned (discontinuous) reinforcement and the solution which excludes non-post-tensioned reinforcement, as with the other three segmental specimens of the test program.

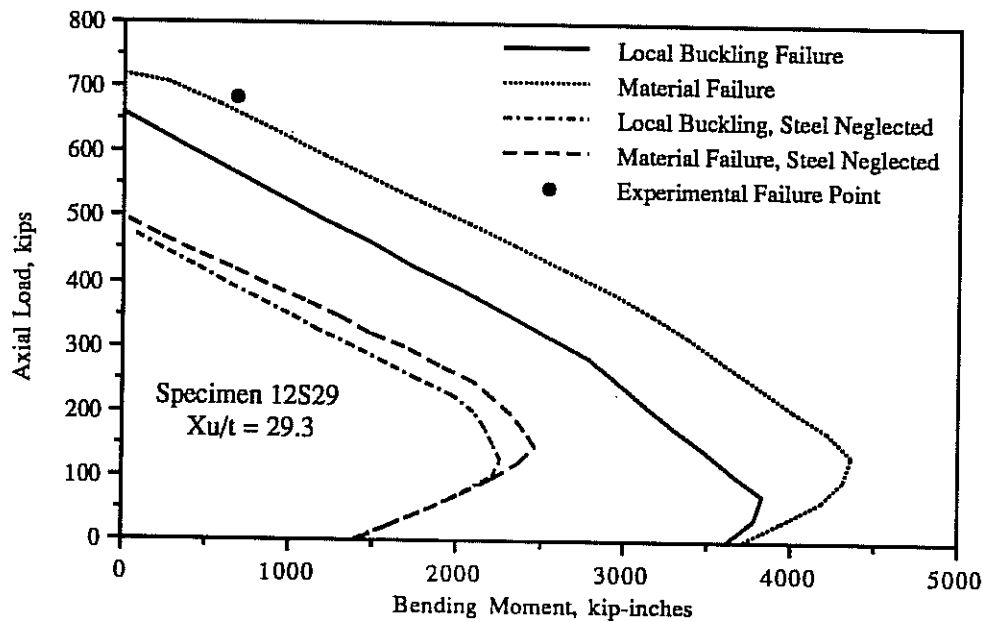


Figure 5.14: Interaction Diagrams for Specimen 12S29

5.4.2. Computed Capacities of Test Specimens of Jobse and Moustafa

5.4.2.1. Specimen 1 (Segmental, 60" x 60", 1.5" walls, $X_u/t = 32.0$)

The analytical solutions and experimental failure point for Jobse's Specimen 1 are shown in Figure 5.15. The experimental data point agrees very closely with the solution which includes local wall buckling and neglects non-post-tensioned

(discontinuous) reinforcement. Notice that the four lines of Figure 5.15 appear in a different hierarchy than with other segmental specimens because the effects of wall slenderness are very pronounced with this specimen, and the specimen was very lightly reinforced. It can be seen that the experimental failure point actually lies in the narrow band between the two local buckling solutions which include and neglect non-post-tensioned reinforcement. Thus Jobse's Specimen 1 exhibits behavior similar to most of the segmental specimens of the present study. The specimen was stronger than indicated by the solution neglecting non-post-tensioned reinforcement, but did not exhibit the full capacity computed by including non-post-tensioned reinforcement.

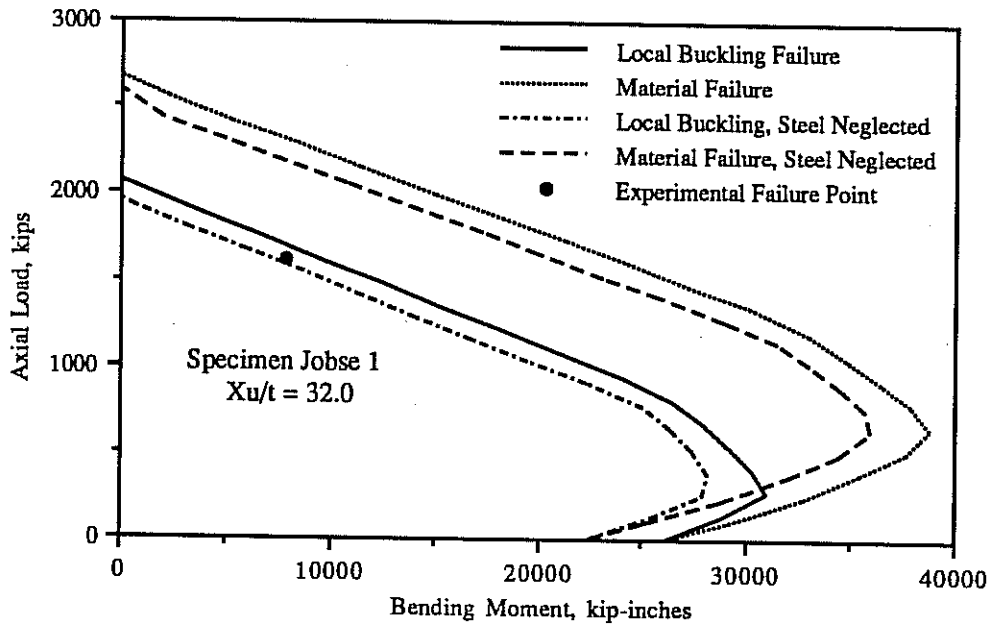


Figure 5.15: Interaction Diagrams for Specimen 1 of Jobse and Moustafa

5.4.2.2. Specimen 2A (Segmental, 60" x 60", 1.5" walls, $X_u/t = 32.0$)

Figure 5.16 shows the experimental and theoretical results for Jobse's Specimen 2A. As with Jobse's Specimen 1 the four solutions shown have a different hierarchy than the segmental specimens of the present study because Jobse's specimens had very slender walls and were lightly reinforced. The experimental failure point lies between the two solutions which neglect local wall buckling and the two solutions

which include local wall buckling. That is, the specimen exhibited strength greater than either of the two local wall buckling solutions (including and neglecting non-post-tensioned reinforcement) would indicate.

Specimen 2A was the second segmental specimen fabricated by Jobse. During fabrication of the first specimen methods of placing and consolidating concrete in the thin walls were studied extensively. When Specimen 2A was fabricated only the least amount of vibration required to consolidate the concrete was applied, so migration of bleed water to the top of the specimen was probably minimal. Thus the strength reduction factor k_3 in the Hognestad constitutive model, which accounts for the water gain effect, should probably have a value greater than 0.85. This would raise the analytical solutions shown in Figure 5.16, making the analytical solutions in better agreement with the experimental failure point.

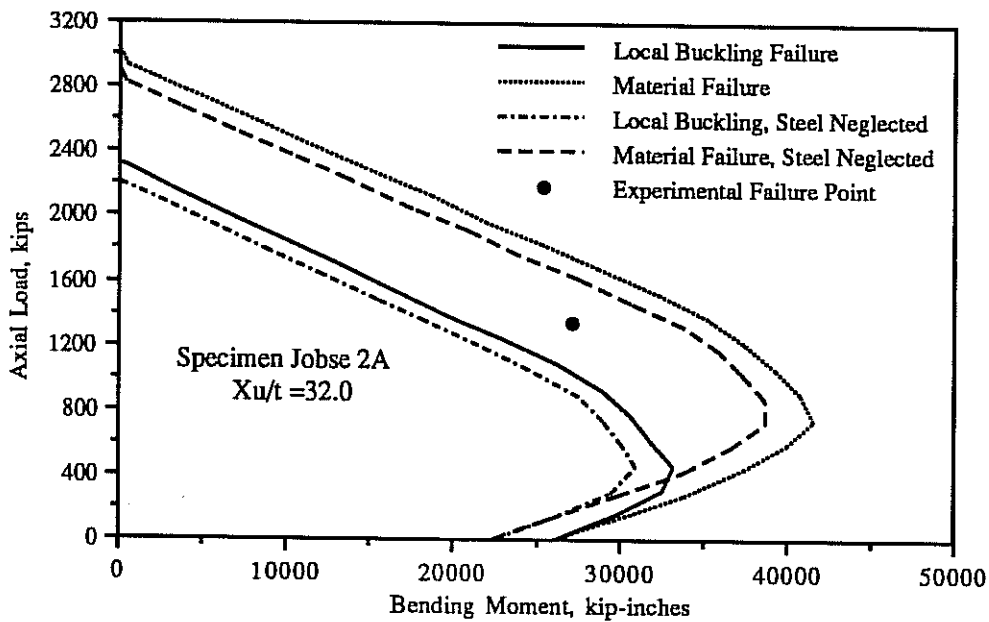


Figure 5.16: Interaction Diagrams for Specimen 2A of Jobse and Moustafa

5.4.3. *Computed Capacities of Test Specimens of Poston et al.*

The four hollow columns tested by Poston et al. were loaded by simultaneous axial load and biaxial bending. Since the analytical model developed in this study is for simultaneous axial load and uniaxial bending, it cannot be used to analyze the specimens of Poston et al. However, Poston used a finite strip program, called BIMPHI, to analyze the four specimens and found excellent agreement between the experimental results and the BIMPHI solutions, as shown in Figure 1.6.

Since BIMPHI includes no provisions for local wall buckling and the agreement between BIMPHI and the experimental results is excellent, it can be concluded that local wall buckling did not influence the behavior of the specimens. Indeed, results from the plate buckling program PLCRST developed in this study indicate that the wall slenderness ratios of the specimens were so low that, practically speaking, local buckling probably could not occur (Table 5.1). Thus the capacities of the specimens were determined purely by material failure, as indicated by the analytical results from BIMPHI.

5.4.4. *Computed Capacities of Test Specimens of Procter*

The plate buckling program PLCRST was used to determine the buckling stresses of the walls of the hollow sections tested by Procter. It was found that all of the specimens had wall slenderness ratios so low that the theoretical wall buckling stress was greater than 99.9% of the crushing stress of the concrete. Since the specimens were all loaded concentrically, interaction diagrams were not generated for these specimens. Instead, a simple hand calculation, outlined in Figure 1.5 gives the capacity of the concentrically loaded sections. (This hand calculation gives exactly the same result as the section analysis program HOLMP for zero applied moment). The theoretical and experimental strengths are compared in Table 5.2. All of the specimens, except for Specimen 1, have observed-to-predicted strength ratios close to 1.0.

The apparent under-strength of Specimen 1 can be attributed to the method of casting employed by Procter. All of Procter's specimens were cast in a horizontal position. This arrangement required that fresh concrete be worked underneath the central core form and around the reinforcement cage to fill the bottom face of the

specimen. Thus considerable vibration of the concrete was probably required, which would promote the migration of water towards the top of the formwork. For this reason, in calculating the strengths of the specimens the value of the water gain strength reduction factor, k_3 , was assumed to be 0.85. The walls of Specimen 1 were only 0.83 inches thick, so Specimen 1 required the most vibration of any specimen to achieve proper consolidation. Therefore the water gain effect would be most pronounced in Specimen 1, perhaps accounting for its reduced strength.

The unique mode of failure of Specimen 1, compared to all other specimens of Procter, further supports the hypothesis that the water gain effect reduced the strength of the specimen. Specimen 1 failed by spalling of the outside layer of concrete on all four faces over about half the height of the specimen. This could indicate stratification of the strength of the concrete through the thickness of the walls due to the upward migration of water during the horizontal casting operation.

5.5. Discussion of Experimental and Analytical Results

5.5.1. *Effect of Wall Slenderness Ratio on Section Capacity*

The experimental member capacities divided by the computed member capacities are plotted against wall slenderness ratio in Figures 5.17 to 5.20. For each of the four figures a different method of computing strength was used: in Figure 5.17 wall slenderness effects were excluded and non-post-tensioned (discontinuous) steel in segmental specimens was excluded; in Figure 5.18 wall slenderness effects were included and non-post-tensioned reinforcement in segmental specimens was excluded; in Figure 5.19 wall slenderness effects were excluded and non-post-tensioned reinforcement in segmental specimens was included; and in Figure 5.20 wall slenderness effects were included and non-post-tensioned reinforcement in segmental specimens was included. Table 5.5 below clarifies the basis of calculations for each of the four figures. Tables 5.2 through 5.4 and Figure 1.6 give the numerical data used to plot the figures.

It should be noted that in Figures 5.17 to 5.20 the capacity ratios (ordinates) are computed on the basis of the experimental and calculated ultimate axial loads. The four figures would be identical if plotted on the basis of experimental and calculated ultimate moments, with the exception of the data from the biaxial bending tests of Poston et al.²⁶ (Figure 1.6). Of the three hollow pier specimens tested by Poston et al., two had moment capacity ratios of 1.04 and 1.09, but the specimen with the highest wall slenderness ratio, 7.6, had a moment capacity ratio of only 0.86. It is not known whether the reduction in moment strength for this one specimen was due to wall slenderness or to some problem with the test apparatus or fabrication of the

specimen. Therefore, strictly speaking, the discussion which follows is applicable to axial capacity and moment capacity for the use of uniaxial bending only, and may not be applicable to the case of biaxial bending. A larger body of experimental data is required before definitive conclusions can be drawn about wall slenderness effects in thin-walled, biaxially loaded concrete compression members.

	Local Wall Buckling Included	Local Wall Buckling Excluded
Non-Post-Tensioned Reinf. Included	Figure 5.20	Figure 5.19
Non-Post-Tensioned Reinf. Excluded	Figure 5.18	Figure 5.17

Table 5.5: Basis of Calculations for Figures 5.17 to 5.20

In the four figures three data points tend to lie outside the overall trend of the data: Specimen 1 of Procter (indicated by the mark "1" in each figure), and specimens 4M18 (indicated by the mark "2") and 12S29 (indicated by the mark "3") of the present study. These are discussed below. All three out the outlying points resulted from unusual conditions encountered in casting scale-model specimens. It is not expected that these conditions would affect the fabrication of full-scale piers and pylons.

As discussed in Section 5.4.4 Specimen 1 of Procter (mark "1" in the figures) probably exhibited an unusually low strength because of difficulties of achieving proper consolidation during casting. The mode of failure of Specimen 1 seemed to indicate the water gain effect was more prominent in this specimen than in the other specimens of Procter.

Specimen 4M18 of the present study (mark "2" in the figures) was discussed in section 5.4.1.4. It was noted that an excessive amount of bleed water was observed at the top of specimen 4M18 after casting, indicating that the water gain effect was especially severe. Because of the low strength observed for specimen 4M18 specimen 10ML18 was constructed using a multiple-lift casting technique which minimized the water gain effect. Notice that the data point of specimen 10ML18, directly above the 4M18 data point in Figures 5.17 to 5.20, agrees more closely with the overall trend of the experimental data.

The strength of specimen 12S29 of the present study (mark "3" in the figures) was discussed in Section 5.4.1.12. It was determined that the water gain effect was probably not prominent in this specimen, resulting in a conservative analytical prediction of strength. The specimen also appeared to gain added strength from the presence of the non-post-tensioned reinforcement, even though the reinforcement was discontinuous at the joints between segments. While this added capacity cannot be relied on for design purposes, it does lead to conservative predictions of the strength of most of the segmental specimens of the test program.

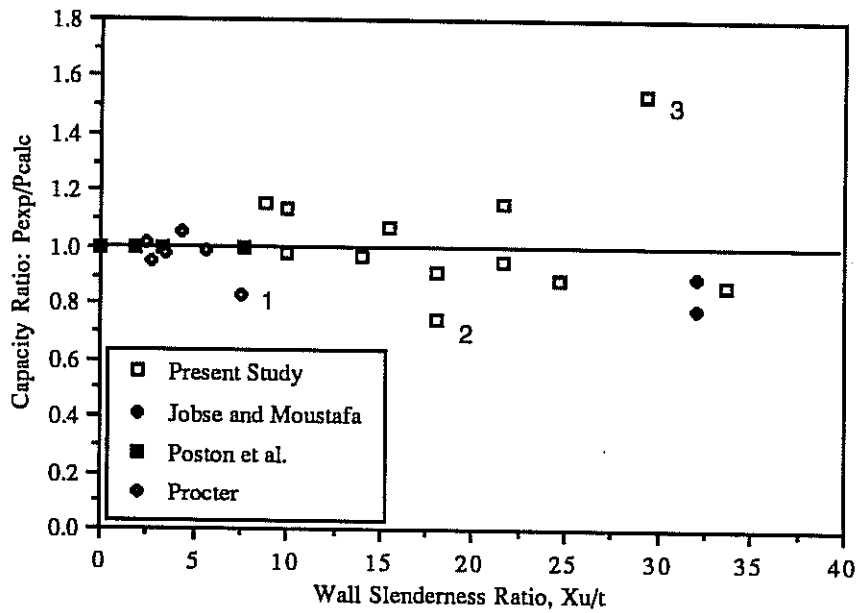


Figure 5.17: Experimental/Analytical Results Excluding Local Wall Buckling, and Excluding Non-Post-Tensioned Reinforcement in Segmental Specimens

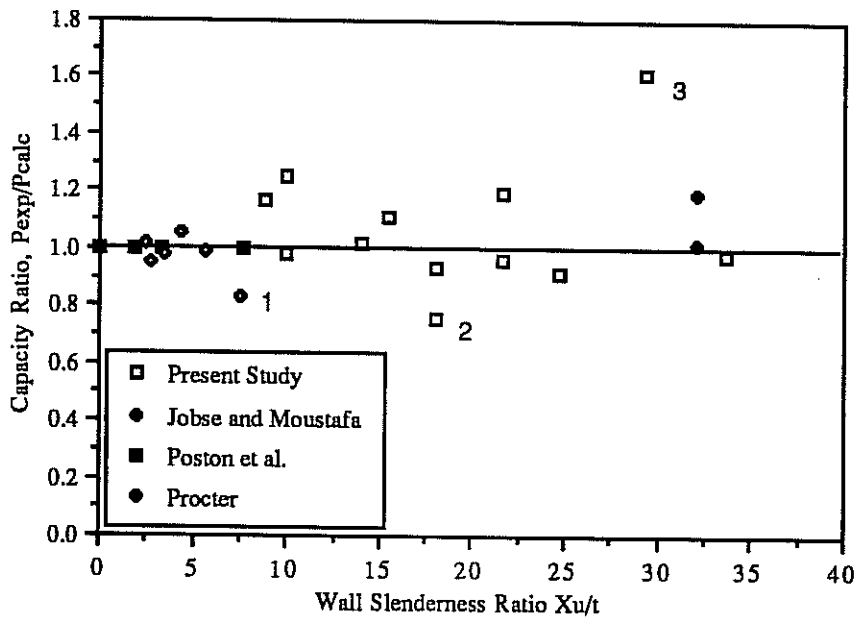


Figure 5.18: Experimental/Analytical Results Including Local Wall Buckling, and Excluding Non-Post-Tensioned Reinforcement in Segmental Specimens

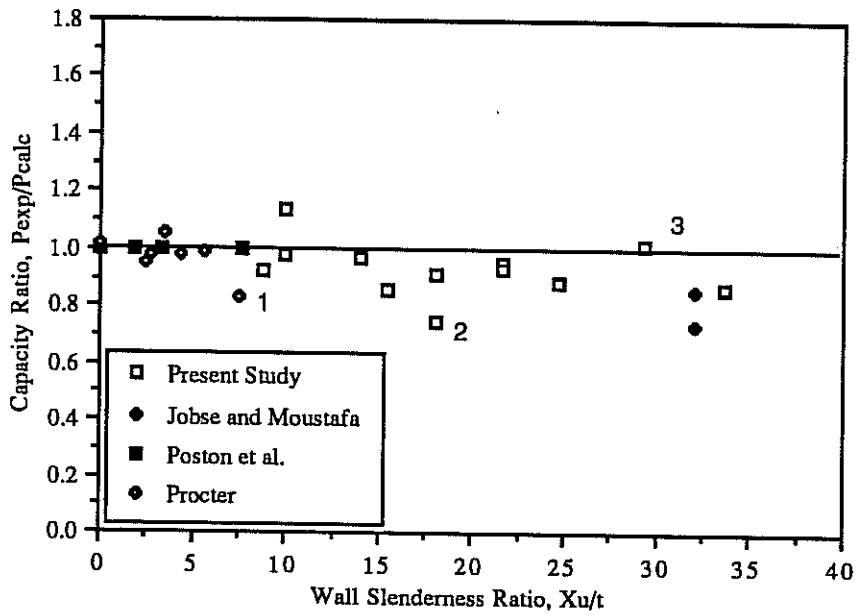


Figure 5.19: Experimental/Analytical Results Excluding Local Wall Buckling, and Including Non-Post-Tensioned Reinforcement in Segmental Specimens

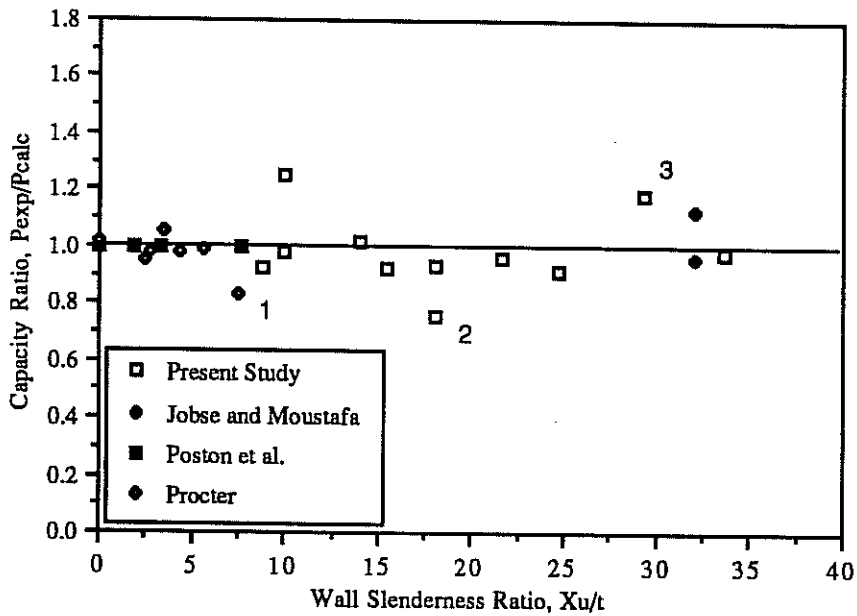


Figure 5.20: Experimental/Analytical Results Including Local Wall Buckling, and Including Non-Post-Tensioned Reinforcement for Segmental Specimens

The figure which most closely reflects current design practice is Figure 5.17, in which wall slenderness effects are neglected and non-post-tensioned (discontinuous) reinforcement in segmental specimens is neglected. It can be seen that this method of computation results in several non-conservative predictions of strength, especially at higher wall slenderness ratios. (The reasons for the positions of the outlying points labeled 1, 2 and 3 in the figure have been discussed above. These points are not included in the present discussion). For wall slenderness ratios of 14 or less the mean value of the data is 1.02, the standard deviation is 0.06, and the lower limit of the 95% confidence interval (the mean minus two standard deviations) is 0.90. However, for wall slenderness ratios of 15 or greater the mean value of the data is 0.94, the standard deviation is 0.12, and the lower limit of the 95% confidence interval is 0.70. These findings indicate that current design practices tend to produce non-conservative predictions of the strength of hollow sections with wall slenderness ratios of 15 or greater.

Figure 5.18 shows the results if local wall buckling effects are considered. The data points in the figure were calculated including the effects of wall slenderness and excluding the presence of non-post-tensioned (discontinuous) reinforcement in segmental specimens. (The outlying points 1, 2 and 3 have been discussed above. These points are not included in the present discussion). For low wall slenderness ratios of 14 or less the mean of the data is 1.03, the standard deviation is 0.08 and the lower limit of the 95% confidence interval is 0.87. These results are nearly the same as when wall slenderness effects were not considered. For high wall slenderness ratios of 15 or greater the mean of the data is 1.04, the standard deviation is 0.11 and the lower limit of the 95% confidence interval is 0.82. These results indicate that improved predictions of member strength are obtained when wall slenderness effects are considered for cross sections with wall slenderness ratios of 15 or greater. The lower limit of the 95% confidence interval, 0.82, is perhaps slightly low, but is still significantly improved over the value of 0.70 obtained when wall slenderness effects are not considered.

In Figure 5.19 local wall buckling is neglected and non-post-tensioned (discontinuous) reinforcement is included for segmental specimens. (Points 1, 2 and 3 are not included in this discussion). Oddly enough, this method of computation,

which is the most unrealistic of the four, produces fairly low scatter in the experimental data. The standard deviation of the data for wall slenderness ratios of 14 or less is 0.05, and for wall slenderness ratios of 15 or greater is 0.06. However, this method also produces the most non-conservative results for high wall slenderness ratios. The mean of the data for wall slenderness ratios of 14 or less is exactly 1.0, but for wall slenderness ratios of 15 or greater the mean is only 0.88. This demonstrates that not only is it important to include local wall buckling effects when calculating the capacities of members with high wall slenderness ratios, but it is also important to neglect the presence of non-post-tensioned reinforcing steel in segmentally-constructed members with high wall slenderness ratios.

Figure 5.20 shows the results obtained if wall slenderness effects are taken into account and non-post-tensioned (discontinuous) reinforcement in segmental specimens is included. (The outlying points 1, 2 and 3 are not included in this discussion). For wall slenderness ratios of 14 or less the predictions of capacity are fairly good, with a mean value of 1.01 and standard deviation of 0.08. The predictions for wall slenderness ratios of 15 or greater are somewhat non-conservative, with a mean of 0.97 and standard deviation of 0.07. This again demonstrates that non-post-tensioned reinforcing steel should be neglected when computing the capacity of segmentally constructed members with high wall slenderness ratios.

In summary, comparisons between the experimental data and various methods of computing the capacity of hollow rectangular concrete compression members indicate that wall slenderness effects must be considered for cross sections with wall slenderness ratios of 15 or greater. If the wall slenderness ratio is less than 15, then the wall slenderness does not appear to influence the capacity of the section. Discontinuous, non-post-tensioned reinforcement must be neglected in computing the capacity of segmentally-constructed members with wall slenderness ratios of 15 or greater. Surprisingly, for segmentally constructed members with wall slenderness ratios less than 15 a fairly good prediction of strength is obtained if discontinuous non-post-tensioned reinforcement is included in the analysis. However, until a rational theory which explains this behavior is developed, and until further tests are performed to confirm this behavior, it is recommended that discontinuous non-post-

tensioned reinforcement be neglected in calculation of the strength of all segmentally-constructed hollow concrete compression members, regardless of wall slenderness ratio.

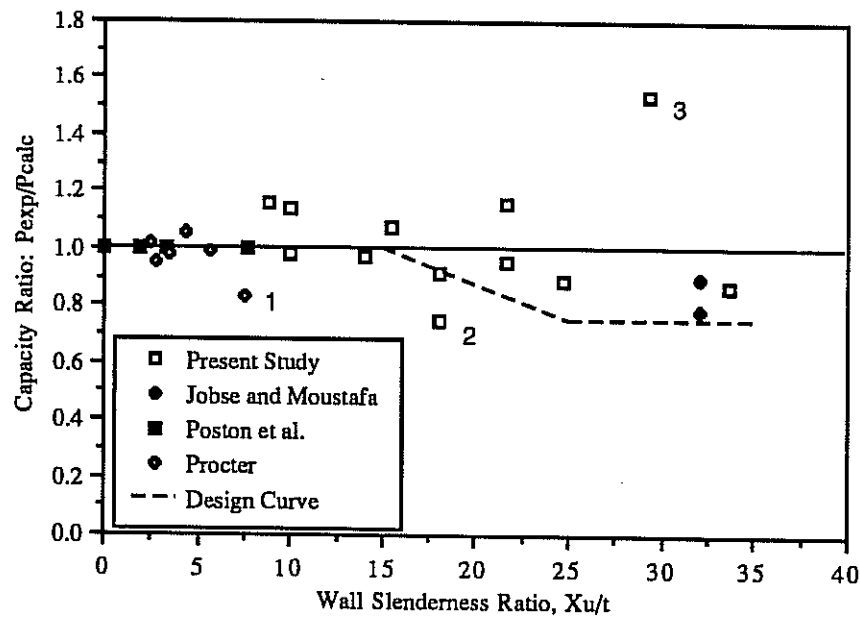


Figure 5.21: Data From Figure 5.17 With Proposed Design Curve

Based on the observations outlined above, a simplified design approach can be suggested which accounts approximately for strength reductions due to local wall buckling. The data points from Figure 5.17 are replotted in Figure 5.21, along with a proposed design curve shown by a dashed line. The design curve represents a reduction factor which should be applied to the calculated strength of the hollow cross section, when the strength has been calculated neglecting local compression flange buckling. (This factor is applied in addition to any other strength reduction factor specified by design codes). The strength reduction factor has a value of 1.0 for wall slenderness ratios up to 15.0. For wall slenderness ratios between 15.0 and 25.0 the factor decreases linearly to a value of 0.75. For wall slenderness ratios of 25.0 to 35.0 the factor has a constant value of 0.75. Since no experimental data exists for wall slenderness ratios greater than about 35.0, the empirically-derived strength reduction factor cannot be extended to higher wall slenderness ratios. It can

be seen in Figure 5.21 that the dashed design curve falls close to or below all of the available experimental data, except for the outlying points 1 and 2, which have been discussed in Section 5.5.1.

5.5.2. *Interaction of Local and Overall Buckling*

The experimental and theoretical phases of this study have both focused on the local wall buckling characteristics of short compression members. No consideration has been given to the overall or "Euler" buckling of tall, slender piers and pylons. Here a brief discussion of the relationship between local and overall buckling is given.

Local wall buckling and overall column buckling each cause a reduction in the capacity of a column below the strength calculated on the basis of material failure alone. In the study of metallic cross sections it has been established that the combined effects of local and overall buckling can reduce the strength of the member more than would be calculated if local and overall buckling effects are considered separately. That is, it is not always sufficient to consider the local and overall buckling strengths of a thin-walled metallic compression member separately and take the lower of the two strengths as the design capacity, for the actual capacity may be lower than either of the two cases. This so-called "interaction buckling" effect is most pronounced when the local buckling stress and overall buckling stress are nearly equal.

The interaction buckling effect for thin-walled metallic compression members has been studied extensively, both analytically and experimentally^{120,121,122,123,124,125,126,127,128,129,130,131,132,133,134,135,136}, but no investigations of interaction buckling are known for thin-walled concrete compression members. The phenomenon of interaction buckling is manifest in metallic compression members because of three factors^{120, 121, 122, 123, 126}: the presence of residual stresses; initial geometric imperfections of the member and its component plates; and, most important, post-buckling strength of the component plates of the cross section. Since residual stresses are not present in hollow concrete compression members, geometric imperfections are relatively small, and reliable post buckling strength of the component plates is not available (Section 1.6.) it could be

reasonably assumed that interaction buckling should not be a factor in determining the strength of hollow concrete piers and pylons. Thus, for tall, slender piers and pylons the local and overall buckling strengths of the member can be computed independently and compared with each other, as well as other limit states, to determine the failure load.

5.5.3. *Hollow Concrete Compression Member Failure Criteria*

In light of the experimental and analytical results obtained in this study, a set of failure criteria for thin-walled hollow concrete compression members can be proposed. Four modes of failure are considered, each of which is discussed below.

5.5.3.1. Tensile Yielding of Reinforcement

If the axial load on the member is relatively low and the bending moment is high then the strength of the cross section may be determined by tensile yielding of the reinforcement. It should not be assumed, however, that all failures occurring on the "tension" branch of the column interaction diagram (below the nose of the diagram) are governed by tensile yielding of the reinforcement. Almost all of the interaction diagrams shown in Figures 5.3 to 5.16 demonstrate that the reduction in the member capacity caused by local wall buckling may extend to the region below the nose of the interaction diagram. Tensile failure truly governs only on the lowest straight line portion of the diagram, where the local buckling and material failure solutions converge. From a design standpoint this observation is important since it demonstrates that local wall buckling should be checked even for members which are apparently governed by tensile yielding of the reinforcing steel.

5.5.3.2. Overall Buckling

If the member is sufficiently slender it may fail due to overall instability. The overall buckling strength is determined by the geometry, type of loading, boundary conditions and material properties of the member. Analytical methods for determining the overall buckling load of slender bridge piers and pylons are discussed by Jackson¹³⁷ and by Heins and Lawrie¹³⁸. As was discussed above in Section 5.52, it appears that the overall buckling load can probably be computed

independent of any local buckling behavior. That is, there should be no interaction between overall and local buckling.

5.5.3.3. Local Buckling

If the local buckling stress of the most highly compressed flange of the cross section is reached then the member may fail due to local wall instability. Determining the local wall buckling stress of thin-walled rectangular hollow concrete sections has been a major objective of this study, and methods have been presented for including the influence of local wall buckling on member capacity.

One part of the analytical model is the plate buckling program PLCRST, which determines the critical buckling stress for the compression flange of a rectangular cross section. PLCRST can be used to study the effects of wall slenderness ratio on the buckling stress of the flange. In Table 5.1 the calculated buckling stress is shown for all the compression flanges of the experimental specimens examined in this study. It can be seen that the calculated buckling stress of all flanges with wall slenderness ratios less than about 18 is nearly equal to the crushing stress of the concrete, $k_3 f_c$. This does not mean that flanges with wall slenderness ratios less than 18 do not buckle, but that the buckling stress of the flange is nearly equal to the crushing stress. From a different viewpoint it could be said that the buckling strain of the flange is nearly equal to the strain at peak compressive stress on the stress-strain diagram, ϵ_0 (Figure 4.1).

Certainly, though, there is a practical lower limit of wall slenderness ratio below which compression flanges simply crush rather than buckle. Members with wall slenderness ratios below this limit could be designed using conventional methods, which neglect wall slenderness effects. Members with wall slenderness ratios above this limit would have to be designed using methods which take wall slenderness effects into account. Tables 5.6 and 5.7 and Figure 5.22 provide the information necessary to establish this limit.

Specimen Number	Wall Slenderness Ratio	Experimental Failure Strain (Maximum Value in Center Region of Compression Flange), Microstrain	Calculated Buckling Strain of Compression Flange, Microstrain	Ratio of Experimental Failure Strain to Normal Design Failure Strain of 0.003	Ratio of Experimental Failure Strain to Calculated Buckling Strain
1M10	10.0	2707	3020	.90	.90
2M10	10.0	13437	1720	4.48	7.81
3M14	14.0	8052	1880	2.68	4.28
4M18*	18.0	1742	2800	0.58	0.62
5S9	8.8	3460	2790	1.15	1.24
6S16	15.5	2309	2210	.77	1.04
7S22	21.7	2700	2590	.90	1.04
8ML25	24.7	2915	2470	.97	1.18
9MLP22	21.7	2461	2570	.82	0.96
10ML18	18.0	1904	2590	.63	0.74
11ML34	33.6	2175	1890	.72	1.15
12S29*	29.3	1952	1910	.65	1.02

*Outlying data points, as discussed in Section 5.5.1

Table 5.6: Ratios of Experimental to Computed Compression Flange Failure Strains

Specimens From Table 5.6 That Are Included in Statistical Calculations	Ratio of Experimental Failure Strain to Normal Design Failure Strain of 0.003	Ratio of Experimental Failure Strain to Calculated Buckling Strain
Only Wall Slenderness Ratios from 15 to 34 Excluding Outlying Data Points*	Average = 0.80 Std. Dev. = 0.12	Average = 1.02 Std. Dev. = 0.16
Only Wall Slenderness Ratios from 15 to 34 Including Outlying Data Points*	Average = 0.76 Std. Dev. = 0.14	Average = 0.97 Std. Dev. = 0.19

* Two outlying data points in this data set are discussed in Section 5.5.1

Table 5.7: Statistical Data for Ratios of Experimental to Computed Failure Strains of Test Specimens

Table 5.6 shows the observed and theoretical compression flange failure strains for the test specimens of the present study. (Data from other studies is not given because insufficient strain data was gathered in those studies). The experimental failure strain, shown in the third column, is the maximum recorded strain in the center region of the plate just prior to failure. This definition of the experimental failure strain of the compression flange is consistent with the observations made of buckling tests on isolated slender concrete plates, described in Section 4.4.3. It was noted that the failure strain predicted by the plate buckling model and the maximum strain recorded in the center region of the plate just prior to failure were in good agreement. That is, the slender test plates buckled when the maximum measured strain in the center region of the plate, rather than the average strain in the plate, reached the predicted buckling strain. In the fourth column of Table 5.6 the predicted flange buckling strains, calculated using the program PLCRST (Reference 141) are listed. The fifth column shows the ratio between the experimental failure strain and the typical value of design failure strain for columns of 0.003. The sixth column shows the ratio between the experimental failure strain and the calculated buckling

strain of the compression flange.

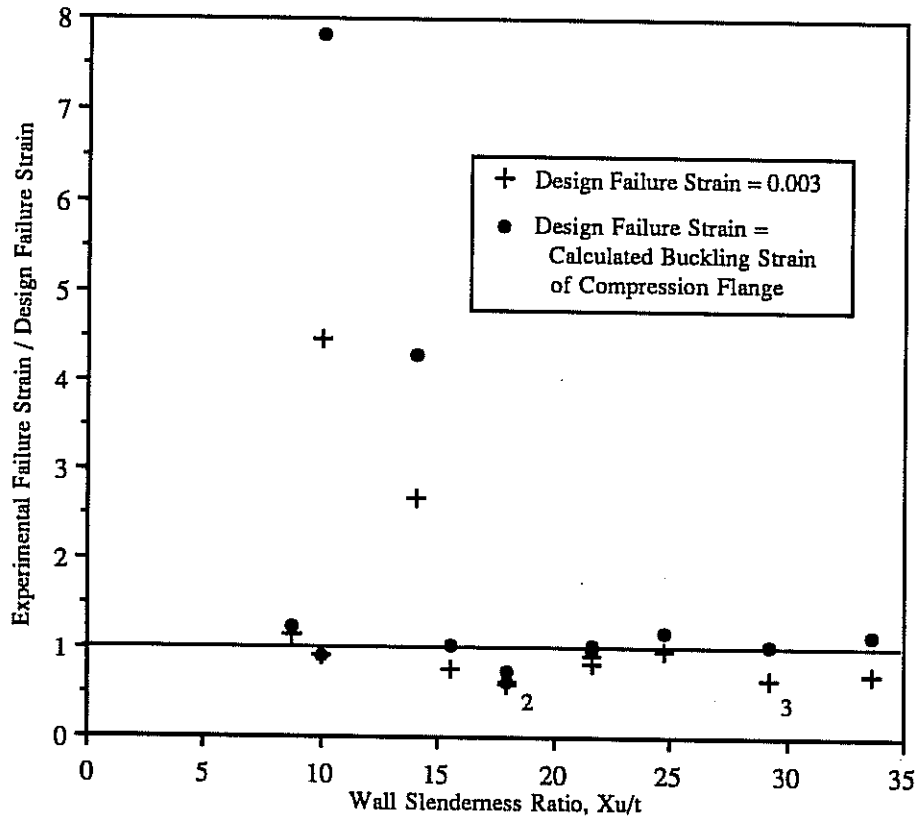


Figure 5.22: Failure Strain Ratios vs. Wall Slenderness Ratio

Statistical information for the data shown in Table 5.6 is given in Table 5.7. There appears to be a difference in behavior between specimens with wall slenderness ratios below 15 and specimens with wall slenderness ratios of 15 or greater, as discussed below. Thus, separate statistical information was desired for the group of specimens with wall slenderness ratios less than 15 and the group of specimens with wall slenderness ratios of 15 or greater. Only four specimens have wall slenderness ratios less than 15, and the data for those specimens is widely scattered, so statistical evaluation of the four data points would have little meaning. That is why no statistical information is given in Table 5.7 for specimens with wall slenderness ratios less than 15. Eight specimens have wall slenderness ratios of 15 or greater. The data for these specimens is not widely scattered, so statistical

evaluation of the data is useful. This information is given in Table 5.7. It was noted in Section 5.5.1 that for various reasons, two of the specimens from the test program of the present study behaved in an atypical manner, and that data points from these tests should probably be considered outliers. (These points are marked "2" and "3" in Figure 5.22). Statistical evaluations of the data set both including and excluding these outliers, are shown in Table 5.7. There is little difference in the results obtained whether or not the outliers are considered.

Figure 5.22 is a plot showing the ratio of experimental failure strain to design failure strain vs. wall slenderness ratio. Data for two values of design failure strain are shown: the constant design failure strain of 0.003 for columns specified by the two major United States concrete design codes (Section 5.2); and the design failure strain equal to the computed buckling strain of the compression flange, as shown in Table 5.6. It should be noted that some of the strain ratios shown in the figure are extremely high, indicating failure strains of 0.008 to 0.012. These were the actual failure strains recorded in the tests. However, the accuracy of strain gages on reinforcing bars after yielding of the bar has occurred is sometimes questionable. While the extremely high strains recorded at failure may not be strictly accurate, the readings do indicate strains well in excess of the yield strain of the steel, on the order of at least 0.005. These high strain readings were corroborated by readings from gages on other nearby bars.

It can be seen in Figure 5.22 that for wall slenderness ratios less than 15 the observed failure strain is generally equal to or greater than 0.003. This indicates that the design failure strain of 0.003 is an adequate, or possibly conservative, value to use in predicting the strength of hollow rectangular concrete compression members with wall slenderness ratios less than 15. However, for wall slenderness ratios of 15 or greater it can be seen that the failure strains are all less than 0.003. Table 5.7 shows that the mean of the data for wall slenderness ratios of 15 or greater is 0.80 and the standard deviation is 0.12. Thus the commonly used design failure strain for columns of 0.003 is significantly non-conservative for wall slenderness ratios of 15 or greater.

It can be seen in Figure 5.22 that for wall slenderness ratios less than 15 the observed failure strain is generally equal to or greater than the calculated buckling

strain of the compression flange. Thus for wall slenderness ratios less than 15 the calculated compression flange buckling strain is an adequate, or possibly conservative predictor of the failure strain. Since the constant design failure strain of 0.003 discussed above produces essentially the same results, and is simpler to apply in design practice, it is recommended that the commonly specified design failure strain of 0.003 be used for hollow rectangular concrete compression members with wall slenderness ratios less than 15.

Figure 5.22 shows that for wall slenderness ratios of 15 or greater the computed compression flange buckling strain is a good predictor of the observed failure strain. As shown in Table 5.7, the mean of the data for wall slenderness ratios between 15 and 34 is 1.02 and the standard deviation is 0.16. This is a substantial improvement over the results obtained using a constant design failure strain of 0.003. Therefore, it is recommended that the design failure strain used to compute the capacity of hollow rectangular concrete compression members with wall slenderness ratios of 15 to 34 be the calculated buckling strain of the compression flange, or the normally specified value of 0.003, whichever is less.

It is interesting to note that failure strains greater than 0.003 are commonly observed in laboratory tests on concrete compression members with solid cross sections. In tests of columns subject to high axial loads and controlled lateral end deformations, and tests on multi-panel building frames subject to both vertical (column) and lateral (floor) loads, Ford, Chang and Breen^{117,118} observed compressive failure strains in the columns of 0.010 or higher. The high strains at failure could be achieved because of the controlled lateral deformations in the column tests, and because of redistribution of shears and moments among the members of the multi-panel tests. It is unlikely that such high extreme fiber concrete compressive strains can ever be utilized in practical applications of hollow concrete piers and pylons for two reasons. First, in order to achieve high extreme fiber compressive strains the hollow concrete compression member must act as part of a frame which is capable of redistributing shears and moments. Careful consideration would have to be given to the structural system employed for a particular bridge to determine if such redistribution was possible. Second, it was noted in Section 5.2 that the calculated capacity of concrete compression members is relatively insensitive to the maximum

compressive strain, for values of maximum compressive strain greater than about 0.003. Thus, even if strains higher than 0.003 could be achieved, the increase in calculated strength would be small.

In summary, the experimental and analytical evidence indicate that a design failure strain of 0.003 may be used for hollow rectangular concrete compression members with wall slenderness ratios less than 15. For wall slenderness ratios of 15 or greater the design failure strain should be taken as the computed buckling strain of the compression flange, or 0.003, whichever is less.

5.6. Design Recommendations

In light of the information gained from the experimental and analytical portions of this study, as well as the review of current design practice, a number of recommendations can be made regarding the design of hollow concrete piers and pylons. These recommendations are divided into two categories: those having to do with analytical methods and those having to do with proportioning and detailing hollow concrete sections.

5.6.1. Analytical Methods

The following recommendations are made concerning the analysis of hollow concrete piers and pylons.

1) Numerical integration procedures are required for the analysis of thin-walled concrete compression members. Equivalent rectangular stress block methods are inadequate because they were developed for solid cross sections and do not reflect the high stresses in the thin walls of hollow cross sections.

2) Nonlinear material properties must be considered in the analysis of thin-walled sections. It was found that the Hognestad constitutive model (Figure 4.1) with k_3 equal to 0.85 provided an adequate representation of the uniaxial stress-strain curve for concretes with compression strengths between 3500 and 8000 psi. The value $k_3 = 0.85$ appeared to be slightly too high for some test specimens, but this was probably due to difficulties with casting the model specimens, which would not occur with prototype members.

3) The assumption that sections which are plane before loading remain plane

after loading is valid up to at least half the ultimate load, and is approximately correct at ultimate load, for hollow rectangular cross sections with wall slenderness ratios of 34 or less.

4) The maximum extreme fiber compressive strain of a hollow section may be limited by crushing or buckling of the compression flange. For concrete strengths up to 8000 psi, if the wall slenderness ratio of the compression flange of a rectangular cross section is 15 or greater it is possible that local wall buckling will control the design. Therefore the usual limit on the extreme fiber compressive strain of 0.003 may be applied for hollow rectangular sections with wall slenderness ratios less than 15. For wall slenderness ratios of 15 or greater the limit on the extreme fiber compressive strain should be the calculated buckling strain of the compression flange, or 0.003, whichever is less.

The possibility of local buckling of the compression flange of the cross section should be considered even if failure is expected on the "tension" branch (below the nose) of the column interaction diagram

5) The buckling stress and strain of the compression flange of a closed box cross section may be calculated, generally without undue conservatism, by assuming simply supported boundary conditions on all four edges of the plate. If the aspect ratio of the plate (length divided by width) is less than about 3 the buckling stress computed in this way may be excessively conservative.

6) Normal amounts of reinforcement in the compression flange of a rectangular cross section (0.5% to 2%) have little influence on the buckling stress of the flange.

7) No fundamental difference was observed between the behavior of monolithically cast hollow compression members and segmentally constructed hollow post-tensioned compression members with epoxied joints. However, in analyzing segmental members three special considerations must be made.

i) Initial strains induced by post-tensioning forces must be added to the strains induced by external loads.

ii) The area of grouted post-tensioned reinforcing steel in the cross section must be considered.

iii) The area of discontinuous non-post-tensioned reinforcing steel in the

cross section must be neglected.

8) Based on the available experimental evidence, a simplified design method has been proposed which accounts approximately for strength reductions due to local wall buckling.

5.6.2. *Detailing of Hollow Concrete Cross Sections*

It is particularly important with thin-walled hollow concrete cross sections that proper detailing procedures be followed if the full calculated strength of the member is to be achieved. In light of the observed behavior of thin-walled hollow concrete test specimens, the analytical methods developed in this study, and the review of current design practice the following recommended detailing practices have been developed for non-seismically-reinforced members.

1) Two layers of reinforcement are recommended in each wall of a hollow cross section, one layer near each face of the wall. This assumes that adequate concrete cover is maintained to guard against corrosion of the reinforcement. Most concrete design codes require or encourage two layers of reinforcement in walls (Section 2.3.1). The majority of hollow bridge piers and pylons surveyed contained two layers of reinforcement in each wall. All of the hollow test specimens from the present study and the study of Poston et al. had two layers of reinforcement in each wall and performed satisfactorily. The test specimens of Procter and of Jobse and Moustafa had one layer of reinforcement in each wall. The specimen of Procter with the thinnest walls exhibited an unusual spalling mode of failure which is probably explained by the method of casting, but which might have been prevented by the presence of two layers of reinforcement. The specimens of Jobse and Moustafa generally performed well, but the failure zones were more extensive than the failure zones of the specimens from the present study.

2) A minimum of 1% non-post-tensioned reinforcing steel is recommended for hollow concrete cross sections. The average reinforcement content of the hollow bridge piers and pylons surveyed in this study was 0.7%, but the average was skewed downward by a few sections with only one layer of reinforcement in each wall. The test specimens examined in this study which had two layers of reinforcement in each wall had reinforcement ratios between 1.5% and 2.6%. All of

these specimens performed satisfactorily. A minimum reinforcement content of about 1% for columns is specified by most concrete design codes (Section 2.3.1). The AASHTO *Specifications for the Design of Highway Bridges*³ allows a reduction below 1% if the full axial capacity of the cross section is underutilized. However, in view of the fact that creep and shrinkage of concrete may induce yielding of the reinforcement in very lightly reinforced members carrying high axial loads¹³⁹, and considering the need to control cracking in the walls of hollow cross sections, an absolute minimum of 1% is recommended for hollow cross sections.

3) A maximum lateral spacing of longitudinal reinforcing bars of 1.5 times the wall thickness or 18 inches, whichever is less, is recommended. This represents approximately the average requirement of most design codes for reinforcement in non-seismic structural walls (Section 2.3.1). In the experimental program of this study two specimens were tested which contained longitudinal bars spaced 3.8 times the wall thickness. There were no apparent adverse effects of this large spacing. However, in view of the limited experimental evidence the closer spacing is recommended.

4) A maximum longitudinal spacing of lateral reinforcement layers of 1.25 times the wall thickness or 12 inches, whichever is less, is recommended. The maximum layer spacing in the bridge plans surveyed was 1.25 times the wall thickness. Some design codes permit spacings of 3.0 times the wall thickness or 18 inches in non-seismically-reinforced walls (Section 2.3.1). However, considering the high axial loads bridge piers and pylons may carry it seems more appropriate to impose a maximum spacing limit of about one member thickness (the wall thickness). Most specimens tested in the present study and the study of Poston et al. had layer spacings of 0.8 to 1.3 times the wall thickness. All of these specimens performed well. Two specimens of the present study had spacings of 1.8 times the wall thickness. These specimens also performed well, but because of the limited data a spacing larger than about 1.25 times the wall thickness cannot be recommended. The specimens of Jobse and Moustafa and of Procter had only one layer of reinforcement in each wall, and longitudinal spacings of lateral reinforcement between 2.2 and 4.8 times the wall thickness. Since problems were noted with the failure modes of some of these specimens (see Item 3 above) they do not provide convincing evidence for

larger longitudinal spacings of lateral reinforcement.

5) Cross ties between layers of reinforcement are recommended at a maximum longitudinal spacing of 24 inches and lateral spacing of 24 inches, arranged in a "checkerboard" pattern. The main purpose of these ties is to contain the longitudinal and lateral reinforcing bars, preventing the bars from buckling outward through the concrete cover. Cross ties were not consistently provided in the bridge plans reviewed, but when they were provided the average spacings were about the same as the spacings recommended above. All the specimens examined in this study which had two layers of reinforcement in each wall also had cross ties positioned (to scale) at about these spacings. The cross ties performed well in confining the longitudinal and lateral reinforcing bars at the failure zone in these specimens. Cross ties should be located at positions where lateral and longitudinal bars intersect, and the hooks of the ties should enclose both the lateral and longitudinal bar at the intersection.

Additional cross ties are recommended along the top and bottom edges of the hollow segments used for post-tensioned construction. The failure mode of specimen 5S9 demonstrated the importance of these ties. In specimen 5S9 the ties along the top edge of one segment were missing. The specimen failed by the compression flange of that segment splitting along its center plane. In all other segmental specimens cross ties were provided along the segment edges at every pair of internal and external longitudinal bars (Figure 2.4). Those specimens did not fail by splitting of the compression flange. The provision of similar additional cross ties is recommended at transitions from hollow to solid cross sections, and at transitions from hollow sections to the superstructure or foundation, where stress concentrations may arise.

6) Lap splices of lateral reinforcing bars should be avoided. Instead lateral reinforcing bars in a layer should be joined by overlapping 90 degree bends at the corners of the cross section. Extra long legs on the bends are recommended. Lap splices of lateral reinforcement in the tests specimens of the present study were observed to perform very poorly. The ends of the splices separated and splayed outward at failure. If lap splices of lateral reinforcement must be used, then the overlapping bars should be enclosed over the length of the lap by the hooks of cross ties located at every intersection of the lateral bars and a longitudinal bar.

7) It is recommended that the corner regions of the cross section be adequately confined, as these regions can be highly stressed if biaxial bending occurs. A detail which performed well in confining the corner regions of the test specimens was two overlapping "hairpin" bars, as shown in Figure 2.3. This detail has the advantage of being easily fabricated.

8) Post-tensioning ducts should also be positively tied into the corner regions of the cross section. In several of the test specimens the corner post-tensioning bars ruptured the inner surface of the cross section and buckled inward at failure. The extent of the rupture was limited to a short region by the diagonal corner ties illustrated in Figure 2.3.

9) Grouting of post-tensioning ducts is recommended, as this ensures integral action of the post-tensioning bars and the concrete cross section.

5.6.3. *Proposed AASHTO Specifications*

The design recommendations summarized above are condensed and presented here in language suitable for inclusion in Section 8.16.4 ("Reinforced Concrete: Strength Design Method: Compression Members") of the *AASHTO Standard Specifications for Highway Bridges*³.

Hollow Rectangular Compression Members

1. *Design Methods*

1.1 The wall slenderness ratio of a hollow rectangular cross section, X_w/t , is defined in Figure 5.23 (below). Wall slenderness ratios greater than 35.0 are not permitted, unless specific analytical and experimental evidence is submitted justifying such values.

1.2 The equivalent rectangular stress block method shall not be employed in the design of hollow rectangular compression members with X_w/t of 15 or greater.

1.3 If X_w/t is less than 15, then the maximum usable strain at the extreme concrete compression fiber is equal to 0.003. If X_w/t is 15 or greater then the maximum usable strain at the extreme concrete compression fiber is equal to the computed local buckling strain of the widest flange of the cross section, or 0.003, whichever is less.

1.4 The local buckling strain of the widest flange of the cross section may be computed assuming simply supported boundary conditions on all four edges of the flange. Nonlinear material behavior shall be considered by incorporating the tangent material moduli of the concrete and reinforcing steel in computations of the local buckling strain.

1.5 In lieu of the provisions of Sections 1.3 and 1.4 the following approximate method may be used to account for the strength reduction due to wall slenderness. The maximum usable strain at the extreme concrete compression fiber shall be taken as 0.003 for all values of X_u/t up to and including 35.0. A strength reduction factor Φ_w shall be applied in addition to the usual strength reduction factor Φ (Section 8.16.1.2). Φ_w shall be taken as 1.0 for values of X_u/t up to and including 15.0. For values of X_u/t greater than 15.0 and less than or equal to 25.0, Φ_w shall be reduced continuously at a rate of 0.025 for every unit increase in X_u/t above 15.0. For values of X_u/t greater than 25.0 and less than or equal to 35.0, Φ_w shall be taken as 0.75.

1.6 Discontinuous, non-post-tensioned reinforcement in segmentally constructed hollow rectangular compression members shall be neglected in computations of member strength.

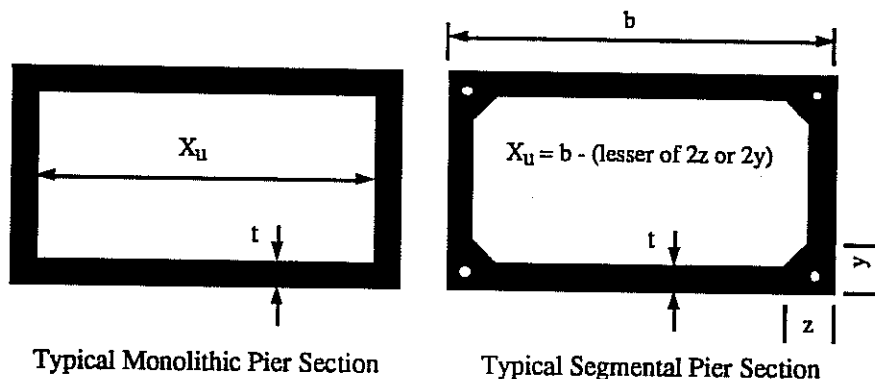


Figure 5.23: Definition of Wall Slenderness Ratio

2. Reinforcement

2.1 The area of longitudinal reinforcement in the cross section shall not be less than 0.01 times the gross area of concrete in the cross section.

2.2 Two layers of reinforcement shall be provided in each wall of the cross section, one layer near each face of the wall. The areas of reinforcement in the two layers shall be approximately equal.

2.3 The center-to-center lateral spacing of longitudinal reinforcing bars shall be no greater than 1.5 times the wall thickness or 18 inches, whichever is less.

2.4 The center-to-center longitudinal spacing of lateral reinforcing bars shall be no greater than 1.25 times the wall thickness, or 12 inches, whichever is less.

2.5 Cross ties shall be provided between layers of reinforcement in each wall. The cross ties shall include a standard 135 degree hook at one end, and a standard 90 degree hook at the other end (Section 8.23.1). Cross ties shall be located at bar grid intersections, and the hooks of cross ties shall enclose both the lateral and longitudinal bars at the intersections. Each longitudinal reinforcing bar and each lateral reinforcing bar shall be enclosed by the hook of a cross tie at a spacing not to exceed 24 inches.

2.6 For segmentally constructed members additional cross ties shall be provided along the top and bottom edges of each segment. These cross ties shall be placed so as to link the ends of each pair of internal and external longitudinal reinforcing bars in the walls of the cross section.

2.7 Lateral reinforcing bars may be joined at the corners of the cross section by overlapping 90-degree bends. Straight lap splices of lateral reinforcing bars are not permitted unless the overlapping bars are enclosed over the length of the splice by the hooks of at least four cross ties located at intersections of the lateral bars and longitudinal bars.

2.8 The longitudinal reinforcing bars in the corners of the cross section shall be enclosed by closed hoops. If closed hoops cannot be provided, then pairs of "U" shaped bars with legs at least twice as long as the wall thickness, and oriented at 90% to one another, may be substituted.

2.9 Post-tensioning ducts located in the corners of the cross section shall be anchored into the corner regions with closed hoops, or by stirrups having a 90-degree bend at each end which encloses at least one longitudinal bar near the outer face of the cross section.

2.10 Post-tensioning ducts shall be grouted in accordance with Section 4.33.9.

Chapter 6

Summary, Conclusions and Recommendations

6.1. Summary of Study Limitations

The conclusions of this study are subject to certain limitations, which are dictated by the scope of the investigation. These limitations are summarized below.

Both the experimental and analytical portions of this study focused on quasi-static, monotonic loading of hollow concrete cross sections. Cyclic loads, such as those induced by earthquakes, have not been considered.

Many of the conclusions drawn in this study apply primarily to rectangular cross sections, and are stated in those terms. In certain cases more general conclusions are made which do not depend on the cross section shape.

The experimental and analytical programs of the present study were limited to the case of loading under simultaneous axial load and uniaxial bending about the weak axis of the cross section. Thus, strictly speaking, the results of this study have not been confirmed for the case of biaxial bending. From a theoretical standpoint uniaxial bending about the weak axis represents the worst case with respect to local buckling of the compression flange. However, further experimental evidence is required before the results of this study can be applied to biaxially loaded members.

The maximum wall slenderness ratio explored in the present experimental program was 34, but the analytical model indicates that the conclusions drawn from the experimental program should be valid for wall slenderness ratios up to about 40.

The range of concrete strengths considered in the experimental and analytical programs was from approximately 3500 psi to 8000 psi.

6.2. Test Program Summary

In the experimental program of this study twelve short hollow rectangular reinforced concrete columns were tested under simultaneous axial load and uniaxial bending about the weak axial of the cross section. The wall slenderness ratios of the wide faces of the cross sections varied from about 9 to 34. Two layers of reinforcement were provided in each wall of the cross section. Four of the test

specimens were segmentally constructed, with the segments epoxied together and post-tensioned.

Data gathered during the experiments included load, overall specimen deformations, local out-of-plane deformation of the compression flange, and strains in longitudinal reinforcing bars. Observations were also made of crack patterns, the failure mode, and the performance of reinforcing details.

In addition to the results of the tests from the present study, data from three other test programs on hollow concrete cross sections were examined. Jobse and Moustafa^{27,28} tested two short hollow concrete square box columns with wall slenderness ratio of 32, subject to simultaneous axial load and uniaxial bending. Poston et al.²⁶ tested three single and multiple cell hollow columns with maximum wall slenderness ratio of 7.6, subject to simultaneous axial load and biaxial bending. Procter²⁵ tested six small-scale hollow stub columns with maximum wall slenderness ratio of 7.5, subject to concentric axial load.

6.3. Analytical Model Summary

An analytical model has been presented which predicts the strength of a hollow rectangular compression member subject to simultaneous axial load and uniaxial bending about the weak axis. Local buckling of the compression flange of the cross section is included in the model, but overall, or "Euler" buckling of the member is not considered. The analytical model consists of two components: a local plate buckling model; and an overall section capacity model.

The local plate buckling model predicts the buckling stress of a rectangular reinforced concrete plate which is elastically restrained against rotation along its two long edges, simply supported along its two short edges, and subject to an in-plane load uniformly distributed along the two short edges. The underlying theory for the model is described in Section 4.4. The primary variables in the model are plate geometry, reinforcement content, concrete and reinforcement material properties, width of side flanges (which determines the degree of elastic rotational restraint provided along the long edges of the plate) and concrete and reinforcement material properties. Nonlinear material behavior is also taken into account. The plate buckling model was implemented in the computer program PLCRST, which can be

run on a personal computer. PLCRST is described in the Appendix and in Reference 141.

The section capacity model generates the axial load-moment interaction diagram for a hollow rectangular cross section, and includes the effects of local compression flange buckling, post-tensioning forces, and nonlinear material properties. The development of the section capacity model is described in Section 4.5. The main variables in the model are cross section geometry, reinforcement content, compression flange buckling stress, magnitude of post-tensioning force, and the material properties of the concrete and reinforcement. Nonlinear material behavior is taken into account. The model was implemented in the program HOLMP, which can be run on a personal computer. HOLMP is described in the Appendix and in Reference 141. HOLMP computes a series of discrete points lying on two axial load-moment interaction diagrams: one diagram includes the effects of local compression flange buckling, and the other diagram neglects the effects of local compression flange buckling.

6.4. Principal Conclusions

As a result of the experimental and analytical programs of this study, an examination of test results by others, and a review of current design practice, the following principal conclusions can be made.

1) Local wall buckling can reduce the capacity of essentially rectangular reinforced concrete compression members with hollow cross sections below the capacity determined by material failure alone.

2) If the wall slenderness ratio of the compression flange of a rectangular cross section (flange width divided by thickness) is less than about 15 then the flange fails due to crushing. In that case the strength of the cross section is conservatively predicted if the commonly specified value of 0.003 is assumed for the extreme fiber compressive strain at failure.

3) If the wall slenderness ratio of the compression flange of a rectangular cross section is 15 or greater then it is likely the flange will fail due to local buckling. In that case the extreme fiber compressive strain at failure should be taken as the calculated buckling strain of the compression flange, or 0.003, whichever is less.

4) The buckling stress and strain of the wide flange of a rectangular cross section can be evaluated without excessive conservatism in practical cases, by

assuming simply supported boundary conditions on all four edges of the plate. Nonlinear material properties must be considered when computing the buckling stress and strain.

5) The assumption that cross sections which are plane before loading remain plane during loading was observed experimentally to be approximately correct at ultimate load for rectangular cross sections with wall slenderness ratios as high as 34.

6) A check for local wall buckling should be made even if a member is found to fail on the "tension" branch of the axial load-moment interaction diagram.

7) The Hognestad constitutive model (Figure 4.1) with $k_3 = 0.85$ was found to adequately predict the uniaxial stress-strain behavior for concretes with strengths between 3500 psi and 8000 psi.

8) No fundamental difference was observed between the behavior of monolithically cast non-post-tensioned, and segmentally constructed post-tensioned test specimens. In analyzing the strength of segmental, post-tensioned members the post-tensioning forces and the presence of post-tensioned reinforcement must be taken into account, and discontinuous, non-post-tensioned reinforcement must be neglected.

9) A number of recommendations for detailing of reinforcement have been outlined in Section 5.6.2. Two of these recommendations are most significant. First, cross ties must be provided between the two layers of reinforcing steel in each wall of the cross section, especially along the top and bottom edges of the hollow segments used for segmental construction. Second, straight lap splices of lateral reinforcing bars should be avoided, substituting instead overlapping 90-degree bends at the corners of the cross section.

10) Based on the available experimental evidence, a simplified design method has been proposed which accounts approximately for strength reductions due to local wall buckling.

6.5. Recommendations for Future Research

Five areas of future research are recommended. The first two of these areas are broad in scope and of primary importance: the behavior of hollow concrete piers and pylons subject to seismic loads; and the biaxial bending behavior of hollow concrete

piers and pylons. The second three areas are more limited in scope but still merit investigation: the influence of the water gain effect on the strength of full scale hollow concrete compression members; methods of providing local stiffening to slender walls in hollow concrete cross sections; and the local buckling of thin compression flanges of flexural members.

The seismic performance of hollow concrete compression members with slender walls has not been investigated in this study. The only known tests on hollow concrete sections in which cyclic lateral loads were applied to simulate earthquake conditions are those conducted by Mander, Priestly and Park³⁰, and Zahn, Park and Priestly²⁹. These are summarized in Section 1.6.2. The walls of the hollow sections in these tests were rather stocky. While the tests provide limited insight into reinforcement detailing requirements for seismic loading, further study is needed to develop a broad understanding of the response of hollow concrete compression members to earthquake loads. In particular, tests on sections with more slender walls are required, limits on reinforcement contents need to be determined, and a more thorough understanding of detailing requirements needs to be established. In this way the proper balance may be struck between the benefits of hollow concrete sections (high stiffness, low weight, and reduced material costs) and the requirements for satisfactory behavior under seismic loading (ultimate strength, overall cross section ductility, and local wall stability).

Biaxial bending of thin-walled hollow concrete sections has not been addressed in the present study. From a purely theoretical standpoint uniaxial bending about the weak axis represents the worst condition with respect to local buckling of a slender compression flange. However, since no specific analytical or experimental results have been obtained in this study for the case of biaxial bending, no conclusion can be drawn for that type of loading. Only one other experimental study is known in which hollow concrete sections were loaded in biaxial bendings²⁶. Of the three hollow specimens tested, the one with the highest wall slenderness ratio, 7.6, exhibited a moment capacity which was only about 85% of the calculated moment capacity (the full calculated axial capacity was achieved in the test). It is not known whether this reduction in moment strength was due to wall slenderness, or to some peculiarity in the experiment or fabrication of the specimen. In light of the very

limited experimental and analytical results available for biaxial bending, further research is required in this area.

In this study it was noted that several of the test specimens exhibited strengths that were lower than predicted. This strength reduction was attributed to the water gain effect (the upward migration of free water in the fresh concrete of vertically-cast columns). The water gain effect is thought to be especially prominent in the test specimens because of the difficulties encountered in casting thin walls at small scale. However, it is not known how severe the water gain effect is in prototype hollow concrete members. Core samples taken from full-scale bridge piers and pylons, or from wall sections cast in the laboratory, would reveal the variations in concrete strength with height. In this way guidelines could be established for casting procedures and maximum lift heights for hollow concrete cross section with thin walls.

It has been established in this study that local wall buckling can reduce the capacity of thin-walled hollow concrete compression members. If cross sections with very thin walls are to be used in practice, then methods for stiffening the walls to prevent local buckling need to be developed. The simplest technique, already employed in some designs, is to provide longitudinal diaphragms inside the hollow section. These divide the cross section into multiple cells, thereby reducing the slenderness ratios of the side walls. However, this method greatly complicates the construction process, and requires a substantial amount of additional materials. Other methods of stiffening, such as longitudinal ribs, lateral collars, and lateral diaphragms, should be investigated.

There are many similarities between the compression flanges of thin-walled hollow box concrete bridge piers and the compression flanges of flexural members with hollow box and "T" cross sections. Local buckling of the thin compression flanges of flexural members has not been adequately addressed by design codes. For example, the U. S. specification for segmental concrete bridge construction¹⁴² permits box girders with flange width-to-thickness ratios as high as 30, without requiring any check for flange instability. In light of the results of this study it would be appropriate to re-examine such provisions and develop specific design guidelines for concrete box and "T" flexural members with thin flanges.

References

- 1 Poston, R. W., Diaz, M. and Breen, J. E., "Design Trends for Concrete Bridge Piers," *Journal of the American Concrete Institute*, January-February 1986, pp 14-20.
- 2 *Building Code Requirements for Reinforced Concrete (ACI 318-89) and Commentary - ACI 318R-89*, American Concrete Institute, Detroit, 1989.
- 3 *Standard Specifications for Highway Bridges, 14th Edition*, American Association of State Highway and Transportation Officials (AASHTO), Washington, D. C., 1989.
- 4 American Concrete Institute Standard ACI 307-XX (Draft standard to supersede ACI 307-79), American Concrete Institute, Detroit, 1987.
- 5 *CEB-FIP Model Code for Concrete Structures*, International System of Unified Standard Codes of Practice for Structures, Volume II, Comité Euro-International du Béton (CEB), 1978.
- 6 *Concrete Structures*, SIA Standard 162, Schweizerischer Ingenieur und Architekten Verein, July 1989, Zurich.
- 7 *Beton und Stahlbeton, Bemessung und Ausführung - DIN 1045*, (Concrete and Reinforced Concrete, Design and Construction - DIN 1045), Deutsches Institut für Normung, July 1988.
- 8 *Code of Practice for the Design of Concrete Structures*, NZS 3101, Parts 1 and 2, Standards Association of New Zealand, Wellington, 1982.
- 9 *Beton-Kalender*, (Concrete Calendar), Wilhelm Ernst und Sohn, Berlin, 1983, Volume II, Section 13.2, p 660.
- 10 *Autobahnbrücke über die Mosel bei Dieblich-Winningen*, Kirschbaum Verlag, Bon - Bad Godesberg, 1972, pp 34-38.
- 11 Podolny, Walter, Jr. and Muller, Jean M., *Construction and Design of Prestressed Concrete Segmental Bridges*, John Wiley and Sons, New York, 1982, p 231.
- 12 Jenkins, Thomas D., "Glade Creek Bridge, Steel Fills a 'Missing Link'," *Modern Steel Construction*, AISC, Number 4, 1989, pp 9-16.

- 13 Stowell, Elbridge Z., Heimerl, George J., Libove, Charles, and Lundquist, Eugene E., "Buckling Stresses for Flat Plates and Sections," *Transactions, ASCE*, Paper No. 2506, Vol. 115, 1952, pp 545-578.
- 14 Lundquist, E. E., Stowell, E. Z. and Schuette, E. H., "Principles of Moment Distribution Applied to Stability of Structures Composed of Bars or Plates," *Wartime Report No. L-326*, National Advisory Committee for Aeronautics, 1943.
- 15 Kroll, W. D., "Tables of Stiffness and Carry-Over Factors for Flat Rectangular Plates Under Compression," *Wartime Report No. L-398*, National Advisory Committee for Aeronautics, 1943.
- 16 Kroll, W. D., Fisher, G. P., and Heimerl, G. J., "Charts for Calculation of the Critical Stress for Local Instability of Columns With I-, Z-, Channel, and Rectangular-Tube Sections," *Wartime Report No. L-429*, National Advisory Committee for Aeronautics, 1943.
- 17 Liew, J. Y. Richard, Shanmugam, N. E. and Lee, S. L., "Local Buckling of Thin-Walled Steel Box Columns," *Thin-Walled Structures*, Vol. 8, Elsevier Science Publishers, Ltd., England, 1989, pp 119-145.
- 18 Shanmugam, N. E., Liew, J. Y. Richard and Lee, S. L., "Thin-Walled Steel Box Columns Under Biaxial Loading," *Journal of Structural Engineering, ASCE*, Vol. 115, No. 11, November, 1989, pp 2706-2726.
- 19 Rawlings, B. and Shapland, P., "The Behavior of Thin-Walled Box Sections Under Gross Deformation," *The Structural Engineer*, Vol. 53, No. 4, April 1975, pp 181-186.
- 20 Snyder, Julian and Lee, Sing-Lip, "Buckling of Elastic-Plastic Tubular Columns," *Journal of the Structural Division, ASCE*, Vol. 94, No. ST1, January 1968, pp 153-173.
- 21 "Interaction Between General Buckling and Local Buckling," *European Constructional Steelwork, Second International Colloquium on Stability, Introductory Report*, Second Edition, De Liege University, Liege, Belgium, 1976/1977, pp 113-118.
- 22 Hancock, G. J., "Design Methods for Interaction Buckling in Box and I-Section Columns," *Proceedings of the Metal Structures Conference, Newcastle, May 11-14, 1981*, pp 6-10.
- 23 Bradford, Mark A. "Elastic Local Buckling of Trough Girders," *Journal of Structural Engineering, ASCE*, Vol. 116, No. 6, June 1990, pp 1594-1610.

- 24 Liew, J. Y. Richard, Shanmugam, N. E. and Lee, S. L., "Behavior of Thin-Walled Steel Box Columns Under Biaxial Loading," *Journal of Structural Engineering*, ASCE, Vol. 115, No. 12, December 1989, pp 3076-3094.
- 25 Procter, A. N., "Hollow rectangular Reinforced Concrete Columns," *Civil Engineering*, (London), September 1977, pp 45-49.
- 26 Poston, R. W., Gilliam, T. E., Yamamoto, Y. and Breen, J. E., "Hollow Concrete Bridge Pier Behavior," *Journal of the American Concrete Institute*, November-December 1985, pp 779-787.
- 27 Jobse, Harold J. and Moustafa, Saad E., "Applications of High Strength Concrete for Highway Bridges," *PCI Journal*, May-June 1984, pp 44-73.
- 28 *Applications of High Strength Concrete for Highway Bridges*, Report No. FHWA/RD 82/096, Offices of Research and Development, Federal Highway Administration, U. S. Department of Transportation, October 1981.
- 29 Zahn, F. A., Park, R. and Priestley, M. J. N., "Strength and Ductility of Reinforced Concrete Piers - A Summary Report," Report 83-7, Department of Civil Engineering, University of Canterbury, December 1983.
- 30 Mander, J. B., Priestly, M. J. N. and Park, R., *Seismic Design of Bridge Piers*, Research Report 84-2, Department of Civil Engineering, University of Canterbury, Christchurch, New Zealand, February 1984.
- 31 Mander, J. B., Priestley, M. J. N. and Park, R., "Behavior of Ductile Hollow Reinforced Concrete Columns," *Bulletin of the New Zealand National Society for Earthquake Engineering*, Vol. 16, No. 4, December 1983, pp 273-290.
- 32 Rowell, Randall B., "Behavior of Thin-Walled, Segmentally Constructed Post-Tensioned Bridge Piers," Master of Science thesis, The University of Texas at Austin, May 1990.
- 33 Ernst, George C., "Stability of Thin-Shelled Structures," *Journal of the American Concrete Institute*, December, 1952, pp 277-291.
- 34 Ernst, George C., Hromadik, Joseph J. and Riveland, Arvin R., "Inelastic Buckling of Plain and Reinforced Concrete Columns, Plates, and Shells," Bulletin Number 3, Univeristy of Nebraska, College of Engineering and Architecture, Engineering Experiment Station, Lincoln, Nebraska, August 1953.

- 35 Swartz, Stuart E., Rosebraugh, Vernon H. and Berman, Mark Y., "Buckling Tests on Rectangular Concrete Panels," *Journal of the American Concrete Institute*, January 1974, pp 33-39.
- 36 Swartz, Stuart E. and Rosebraugh, Vernon H., "Buckling of Reinforced Concrete Plates," *Journal of the Structural Division*, ASCE, Vol. 100, No. ST1, January 1974, pp 195-208.
- 37 Swartz, S. E., Rosebraugh, V. H., and Rogacki, S. A., "A Method for Determining the Buckling Strength of Concrete Panels," *Experimental Mechanics*, Vol. 14, No. 4, April 1974, pp 138-144.
- 38 Sherbourne, A. N., Liaw, C. Y. and Marsh, C., "Stiffened Plates in Uniaxial Compression," *Publications*, International Association for Bridge and Structural Engineering, Vol. 31, No. 1, 1971, pp 145-177.
- 39 Timm, Reiner and Kordina, Karl, "Stabilität mehrseitig gelagerter Betonwände, 1. Stufe," (Stability of Concrete Plates Supported on More Than One Side), Institut für Baustoffe, Massivbau und Brandschutz der Technischen Universität Braunschweig, Braunschweig, July 1979.
- 40 Kiel, Michael and Kordina, Karl, "Stabilität mehrseitig gelagerter Betonwände, 2. Stufe," (Stability of Concrete Plates Supported on More Than One Side), Institut für Baustoffe, Massivbau und Brandschutz der Technischen Universität Braunschweig, Braunschweig, May 1982.
- 41 Bozorgzadeh, M. Ebrahim, Grzeschkowitz, Rainer, Schönhoff, Brigitte, Teutsch, Manfred and Kordina, Karl, "Stabilität mehrseitig gelagerter Betonwände, 3. Stufe," (Stability of Concrete Plates Supported on More Than One Side), Institut für Baustoffe, Massivbau und Brandschutz der Technischen Universität Braunschweig, Braunschweig, June 1986.
- 42 Storkebaum, K.-H., "Ein Beitrag zur Traglastermittlung von vierseitig gelagerten Stahlbetonwänden," (A Contribution to the Determination of the Ultimate Load of Reinforced Concrete Walls Supported on Four Sides), Dissertation, Institut für Baustoffe, Massivbau und Brandschutz der Technischen Universität Braunschweig, Braunschweig, October 1977.
- 43 Wiegand, Erich, "Ein Beitrag zur Beulstabilität von Stahlbetonwänden mit nichtlinear-elastischem Werkstoffgesetz," (An Approach to Buckling of Reinforced Concrete Plates With a Nonlinear Material Law), Dissertation, Technischen Hochschule Darmstadt, 1970.

- 44 Aghayere, A. O. and Mac Gregor, J. G., "Stability of Concrete Plates," Structural Engineering Report 157, University of Alberta, Department of Civil Engineering, February 1988.
- 45 Massicotte, B., Elwi, A. E. and Mac Gregor, J. G., "Analysis of Reinforced Concrete Panels Loaded Axially and Transversely," University of Alberta, Department of Civil Engineering, July 1988.
- 46 Tran, Tan Dai, "Local Buckling of Thin, In-Plane Loaded Reinforced Concrete Plates," Master of Science thesis, The University of Texas at Austin, August, 1989.
- 47 Guralnick, S. A., Swartz, S. E., and Longinow, A., "Buckling of Reinforced Concrete Folded Plate Structures," *Concrete Shell Buckling*, ACI Special Publication No. 67, American Concrete Institute, Detroit, 1981, pp 111-134.
- 48 Swartz, Stuart E., and Rosebraugh, Vernon H., "Local Buckling of Long-Span Concrete Folded Plates," *Journal of the Structures Division*, Proceedings ASCE, Vol. 102, No. ST10, October 1976, pp 1981-1988.
- 49 Seide, Paul, "Stability of Cylindrical Reinforced Concrete Shells," *Concrete Shell Buckling*, ACI Special Publication No. 67, American Concrete Institute, Detroit, 1981, pp 43-62.
- 50 Griggs, P.H., "Buckling of Reinforced Concrete Shells," *Journal of the Engineering Mechanics Division*, Proceedings ASCE, Vol. 97, No. EM3, June 1971, pp 680-700.
- 51 Furnes, Olav, "Buckling of Reinforced and Prestressed Concrete Members - Simplified Calculation Methods," *PCI Journal*, July-August 1981, pp 86-115.
- 52 Song, Qi-gen and Scordelis, Alexander C., "Shear-Lag analysis of T-, I-, and Box Beams," *Journal of Structural Engineering*, ASCE, Vol. 116, No. 5, May 1990, pp 1290-1305.
- 53 Song, Qi-gen and Scordelis, Alexander C., "Formulas for Shear-Lag Effect of T-, I-, and Box Beams," *Journal of Structural Engineering*, ASCE, Vol. 116, No. 5, May 1990, pp 1306-1318.
- 54 *Building Code Requirements for Reinforced Concrete (ACI 318-89)*, American Concrete Institute, Detroit, 1989, Section 8.10.3.
- 55 *Manual of Steel Construction, Load and Resistance Factor Design, First Edition*, American Institute of Steel Construction, Chicago, 1986, Section I3.1.

- 56 Podolny, Walter, Jr. and Muller, Jean M., *Construction and Design of Prestressed Concrete Segmental Bridges*, John Wiley and Sons, New York, 1982, pp 38-40.
- 57 Finsterwalder, Ulrich and Schambeck, Herbert, "Die Elztalbrücke," *Der Bauingenieur*, Vol. 41, No. 6, 1966, pp 251-258.
- 58 Finsterwalder, Ulrich and Schambeck, Herbert, "Die Elztalbrücke," *Der Bauingenieur*, Vol. 42, No. 1, 1967, pp 14-21.
- 59 Podolny, Walter, Jr. and Muller, Jean M., *Construction and Design of Prestressed Concrete Segmental Bridges*, John Wiley and Sons, New York, 1982, pp 296-299.
- 60 Podolny, Walter, Jr. and Muller, Jean M., *Construction and Design of Prestressed Concrete Segmental Bridges*, John Wiley and Sons, New York, 1982, pp 243-244.
- 61 Podolny, Walter, Jr. and Muller, Jean M., *Construction and Design of Prestressed Concrete Segmental Bridges*, John Wiley and Sons, New York, 1982, pp 329-331.
- 62 Podolny, Walter, Jr. and Muller, Jean M., *Construction and Design of Prestressed Concrete Segmental Bridges*, John Wiley and Sons, New York, 1982, p 236.
- 63 Podolny, Walter, Jr. and Muller, Jean M., *Construction and Design of Prestressed Concrete Segmental Bridges*, John Wiley and Sons, New York, 1982, pp 304-311.
- 64 Podolny, Walter, Jr. and Muller, Jean M., *Construction and Design of Prestressed Concrete Segmental Bridges*, John Wiley and Sons, New York, 1982, pp 122, 240.
- 65 Podolny, Walter, Jr. and Muller, Jean M., *Construction and Design of Prestressed Concrete Segmental Bridges*, John Wiley and Sons, New York, 1982, pp 45-48.
- 66 Seven Mile Bridge, project plans, State of Florida Department of Transportation Structures, 1978.
- 67 Escatawpa River Bridge, project plans, Mississippi State Highway Department, 1983.

- 68 Podolny, Walter, Jr. and Muller, Jean M., *Construction and Design of Prestressed Concrete Segmental Bridges*, John Wiley and Sons, New York, 1982, pp 238,241.
- 69 Quinn, Stephen B. "Record Concrete Box Girder Spans Houston Ship Channel," *Civil Engineering*, ASCE, November 1983, pp 46-50.
- 70 Sunshine Skyway Bridge, project plans, State of Florida Department of Transportation Structures, 1982.
- 71 Cezard, C., Maurin, J., Vassord, J., Giacomelli, D., Beauveil, Y. and Moussard, M. "Construction des Viaducs de Nantua et des Neyrolles," *Travaux*, January 1986, pp 20-34.
- 72 Taylor, Peter R. and Torrejon, Jorge E., "Annacis Bridge, Simplicity Pays in Cable-Stayed Construction," *Concrete International*, July 1987, pp 13-22.
- 73 Schottwien Bridge, project plans, Semmering Schnellstrasse (S-6), Autobahnen- und Schnellstrassen-Aktiengesellschaft, 1985.
- 74 Bishara, Alfred G. and Papakonstantinou, Nicholas G., "Analysis of Cast-in-Place Concrete Segmental Cantilever Bridges," *Journal of Structural Engineering*, ASCE, Vol. 116, No. 5, May 1990, pp 1247-1268.
- 75 Houston Ship Channel Crossing La Porte-Baytown, project plans, Texas State Department of Highways and Public Transportation, 1990.
- 76 Billington, David P., *Robert Maillart's Bridges, the Art of Engineering*, Princeton University Press, Princeton, New Jersey, 1979, pp 51-62.
- 77 Janney, Jack R., Breen, John E., Geymayer, Helmut, Lockman, William T. and Rocha, Manuel, "The Use of Models in Structural Engineering," Paper SP 24-1, *Models for Concrete Structures*, ACI Special Publication SP-24, American Concrete Institute, Detroit, 1970, pp 1-18.
- 78 *Models for Concrete Structures*, ACI Special Publication SP-24, American Concrete Institute, Detroit, 1970, pp 1-18.
- 79 *Structural Models Conference*, Proceedings of the Structural Models Conference, Sydney 1972, sponsored by the School of Architectural Science at the University of Sydney, The Institution of Engineers, Australia, N. S. W. Division, and the Cement and Concrete Association of Australia, 1972.

- 80 Sabnis, Gajanan M., Harris, Harry G., White, Richard N. and Mirza, M. Saeed, *Structural Modeling and Experimental Techniques*, Prentice-Hall, Englewood Cliffs, 1983.
- 81 Zia, Paul, White, Richard N. and Vanhorn, David A., "Principles of Model Analysis," Paper SP 24-2, *Models for Concrete Structures*, ACI Special Publication SP-24, American Concrete Institute, Detroit, 1970, pp 19-39.
- 82 Fialho, J. F. Lobo, "Static Model Studies for Designing Reinforced Concrete Structures," Paper SP 24-9, *Models for Concrete Structures*, ACI Special Publication SP-24, American Concrete Institute, Detroit, 1970, pp 215-250.
- 83 Paulay, Thomas "The Design of Ductile Reinforced Concrete Structural Walls for Earthquake Resistance," *Earthquake Spectra*, Vol. 2, No. 4, Earthquake Engineering Research Institute, 1986, pp 783-823.
- 84 Priestley, M. J. N. and Park, R., *Strength and Ductility of Bridge Substructures*, Research Report 84-20, Department of Civil Engineering, University of Canterbury, Christchurch, New Zealand, December 1984.
- 85 Johnson, R. Paul, "Strength Tests on Scaled-Down Concretes Suitable for Models, With a Note on Mix Design," *Magazine of Concrete Research*, Vol. 14, No. 40, March 1962, pp 47-53.
- 86 Carpenter, James E., Roll, Frederic and Zelman, Maier I., "Techniques and Materials for Structural Models," Paper SP 24-3, *Models for Concrete Structures*, ACI Special Publication SP-24, American Concrete Institute, Detroit, 1970, pp 41-63.
- 87 Aldridge, Weldon W. and Breen, John E., "Useful Techniques in Direct Modeling of Reinforced Concrete Structures," Paper SP 24-5, *Models for Concrete Structures*, ACI Special Publication SP-24, American Concrete Institute, Detroit, 1970, pp 125-140.
- 88 Kosmatka, Steven H. and Panarese, William C., *Design and Control of Concrete Mixtures*, Thirteenth Edition, Portland Cement Association (PCA), Skokie, Illinois, 1988, p 36.
- 89 "Standard Specification for Concrete Aggregates," ASTM C33-86, American Society for Testing and Materials, Philadelphia, 1986.
- 90 "Standard Specification for Deformed and Plain Billet-Steel Bars for Concrete Reinforcement," ASTM A615-87, American Society for Testing and Materials, Philadelphia, 1987.

- ⁹¹ "Standard Test Method for Compressive Properties of Rigid Plastics," ASTM D695-88, American Society for Testing and Materials, Philadelphia, 1988.
- ⁹² "Standard Method of Making and Curing Concrete Test Specimens in the Laboratory," ASTM Standard C192-81, American Society for Testing and Materials, Philadelphia, 1981.
- ⁹³ *PCI Design Handbook*, Third Edition, Prestressed Concrete Institute, Chicago, 1985, p 4-40.
- ⁹⁴ Guyon, Y., *Prestressed Concrete*, John Wiley and Sons, New York, 1953, pp 127-174.
- ⁹⁵ Nilson, Arthur H., *Design of Prestressed Concrete*, John Wiley and Sons, New York, 1978, p 48.
- ⁹⁶ Hognestad, Eivind, "A study of Combined Bending and Axial Load in Reinforced Concrete Members," *University of Illinois Engineering Experiment Station Bulletin*, Series No. 399, 1951.
- ⁹⁷ Hognestad, Eivind, "Fundamental Concepts in Ultimate Load Design of Reinforced Concrete Members," *Journal of the American Concrete Institute*, June 1952, pp 809-828.
- ⁹⁸ Hognestad, Eivind, "Inelastic Behavior in Tests of Eccentrically Loaded Short Reinforced Concrete Columns," *Journal of the American Concrete Institute*, October 1952, pp 117-139.
- ⁹⁹ Hognestad, Eivind, Hanson, N. W. and McHenry, Douglas, "Concrete Stress Distribution in Ultimate Strength Design," *Journal of the American Concrete Institute*, December 1955, pp 455-479.
- ¹⁰⁰ Wang, P. T., Shah, S. P. and Naaman, A. E., "Stress-Strain Curves of Normal and Lightweight Concrete in Compression," *Journal of the American Concrete Institute*, November 1978, pp 603-611.
- ¹⁰¹ Carreira, Domingo J. and Chu, Kuang-Han, "Stress-Strain Relationship for Plain Concrete in Compression," *Journal of the American Concrete Institute*, November-December 1985, pp 797-804.
- ¹⁰² Desayi, Prakash and Krishnon, S., "Equation for the Stress-Strain Curve of Concrete," *ACI Journal Proceedings*, March 1964, pp 345-350.

- 103 Carrasquillo, Ramon L., Nilson, Arthur H. and Slate, Floyd O., "Properties of High Strength Concrete Subject to Short-Term Loads," *Journal of the American Concrete Institute*, May-June 1981, pp 171-178.
- 104 Pauw, Adrian, "Static Modulus of Elasticity of Concrete as Affected by Density," *ACI Journal, Proceedings*, December 1960, pp 679-688.
- 105 Brockenbrough, R. L. and Johnston, B. G., *USS Steel Design Manual*, United States Steel Corporation, Pittsburgh, 1981, p 72.
- 106 Timoshenko, Stephen P. and Gere, James M., *Theory of Elastic Stability*, Second Edition, McGraw-Hill Book Company, New York, 1961, pp 348-429.
- 107 Timoshenko, Stephen P. and Gere, James M., *Theory of Elastic Stability*, Second Edition, McGraw-Hill Book Company, New York, 1961, p 373.
- 108 Breen, John E. "The Restrained Long Concrete Column as a Part of a Rectangular Frame," PhD dissertation, The University of Texas at Austin, 1962, pp 34-36.
- 109 Fowler, Timothy J., "Reinforced Concrete Columns Governed by Concrete Compression," PhD dissertation, The University of Texas at Austin, 1966, pp 23-25.
- 110 "Standard Method of Making and Curing Concrete Test Specimens in the Laboratory," ASTM C192-81, American Society for Testing and Materials, Philadelphia, 1981.
- 111 "Standard Test Method for Compressive Strength of Cylindrical Concrete Specimens," ASTM C39-86, American Society for Testing and Materials, Philadelphia, 1986.
- 112 Hognestad, Eivind, "Fundamental Concepts in Ultimate Load Design of Reinforced Concrete Members," *Journal of the American Concrete Institute*, June 1952, pp 809-828.
- 113 Petersons, N., "Strength of Concrete in Finished Structures," *Transactions, Royal Institute of Technology*, Stockholm, Sweden, No. 232, 1964.
- 114 Fowler, Timothy J., "Reinforced Concrete Columns Governed by Concrete Compression," PhD dissertation, The University of Texas at Austin, January 1966, pp 209-212, 292.

- 115 *Building Code Requirements for Reinforced Concrete and Commentary (ACI 318-89) and Commentary - ACI 318R-89*, American Concrete Institute, Detroit, 1989, Section 10.2.3.
- 116 *Standard Specifications for Highway Bridges, 14th Edition*, American Association of State Highway and Transportation Officials (AASHTO), Washington, D. C., 1989, Section 8.16.2.3.
- 117 Ford, J. S., Chang, D. C. and Breen, J. E., "Behavior of Concrete Columns Under Controlled Lateral Deformation," *Journal of the American Concrete Institute*, January-February 1981, pp 3-20.
- 118 Ford, J. S., Chang, D. C. and Breen, J. E., "Experimental and Analytical Modeling of Unbraced Multipanel Concrete Frames," *Journal of the American Concrete Institute*, January-February 1981, pp 21-35.
- 119 Hognestad, Eivind, Hanson, N. W. and McHenry, Douglas, "Concrete Stress Distribution in Ultimate Strength Design," *Journal of the American Concrete Institute*, December 1955, p 471.
- 120 Bulson, P. S., "Local Stability and Strength of Structural Sections," *Thin-Walled Structures*, A. H. Chilver, Editor, John Wiley and Sons, New York, 1967, pp 153-207.
- 121 "Interaction Between General Buckling and Local Buckling," *Introductory Report, Second Edition*, European Convention for Constructional Steelwork, Second International Colloquium on Stability, DeLiege University, Liege, Belgium, 1976-1977, pp 113-118.
- 122 Braham, M., Rondal, J. and Massonnet, Ch., "Large Size Buckling Tests on Steel Columns With Thin-Walled Rectangular Hollow Sections," *Thin-Walled Structures*, Rhodes, J. R. and Walker, A. C., Editors, International Conference at the University of Strathclyde, Glasgow, Scotland, John Wiley and Sons, New York, 1980, pp 3-13.
- 123 Hancock, Gregory J., "Design Methods for Thin-Walled Box Columns," Research Report No. R 359, The University of Sydney, School of Civil Engineering, Civil Engineering Laboratories, January 1980.
- 124 Hancock, Gregory J., "Nonlinear Analysis of Thin Sections in Compression," Research Report No. R 355, The University of Sydney, School of Civil Engineering, Civil Engineering Laboratories, November 1979.

- 125 Hancock, Gregory J., "Nonlinear Analysis of Thin Sections in Compression," *Journal of the Structural Division*, ASCE, Vol. 107, No. ST3, March 1981, pp 455-471.
- 126 Dubas, P., Maquoi, R. and Massonnet, Ch., "Behaviour and Design of Steel Plated Structures," IABSE Surveys S-31/85, International Association for Bridge and Structural Engineering, August 1985.
- 127 Koiter, W. T. and van der Neut, A., "Interaction Between Local and Overall Buckling of Stiffened Compression Panels," *Thin-Walled Structures*, Rhodes, J. R. and Walker, A. C., Editors, International Conference at the University of Strathclyde, Glasgow, Scotland, John Wiley and Sons, New York, 1980, pp 61-85.
- 128 Braham, M., Grimault, J. P., Massonnet, Ch., Mouty, J. and Rondal, J., "Buckling of Thin-Walled Hollow Sections. Cases of Axially-Loaded Rectangular Sections," *Steel*, January 1980, pp 30-36.
- 129 Sridharan, Srinivasan and Ali, M. Ashraf, "Interactive Buckling in Thin-Walled Beam-Columns," *Journal of Engineering Mechanics*, ASCE, Vol. 11, No. 12, December 1985, pp 1470-1486.
- 130 Hancock, G. J., "Design Methods for Interaction Buckling in Box and I-Section Columns," Proceedings, Metal Structures Conference, Newcastle, May 11-14, 1981, pp 6-10.
- 131 Lee, Sing-Lip, Shanmugam, Nandivaram E. and Chiew, Sing-Ping, "Thin-Walled Box Columns Under Arbitrary End Loads," *Journal of Structural Engineering*, ASCE, Vol. 114, No. 6, June 1988, pp 1390-1402.
- 132 Chiew, Sing-Ping, Lee, Seng-Lip and Shanmugam, E., "Experimental Study of Thin-Walled Steel Box Columns," *Journal of Structural Engineering*, Vol. 113, No. 10, October 1987, pp 2208-2220.
- 133 Shanmugam, Nandivaram E., Chiew, Sing-Ping and Lee, Seng-Lip, "Strength of Thin-Walled Square Steel Box Columns," *Journal of Structural Engineering*, April 1987, pp 818-831.
- 134 Usami, Tsutomu and Fukumoto, Yuhshi, "Local and Overall Buckling of Welded Box Columns," *Journal of the Structural Division*, ASCE, Vol. 108, No. ST3, March 1982, pp 525-542.
- 135 Little, G. H., "The Strength of Square Steel Box Columns - Design Curves and Their Theoretical Basis," *The Structural Engineer*, Vol. 57A, No. 2, February 1979, pp 49-61.

- 136 Little, G. H., "Square Box Sections - Experimental Behaviour Under Combined Bending and Compression," *Journal of Strain Analysis*, Vol. 13, No. 3, 1978, pp 165-176.
- 137 Jackson, P. A., "The Buckling of Slender Bridge Piers and the Effective Height Provisions of BS5400: Part 4," Technical Report 561, Cement and Concrete Association (Wexham Springs, England), June 1985.
- 138 Heins, Conrad P. and Lawrie, Richard A., *Design of Modern Concrete Highway Bridges*, John Wiley and Sons, New York, 1984, pp 492-501.
- 139 *Building Code Requirements for Reinforced Concrete and Commentary (ACI 318-89) and Commentary - ACI 318R-89*, American Concrete Institute, Detroit, 1989, Commentary Section R10.9.1.
- 140 Gerard, George, and Becker, Herbert, *Handbook of Structural Stability, Part I, Buckling of Flat Plates*, NACA Technical Note 3781, United States National Advisory Committee for Aeronautics, Washington, D.C., 1957.
- 141 Taylor, Andrew W., "Behavior of Thin-Walled Hollow Concrete Bridge Piers and Pylons," Ph.D. dissertation, The University of Texas at Austin, December 1990, 313 pp.